



University
of Glasgow

Crooks, David R.M. (2002) *Mechanical loss and its significance in the test mass mirrors of gravitational wave detectors*. PhD thesis.

<http://theses.gla.ac.uk/2893/>

Copyright and moral rights for this thesis are retained by the author

A copy can be downloaded for personal non-commercial research or study, without prior permission or charge

This thesis cannot be reproduced or quoted extensively from without first obtaining permission in writing from the Author

The content must not be changed in any way or sold commercially in any format or medium without the formal permission of the Author

When referring to this work, full bibliographic details including the author, title, awarding institution and date of the thesis must be given

Mechanical Loss and its Significance in the Test
Mass Mirrors of Gravitational Wave Detectors

David R. M. Crooks, M. Sci.

Department of Physics and Astronomy,
University of Glasgow

Presented as a thesis for the degree of Ph.D.
in the University of Glasgow, University Avenue,
Glasgow G12 8QQ.

November 18, 2002

Contents

Acknowledgements	xxi
Preface	xxiii
Summary	xxvi
1 The Nature, Sources and Detection of Gravitational Waves	1
1.1 Introduction	1
1.2 The Nature of Gravitational Waves	3
1.2.1 Relativity	3
1.3 Sources of Gravitational Waves	6
1.3.1 Burst Sources	6
1.3.2 Continuous Sources - Spinning Neutron Stars	8
1.3.3 Stochastic Background	10

1.4	Types of detector	12
1.4.1	Ground based detectors - Resonant Bar	12
1.4.2	Ground Based - Interferometric	14
1.4.3	Space Based Interferometers	19
1.5	Noise sources	20
1.5.1	Quantum Noise Sources	21
1.5.2	Seismic Noise	23
1.5.3	Thermal noise	24
1.5.4	Other Noise Sources	25
1.6	GEO600	26
1.6.1	Dual recycling	29
1.7	Advanced LIGO	31
1.7.1	Suspension Design/ Test Masses	33
1.8	Conclusion	34
2	Thermal Noise	35
2.1	The First Observations of Thermal Noise	36
2.2	The Fluctuation Dissipation Theorem	37

2.3	Potential sources of dissipation	37
2.3.1	External suspension dissipation	38
2.3.2	Internal dissipation	38
2.3.3	The Internal Loss Factor $\phi(\omega)$	40
2.4	Thermal Noise Level	42
2.4.1	Single resonance	42
2.5	Multi Resonance System	44
2.6	Thermoelastic Damping	47
2.7	The Dilution Factor	50
2.8	Summary of Suspension System Thermal Noise Sources	53
2.8.1	Internal Modes	53
2.8.2	Suspension Modes	54
2.9	Calculation of Thermal Noise Level Due to Test Masses in an Interferometric Gravitational Wave Detector	56
2.9.1	Displacement Contribution of End Test Mass Per Arm	57
2.9.2	Displacement Contribution of Inboard Test Mass Per Arm	58
2.9.3	Displacement Contribution of Beamsplitter	59
2.9.4	Path Length Change in Terms of h	61

2.10	Conclusions	63
3	Dielectric coatings	64
3.1	Nature of dielectric coatings	64
3.2	Manufacturing techniques	67
3.2.1	Introduction	67
3.2.2	Coating Processes	68
3.2.3	Ion Beam Sputtering	69
3.2.4	Ion Assisted Deposition and Dual Ion Beam Sputtering .	71
3.2.5	Properties of Ion Sputtered Coatings	71
3.3	Dielectric Coating as Source of Mechanical Loss	72
3.4	Analysis technique	73
3.4.1	Loss Parameterisation	73
3.4.2	Analysis Requirements	75
3.5	Establishing Resonant Mode Shapes	76
3.5.1	Experimental Setup (Direct Modeshape)	77
3.6	Potential Source of Coating Loss	79
3.7	Conclusions	80

4	Numerical Calculation of Strain Energy	82
4.1	Definition of strain	83
4.1.1	One dimension	83
4.1.2	Two dimensions	83
4.1.3	Rotation and symmetry	84
4.2	Strain energy	85
4.2.1	Bulk Energy	86
4.2.2	Shear energy	87
4.3	Finite element analysis (FEA) and Algor	89
4.3.1	Model Construction and Assumptions	89
4.3.2	Verification of Algor Displacements	92
4.4	Ocean	94
4.4.1	Numerical scheme	95
4.4.2	Typical Ocean Usage (ocean.ini)	101
4.4.3	Ocean Stages - Data Import	104
4.4.4	Model used for different parameters	104
4.5	Verification	105
4.5.1	Results	111

4.5.2	Convergence	112
4.6	Conclusion	113
5	Analysis of Coated Silica Test Masses	115
5.1	Introduction	115
5.2	Initial Study - 10m Prototype Masses	116
5.2.1	Nature of samples	116
5.2.2	Results	117
5.2.3	Analysis	118
5.3	Analytical Ratio Calculation	119
5.3.1	Initial Case - Bar	121
5.4	Second Case: Cylinder	123
5.4.1	Regression Analysis	127
5.5	Mode Identification Confirmation	134
5.5.1	Results	135
5.5.2	Effect of Extra Mode on Analysis	138
5.6	Implications For Advanced Detectors	140
5.7	Extended Investigation (Silica/ Tantalum)	141

5.7.1	Nature of samples	141
5.7.2	Results	142
5.7.3	Analysis Case Study (30 layer $\lambda/4, \lambda/4$)	144
5.7.4	Results of Analysis	149
5.7.5	Coating split analysis	151
5.8	Alumina/ Tantara Coatings	155
5.9	Conclusions	156
6	Analysis of Coated Sapphire Substrates	157
6.1	Introduction	157
6.2	The Stiffness Tensor	158
6.2.1	Hooke's Law & the Stress Tensor	158
6.2.2	The Stiffness Tensor	161
6.2.3	Stiffness Matrix Rotation	163
6.2.4	Full Energy Description	165
6.3	Sapphire	165
6.3.1	Crystal Nature	165
6.3.2	Conversion from <i>c</i> - to <i>m</i> - axis	166

6.3.3	Manufacture	167
6.4	I-DEAS	167
6.4.1	I-DEAS Radial Mesh Construction	169
6.5	Necessary Changes to Ocean	171
6.6	Testing of Aocean & I-DEAS Models	173
6.6.1	Comparison of Algor (Isotropic) and I-DEAS (Full) Models	173
6.6.2	Comparison of Algor Energy Ratios (Isotropic) and I- DEAS Energy Ratios (Full)	175
6.7	Loss Measurement of a Coated <i>M</i> -axis Sapphire Sample	176
6.7.1	Experimental Losses	176
6.7.2	Analysis	176
6.7.3	Regression	179
6.8	Conclusions	182
7	Conclusions	183
A	Low Suspension Loss Measurement	185
A.1	Experimental Setup	186
B	10 m Prototype Modeshapes	188

C	Extended Study Silica Modeshapes	193
D	Sapphire Modeshapes	196
E	Ocean Source Code	200
F	ocean Source Code	239
G	Additional Papers	270
	References	272

List of Figures

1.1	<i>The two polarisations of gravitational waves - the “+” and “×” polarisations.</i>	5
1.2	<i>Likely sources detectable by advanced detectors[1]. The magenta lines indicate the sensitivity curves of current and mature detectors. The blue lines indicate the expected magnitude of the signal from binary inspirals, with the green offshoots indicating the signal magnitude from the merger of these binaries.</i>	11
1.3	<i>Basic Michelson interferometer</i>	15
1.4	<i>Schematic diagram showing a delay line interferometer design</i> .	16
1.5	<i>Schematic diagram showing a Fabry-Perot interferometer design</i>	18
1.6	<i>The proposed orbit of LISA</i>	20
1.7	<i>The optical layout of GEO600</i>	27
1.8	<i>The modecleaner suspension system used in GEO600 (suspension here shown without reaction mass)</i>	28
1.9	<i>The end test mass suspension system used in GEO600</i>	29

1.10	<i>The quasi monolithic silica suspension system used in GEO600</i>	30
1.11	<i>Expected noise curves for GEO600 (Broadband configuration)</i>	32
1.12	<i>Expected noise curves for GEO600 (Narrowband configuration)</i>	32
2.1	<i>Simplified optical path of GEO600. The length of these paths is shown in red (i.e. x_1, x_2, x_3 and x_6)</i>	57
2.2	<i>Optical path length change caused by movement of ETM</i>	58
2.3	<i>Optical path length change caused by movement of ITM</i>	59
2.4	<i>Optical path length change caused by movement of BS</i>	60
2.5	<i>Motion of the masses at the interferometer caused by an incident gravitational wave</i>	62
3.1	<i>Diagram of a dielectric coating with 2 different materials in alternating layers</i>	66
3.2	<i>A simple sputtering setup[2]</i>	70
3.3	<i>A DC glow discharge sputtering scheme[2]</i>	70
3.4	<i>A dual ion beam sputtering setup</i>	72
3.5	<i>Experimental arrangement used to determine the modeshapes of test masses</i>	77
3.6	<i>Location of substrate/ coating interface</i>	79
3.7	<i>Location of coating/ coating interface</i>	79

4.1	<i>Typical one dimensional shear deformation</i>	83
4.2	<i>Rotation of square plate</i>	84
4.3	<i>Typical shear deformation</i>	87
4.4	<i>Diameter of cylindrical mass divided into sections</i>	91
4.5	<i>One radially meshed disc</i>	91
4.6	<i>Full cylinder</i>	92
4.7	<i>Algor screenshot showing typical deformation of substrate in one of its natural modes</i>	92
4.8	<i>Screenshot from Algor showing the fundamental longitudinal mode used in the displacement graph in figure 4.8</i>	93
4.9	<i>Graph of displacements in the z direction vs. the original posi- tions of the nodes on the z axis for the fundamental longitudinal mode of a cylindrical mass</i>	94
4.10	<i>Local cartesian coordinates</i>	96
4.11	<i>Typical node neighbourhood. \mathbf{r} refers to the centre point</i>	97
4.12	<i>Local cartesian coordinates</i>	99
4.13	<i>Local neighbourhood of points for one node in a meshed disc</i>	100
4.14	<i>Bar bent into half parabola</i>	106
4.15	<i>Displacement of point on the centreline of the bar after bar is bent into a parabola</i>	107

4.16	<i>Rotation of cross section</i>	108
4.17	<i>Convergence of energy values calculated by Ocean</i>	112
4.18	<i>Example convergence</i>	113
5.1	<i>Convergence of energy ratio for the asymmetric drum, fitted with an exponential curve</i>	120
5.2	<i>Graph plotting all the relevant energy ratios per μm of coating material. Points \times are those of the surface ratio and those marked $+$ are those of the barrel</i>	120
5.3	<i>Diagram of a bent bar</i>	121
5.4	<i>A segment of a cylindrical mass</i>	124
5.5	<i>Diagram of a mass distorted into its asymmetric drum mode</i>	124
5.6	<i>Close up of segment</i>	124
5.7	<i>Variation of measured loss factor against front surface energy ratio per micron thickness of coating for each mode of the 7940 and 7980 silica test masses</i>	128
5.8	<i>Comparison of the experimental loss with that predicted using a three-parameter multiregression analysis for (a) the 7940 and (b) the 7980 mass, assuming that the barrel is completely covered in coating.</i>	129
5.9	<i>Graph of experimental loss against predicted loss for 7980 mass using a partial barrel coating</i>	130

5.10	<i>Graph of experimental loss against predicted loss for 7980 mass using shear and bulk front surface energy ratios</i>	131
5.11	<i>Graph of experimental loss against predicted loss for the 7980 mass using shear and bulk front surface energy ratios and total barrel energy ratios</i>	132
5.12	<i>Comparison of the experimental loss with that predicted using a three-parameter multiregression analysis for (a) the 7940 and (b) the 7980 mass, with the symmetric drum removed</i>	134
5.13	<i>Photograph of experiment to determine modeshapes of cylindrical mass</i>	135
5.14	<i>Diagram showing the various accelerometer sites on the front surface of a cylindrical mass</i>	136
5.15	<i>Transfer function between the centre of the surface and the drive</i>	137
5.16	<i>Transfer function between the drive and accelerometer placed at the edge of the mass</i>	138
5.17	<i>Transfer function between accelerometer and drive with no mass present</i>	139
5.18	<i>Graph of experimental losses against predicted losses for the 7980 mass using front surface and total barrel energy ratios, including the new mode</i>	139

5.19	<i>Representative losses for each of the coating types, including the annealed mass. “Before” indicates the loss before the sample has been treated/ coated and “After” refers to the loss after coating/ treatment. The different modes are “c4” - clover-4, “a” - asymmetric drum, “f” - fundamental, “2a” - second asymmetric drum and “s” - symmetric drum. Pictures of these modes may be found in appendix C.</i>	143
5.20	<i>Graph of experimental coated loss minus measured intrinsic loss against predicted loss for two masses, each with a 30 layer $\lambda/4$, $\lambda/4$ coating. The blue set of data corresponds to that shown in figure 5.19.</i>	144
5.21	<i>The losses measured before and after an uncoated sample had been heated to the temperature used to anneal the coatings on other samples. This data is the same as the annealed sample in figure 5.19</i>	145
5.22	<i>Graph of experimental coated loss minus appropriate annealed loss against predicted loss for two 30 layer $\lambda/4$, $\lambda/4$ coated masses. The blue data set refers to the sample shown in figure 5.19 . . .</i>	146
5.23	<i>Graph of experimental coated loss minus appropriate annealed loss against predicted loss using only 4 modes for two 30 layer $\lambda/4$, $\lambda/4$ coated samples, where the blue data set corresponds to the data in figure 5.19</i>	147
5.24	<i>Graph of the magnitudes of displacements of the edge of the sample in various modes. Note the particularly large curvature of the symmetric drum</i>	147

5.25	<i>Graph of experimental coated loss minus appropriate 2 layer loss against predicted loss using only 4 modes for two 30 layer $\lambda/4, \lambda/4$ coated masses. Again, the blue data set refers to the sample shown in figure 5.19</i>	149
6.1	<i>A small body which we may use to define the terms of the stress tensor</i>	159
6.2	<i>View onto the xy plane showing the relevant stress components for the torque as described in the text</i>	160
6.3	<i>Diagram of crystal axes of sapphire[3]</i>	165
6.4	<i>Tetrahedral mesh as used in I-DEAS</i>	168
6.5	<i>Initial stage of radial meshing in I-DEAS</i>	169
6.6	<i>Meshed rectangle</i>	170
6.7	<i>Final radial mesh in I-DEAS</i>	170
6.8	<i>Fit of experimental coated loss against energy ratio</i>	180
6.9	<i>Fit of experimental coated loss against energy ratio</i>	181
A.1	<i>Experimental arrangement used to measure the loss factors of suspended test masses</i>	187
B.1	<i>“Bending” mode</i>	188
B.2	<i>“Asymmetric Drum” mode</i>	189

B.3	<i>“Fundamental” mode</i>	189
B.4	<i>“Bar” mode</i>	190
B.5	<i>“Clover-4” mode</i>	190
B.6	<i>“Symmetric Drum” mode</i>	191
B.7	<i>“Expansion” mode</i>	191
B.8	<i>“2nd Asymmetric Drum” mode</i>	192
C.1	<i>“Asymmetric Drum” mode</i>	193
C.2	<i>“Fundamental” mode</i>	194
C.3	<i>“Clover-4” mode</i>	194
C.4	<i>“Symmetric Drum” mode</i>	195
C.5	<i>“2nd Asymmetric Drum” mode</i>	195
D.1	<i>Mode “i”</i>	196
D.2	<i>Mode “ii”</i>	197
D.3	<i>Modes “iii” & “iv”</i>	197
D.4	<i>Mode v</i>	198
D.5	<i>Modes “vi” & “vii”</i>	198
D.6	<i>Mode “viii”</i>	199

D.7 Mode “ix”	199
-------------------------	-----

List of Tables

1.1	<i>Current resonant bar detectors</i>	13
1.2	<i>Current resonant bar detector sensitivities</i>	13
1.3	<i>Comparison of features of LIGO with its proposed upgrade Advanced LIGO</i>	33
2.1	<i>Properties used in calculation of $\sqrt{S_x(\omega)}$ for fused silica</i>	46
4.1	<i>Partial strain values used to calculate strain components in local cartesian frame</i>	97
4.2	<i>Test constants</i>	111
4.3	<i>Comparison between analytical and Ocean test energies</i>	112
5.1	<i>Experimental losses with mode classification (due to McMahon[4]) and modelled and measured frequencies</i>	117
5.2	<i>Material properties used for coatings and substrate</i>	119

5.3	<i>Coating loss results for the 7980 and 7940 masses. Errors are at the 1 standard deviation level</i>	133
5.4	<i>Results of oscilloscope modeshape experiment showing phase and node position</i>	136
5.5	<i>Table showing different coating compositions used in investigation of the source of the coating loss</i>	142
5.6	<i>Results of coating analysis</i>	150
5.7	<i>Values used in the simultaneous equations involved in the calculation of individual losses due to different coating materials . . .</i>	153
5.8	<i>Physical thicknesses associated with different optical thicknesses of silica and tantala coating layers</i>	154
5.9	<i>Mean values of individual coating losses using errors from spread rather than those calculated</i>	155
6.1	<i>Stages of verification of I-DEAS derived energy ratios</i>	173
6.2	<i>Comparison of Algor and I-DEAS FEA models</i>	174
6.3	<i>Comparison of Algor and I-DEAS generated energy ratios</i>	175
6.4	<i>Experimental losses measured on m-axis sapphire sample</i>	177
6.5	<i>Mode candidates for m axis sapphire sample. Modeshapes are given in appendix D</i>	178

Acknowledgements

First of all, I would like to thank my supervisors Jim Hough and Norna Robertson for all their support and encouragement over the past three years. I would also like to thank Geppo Cagnoli and Sheila Rowan for the many useful discussions we had. In addition, without the work of Peter Sneddon I would not have been able to complete the work in this thesis. My thanks also go to Colin Craig, Allan Latta and Neil Robertson for their help in the assembly of experimental apparatus. I also appreciated the help of Vickie Livingstone, our secretary, for her help during the writing of my thesis. -

I should say a big thank you to my office mates over the past three years: Calum Torrie, Peter Sneddon, Mike-Perruer Lloyd and latterly Bryan Barr, Eoin Elliffe and Christian Killow. All have brought their own unique qualities to the office (some more than others) and somehow managed to put up with me on a daily basis. I would also like to thank the rest of the Institute for Gravitational Research for their support and assistance.

I would like to acknowledge the support of PPARC who funded my research.

Outside the group I would also like to thank Gordon, Christine, Marie, Kate, Tedd, Claire, and Ewan my flatmate. I would also like to thank Christine Stewart, my Alexander Technique teacher.

Finally, I would like to thank my parents and sister Elaine for their endless support over the past few years which has helped keep me on an even keel throughout.

Preface

This thesis is an account of the work carried out between October 1999 and October 2002 towards the investigation of the mechanical loss associated with dielectric coatings used to turn the silica test masses used in current gravitational wave detectors into mirrors.

Chapter One discusses the nature, sources and detection methods of gravitational waves. This work has been derived from published literature.

Chapter Two gives an introduction to thermal noise; its calculation, methods of minimisation and its influence on the design of gravitational wave detectors. This work has derived from current literature with some aspects begin derived by the author in conjunction with G. Cagnoli and J. Hough.

Chapter Three contains firstly some relevant aspects of multilayer and composite material theory. Subsequently methods of applying coatings are described. These discussions are derived from literature. The latter sections of the chapter deal with the theoretical description of the mechanical loss associated with dielectric coatings and an experimental technique for determining mode shapes useful in the preceding analysis. This latter work was carried out by the author in conjunction with J. Hough and S. Rowan; the experimental technique was designed and carried out by the author.

Chapter Four initially discusses the theory of strain energy; this is drawn from literature. The remainder of the chapter discusses the methods required to calculate strain energy ratios in test substrates using finite element analysis and analytical software written by the author. This work was primarily carried out by the author, in conjunction with G. Cagnoli.

Chapter Five discusses the effects on their loss factors of applying a dielectric mirror coating to silica substrates. The substrates were modelled by the author in the fashion described previously. The results were then analysed; two investigations are presented. The experimental results were gathered by P. Sneddon and subsequent discussions were held between the author, P.H. Sneddon, G. Cagnoli, S. Rowan and J. Hough.

Chapter Six presents the necessary theory necessary to obtain the strain energy ratios for an anisotropic material. The appropriate changes to the calculation software are then discussed. Finally, an initial investigation into the effects of applying a coating to a sapphire substrate is presented. The experimental work was again carried out by P.H. Sneddon. The modelling was carried out by the author and discussions were held again between the author, P.H. Sneddon, G. Cagnoli, S. Rowan and J. Hough.

Chapter Seven gives the conclusions to the work presented. In addition, some discussion is given on the potential future avenues the work may follow.

Appendix A details the experimental loss measurement system used in chapters five and six. This was developed by S. Rowan, J. Hough, G. Cagnoli and P.H. Sneddon.

Appendix B shows the modeshapes for the substrate used in the initial part of chapter five.

Appendix C shows the modeshapes for the substrate used in the latter part of chapter five.

Appendix D shows the modeshapes for the substrate used in chapter six.

Appendix E gives the source code for Ocean, written by the author.

Appendix F gives the source code for Aocean, written by the author.

Summary

In 1916, Einstein predicted the existence of gravitational waves in his General Theory of Relativity. These waves may be considered to be ripples in the curvature of space-time. There is currently only indirect evidence for their existence; the search for direct evidence of gravitational waves is one of the most challenging goals in experimental physics today. Their discovery will not only provide tests of some of the predictions of Einstein's theory but also fascinating insights into many astrophysical phenomena.

Gravitational waves are quadrupole in nature and produce a tidal strain in space. They interact only weakly with matter which means that they are not shielded over long distances in the same way as EM waves are; however this also means that gravitational waves are very hard to detect. Waves emitted by violent astrophysical sources are predicted to produce rms strains at the Earth of the order $\sim 10^{-21}$ to $\sim 10^{-22}$ at frequencies amenable to detection by ground based detectors (i.e. a few Hz to a few kHz). All detection schemes involve the detection of these strains; one of the most promising of these is based on laser interferometry.

There are at the current time a number of laser interferometric detectors under construction; GEO600 in Germany. LIGO in America. VIRGO in Italy and TAMA in Japan. LISA is a space based interferometer planned for launch

in the next ten years. The GEO600 observatory in Germany is the work of a collaboration between the Albert Einstein Institute at Hannover and Golm, the Max-Planck-Institut für Quantenoptik at Garching, the University of Glasgow and the University of Wales, Cardiff, with contributions from the Laser-Zentrum, Hannover. GEO600 is a 600m arm length interferometer and is close to the end of commissioning.

GEO600 is designed to operate over a frequency range of 50 Hz to a few kHz. Between 50 Hz and 200 Hz the limit to the sensitivity of the detector is set by the thermal noise associated with the test masses that form the mirrors of the interferometer, which in GEO600 are manufactured from fused silica. The level of this thermal noise is set by the level of mechanical loss factors of the materials for the test masses and suspension elements within the system. The thermal noise contribution to GEO600 is expected to be $2 \times 10^{-22} / \sqrt{Hz}$ at 50 Hz. There are two possible methods which may be used to improve sensitivity; the first is to transplant GEO600 technology to an interferometer with longer arm length such as the American 4 km detector LIGO. The second is to pursue test masses with a lower thermal noise contribution.

Both of these are being used for the proposed upgrade to LIGO called “Advanced LIGO”, which will employ a suspension similar but more advanced than that used in GEO600. It is currently planned that Advanced LIGO will use sapphire test masses which are expected to yield a lower thermal noise contribution than fused silica.

As a result of the pursuit of the lowest possible contribution of thermal noise to the overall noise level of current and future detectors, all possible sources of thermal noise beyond that intrinsic to the material are under strenuous examination. One possible source of excess thermal noise is the dielectric coatings used to turn fused silica test masses into mirrors.

The work of this thesis involves the analysis of mechanical losses associated with coated test masses manufactured from fused silica, to determine the existence and level of excess loss associated with the coatings on these substrates. In particular, a major part of this analysis requires the calculation of the ratio of the strain energy stored in the dielectric coating to the strain energy stored in the substrate for a number of the resonant modes of the test mass. This is extremely difficult to calculate analytically for all but the simplest of modes. Finite element analysis had to be used to calculate the modeshapes of a number of resonant modes of the test masses. A piece of analytical software was specifically written to use the output of the finite element analysis package to calculate these energy ratios. The majority of this thesis is concerned with the methodology and usage of this software in the context of a number of analyses of different coated test masses. In addition, a technique was developed to allow experimental determination of modeshapes. This method could then be used to confirm or identify the nature of different modes.

An initial investigation suggested that the loss associated with the coatings may prove significant for future generations of detectors such as Advanced LIGO. Further investigations suggested that the principle source of coating loss was due to the materials used in the coatings themselves. These investigations also suggested that for the coatings used, which were manufactured using tantalum pentoxide and silica, the tantalum pentoxide had a higher mechanical loss than the silica. Investigations into different coating materials have been initiated. Finally, preliminary tests on a coated sapphire mirror have been completed which give an upper limit to the loss of a coating on a sapphire mass. These tests required comprehensive changes to be made to the analytical energy ratio software to allow the analysis of anisotropic materials such as sapphire and to allow the output from different finite element packages to be used.

Chapter 1

The Nature, Sources and Detection of Gravitational Waves

1.1 Introduction

One consequence of Einstein's General Theory of Relativity[5] was that a gravitational field does not change instantaneously at an arbitrary distance from a moving source; indeed, Einstein proposed that gravitational effects propagate at the speed of light. In addition, he proposed that there exist wave solutions to the linearised Einstein Field Equations, suggesting that gravitational radiation would be emitted by masses under acceleration

The detection of such waves would have two major consequences: firstly it would provide further verification of Einstein's General Theory of Relativity in the weak field limit and a test of General Relativity in the non-linear strong

field. Secondly, it will allow observations of violent astrophysical phenomena to be made which would both complement and extend current observations. For example, gravitational wave astronomy would allow us to see into the heart of the coalescence of black hole/ black hole binaries (see section 1.3.1). This is a very similar situation to that extant before the rise of X-ray astronomy.

Current evidence of the existence of gravitational waves is indirect in nature. In 1973 Hulse and Taylor observed the binary pulsar PSR 1913+16[6] and over the following years a great number of observations were made of this binary. They used the orbit of the binary to predict the rate of energy loss due to gravitational radiation. This was then used to predict the rate of binary inspiral which was compared to the observed rate. These were found to agree. Indeed, Taylor and Weisberg [7, 8] found that the observed rate of decrease of the orbital period and the calculated value of the decrease expected as a result of the emission of gravitational radiation agreed to within 1%.

The direct detection of gravitational waves has been sought for over 30 years and remains one of the most challenging goals in experimental physics. The first generation of long baseline ground based interferometric detectors (section 1.4.2) are nearing completion; detectors in this generation include GEO 600[9], VIRGO[10], LIGO[11] and TAMA[12] (see section 1.4.2). These detectors have a significantly greater sensitivity than that of previous systems, but even with this improvement only a few astrophysical sources may be expected to be detected in the first instance. Hence there is a great deal of research currently being carried out into upgrades to these detectors to give advanced, or mature, detectors with which real astronomy may be carried out. In particular, with respect to this thesis, the LIGO project is investigating an upgrade to its detectors, “Advanced” LIGO[13]. The work in this thesis is applicable to the majority of the current detectors but is particularly directed towards the GEO

600 and Advanced LIGO projects. In this chapter the fundamental nature of gravitational waves, possible sources and proposed methods of detection will be discussed.

1.2 The Nature of Gravitational Waves

1.2.1 Relativity

From Special Relativity, the spacetime interval ds is described as:

$$ds^2 = -c^2 dt^2 + dx^2 + dy^2 + dz^2 \quad (1.1)$$

or, more generally,

$$ds^2 = \eta_{\mu\nu} dx^\mu dx^\nu \quad (1.2)$$

using the ‘Minkowski’ metric of flat spacetime $\eta_{\mu\nu}$;

$$\eta_{\mu\nu} = \begin{pmatrix} -1 & 0 & 0 & 0 \\ 0 & 1 & 0 & 0 \\ 0 & 0 & 1 & 0 \\ 0 & 0 & 0 & 1 \end{pmatrix} \quad (1.3)$$

In General Relativity, spacetime is no longer necessarily flat and the spacetime interval is generalised to

$$ds^2 = g_{\mu\nu} dx^\mu dx^\nu \quad (1.4)$$

with spacetime metric $g_{\mu\nu}$. Consider a perturbation in spacetime. If viewed from great distance (as the Earth would be from any astrophysical sources), we may describe this perturbation in the following way

$$g_{\mu\nu} = \eta_{\mu\nu} + h_{\mu\nu} \quad (1.5)$$

where $h_{\mu\nu}$ is some small perturbation.

We have a certain amount of freedom in the description of $h_{\mu\nu}$. One particular “gauge” in which the mathematics and physics become particularly clear is the *transverse - traceless gauge*, or TT gauge, in which the co-ordinates are marked by the world lines of a number of freely falling masses. In this gauge, the weak field limit of the linearised Einstein Field Equations may be written as

$$\left(\nabla^2 - \frac{1}{c^2} \frac{\partial^2}{\partial t^2}\right) h_{\mu\nu} = 0 \quad (1.6)$$

i.e, a wave equation to which there are consequent wave solutions. Note particularly the result that the waves always travel with velocity c .

Consider now the form of $h_{\mu\nu}$. Since it is transverse and traceless, it must take the form

$$h_{\mu\nu} = \begin{pmatrix} 0 & 0 & 0 & 0 \\ 0 & a & b & 0 \\ 0 & b & -a & 0 \\ 0 & 0 & 0 & 0 \end{pmatrix} \quad (1.7)$$

$h_{\mu\nu}$ may therefore be described as the linear combination $h_{\mu\nu} = ah_+ + bh_\times$ with

$$h_+ = \begin{pmatrix} 0 & 0 & 0 & 0 \\ 0 & 1 & 0 & 0 \\ 0 & 0 & -1 & 0 \\ 0 & 0 & 0 & 0 \end{pmatrix} \quad h_\times = \begin{pmatrix} 0 & 0 & 0 & 0 \\ 0 & 0 & 1 & 0 \\ 0 & 1 & 0 & 0 \\ 0 & 0 & 0 & 0 \end{pmatrix} \quad (1.8)$$

Thus there exist two polarisations of waves at 45° to each other. The effect of each polarisation of wave, incident perpendicular to the page, is shown in

figure 1.1. The effect of a gravitational wave of amplitude h on the masses shown in the figure is to give a strain in each axis of $\Delta L/L$, where ΔL is the change in the diameter of the ring in one axis by the wave with L the original diameter of the ring. The total strain will therefore be $2\Delta L/L$. The relationship between h and this strain is given by,

$$h = \frac{2\Delta L}{L} \quad (1.9)$$

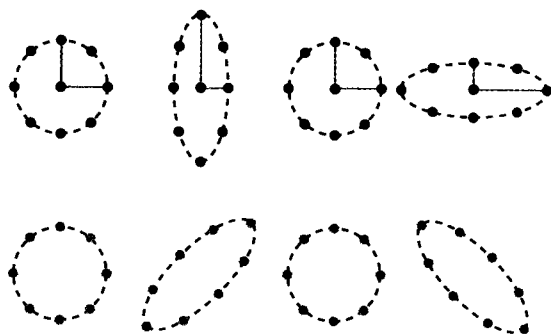


Figure 1.1: *The two polarisations of gravitational waves - the “+” and “x” polarisations.*

Illuminating insight into the nature of gravitational waves may be gained by analogy with electromagnetic radiation. In the same way that conservation of charge prevents the existence of electromagnetic monopoles, conservation of energy indicates that gravitational monopoles do not exist. Similarly, conservation of momentum precludes gravitational dipoles. Hence the lowest order of gravitational radiation must be quadrupole in nature; i.e. gravitational waves will only be caused by the asymmetric acceleration of mass.

1.3 Sources of Gravitational Waves

Ideally, one would wish to generate gravitational waves in a laboratory situation (in a similar way to that used by Heinrich Hertz for the detection of electromagnetic waves) in order to have complete control of the experiment. However, Saulson[14] suggests an interesting thought experiment concerning a “typical” lab generator of gravitational waves. This consisted of 2 masses each with a mass of 1 tonne, 2 metres apart, rotating about their common centre of mass with a frequency 1 kHz. The magnitude of h which this generator might create was calculated to be $h \approx 1 \times 10^{-38}$ at a distance of one wavelength from the source. This strain would result in a displacement of $\sim 1 \times 10^{-35}$ m on a length scale of kilometres. This is too small to provide a useful source of gravitational waves. Hence we must look elsewhere, to astrophysical sources. The remainder of this section will deal with a number of such sources. We shall be concerned primarily with ground based detectors during the course of this work, which are limited to a bandwidth of ~ 10 Hz to \sim few kHz due to noise sources which will be discussed shortly. Hence it is sources in this bandwidth that will feature here. First, *transient* or *burst* sources will be discussed.

1.3.1 Burst Sources

Burst sources are those which occur over a short timescale, from milliseconds to minutes.

Coalescing Binaries

Systems of pairs of high density stars rotating about their common centre of mass are known as *compact binaries*. There are three types which interest us:

black hole/black hole (BH/BH) , neutron star/neutron star (NS/NS)and neutron star/black hole (NS/BH) binaries. PSR 1913+16, mentioned earlier, is a NS/NS binary in which, as previously mentioned, the orbital frequency and hence the radiated gravitational wave frequency increases with time. Eventually, the two stars will coalesce; for example, PSR1913+16 will coalesce in $\sim 10^8$ years. In the last few seconds before this coalescence, the gravitational wave frequency will be high enough to be within the valid bandwidth for ground based detectors. Schutz[15] calculated that the approximate strain amplitude h from coalescing NS/NS binaries as:

$$h \approx 1 \times 10^{-23} \left(\frac{100\text{Mpc}}{r} \right) \left(\frac{M_b}{1.2M_\odot} \right)^{\frac{5}{3}} \left(\frac{f}{200\text{Hz}} \right)^{\frac{2}{3}} \quad (1.10)$$

where $M_b = (M_1 M_2)^{3/5} / (M_1 + M_2)^{1/5}$ is the mass parameter of the binary and M_1 and M_2 are the masses of the two stars. The binary is at a distance from the Earth r and the radiation is at frequency f . M_\odot is the solar mass.

BH/BH binaries are expected to be rarer than NS/NS binaries, but their greater mass and greater wave amplitude generated makes it likely that more BH/BH binaries will be detected. It is estimated [16] that initial LIGO type detectors will have a NS/NS detection rate of $\sim 0.03 \text{ yr}^{-1}$ and a BH/BH rate of up to 0.5 yr^{-1} . Advanced configurations should have equivalent rates of $0.5 - 100 \text{ yr}^{-1}$ and $100 - 2000 \text{ yr}^{-1}$ respectively.

Supernovae

Supernovae, amongst the most spectacular events to occur in the Universe, are classified into two types. Type I supernovae are believed to involve binary systems of low mass stars such as white dwarfs. One process leading to a type

I supernova, accretion induced collapse of white dwarfs, is thought to produce gravitational waves.

Type II supernovae involve the violent collapse of a massive stellar core to produce a neutron star or a black hole. If such a collapse is symmetrical then no gravitational waves will be created. If the collapse is asymmetric due to the star's core having significant angular momentum, gravitational waves may be produced. Schutz[17] estimated the typical magnitude of h expected from a supernova to be

$$h \approx 5 \times 10^{-22} \left(\frac{E}{10^{-3} M_{\odot} c^2} \right) \left(\frac{15 \text{Mpc}}{r} \right) \left(\frac{1 \text{kHz}}{f} \right) \left(\frac{1 \text{ms}}{\tau} \right)^{\frac{1}{2}} \quad (1.11)$$

where E is the energy emitted in the form of gravitational waves by the source at a distance r from the detector and predominately at a frequency f over a timescale τ .

The event rate for both Type I and II supernovae, out to the Virgo cluster at a distance of $\sim 15 \text{Mpc}$, has been estimated as several per month[18].

1.3.2 Continuous Sources - Spinning Neutron Stars

Although binary stars generate waves throughout their lives, these waves have too low a frequency to be detected by ground based detectors until their final seconds of life (space based detectors should, however, be able to observe such sources). There exist, however, other potential continuous sources. The signal to noise ratio for all of these sources can be increased by increasing the integration time.

Single spinning neutron stars can be a source of gravitational waves if they

spin non-axisymmetrically. A typical pulsar will emit gravitational waves at twice its rotational frequency f_{rot} . An estimate of the likely amplitude from such a source is[19]

$$h \approx 6 \times 10^{-25} \left(\frac{f_{rot}}{500Hz} \right)^2 \left(\frac{1kpc}{r} \right) \left(\frac{\epsilon}{10^{-6}} \right) \quad (1.12)$$

where ϵ , the equatorial eccentricity, is a measure of the asymmetry of the star and r is the distance of the star from the Earth.

One known pulsar, the Crab pulsar, is expected to be emitting gravitational waves at approximately 60 Hz. An upper limit of the signal from the Crab pulsar of $h \approx 10^{-24}$ has been calculated for $\epsilon = 7 \times 10^{-4}$, $r = 1.8$ kpc and $f_{rot}=30$ Hz[19]. The sensitivity of an instrument to signals from “unknown” neutron stars is reduced by a factor of 10 due to the increased size of the parameter space over which a search must take place[20].

Low Mass X-Ray Binaries

An interesting class of objects which contains deformed spinning neutron stars is the class of low mass X-ray binaries (LMXBs). These systems consist of neutron stars being torqued by accretion from a companion. Current predictions suggest that a mature detector such as Advanced LIGO should be able to detect the LMXB Sco-X1 with three weeks of integration; in addition, a further 7 LMXBs will be visible on a similar timescale at frequencies around 600 Hz if the detector is used in a narrow band configuration[21] (see section 1.6.1).

Accretion Induced White Dwarf Collapse

If the collapse of a white dwarf due to accretion from a neighbour results in a fast spinning neutron star and if this can be reasonably modelled, it is likely that Advanced LIGO, for example, should be able to detect such sources at a rate of $\sim 500 \text{ yr}^{-1}$ [20].

1.3.3 Stochastic Background

The final type of gravitational wave signals that will be discussed here are in the form of stochastic background. This is not in itself a single source, but rather a superposition of “random”, uncorrelated signals which are not individually resolvable. The stochastic background may be seen as a source of noise in a single detector; indeed, it cannot be detected by a single detector but requires a correlation between two detectors. Nonetheless, with care useful information can be drawn.

Perhaps the most important source of stochastic background waves results from the dynamics of the early universe, a source covering the entire sky in a similar way to the cosmic microwave background.

One prediction of the magnitude of h likely to occur due to the stochastic background, which uses the cosmic string scenario for the formation of the universe, is[22]:

$$h \approx 1.8 \times 10^{-25} \left(\frac{H_0}{100 \text{ km s}^{-1} \text{ Mpc}^{-1}} \right) \left(\frac{\Omega_{\text{gw}}}{10^{-8}} \right)^{\frac{1}{2}} \left(\frac{f}{100 \text{ Hz}} \right)^{-\frac{3}{2}} \left(\frac{B}{2 \text{ Hz}} \right)^{\frac{1}{2}} \quad (1.13)$$

in a bandwidth B about a frequency f . where Ω_{gw} is the energy density per

logarithmic frequency interval required to close the universe and H_o is the present value of Hubble's Constant.

In summary, a chart showing all of the sources likely to be detected by an advanced detector is shown in figure 1.2, where WB refers to a broadband advanced detector and NB refers to a narrowband; these refer to the different modes of operation possible with signal recycling (section 1.6.1).

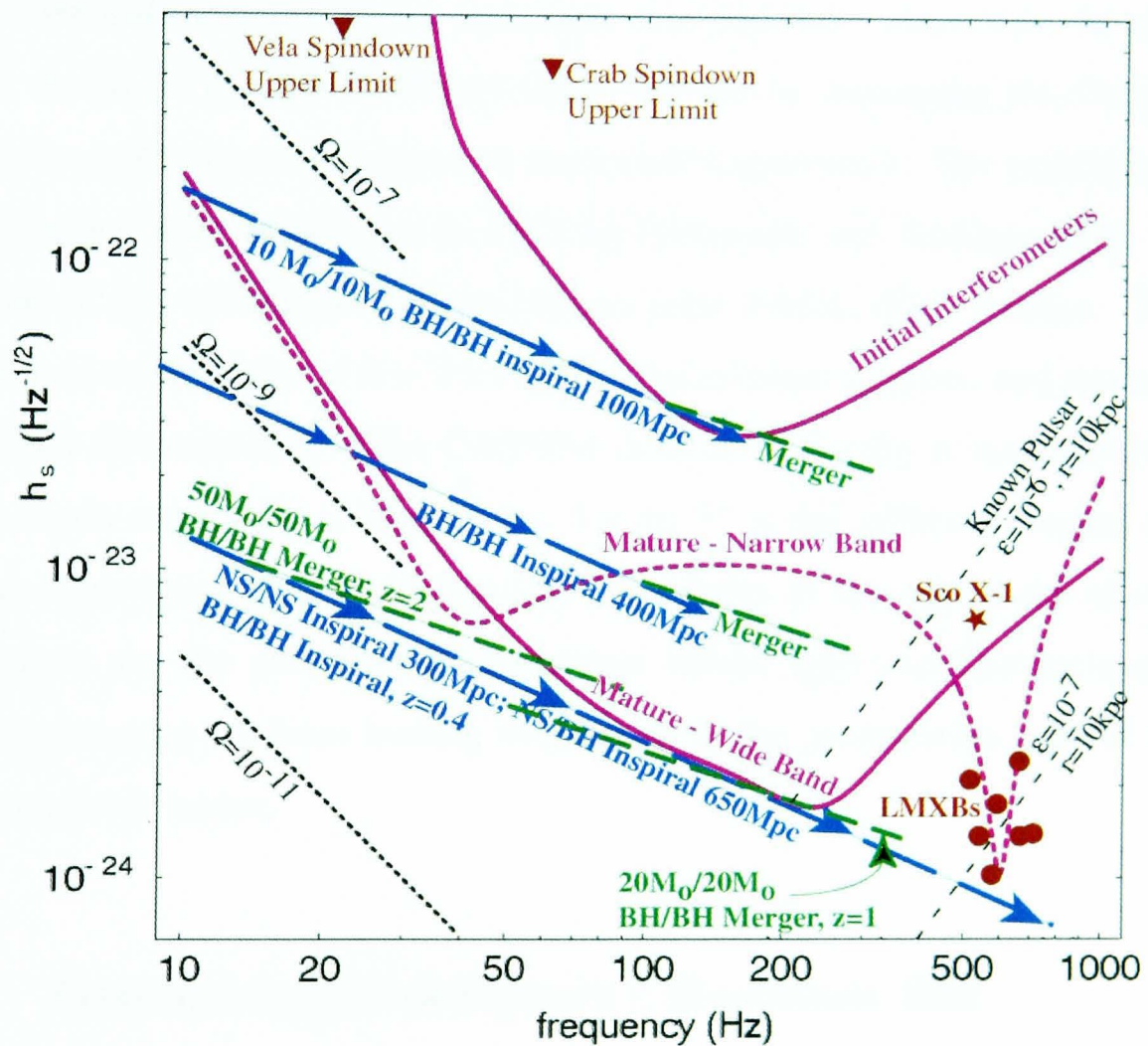


Figure 1.2: *Likely sources detectable by advanced detectors*[1]. The magenta lines indicate the sensitivity curves of current and mature detectors. The blue lines indicate the expected magnitude of the signal from binary inspirals, with the green offshoots indicating the signal magnitude from the merger of these binaries.

1.4 Types of detector

There exist several designs of instrument suitable for the detection of gravitational waves, all of which must deal with the common problem of the extremely small expected magnitude of h . Although the detector types fall mainly into two sections, resonant bar and interferometric (ground- and space-based), there do exist other possible strategies. One of these is to use the small changes in the relative separation of the Earth and some interplanetary spacecraft. In principle it would be possible to detect these changes by measuring the Doppler shift of the radio signals employed to track such a spacecraft. The principles of this technique were established in 1975 by Estabrook and Wahlquist[23]. An early use of this technique was the Ulysses joint NASA/ ESA mission. This mission had a sensitivity of $h \sim 3 \times 10^{-15}$ in the millihertz region, and returned no positive detections[24]. The CASSINI mission to Saturn is anticipated to have a strain sensitivity of around $h \sim 5 \times 10^{-17}$ in the millihertz region and with an observation time of 40 days[25]. The limits to the sensitivity of such a technique are the precision of the master clocks used and fluctuations in the interplanetary medium leading to changes in the propagation time of the electromagnetic waves.

1.4.1 Ground based detectors - Resonant Bar

The original experimental instrument used in the search for gravitational waves was the resonant bar[26]. In essence such detectors consist of a large bar of metal whose motion will be excited by the incidence of a pulse of gravitational wave. The resulting resonant motion would then be picked up and amplified using transducers well coupled to the bar.

Indeed, in the 1960s, Weber constructed a pair of resonant bar detectors and claimed to have detected gravitational waves using the coincident signals of the two detectors. The sensitivity of these original detectors was $\tilde{h} \sim 2 \times 10^{-16}/\sqrt{Hz}$ [27] However, following this, further bars were constructed with initially similar and subsequently better sensitivity and no further detections were made. At the current time, a number of improved resonant bar detectors cooled to reduce the effects of thermal noise are being used around the world. These are shown in table 1.1.

Name	Bar Mass (kg)	Material	Location	Operational Since	Working Temp. (K)
ALLEGRO	2300	Al	Baton Rouge (Louisiana,USA)	1991	4.2
AURIGA	2230	Al	Legnaro (Padova, Italy)	1997	2×10^{-1}
EXPLORER	2270	Al	CERN (Geneva, Switzerland)	1990	2.6
NAUTILUS	2260	Al	Frascati (Rome, Italy)	1995	1.3×10^{-1}
NIOBE	1500	Nb	Perth (Western Australia)	1993	5

Table 1.1: *Current resonant bar detectors*

A recent study[28, 29] suggests that these detectors will be capable of strain sensitivity to burst sources of $\tilde{h} \sim 10^{-19}/\sqrt{Hz}$. The current sensitivities are shown in table 1.2

Name	Burst Sensitivity ($\times 10^{-19}/\sqrt{Hz}$)
ALLEGRO	16
AURIGA	2.3
EXPLORER	2.0
NAUTILUS	2.4
NIOBE	4-5

Table 1.2: *Current resonant bar detector sensitivities*

Improvements in the sensitivity of this type of detector have been gained by cooling and hence the temperatures noted in the table. The drawback of this type of detector is that the bandwidth is limited by the resonant nature of

these detectors. Often the current set of detectors may have two resonances, separated by tens of Hz. A possible improvement may be possible through the use of *spherical* detectors. These detectors will have five resonances, allowing a much improved bandwidth. Two such detectors are in planning or construction. The “Mario Schenberg” detector, with a planned sensitivity of $h \leq 10^{-21}$ over a bandwidth of 3.0 - 3.4 kHz, in Brazil is at the site construction phase[30]. The MiniGRAIL detector in Holland, with similar sensitivity and bandwidth, has been constructed and initial measurements of quality factors and cooling procedures are underway[31].

1.4.2 Ground Based - Interferometric

The motion of the ring of particles shown in figure 1.1 as caused by gravitational waves suggests the possibility of their detection using a Michelson interferometer, a simple diagram of which is shown in figure 1.3. The first work on such detectors was carried out in the 1970s by Forward [32] and Weiss[33]. It is relevant at this stage to recall the basic working principals of a Michelson interferometer. Laser light is directed at a beamsplitter, as shown in figure 1.3. The light is then split into two beams, each of which is directed along a separate arm of the interferometer. These are reflected at the end mirrors (hung on pendulum suspensions for seismic isolation) back towards the beamsplitter where they recombine and are directed to a photodiode. An incident wave would move the end mirrors of a correctly oriented interferometer differentially, thus changing the output power detected at the photodiode, albeit by a tiny amount. More precisely, the effect of an optimally oriented wave incident on the detector would be to increase the optical path length of one arm by δL and reduce the path length in the orthogonal arm by the same amount, giving a total change in arm length of $2\delta L$. This change in arm length gives

a relative phase shift in the return beams of the interferometer, which can be detected as a change in the power of the output photodiode. In reality, current interferometer designs hold the photodiode to a constant power level (usually a dark fringe; hence the common description of the output photodiode as a “dark port”) by using feedback to control the positions of the mirrors. The gravitational wave signal is then encoded in the control signals.

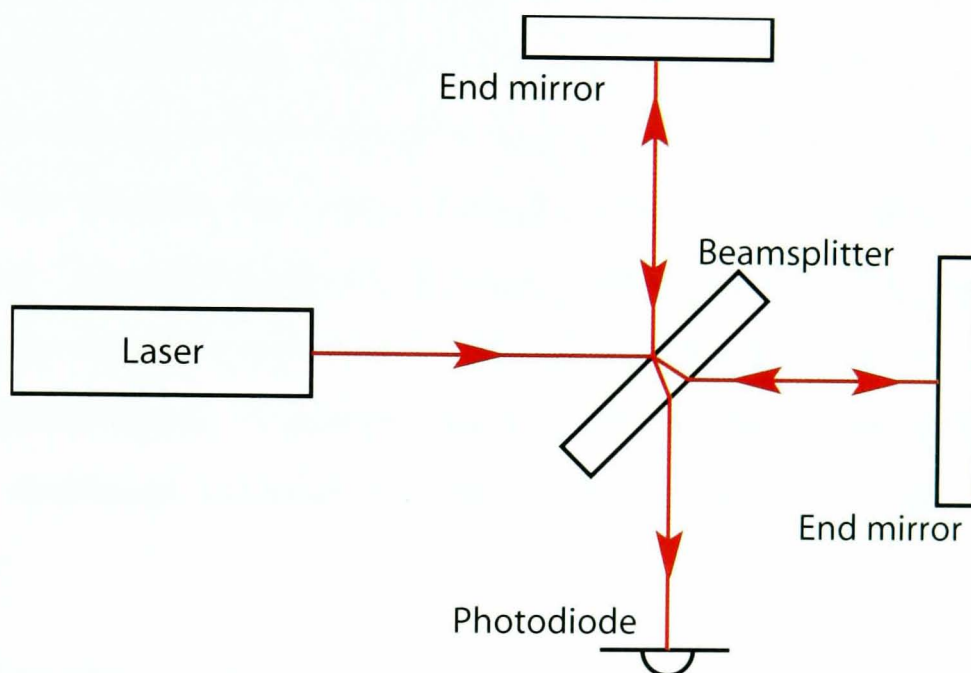


Figure 1.3: *Basic Michelson interferometer*

One of the major advantages of the laser interferometric design is that the gravitational wave signal can be increased by increasing the length of the arms since this will increase δL . In reality there is a limit to the practical maximum length of arm. This is ~ 4 km and arises from the curvature of the Earth. In addition there are storage time effects (see section 1.4.2) which arise when the length of time light spends in the arms is greater than half the period of the gravitational wave.

It is, however, possible to increase the optical path length by making the light remain in the interferometer for longer periods. There are two ways of achieving this: firstly to use a delay line interferometer, and secondly to use a

Fabry-Perot cavity. We will examine these below.

Delay Line Interferometers

This type of interferometer design, first suggested by Weiss [33], is shown schematically in figure 1.4. This type of interferometer adds additional inboard mirrors to the basic Michelson design, which allows the laser light to spend more time in the interferometer itself. This effectively increases the arm length of the detector and hence the optical path length and phase shift of the detector. The additional mirrors allow multiple, non-overlapping beams to coexist in the interferometer arms. The light enters each arm via a small hole in each inboard mirror. A group in the Max-Planck-Institut für Quantenoptik, Germany, developed a system whereby the light exited the delay line by the same hole.

The Garching 30 m prototype demonstrated a strain sensitivity of $\tilde{h} \sim 1 \times 10^{-19}/\sqrt{Hz}$ above 1.5 kHz in 1988 [34].

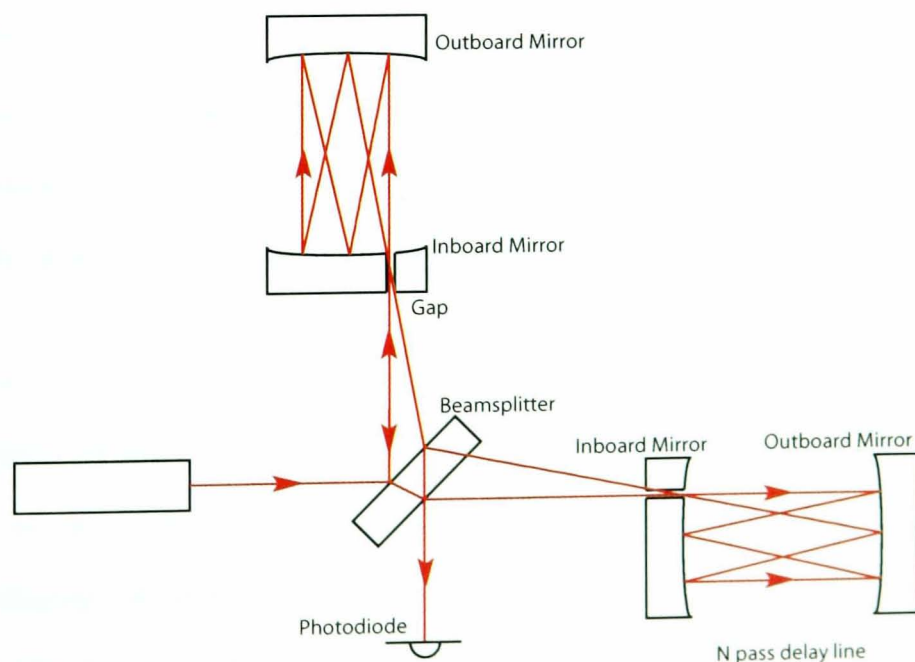


Figure 1.4: *Schematic diagram showing a delay line interferometer design*

The delay line interferometer provides a simple way to understand the idea of a storage time limit. Consider the light beams repeatedly reflecting off the end and inboard mirrors. As the length of time the light spends within the arms increases (the *storage time*), the phase change of the light due to the gravitational wave gradually accumulates. The phase change registered by the interferometer output is effectively the integration of these phase changes over time. If the storage time is too great then the phase changes will start to cancel as the gravitational wave progresses through its cycle. This gives rise to a storage time limit which is of the order of half a period of the gravitational wave[14].

Fabry-Perot Interferometers

This design for increasing the light storage time, adapted in Glasgow for use in gravitational wave detectors [35], uses a pair of Fabry-Perot cavities, one in each arm of the interferometer. An example of such a design is shown in figure 1.5. Each cavity is formed using one partially reflective mirror and one fully reflective mirror. One cavity (the reference cavity) is held on resonance (wherein the cavity length L is set to an integer number of half wavelengths) using feedback to the laser. The secondary cavity is then held on resonance using feedback signals to an actuator at the end mirror of the cavity.

When a gravitational wave is incident on the interferometer, thus changing the arm length of the primary cavity, it is held on resonance by changing the wavelength of the laser. Hence the change in wavelength contains information about the change of arm length of the primary cavity. The incident wave will also change the length of the secondary cavity.

The size of the signal required to hold the secondary cavity on resonance (by

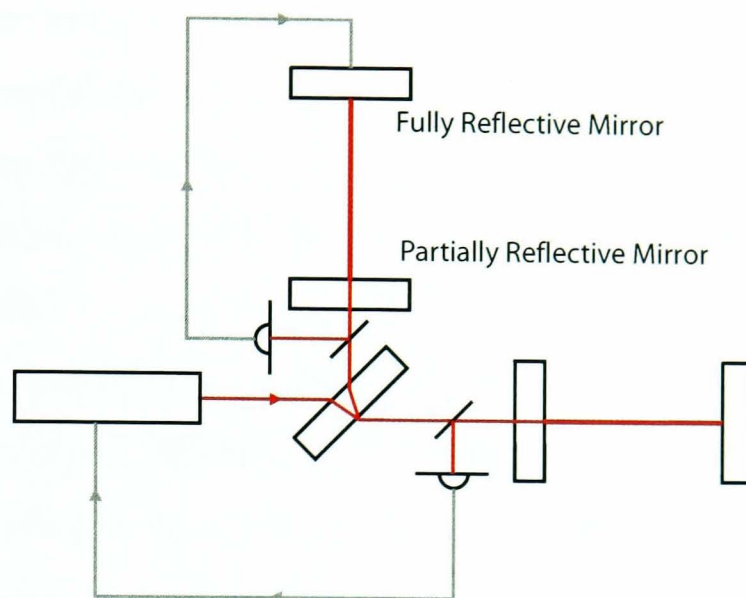


Figure 1.5: *Schematic diagram showing a Fabry-Perot interferometer design*

moving one of the cavity mirrors) and hence keep the null condition at the photodiode will be proportional to $2\delta L$.

The main advantages of a Fabry-Perot type interferometer over those using delay lines are that the mirrors can be much smaller and scattered light within the interferometer is reduced[36]; however a greater amount of servo-control is required to hold all the cavities on resonance[37].

The strain sensitivity achieved in the kHz region by the prototype Fabry-Perot detectors in Glasgow (10 m) and Caltech (40 m) is of the order of a few times $10^{-19} - 10^{-18}/\sqrt{Hz}$ [38, 39, 40] for wideband bursts.

Current Ground Based Interferometric Detectors

There are several ground based laser interferometric detectors currently under construction. LIGO[11] is the largest in scale of these, with 4 km arm-length interferometers in Hanford (Washington, USA) and Livingston (Louisiana,

USA). There also exists at Hanford a 2 km detector which shares the beam tubes and main assembly of the 4 km one. These detectors are currently being commissioned and have undertaken engineering test runs. There is extensive planning and research underway for an upgrade to the LIGO system, known as “Advanced LIGO”. More details of this will be given in section 1.7. In Cascina, Italy an Italian/ French collaboration is building an interferometer of arm length 3 km called VIRGO[10]. This is still under construction and should be commissioned within the next year or so. GEO600, located in Ruthe near Hannover, Germany, is a joint German/ British 600 m arm length detector currently being commissioned[9]. This detector has already undergone an engineering run in coincidence with the LIGO detectors. Although smaller in arm length, GEO600 uses advanced technology which should allow its noise level to approach that of LIGO over a range of frequencies. GEO 600 will be discussed in greater depth in section 1.6. TAMA[12] is a Japanese interferometer with 300 m arms built in the grounds of Tokyo National Astronomical Observatory. This observatory is currently in operation. Plans are in place for a second, underground, Japanese detector which is likely to be cooled. Finally, there exist plans for an Australian detector produced by ACIGA (Australian Consortium for Interferometric Gravitational Astronomy)[41]. The site for this detector can accommodate an arm length of up to 4 km and a preliminary detector of 80 m arm length is currently being built.

1.4.3 Space Based Interferometers

There is only one dedicated space based interferometer for gravitational wave detection planned at the current time. The Laser Interferometer Space Observatory (LISA)[42], a joint NASA/ESA project, is currently planned for launch in 2011. Another year will then be required for the spacecraft to reach their

operational positions. LISA will consist of 3 drag free spacecraft separated by 5×10^9 m in a heliocentric orbit as shown in figure 1.6.

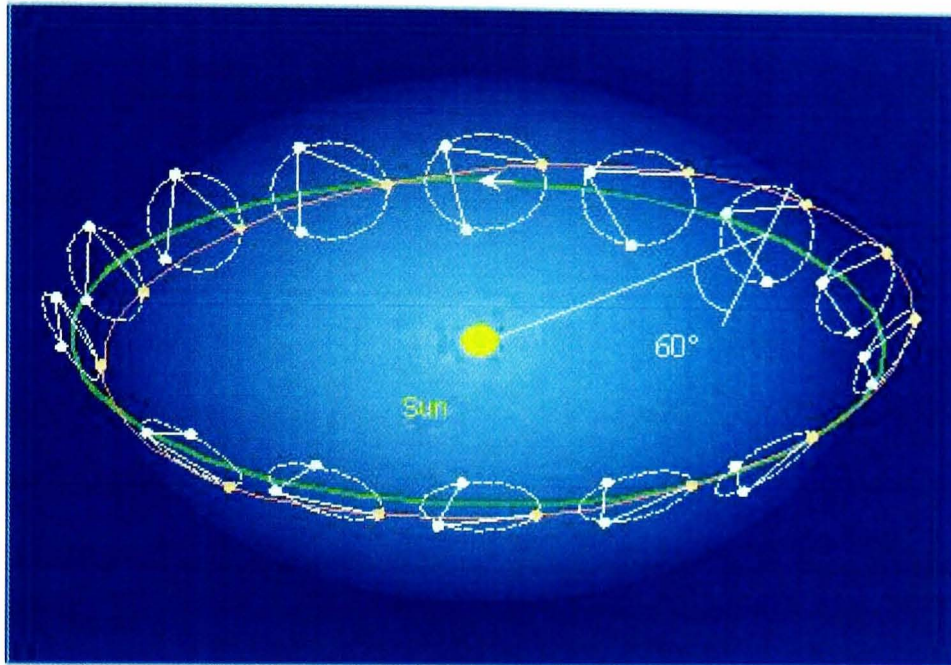


Figure 1.6: *The proposed orbit of LISA*

LISA will not be subject to gravity gradient noise and so will be able to detect gravitational waves with frequencies in the mHz to 1 Hz range. This means that it will be in an excellent position to observe continuous sources such as binary star systems which generate waves of a frequency too low to be detected by ground based detectors. Space and ground based detectors are thus complementary. They operate over different frequency ranges and can search, therefore, for different types of source.

1.5 Noise sources

The gravitational waves emitted from even violent astrophysical sources will produce extremely small displacements in current detectors. Thus an extremely important topic in the discussion of interferometric (or, indeed, any) detectors is that of the various relevant noise sources. This section will cover

the major noise sources present in an interferometric detector, the frequencies at which they are present and the measures which may be taken to minimise their effect.

1.5.1 Quantum Noise Sources

Quantum noise associated with Heisenberg's Uncertainty Principle gives at present a limit at certain frequencies to the sensitivity level possible in current interferometric detectors. In a detector such as LIGO, the quantum noise can be fully described by a pair of optical noise sources, photon shot noise and radiation pressure.

Photon Shot Noise

The output intensity of light from an interferometer is measured using a photodiode. From Poissonian counting statistics, for N detected photons in the photodiode, the uncertainty in the number of photons detected is \sqrt{N} . Such an error gives rise to an uncertainty in the detected value of h , specifically because the output power level from the photodiode is used as a measure of the light exiting the interferometer. This noise is described as photoelectron shot noise, or shot noise. For a delay line interferometer, the shot noise sensitivity is given as[22]

$$h_{\text{shot}}(f) = \left(\frac{\pi \hbar \lambda}{2\epsilon P_{in} c} \right)^{\frac{1}{2}} \frac{f}{\sin(\pi f \tau)} \frac{1}{\sqrt{\text{Hz}}} \quad (1.14)$$

where \hbar is the reduced Planck's constant, λ is the wavelength of the light, ϵ is the quantum efficiency of the photodiode, P_{in} is the input power of the laser.

c the speed of light, f the frequency of the gravitational wave and τ the light storage time. The delay line nature of the interferometer is entered via τ . Shot noise is the dominant noise source at high frequencies and leads to a practical upper limit to useful sensitivity at \sim kHz for ground based detectors. It may be noted that the effect of shot noise on the sensitivity may be minimised by setting the light storage time to half the period of the gravitational wave. i.e. $f\tau = \frac{1}{2}$. The effect of shot noise on detector sensitivity can also be reduced by increasing the input power of the laser as can be seen from equation 1.14.

Radiation Pressure Effects

There is a limitation to interferometer sensitivity caused by fluctuations in the number of photons reflected off the surfaces of the test masses. There is a force on the mirrors of an interferometer due to the momentum imparted to them by the reflections of these photons. As the number of photons fluctuates the force on the mirror also fluctuates in turn. It may be expressed for a delay line interferometer as[14]:

$$h_{\text{rp}}(f) = \frac{N}{mf^2L} \sqrt{\frac{2\hbar P_{\text{in}}}{\pi^3 c \lambda}} \frac{1}{\sqrt{\text{Hz}}} \quad (1.15)$$

where P_{in} is the input power, N is the number of round trips the light makes, m is the mirror's mass, L is the arm length, c is the speed of light and λ is the laser wavelength. The level of radiation pressure noise falls off at higher frequency and at a given frequency the noise increases with P_{in} .

Radiation pressure and shot noise contribute to the ‘‘optical noise’’: the total optical noise level is the quadrature sum of these. It can be seen from equations 1.14 and 1.15 that radiation pressure noise dominates at the low

frequency end of the spectrum and shot noise at high frequencies. Since increasing the input laser power reduces shot noise but increases radiation pressure noise for each frequency, there clearly exists an *optimal* input power, at which $h_{\text{shot}} = h_{\text{radiation pressure}}$ [14]. The minimum of optical noise at this power is described as the quantum limit and in principle could be the limiting factor for the current generation of detectors[43]. A recent study[44] has suggested, however, that for an interferometer using signal recycling (see section 1.6.1) the radiation pressure and photon shot noise may be correlated, leading to an altered quantum noise limit which may be below the standard quantum limit for some configurations. However, below several hundred Hz the quantum limit is below other sources of noise for current detectors; in particular seismic noise tends to limit performance at low frequencies and thermal noise at higher frequencies.

1.5.2 Seismic Noise

Indirect coupling

Seismic noise originates from environmental phenomena such as ocean waves, earth tremors, traffic and people. There are two complementary strategies for dealing with seismic noise. The first is to site the detector in a seismically quiet region. In addition, one must isolate the test masses, for example using pendulums: GEO600 uses triple pendulums. A single, low loss pendulum with resonant frequency f_0 will provide attenuation of $\sim (f_0/f)^2$ at a frequency $f \gg f_0$. A greater factor can be achieved at a frequency f by using more pendulum stages. This technique provides greater attenuation in the horizontal direction than in the vertical; this is because the resonant frequencies of the horizontal modes are lower than those of the vertical modes. GEO600 employs

a triple suspension system with two sets of cantilever springs to give a low vertical resonant frequency and hence sufficient vertical isolation[45]. LIGO uses single pendulum suspensions but it should be noted that Advanced LIGO will use a quadruple pendulum design, with three sets of cantilever blades, adapted from the current GEO600 design.

Direct coupling

There is another source of seismic noise from which the test masses cannot be isolated. This is noise caused by direct gravitational coupling between the masses and objects moving in the wider environment of the detector[46, 47]. There is no easy way to reduce this on the ground although ways of sensing and correcting for this noise are being proposed[48]. Currently this noise sets an important lower limit to the bandwidth of ground based detectors at low frequency[49].

1.5.3 Thermal noise

Thermal noise arises from the random vibrations of atoms in the mirrors of an interferometer and their suspensions. The thermal noise for a mirror and its suspension is peaked at the resonances of that system; there exists $\frac{1}{2}k_B T$ energy per degree of freedom of the system at a given temperature. It is possible to *shape* the thermal noise so that its spectral contribution is minimised in the operating bandwidth of the gravitational wave detector. In particular we may concentrate the noise at the resonances of the mirror and suspension, thus reducing the off resonance noise. Since the frequencies of the resonances will be well known, they can then in many cases be removed from the detection band using notch filters. The major sources of thermal noise include the pendulum

modes of the suspension, the violin modes of the suspension wires and the internal thermal noise in the test masses themselves. The resonances in the suspension tend to be at low frequency and the resonances of the test masses themselves tend to start much higher (> 10 kHz for GEO and LIGO). Hence the internal modes of the masses will not intrude on the detection band.

For current detectors, GEO600 in particular, thermal noise from the internal modes of the masses is one of the most significant noise sources; i.e. to reduce overall noise further it is necessary to reduce thermal noise. Hence the reduction of the contribution of thermal noise to the total noise level of a detector over its operating bandwidth is one of the most important areas of research in the gravitational wave detector field. In chapter 2 aspects of thermal noise at its minimisation will be discussed.

1.5.4 Other Noise Sources

There exist other noise sources, mainly concerned with the laser. For example, both the laser frequency and intensity are subject to fluctuation. The use of RF modulation moves the measurement frequency to a frequency where intensity noise is insignificant. In addition, frequency noise can be reduced by using a frequency stable reference cavity. For a Michelson interferometer with matching arm lengths, any common mode noise, such as frequency noise, will cancel between the arms and not intrude on the output signal. Another source of “laser” noise is scattered light. This scattered light will have a random phase which consequently contaminates the main beam. Scattering can be reduced by a series of baffles within the beam tubes.

Thermorefractive noise arises from the temperature dependence of the refractive indices of the materials used in the bulk of the beamsplitter and in the

dielectric coatings used as mirrors on the test masses. There exist natural fluctuations in the temperature of the materials which gives rise to changing refractive indices of the materials. These changes alter the phase of the transmitted light through the beamsplitter or the reflectivity of the mirror coatings which leads to phase noise[50].

Finally, the suspension systems (and indeed the entire interferometer) sit in vacuum during operation. This vacuum is unlikely to be perfect, however. Residual gas is a source of thermal noise as it is a source of dissipation (viscous damping). Secondly, however, there will exist density fluctuations in the gas giving rise to fluctuations in the index of refraction of the arms, and hence in the relative phases of the light from the two arms.

1.6 GEO600

The GEO600 gravitational wave detector is currently undergoing commissioning in Ruthe, near Hannover, Germany. Construction on the detector began in 1995. It was conceived and designed on the basis of experience gained from the Glasgow 10 m interferometer and the 30 m interferometer at the Max-Planck-Institut für Quantenoptik in Garching, near Munich, Germany. GEO600 is now being developed by a collaboration of groups from the Albert Einstein Institute at Hannover and Golm, the Max-Planck-Institut für Quantenoptik at Garching, the University of Glasgow, the University of Wales, Cardiff with contributions from the Laser-Zentrum, Hannover.

GEO600 is a delay line interferometer with 600m arm length, powered by an injection-locked laser-diode-pumped Nd:YAG system with an output power of 12W (the optical layout scheme is shown in figure 1.7). Light from the laser

is passed through two modecleaners to reduce beam geometry noise [51]. The interferometer mirrors are suspended as triple pendulums to provide seismic isolation.

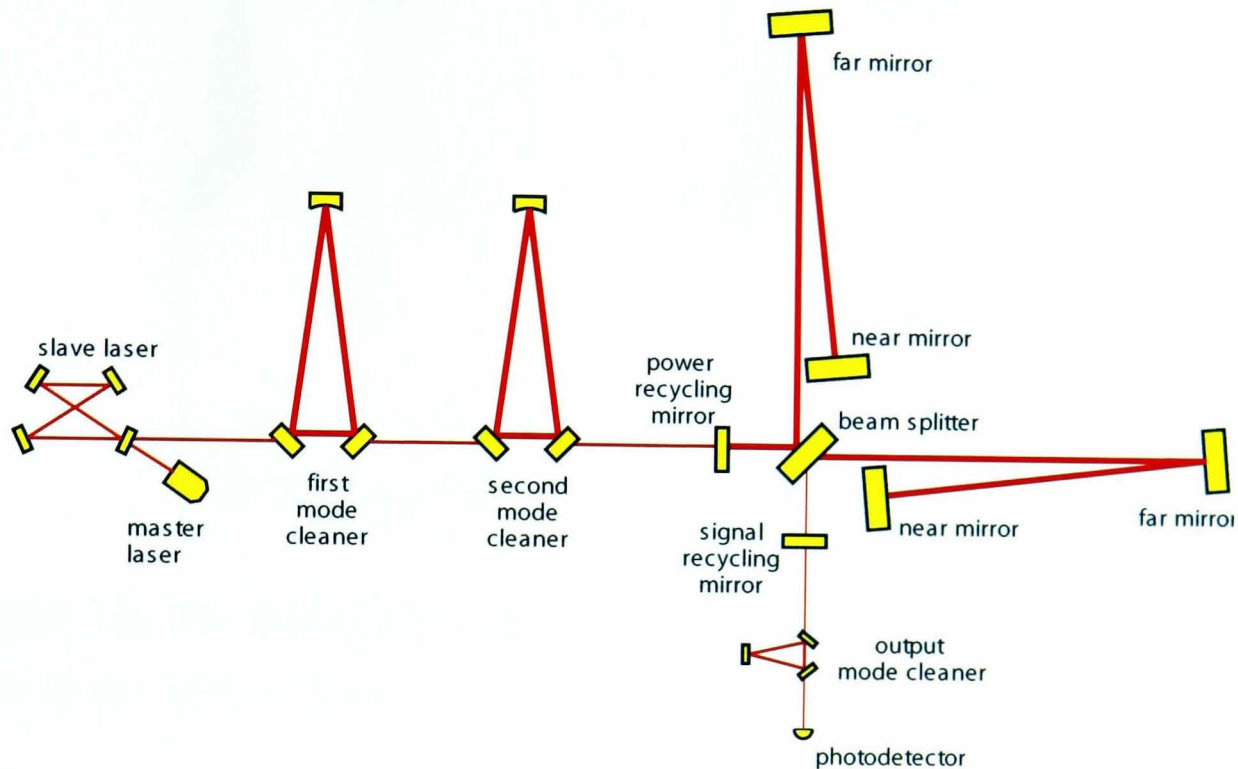


Figure 1.7: *The optical layout of GEO600*

To reduce fluctuations in the optical path length due to a fluctuating index of refraction in the beam tube, the entire optical system is held in a vacuum; the current pressure is in the upper 10^{-9} mbar region[9].

GEO600 employs two different suspension arrangements. The modecleaner mirrors are suspended in a double pendulum system with an upper mass made of stainless steel and a lower mass made of fused silica. Reaction pendulums, placed a few millimetres behind many of the mirrors in the interferometer, are used to provide a stable platform from which to give actuation for longitudinal control. The lower mass of this double pendulum has coils on its surface which interact with magnets attached to the back to the modecleaner mirror. The whole suspension is supported on three legs, each of which contains a stack of two layers of passive isolation and a rotational flexure to isolate the pendulum

further from seismic noise. The entire suspension can be seen in figure 1.8

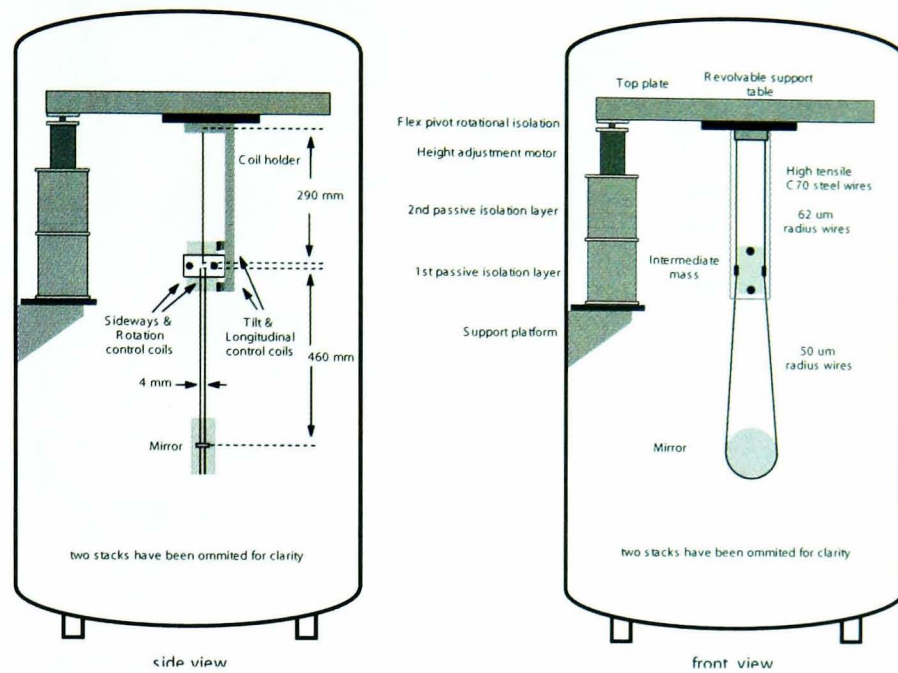


Figure 1.8: *The modecleaner suspension system used in GEO600 (suspension here shown without reaction mass)*

The suspension systems for the end mirrors (figure 1.9) are similar in many respects, but have additional aspects for further noise reduction. The most obvious difference is that a triple pendulum is now employed which uses an additional fused silica mass between the upper steel mass and the fused silica test mass. The upper mass is suspended from cantilever springs (or “blades”) which provide vertical isolation. The additional fused silica mass (the “intermediate” mass) is suspended by wire loops from the upper steel mass. The 6 kg lower mass is jointed to the intermediate mass by fused silica fibres, thus creating a quasi-monolithic fused silica suspension. In this case the reaction pendulums use electrostatic forces to act on the test mass instead of coils and magnets; magnets on the back of the test mass would lead to an increase in the thermal noise. The three stacks supporting the triple pendulum suspensions have one passive and one active layer, and a flex pivot for rotational isolation. A picture of this type of suspension installed in the GEO600 interferometer is shown in figure 1.10.

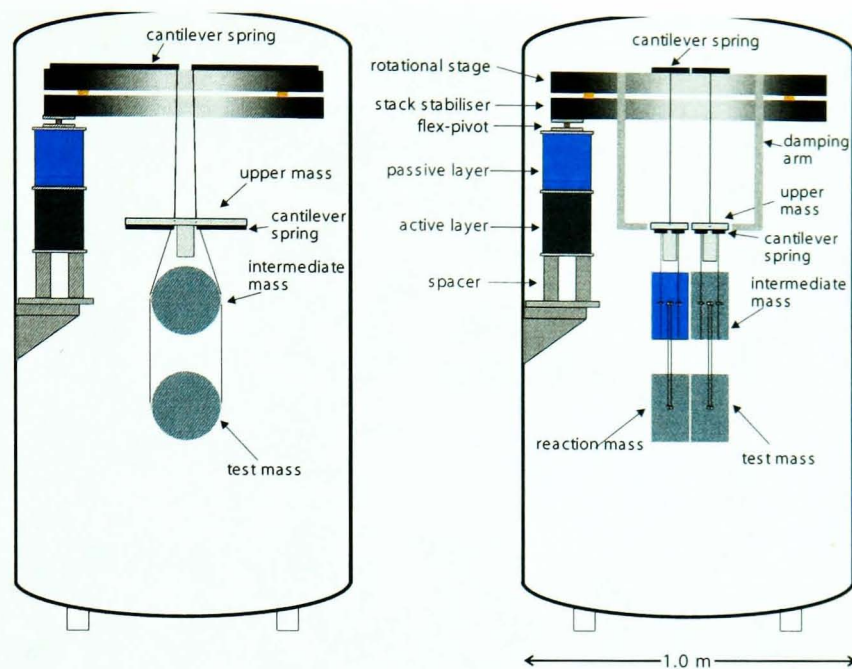


Figure 1.9: *The end test mass suspension system used in GEO600*

The purpose of this quasi-monolithic suspension design is to minimise thermal noise; this will be discussed in full in chapter 2.

1.6.1 Dual recycling

One of the major design aims of GEO600 is to approach closely the expected sensitivity of the longer LIGO type detectors over a certain frequency band. As mentioned earlier, this is being enabled by the use of more advanced technology. The first example of this was seen in the previous section where the quasi-monolithic suspension systems were described. Another advance is the extension of recycling to not only the power in the system (power recycling) but also the signal sidebands in the output of the detector (signal recycling).

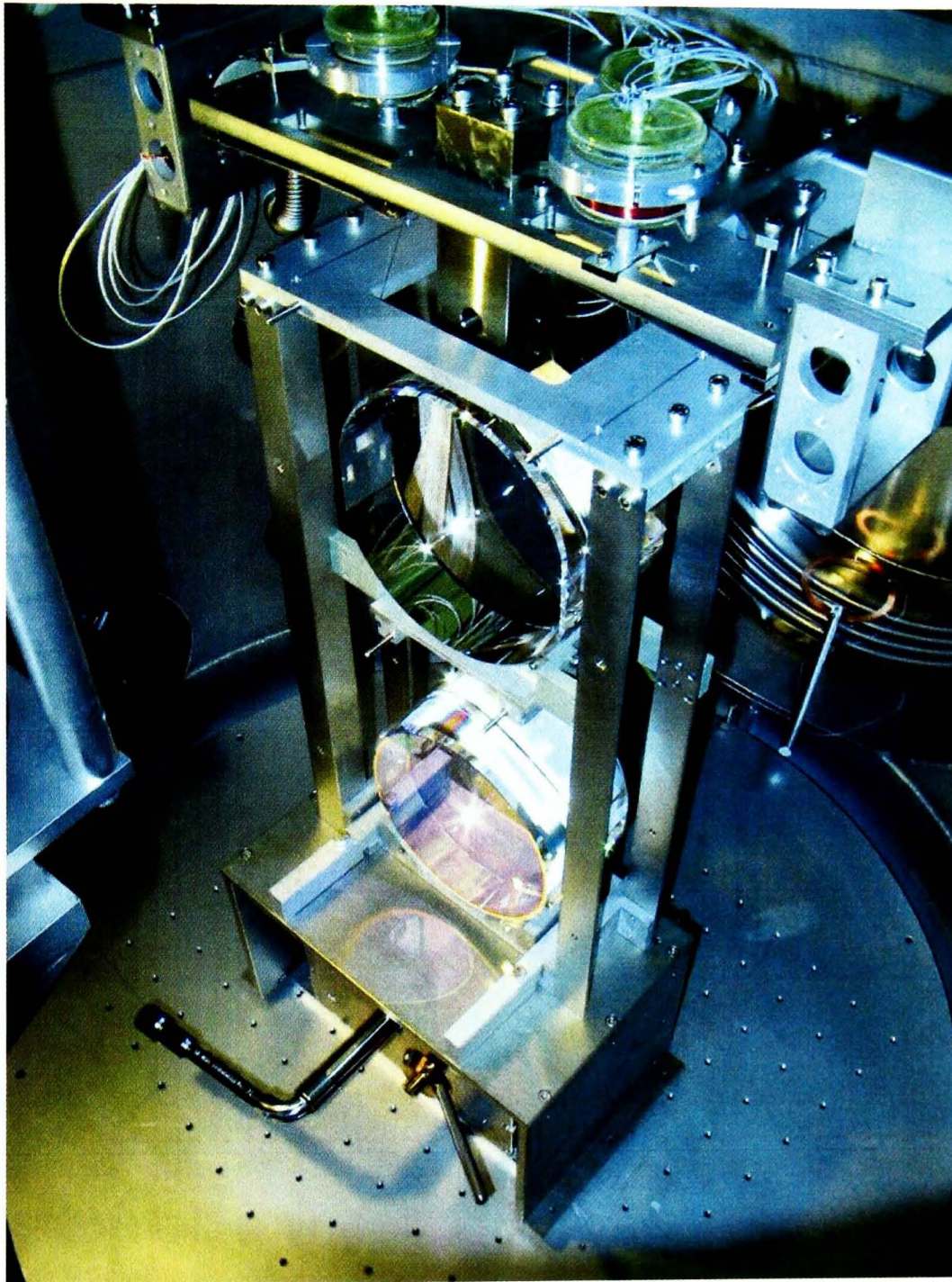


Figure 1.10: *The quasi monolithic silica suspension system used in GEO600*

Power Recycling

GEO600 is operated with a dark fringe at its output as discussed in section 1.4.2. In this configuration, most of the light injected into the interferometer will be reflected back towards the laser system; in effect, the interferometer acts as one, highly reflective, mirror. A partially reflective mirror placed between the laser and the interferometer proper will therefore give a

cavity between that mirror and the effective mirror of the interferometer[52]. If this cavity is held on resonance there will be a buildup of light within this cavity which in turn leads to a power increase at the beamsplitter of the interferometer. The increase in GEO600 is anticipated to be ~ 2000 , leading to a power at the beamsplitter of ~ 10 kW; this in turn leads to an improvement in the shot noise limited sensitivity of, in principle, a factor of $\sqrt{2000} \approx 45$ (equation 1.14).

Signal Recycling

Any differential change in the arm length of the interferometer such as that which might result from an incident gravitational wave will cause light to leak out of the interferometer. A further mirror placed after the interferometer to reflect the light back will form another cavity: the signal recycling cavity. At certain Fourier frequencies this cavity will enhance the light power representing the signal. Thus the signal is enhanced at certain frequencies; the interferometer can be *tuned* by changing the position of the signal recycling mirror and the bandwidth can be varied by altering the reflectivity of this mirror[53]. Figures 1.11 and 1.12 show noise curves for both broad and narrow band operation; figure 1.11 shows the broadband mode and 1.12 the narrowband.

1.7 Advanced LIGO

As was mentioned in the introduction to this chapter, the work in this thesis is directly applicable to Advanced LIGO, the proposed upgrade to the LIGO project. In this section a brief summary will be given of the main features of

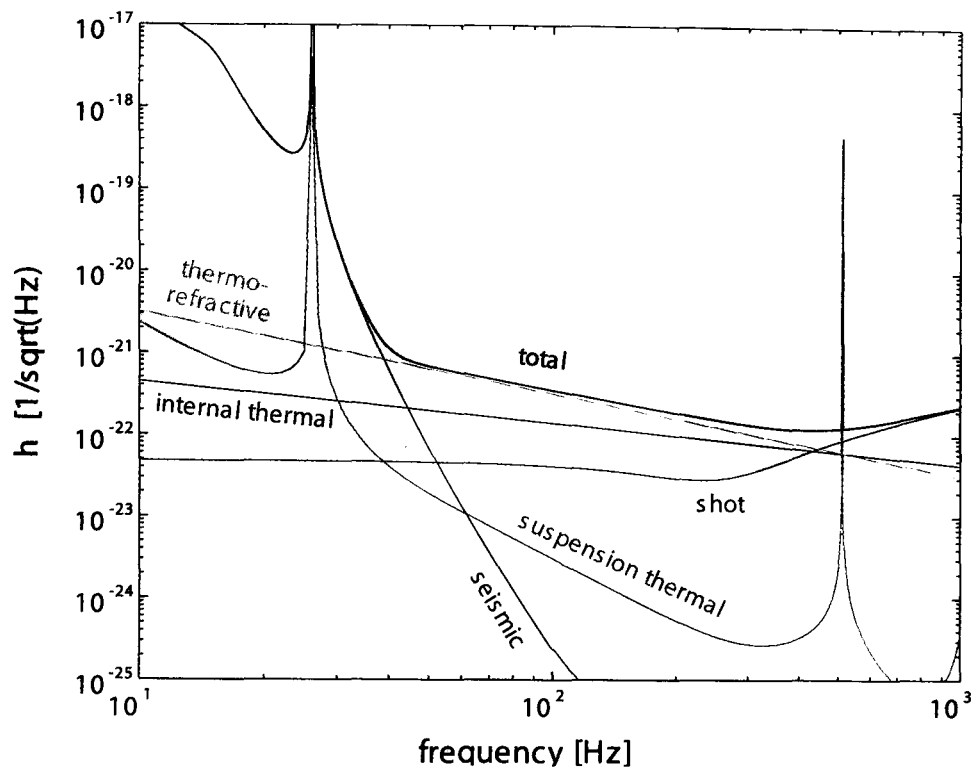


Figure 1.11: *Expected noise curves for GEO600 (Broadband configuration)*

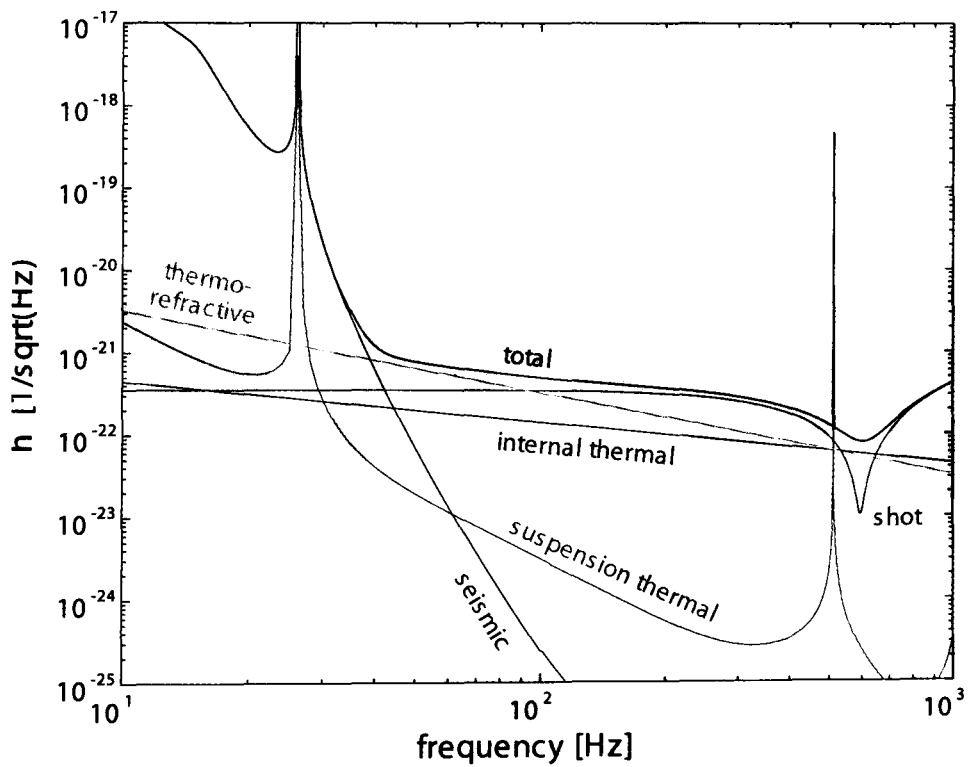


Figure 1.12: *Expected noise curves for GEO600 (Narrowband configuration)*

the upgrade.

1.7.1 Suspension Design/ Test Masses

The current LIGO suspension design, in contrast to GEO600, is a single pendulum with a 10.7 kg fused silica test mass. The mass is suspended by a single steel wire loop and control is achieved using magnets attached to the back and sides of the mirror [54]. The proposed changes are detailed in table 1.3

Design feature	LIGO	Adv LIGO
Mass	10.7 kg Silica	40 kg Sapphire
Pendulum type	Single	Quadruple
Test mass suspension	Steel wire	Silica fibres/ ribbons
Local control point	At test mass	At highest point in pendulum chain

Table 1.3: *Comparison of features of LIGO with its proposed upgrade Advanced LIGO*

The local control point refers to the point at which signals are applied to damp the low frequency resonances of the pendulum. Global control of Advanced LIGO, used to control the interferometer, will possibly be achieved using electrostatic forces on the test masses themselves. The use of sapphire is due to its extremely low intrinsic loss [55]. The quadruple pendulum system will give additional seismic isolation. The use of control at the upper stages of the pendulum as opposed to at the test mass level will reduce the level of control noise, as well as removing the requirement of having magnets attached to the back of the test mass which currently leads to greater thermal noise.

Optical Layout

The other major changes to LIGO involve the optical layout, which will be altered by the addition of an additional recycling mirror at the interferometer output to provide signal recycling, as well as a new laser operating at ~ 200 W.

1.8 Conclusion

The experimental search for gravitational waves has been carried out for over 30 years. We find ourselves now on the threshold of a new stage in this search as a number of broadband detectors reach the commissioning stage of their construction. First generation ground based interferometric detectors are expected to reach sensitivities of $\sim 10^{-22}/\sqrt{Hz}$ over the frequency range of a few Hz to a few kHz, with mature detectors being improved by a factor of 10-15 over the next ten years. Amongst the most likely sources to be observed are black hole/black hole binaries.

GEO600 is now in the commissioning phase and uses advanced techniques which should reach a sensitivity approaching that of the longer detectors. This will allow it to run coincidentally with LIGO. An advanced design of LIGO is expected to begin implementation in the 2006 timeframe.

Within the next ten years LISA will be launched which will allow observations to be made in the millihertz region of gravitational radiation.

Chapter 2

Thermal Noise

Associated with every degree of freedom of a mechanical system is $\frac{1}{2}k_B T$ of thermal energy (with k_B Boltzmann's constant and T temperature), by the Equipartition Theorem. Such a mechanical system is the mirror and suspension system used in an interferometric gravitational wave detector. This energy manifests itself as thermally induced motion of the system. The combined motion due to all degrees of freedom of the suspension is such that this displacement noise (*thermal noise*) is potentially of the same order as the displacement of the mirror due to an incident gravitational wave in the operating bandwidth of the detector. The reduction of the effect of thermal noise on the sensitivity of the detector within its operating bandwidth is thus an important area of research.

The most obvious route to the reduction of thermal noise is to reduce the temperature at which the detector operates; indeed, resonant bar detectors already use this method[28]. Cryogenic techniques are being considered and investigated for future interferometric detectors (for example in Japan[56]), but are not in place for the current generation of detectors.

The integrated level of thermal noise present in a current generation suspension would therefore appear to be a fixed quantity; however methods exist which can *shape* this noise over the frequency domain.

Initially in this chapter a more detailed introduction to thermal noise will be given.

2.1 The First Observations of Thermal Noise

In 1827 Robert Brown observed the erratic, random movement of pollen grains suspended in water[57]; he believed this motion to be associated with the pollen grains themselves. In 1905 Einstein noted that the motion was instead associated with the water[58]. He saw that the random motion of the grains arose as a result of random fluctuations in the number of impacts of water molecules on the grains. Einstein realised that these impacts also resulted in the pollen grains losing kinetic energy as they moved through the water. This was the first instance of a relationship being recognised between fluctuation (which, in this case, excites the system on a microscopic scale i.e. the random displacement of the pollen grains) and dissipation (which dissipates energy, in this case on a macroscopic scale i.e. the viscosity of the water).

Later, Callen et al[59, 60] developed a general form of this association between fluctuation and dissipation which forms the basis of the study of thermal noise in gravitational wave detectors. It was called the Fluctuation Dissipation Theorem.

2.2 The Fluctuation Dissipation Theorem

The fluctuation dissipation theorem relates the power spectral density of the thermal driving force $S_f(\omega)$ to the real (or dissipative) part of the impedance, $Z(\omega)$ of the mechanical system in question in the following way:

$$S_f(\omega) = 4k_B T \Re[Z(\omega)] \quad (2.1)$$

Since $Z \equiv \frac{F}{v}$, where v is the resultant velocity due to an applied force F , this may be equivalently written in terms of the power spectral density of the thermal displacement, $S_x(\omega)$;

$$S_x(\omega) = \frac{4k_B T}{\omega^2} \Re[Y(\omega)] \quad (2.2)$$

where $Y(\omega)$, the admittance of the system, is equivalent to $Z^{-1}(\omega)$.

Hence, if we can macroscopically describe the impedance of a system, we are immediately able to determine the relevant thermal noise contribution.

2.3 Potential sources of dissipation

On consideration of a suspension system, there are a number of possible sources of dissipation of energy, both in the suspension and also in the test mass itself

2.3.1 External suspension dissipation

The first source is that of residual gas molecules within an imperfect vacuum causing viscous damping. This is perhaps the most clear analogue to the original pollen grain observation.

Other possible sources of dissipation are:

- Energy loss due to eddy current damping or hysteresis
- Suspension point friction
- Electrostatic charging of the test mass
- Energy loss due to surface damage of the suspension fibres

These sources should be able to be reduced by the design of the pendulum system and so should not lead to high levels of noise.

2.3.2 Internal dissipation

Once the external sources of dissipation have been removed or reduced to an insignificant level, the dominant source of dissipation (or, equivalently, damping) in these circumstances will be internal damping in the suspension wires and test masses. Internal damping arises from a process known as *anelastic relaxation*.

Consider a force acting on a mass. The reaction of the body to that force will not be instantaneous, due to internal imperfections in the solid. The time taken for this reaction is known as the relaxation time; this process is anelastic

relaxation. To find the thermal noise contribution of such a process, consider first the standard reaction force experienced by a dissipationless simple harmonic oscillator, $F = -kx$, Hooke's Law. Anelastic relaxation introduces a time delay that in the frequency domain appears as a phase lag:

$$F = -k[1 + i\phi(\omega)]x \quad (2.3)$$

where $\phi(\omega)$ is the loss angle or factor. It represents the phase lag in radians of the response x of the system to the applied force F . The equation of motion of a harmonic oscillator displaying internal friction is:

$$F(\omega)x(\omega) = -m\omega^2 + k[1 + i\phi(\omega)]x(\omega) \quad (2.4)$$

In order to calculate the impedance we need this in velocity form:

$$F(\omega) = i\omega m v(\omega) - i\frac{k}{\omega}[1 + i\phi(\omega)]v(\omega) \quad (2.5)$$

where $x = v/i\omega$ if we take $x \propto e^{i\omega t}$. This gives $Z = F/v$ as:

$$Z(\omega) = i\omega m - i\frac{k}{\omega}[1 + i\phi(\omega)] = i\left(\omega m - \frac{k}{\omega}\right) + \phi(\omega)\frac{k}{\omega} \quad (2.6)$$

We, however, want $Y = Z^{-1}$:

$$Y = Z^{-1} = \frac{\omega}{k\phi(\omega) + i(\omega^2 m - k)} \quad (2.7)$$

$$= \frac{1}{\frac{k}{\omega}\phi(\omega) + i(\omega m - \frac{k}{\omega})} \cdot \frac{\phi(\omega)\frac{k}{\omega} - i(\omega m - \frac{k}{\omega})}{\phi(\omega)\frac{k}{\omega} - i(\omega m - \frac{k}{\omega})} \quad (2.8)$$

$$= \frac{\phi(\omega)\frac{k}{\omega} - i(\omega m - \frac{k}{\omega})}{[\phi(\omega)\frac{k}{\omega}]^2 + (\omega m - \frac{k}{\omega})^2} \quad (2.9)$$

This may be simplified by using $k = \omega_0^2 m$:

$$Y = \frac{\phi(\omega)m\omega_0^2/\omega - i(\omega m - m\omega_0^2/\omega)}{[\phi(\omega)m\omega_0^2/\omega]^2 + (\omega m - m\omega_0^2/\omega)^2} \quad (2.10)$$

If this expression is substituted in equation 2.2 we get:

$$S_x(\omega) = \frac{4k_B T}{\omega^2} \Re(Y(\omega)) \text{ per Hz} \quad (2.11)$$

$$= \frac{4k_B T}{\omega^2} \frac{\phi(\omega)m\omega_0^2/\omega}{[\phi(\omega)m\omega_0^2/\omega]^2 + (\omega m - m\omega_0^2/\omega)^2} \quad (2.12)$$

$$= \frac{4k_B T}{\omega} \frac{\phi(\omega)\omega_0^2}{m[\phi^2(\omega)\omega_0^4 + (\omega_0^2 - \omega^2)^2]} \quad (2.13)$$

2.3.3 The Internal Loss Factor $\phi(\omega)$

In this section two possibilities are presented for the form that the internal loss factor $\phi(\omega)$ may take, frequency dependent and frequency independent.

One form of frequency dependent loss would take the form $\phi(\omega) = \beta\omega$ where β is some constant. Substituting into equation 2.3 gives as the imaginary term:

$$F_{friction} = -bv \quad (2.14)$$

where $v = i\omega x$ and $b = k\beta$. This velocity dependence results in this form of loss being called internal viscous damping.

There is, however, evidence which suggests that it is more likely that many substances do not exhibit velocity damping. Experiments[61] suggest that a frequency *independent* loss is more realistic. Such a damping form is called “structural” damping. It is thought that in such a situation there exist many internal damping mechanisms which all contribute to a total loss factor. Each of these mechanisms has its own resonant peak (known commonly as a Debye peak) at a characteristic frequency of the process; it is at these peaks that the individual loss factors (which *are* frequency dependent) are at a maximum. The frequencies of the separate resonant peaks range over several orders of magnitude. Between these frequencies (where the bandwidth of gravitational wave detectors is thought to lie) the overall observed loss factor is essentially constant[62].

Hence for all intents and purposes we may consider the internal damping loss factor to be constant, with one important exception. This is *thermoelastic* damping and will be dealt with later in this chapter.

The level of thermal displacement noise is crucial to current ground based gravitational wave detectors and so predicting the correct form of the internal loss is very important. It is extremely difficult to measure the loss factor $\phi(\omega)$ at frequencies interesting for gravitational wave detection for a pendulum system because its magnitude is very small. A technique is available, however, which will allow us to measure the level of the internal loss factor at the resonance of a system.

It is first interesting to note that the definition by French[63] of the quality factor, Q , of a resonant system in terms of its damping coefficient b , mass m and resonant frequency ω_0 is,

$$Q(\omega_0) = \frac{m\omega_0}{b} \quad (2.15)$$

The damping term in a resonant system comes from the real part of its impedance Z . From equation 2.6 we see that in the case of internal damping it is $\phi(\omega)\frac{k}{\omega}$ which is equivalent to b in equation 2.15 (note that b is constant for velocity damping and variable for structural). Substitution into equation 2.15 (with $\omega = \omega_0$) leads to a relationship between $Q(\omega_0)$ and $\phi(\omega_0)$:

$$Q(\omega_0) = \frac{1}{\phi(\omega_0)} \quad (2.16)$$

The technique for measuring the loss of a system is consequently to measure the loss (or Q) at resonance and then, where applicable, to assume structural damping to evaluate the loss at all frequencies.

2.4 Thermal Noise Level

2.4.1 Single resonance

We are now in a position to calculate the level of thermal noise present in a simple resonant system such as that presented above. Following this, techniques for calculating the thermal noise contribution of a many mode system such as that present in reality will be presented.

Recall initially equation 2.13. There are three distinct regions of interest in the frequency domain; firstly, the region far below resonance, ie $\omega \ll \omega_0$:

$$\begin{aligned}
 S_x(\omega) &= \frac{4k_B T}{\omega} \frac{\phi(\omega)\omega_0^2}{m[\phi^2(\omega)\omega_0^4 + (\omega_0^2 - \omega^2)^2]} \\
 &\approx \frac{4k_B T \phi(\omega)\omega_0^2}{m\omega(\omega_0^4 \phi^2(\omega) + \omega_0^4)} \text{ per Hz} \\
 &\approx \frac{4k_B T \phi(\omega)}{m\omega\omega_0^2(\phi^2(\omega) + 1)} \tag{2.17}
 \end{aligned}$$

which, assuming $\phi^2(\omega) \ll 1$ becomes:

$$S_x(\omega) \approx \frac{4k_B T}{m\omega_0^2} \left(\frac{\phi(\omega)}{\omega} \right) \tag{2.18}$$

Secondly, consider the situation far above resonance, ie $\omega \gg \omega_0$:

$$S_x(\omega) \approx \frac{4k_B T \phi(\omega)\omega_0^2}{m\omega((\omega^2)^2 + \omega_0^4 \phi^2(\omega))} \tag{2.19}$$

which becomes, if again it is assumed $\phi^2(\omega) \ll 1$:

$$S_x(\omega) \approx \frac{4k_B T \omega_0^2}{m} \frac{\phi(\omega)}{\omega^5} \tag{2.20}$$

From equations 2.18 and 2.20 it can be seen that the thermal displacement spectral density can be greatly reduced if the mechanical loss factor is very small (hence $\phi(\omega) \ll 1$). However, since energy must be conserved (recall the equipartition theorem does in fact give the total integrated thermal noise as

$\frac{1}{2}k_B T$ per mode) the corresponding spectral density at resonance ($\omega = \omega_0$ with $\phi(\omega) \ll 1$ must be consequently very high:

$$\begin{aligned} S_x(\omega) &= \frac{4k_B T \phi(\omega_0) \omega_0^2}{m \omega_0 \omega_0^4 \phi^2(\omega)} \text{ per Hz} \\ &= \frac{4k_B T}{m \omega_0^3} \left(\frac{1}{\phi(\omega_0)} \right) \end{aligned} \quad (2.21)$$

Equation 2.18 can be used to calculate the thermal noise spectral density below the frequency of the internal test mass resonances which is where the detection band for gravitational wave detectors lies.

2.5 Multi Resonance System

In reality, the suspension systems used in gravitational wave detectors have several resonance modes. One method of calculating the thermal noise contribution below resonance would be to generalise 2.18 as follows:

$$S_x(\omega) = \sum_n \frac{4k_B T \phi_{internal_n}(\omega)}{\alpha_n m \omega_n^2 \omega} \quad (2.22)$$

Where $\phi_{internal_n}$ is the loss factor associated with the n^{th} internal mode and $\alpha_n m$ is the effective mass of the same mode. α_n is an empirical factor characterising the coupling between the internal mode and the optical mode and depends on the laser beam width[64], the mass of the mirror and the resonant frequency ω_n .

There is, however, a problem with this method. Unless the losses in the mass

are evenly distributed throughout the mass (homogenous), this method is incorrect. The reason for this is that in the case of inhomogeneous loss modes, the modes may share a common Langevin driving force; there exists a correlation between the modes which means that the summation is inaccurate.

There are two solutions to this problem. The first is to enumerate these mode correlations[65] and the second is to use a different method to calculate the thermal noise in the first place. Levin[66] considered the effect of applying an oscillating pressure to the front face of the form:

$$P = F_0 \frac{e^{-r^2/r_0^2}}{\pi r_0^2} \cos(\omega t) \quad (2.23)$$

where F_0 is a constant force amplitude and r_0 is the radius of the laser beam at a point where the intensity of the beam has fallen to a point $1/e$ of its maximum. This Gaussian profile matches that of the laser beam. Levin derives the admittance in terms of a power averaged over a period $2\pi/\omega$ calculated from the applied force to give the following:

$$|\Re[Y(\omega)]| = \frac{2W_{diss}}{F_0^2} \quad (2.24)$$

where W_{diss} is the power fed into the mass by the oscillating pressure. This results in a thermal noise spectral density of:

$$S_x(\omega) = \frac{8k_B T W_{diss}}{\omega^2 F_0^2} \quad (2.25)$$

Using the W_{diss} calculated in[67] for a half infinite mass, the thermal noise spectral density due to internal loss in a test mass at temperature T at a frequency well below resonance is as follows:

Property	Value
Y (kg/ms ²)	7.2×10^{10}
σ	0.17
r_0 (m)	0.017[68]
$\phi_{fused\ silica}$	5×10^{-8}
T (K)	300
ω (s ⁻¹)	$2\pi \times 50$

Table 2.1: *Properties used in calculation of $\sqrt{S_x(\omega)}$ for fused silica*

$$S_x(\omega) = \frac{4k_B T}{\omega} \frac{1 - \sigma^2}{\sqrt{2\pi} Y r_0} \phi(\omega) \quad (2.26)$$

where σ and Y are the Poisson's ratio and Young's modulus of the test mass material respectively. We may calculate the thermal motion, $\sqrt{S_x(\omega)}$, for the GEO600 test mass material fused silica using the values given in table 2.1. This gives a value $\sqrt{S_{x_{fused\ silica}}(\omega)} = 2.9 \times 10^{-20} \text{ m}/\sqrt{\text{Hz}}$.¹

Nakagawa et al.[69, 70, 71] have developed a method of calculating the thermal noise in a half infinite test mass. The basic technique they used was to relate the loss parameters to the power spectrum of the 2 point displacement correlation function. They do this by relating the power spectral density to the linear response of a body under traction using the method of Kubo[72]. This method was first used to analyse a test mass of homogeneous loss, the results of which agreed with the Levin result given in equation 2.26. Most recently, they have calculated that the addition of a slab of different material properties to the surface of the substrate (for example a coating layer) would

¹It should be noted that there is a correction factor for finite masses, which is calculated for a 30kg sapphire mass (as proposed for use in Advanced LIGO) test mass in [67]. The correction factor is of order unity for $r_0 \sim 10 \times 10^{-3} \text{ m}$

increase the thermal noise contribution of the mass by a factor:

$$R = 1 + \left\{ \frac{1}{\sqrt{\pi}} \frac{(1 + \sigma_{coating})}{(1 - \sigma_{substrate}^2)(1 - \sigma_{coating})} \frac{\phi_{coating}}{\phi_{substrate}} \frac{Y_{substrate}}{Y_{coating}} \right\} \times \quad (2.27)$$

$$\left\{ \left[(1 - 2\sigma_{coating}) + (1 - 2\sigma_{substrate})^2 \frac{(1 + \sigma_{substrate})^2}{(1 + \sigma_{coating})^2} \left(\frac{Y_{coating}}{Y_{substrate}} \right)^2 \right] \left(\frac{d}{w} \right) \right\}$$

where d is the thickness of the slab of coating, w is the radius of the laser beam where the amplitude has fallen to $1/e$ of its maximum, Y is the Young's modulus of each component and σ is the Poisson's ratio of each component.

Yamamoto[65] derived an "advanced" modal expansion technique which calculates the coupling between modes to render the modal expansion method more accurate. This advanced modal expansion also agrees with corrected Levin method. He then calculated the thermal noise due to a silica mass using finite element analysis (see section 4.3 for a description of this type of analysis) with Levin's method and compared the results to the same calculation using a traditional modal expansion. This confirmed the discrepancy between the traditional modal expansion technique. He performed further experiments using an aluminium drum which confirmed the Levin approach for inhomogenous loss.

2.6 Thermoelastic Damping

It was commented in section 2.3.3 that there existed a form of internal loss which was not constant with frequency, thermoelastic damping. When an object, for example a suspension wire, bends back and forth there is differential

heating across the object. While one side expands (and cools) the other contracts (and is heated) and vice versa, hence causing a thermal gradient across the object. This leads to a flow of heat as the material attempts to return to thermal equilibrium, which is a source of dissipation.

When the system is at rest, local temperature fluctuations lead to motion through the thermal expansion coefficient $\alpha = l^{-1} \left(\frac{dl}{dT} \right)$. The mechanical loss associated with thermoelastic damping is given by Nowick and Berry as[73]

$$\phi(\omega)_{te} = \frac{Y\alpha^2 T}{\rho C} \frac{\omega\tau}{1 + (\omega\tau)^2} \quad (2.28)$$

where Y is the Young's modulus, α the thermal coefficient of expansion, ρ is the density, τ is the relaxation time and C is the specific heat per unit volume of the suspension wire material. For a cylindrical fibre, the characteristic frequency (the frequency at which the maximum loss occurs) is given by

$$\begin{aligned} f_{char} &= \frac{1}{2\pi\tau} \\ &= 2.16 \frac{\kappa}{\rho C d^2} \end{aligned} \quad (2.29)$$

where κ is the thermal conductivity of the material and d the diameter of the suspension fibre.

If, instead of a cylindrical fibre, a fibre with rectangular cross section (a ribbon) is used, this characteristic frequency becomes:

$$f_{char} = \frac{\pi\kappa}{2\rho C t^2} \quad (2.30)$$

where t is the thickness of the ribbon. This allows the frequency at which maximum thermoelastic damping occurs to be altered while maintaining the same tension in the suspension wire.

Recently, this theory has been extended to include a temperature dependent Young's modulus. This leads to a replacement of α in equation 2.28 by the following effective thermal coefficient of expansion[74];

$$\alpha_{eff} = \alpha - \left(\frac{1}{Y} \frac{dY}{dT} \right) \frac{\sigma_0}{Y} \quad (2.31)$$

where σ_0 is the stress on the fibre. This indicates that it would be possible, given the correct stress, to set α_{eff} to zero (providing that the Young's modulus is in fact temperature dependent). This would then remove the effect of thermoelastic damping from the suspension fibres.

Braginsky et al.[75] have derived a similar expression for the power spectral density for the thermoelastic damping in a test mass;

$$S^{TE}(\omega) = \frac{8}{\sqrt{2\pi}} \frac{k_B T^2 \alpha^2 (1 + \sigma^2) \kappa}{\rho^2 C^2 r_0^3 \omega^2} \quad (2.32)$$

where r_0 is the beam radius at the point where its intensity has fallen to $1/e$ of the maximum value. This expression was derived for an infinite test mass: Liu and Thorne[67] determined a correction factor for finite test masses. This factor, which is dependent on the dimensions of the test mass, is of order unity for typical test masses.

2.7 The Dilution Factor

It has been noted that the test mass is suspended in a pendulum to attenuate seismic noise (section 1.5.2). A pendulum will also have associated with it thermal noise which may be reduced by careful construction. There are two main methods involved in this. The first is to set the pendulum resonant frequency to be below that of the detection bandwidth of the interferometer, so that at 50 Hz the thermal noise due to the pendulum will be that given by equation 2.20 with the total pendulum loss factor $\phi_{pend_{total}}$ substituted for $\phi(\omega)$. Secondly, as will be explained below, this loss factor is much less than that for the intrinsic loss of the material used to manufacture the suspension wires.

Consider a pendulum, mass m , hanging at rest from a rigid support by a suspension wire of length l . Now, consider what happens if the pendulum is pushed to one side. There will be two restoring forces acting on the pendulum; the transverse elastic force and the gravitational restoring force. If the wire is thin then most of the restoring force will come from gravity; the wire will bend only in a small region at the top near the suspension point[76]. Since the gravitational restoring force is lossless, the only loss will come from the small contribution from the transverse elastic spring constant which is itself a small fraction of the total spring constant.

Following this qualitative example, we can now proceed to derive an expression for the pendulum loss factor with respect to the intrinsic loss of the material from which the suspension is manufactured. First, consider the following alternative description of loss:

$$\phi(\omega_0) = \frac{1}{Q(\omega_0)} = \frac{E_{lost \text{ per cycle}}}{2\pi E_{stored}} \quad (2.33)$$

The energy lost per cycle is in this case dissipated in the bending of the wire. The energy stored in bending the wire is:

$$E_{stored_{wire}} = \frac{1}{2}k_{wire}x^2 \quad (2.34)$$

where x is the horizontal displacement of the pendulum from its equilibrium position and k_{wire} is the elastic spring constant of the wire.

The energy lost per cycle is a fraction α of the total elastic energy;

$$E_{lost \text{ per cycle}} = \frac{1}{2}\alpha k_{wire}x^2 \quad (2.35)$$

The total energy stored in a cycle of the swinging pendulum is

$$E_{stored_{pend}} = \frac{1}{2}(k_{wire} + k_{grav})x^2 \quad (2.36)$$

where k_{grav} is the effective “spring constant” associated with gravity[77]

$$k_{grav} = \frac{mg}{l} \quad (2.37)$$

Hence

$$\phi_{mat_{total}}(\omega_0) = \frac{\frac{1}{2}\alpha k_{wire}x^2}{2\pi \frac{1}{2}k_{wire}x^2} = \frac{\alpha}{2\pi} \quad (2.38)$$

and

$$\begin{aligned}
\phi_{pend_{total}}(\omega_0) &= \frac{\frac{1}{2}\alpha k_{wire}x^2}{2\pi\frac{1}{2}(k_{wire} + k_{grav})x^2} \\
&= \frac{\alpha k_{wire}x^2}{2\pi(k_{wire} + k_{grav})}
\end{aligned} \tag{2.39}$$

Dividing equation 2.39 by equation 2.38 gives the following:

$$\frac{\phi_{pend_{total}}(\omega_0)}{\phi_{mat_{total}}(\omega_0)} = \frac{k_{wire}}{k_{wire} + k_{grav}} \tag{2.40}$$

Since $k_{grav} \gg k_{wire}$ (provided the wire is thin), this simplifies to:

$$\phi_{pend_{total}}(\omega_0) \approx \phi_{mat_{total}}(\omega_0) \frac{k_{wire}}{k_{grav}} \tag{2.41}$$

Thus the loss factor displayed by the pendulum mode is a reduced level of that associated with the suspension material, again since $k_{grav} \gg k_{wire}$. The value $\frac{k_{wire}}{k_{grav}}$ is known as the *dilution factor*.

The situation may now be generalised to that of n suspension wires of length l suspending a mass m .

The elastic spring constant of a bending wire under tension is given by[77]

$$k_{wire} = \frac{n\sqrt{TYI}}{2l^2} \tag{2.42}$$

where T is the tension per wire, Y is the Young's modulus of the wire material and I is the moment of cross sectional area ($\frac{\pi r^4}{4}$ for a cylindrical wire of radius r). Substituting for k_{wire} and k_{grav} (equations 2.37 and 2.42) into equation 2.41 gives:

$$\phi_{pend_{total}}(\omega_0) = \phi_{mat_{total}}(\omega_0) \frac{n\sqrt{TYI}}{2mgl} \quad (2.43)$$

This can be generalised further by the addition of a factor ξ which has value 1 or 2 depending on whether the wires are constrained to bend only at the top or at the top and bottom respectively:

$$\phi_{pend_{total}}(\omega_0) = \phi_{mat_{total}}(\omega_0) \frac{\xi n\sqrt{TYI}}{2mgl} \quad (2.44)$$

Note that although equation 2.44 is defined at ω_0 , the relationship between the pendulum loss and the material loss at the same frequency ω still holds for all ω .

2.8 Summary of Suspension System Thermal Noise Sources

We have discussed the fact that thermal noise is greatest at the resonances of a system. In this section a summary is given of all major modes in a suspension chain. These essentially fall into two major areas; those due to the internal motion of the test mass and those due to the suspension itself.

2.8.1 Internal Modes

These modes, in which the test mass is considered to be an elastic body, occur as the test mass itself vibrates. While the centre of mass of the test mass remains fixed the shape of the test mass changes. Some of these modes couple

into the interferometer; others do not. The consequences of these modes are dealt with in the later chapters of this thesis.

The typical materials and geometry of the test masses used in gravitational wave detectors tend to set the lower limit for the frequencies of such modes at ~ 10 kHz. Thus, as discussed earlier, we are not concerned with the actual resonances (except for some control issues) but their contribution to thermal noise at frequencies much lower than the lowest internal mode.

2.8.2 Suspension Modes

The suspension modes essentially fall into three groups; pendulum modes, transverse vibrational (or violin) modes and other modes. In the case of these modes, the test mass may be considered to be a rigid body. These will be dealt with in turn.

Pendulum Mode

The pendulum mode excited in the direction of the arm of the interferometer has associated with it thermal noise which will directly couple into the interferometer signal, reducing its sensitivity. This is because the relative displacement of the masses will be altered by the thermal motion in the same way that it would be altered by an incident gravitational wave. However, as was discussed in section 2.7, the resonant frequency of the pendulum mode should be set to a value below the detection bandwidth of a detector. Indeed, the length and cross section of the suspension fibres/ wires is determined in part by this consideration, as well as by considerations of breaking stress and thermoelastic damping. Thus with careful engineering the thermal noise associated

with the pendulum mode may be reduced.

Violin Modes

The modes occur because of transverse vibrations in the suspension chain. Unlike the pendulum modes, the violin modes form a harmonic series with frequencies within the detection band. The loss is reduced from the intrinsic loss of the material in the same way as for the pendulum modes; the thermal displacement noise of the test mass due to the violin modes is the noise of the violin mode suppressed by a factor $\frac{m}{m_{wire}}$ where m is the mass of pendulum and m_{wire} is the mass of the suspension fibre/ wire. If the damping is homogeneous and the rocking mode of the suspension has been constrained then the loss due to the violin mode is related to the loss of the pendulum mode in the following way[78, 79],

$$\phi_{violin}(\omega) = 2\phi_{pend}(\omega) \quad (2.45)$$

The loss of the suspension is designed to be very low, hence the thermally induced noise due to the violin modes will be concentrated in very narrow bands around the resonant frequencies. Thus it would be relatively straightforward to notch these frequencies out of the detection band with only a small reduction in the useful bandwidth.

Other Modes

There is also thermal noise associated with the torsional and tilt modes of the suspension. However, the noise due to these modes can be kept within accept-

able limits by ensuring that the laser beam is positioned at the centre of the test mass. The thermal noise due to the vertical spring modes of the suspension cannot be reduced in the same way; for long baseline detectors the vertical modes couple into the horizontal direction by a factor (arm length/radius of the earth) which for a 4 km arm length detector such as LIGO is $\sim 0.1\%$. Experimental studies of the Glasgow 10 m prototype yield a similar coupling factor[80].

2.9 Calculation of Thermal Noise Level Due to Test Masses in an Interferometric Gravitational Wave Detector

We may use the methods above to calculate the thermal noise due to, say, a single test mass. The question remains as to how these noise levels combine in an actual interferometer. Hence in this section the calculation of the summation of thermal noise sources in the GEO600 detector will be detailed.

The following calculations are valid where the length of time the light remains in the interferometer is less than the storage time limit, as discussed in chapter 1. Consider the simplified optical layout of GEO600, as shown in figure 2.1. This figure shows the order in which the laser beam travels through one of the arms. It is assumed that paths 2 and 5 are the same length (x_2), as are paths 3 and 4 (x_3).

This consists of a beamsplitter, two inboard test masses and two outboard test masses. It should be noted that the inboard test masses actually sit along the same axis as the end test masses but are drawn here to one side for clarity.

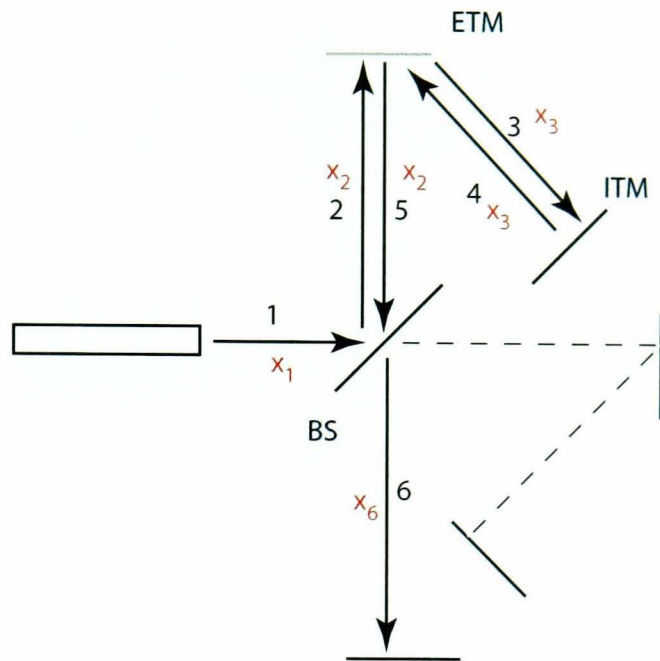


Figure 2.1: *Simplified optical path of GEO600. The length of these paths is shown in red (i.e. x_1 , x_2 , x_3 and x_6)*

We will discuss the thermal noise contribution to the GW signal h in 2 stages. Firstly, we will discuss the displacement changes due to motion of the different mirrors. This will be achieved by considering the effect of 3 displacements; Δx_{ETM} , associated with each end test mass (ETM), Δx_{ITM} , associated with inboard test mass (ITM) and Δs_{BS} associated with the beamsplitter.

2.9.1 Displacement Contribution of End Test Mass Per Arm

The path length of one arm before a displacement of Δx_{ETM} will be, according to 2.2,

$$x_1 + x_2 + x_3 + x_3 + x_2 + x_6 \tag{2.46}$$

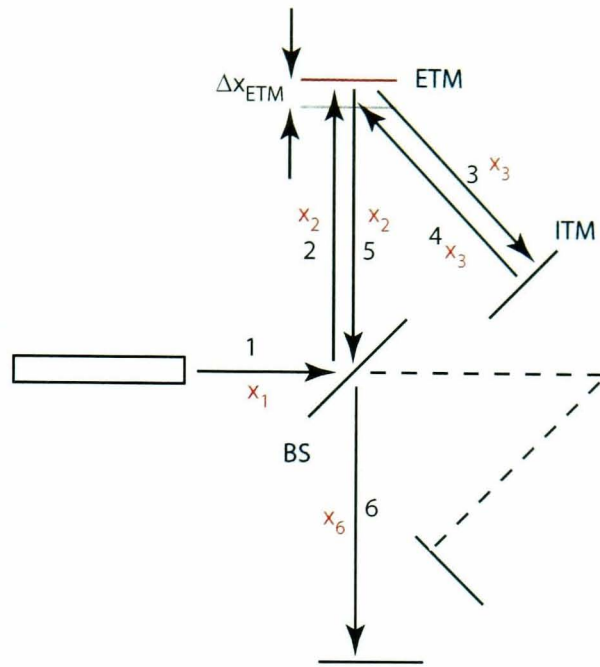


Figure 2.2: *Optical path length change caused by movement of ETM*

Afterwards, the path length will be

$$x_1 + x_2 + \Delta x_{ETM} + \Delta x_{ETM} + x_3 + x_3 + \Delta x_{ETM} + \Delta x_{ETM} + x_2 + x_6 \quad (2.47)$$

that is, there will be an increase of $2\Delta x_{ETM}$ for each bounce of the light off the end test mass. Hence the total displacement increase for each ETM will be

$$4\Delta x_{ETM} \quad (2.48)$$

2.9.2 Displacement Contribution of Inboard Test Mass Per Arm

The path length of one arm before a displacement of Δx_{ITM} will again be

$$x_1 + x_2 + x_3 + x_3 + x_2 + x_6 \quad (2.49)$$

according to 2.3.

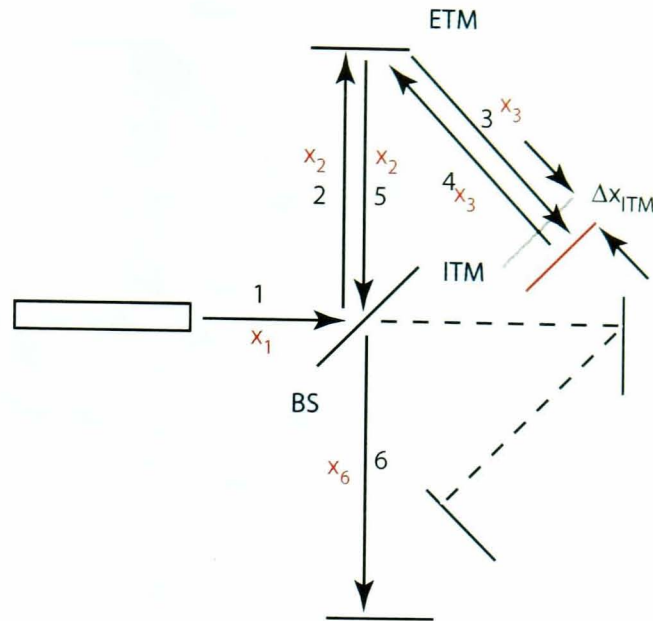


Figure 2.3: *Optical path length change caused by movement of ITM*

This time, the path length after displacement will be

$$x_1 + x_2 + x_3 + \Delta x_{ITM} + \Delta x_{ITM} + x_3 + x_2 + x_6 \quad (2.50)$$

Hence the total displacement increase for each ITM will be

$$2\Delta x_{ITM} \quad (2.51)$$

2.9.3 Displacement Contribution of Beamsplitter

The contribution of Δs_{BS} is slightly more complicated since it affects both arms at the same time. The path length in the “North” arm *after* a displacement Δs_{BS} (which in turn leads to a displacement R in the axes of the arms, as shown in figure 2.4) will be

$$x_1 + R + x_2 + x_3 + x_3 + x_2 + R + x_6 - R \quad (2.52)$$

according to 2.4.

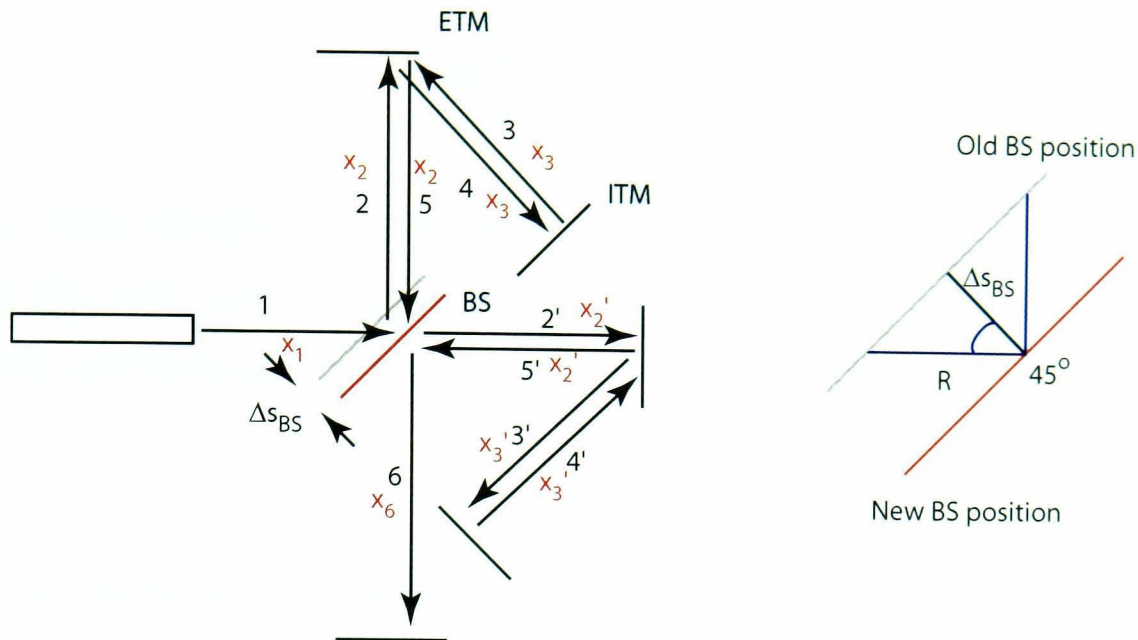


Figure 2.4: *Optical path length change caused by movement of BS*

Also from figure 2.4, $R = \frac{\Delta s_{BS}}{\cos 45^\circ}$, giving a displacement

$$x_1 + \frac{\Delta s_{BS}}{\cos 45^\circ} + x_2 + x_3 + x_3 + x_2 + x_6 \quad (2.53)$$

The path from the BS to the ETM is unchanged. The reason for this is that the motion of the BS only causes the light to hit a different part of the ETM (the point at which the light strikes the ETM moves slightly to the right).

The path length after displacement in the “East” arm will be, where the dashed quantities indicate the East arm;

$$x_1 + \frac{\Delta s_{BS}}{\cos 45^\circ} + x_2' + x_3' + x_3' + x_2' + \frac{\Delta s_{BS}}{\cos 45^\circ} + x_6 - \frac{\Delta s_{BS}}{\cos 45^\circ} \quad (2.54)$$

using similar arguments as were used for the North arm.

Hence the total increase in path length due to the displacement Δs_{BS} will be

$$2\frac{\Delta s_{BS}}{\cos 45^\circ} = 2\sqrt{2}\Delta s_{BS} \quad (2.55)$$

Now, these changes are uncorrelated and so must be added in quadrature. Thus the total path change due to thermally induced displacements in the mirrors and beamsplitter is:

$$\begin{aligned} & \sqrt{(4\Delta x_{ETM})^2 + (4\Delta x_{ETM})^2 + (2\Delta x_{ITM})^2 + (2\Delta x_{ITM})^2 + (2\sqrt{2}\Delta s_{BS})^2} \\ = & \sqrt{32\Delta x_{ETM}^2 + 8\Delta x_{ITM}^2 + 8\Delta s_{BS}^2} \end{aligned} \quad (2.56)$$

2.9.4 Path Length Change in Terms of h

If we consider now the incidence of a gravitational wave, how might this displacement change be written in terms of h ? Consider a gravitational wave incident normal to the plane of the detector. Then, as commented earlier the increase in the length of one arm will be $\Delta L = hL/2$. The other arm will at the same time decrease in length by the same amount (see figure 2.5). Note that we assume here that the ITMs are close to the beamsplitter, otherwise they would move as well as the end test masses.

Hence the change in the path length of one arm will be $2hL/2$ on the initial bounce off the ETM and a further $2hL/2$ on the return, giving a total of $4hL/2$ path length difference. The change in the other arm will be the same in magnitude but opposite in sign. These path length difference are combined linearly, because they are now correlated. This leads to a path length change in terms of h as $4hL$.

These two definitions of the path length change must be equivalent, giving:

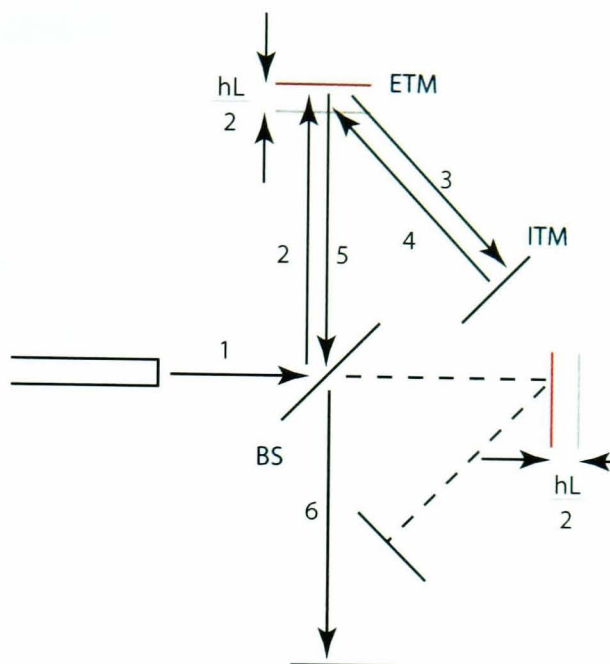


Figure 2.5: *Motion of the masses at the interferometer caused by an incident gravitational wave*

$$\begin{aligned}
 4hL &= \sqrt{32\Delta x_{ETM}^2 + 8\Delta x_{ITM}^2 + 8\Delta s_{BS}^2} \\
 h &= \frac{1}{L} \frac{\sqrt{32\Delta x_{ETM}^2 + 8\Delta x_{ITM}^2 + 8\Delta s_{BS}^2}}{4} \\
 &= \frac{1}{L} \sqrt{2\Delta x_{ETM}^2 + \frac{1}{2}\Delta x_{ITM}^2 + \frac{1}{2}\Delta s_{BS}^2} \quad (2.57)
 \end{aligned}$$

This is the total thermal noise contribution of 5 test mass mirrors in GEO600. An example value for the total thermal noise contribution may be obtained by using the value of $S_x(\omega) = \Delta x^2$ calculated for fused silica in section 2.5, $S(\omega) = 8.2 \times 10^{-40} \text{ m}^2/\text{Hz}$. Using this value for the three different types of mirror yields an estimate of the total thermal noise contribution for the test masses themselves (neglecting all other sources of loss) of $\tilde{h} = 8.2 \times 10^{-23} / \sqrt{Hz}$.

2.10 Conclusions

Thermal noise is one of the most important noise sources with an impact on interferometric gravitational wave detectors. We have discussed possible sources of thermal noise in the suspension systems of a typical detector and methods by which the level of this noise may be reduced where possible. In addition, where the thermal noise cannot be reduced completely methods have been introduced to minimise the impact of the noise, either by the use of notch filters or by setting the frequency at which the noise is a maximum to be below the detection bandwidth of the detector.

Finally, a method of combining the thermal noise contribution due to different sources in the GEO600 gravitational wave detector was introduced.

Chapter 3

Dielectric coatings

All current ground based interferometric gravitational wave detectors use a multi bounce interferometer design and hence require mirrors with a very high reflectivity. As a result, metallic mirror coatings are not used since their optical absorption is too high [81] and the high power of the laser system can damage the coatings. Another possible mirror coating is a dielectric coating. Such coatings are more durable than metallic coatings and have a high degree of flexibility in terms of reflectivity and frequency response. In this chapter the nature and process of applying such coatings will be discussed. Following this, the investigation of the magnitude of the potential contribution to the total loss factor of a mirror due to the presence of a dielectric coating will be described.

3.1 Nature of dielectric coatings

A dielectric coating consists of a number of layers of alternating dielectric materials of different refractive index. Common examples of such materials in

use in coatings are tantalum pentoxide, silica, titanium oxide, hafnium oxide and niobium oxide. In general, the optical thickness in wavelengths for highly reflecting coatings is the same for each layer. This optical thickness is generally $\lambda/4$. The optical thickness is related to the actual thickness in the following way:

$$\delta = nh \quad (3.1)$$

where δ is the optical thickness, n is the index of refraction of the material at that wavelength and h is the physical thickness. Care has to be taken in discussions about coatings as to whether physical or optical thickness is meant.

The alternating layers of material have different indices of refraction; it is this difference which leads to the reflectivity of the coating. Consider a laser incident on a coating of an even number of quarter wave ($\delta = \lambda/4$) layers, $2N$, of indices n_H and n_L with $n_H > n_L$. If the beam is incident from a material with index n_0 and the substrate has index n_s , then the reflectivity of the coating will be [82](see figure 3.1)

$$R_{2N} = \left(\frac{n_s f - n_0}{n_s f + n_0} \right)^2 \quad (3.2)$$

where $f = (n_H/n_L)^{2N}$.

For an odd number of layers $2N + 1$ this becomes

$$R_{2N+1} = \left(\frac{f n_H^2 - n_0 n_s}{f n_H^2 + n_0 n_s} \right)^2 \quad (3.3)$$

Two conclusions can be made from these equations. The first is that the greater

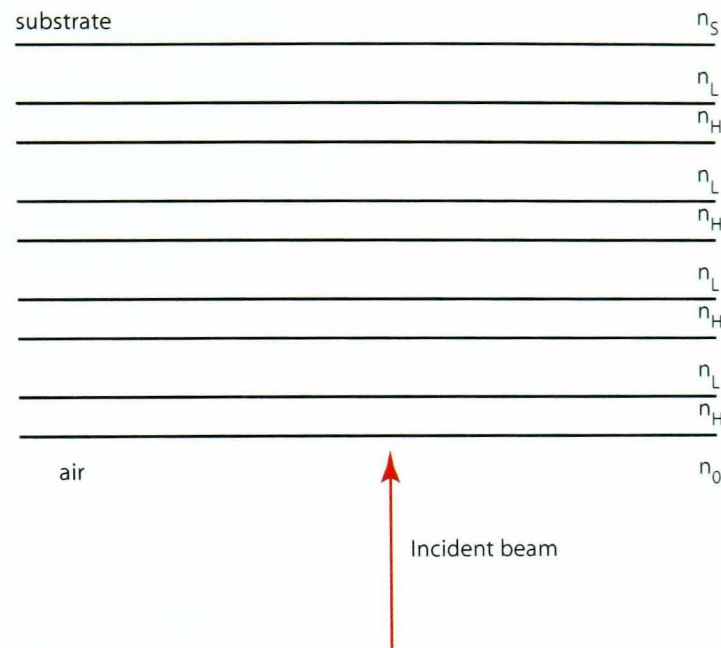


Figure 3.1: *Diagram of a dielectric coating with 2 different materials in alternating layers*

the number of layers the higher reflectivity and secondly that the greater the difference between n_L and n_H the greater the reflectivity. This means that for a given reflectivity the number of layers can be reduced by using materials with widely different indices of refraction; alternatively, if the desired materials have very close indices then a much greater number of layers is required to attain a given reflectivity.

For example, take the case of a 30 quarter wave layer coating made from tantala (Ta_2O_5) and silica (SiO_2), with $n_{silica} = n_L = 1.45$ and $n_{tantala} = n_H = 2.03$ at 1064 nm. Using equation 3.2 this gives a reflectivity of $[1 - (1 \times 10^{-4})]$.

Alternatively, if alumina (Al_2O_3 , $n_{alumina} = 1.65$) is used in place of silica, the reflectivity drops to $[1 - (6 \times 10^{-3})]$. In order to reach an equivalent reflectivity to the silica/ tantala coating, ~ 50 layers would be required.

For the work done in this thesis, it is necessary to be able to treat the entire coating as consisting of 1 composite material as opposed to 2 separate materi-

als. This is for the energy calculation which will be discussed in more detail in chapter 4. From composite materials theory, it can be shown that the effective Young's modulus and Poisson's ratio for an isotropic multilayer coating with two different materials are [83, 84]

$$Y_{eff} = \frac{Y_1 h_1 + Y_2 h_2}{h_1 + h_2} \quad (3.4)$$

$$\sigma_{eff} = \frac{h_1 \sigma_1 Y_1 (1 - \sigma_1^2) + h_2 \sigma_2 Y_2 (1 - \sigma_2^2)}{h_1 Y_1 (1 - \sigma_1^2) + h_2 Y_2 (1 - \sigma_2^2)} \quad (3.5)$$

where Y_x , t_x and σ_x are the Young's modulus, layer physical thickness and Poisson's ratio of material x .

Again, consider our 30 quarter wave layer coating of silica/ tantala. Substituting the properties of these two materials into equation 3.1 and subsequently 3.4 and 3.5 gives $Y_{eff} = 1 \times 10^{11} \text{ kg/ms}^2$, $\sigma_{eff} = 0.20$ and the total physical thickness of the coating as $4.72 \times 10^{-6} \text{ m}$.

3.2 Manufacturing techniques

3.2.1 Introduction

There are a number of techniques used to apply multilayer coatings of thin films onto a substrate. In this section a brief overview of these techniques will be given. Following this, a more detailed discussion of ion beam sputtering, the technique used to create the coatings used in this thesis, will be given. The material in this section is drawn primarily from [85, 81, 86, 87].

3.2.2 Coating Processes

One of the oldest methods of applying a coating (or thin film deposition as it is more commonly referred to), is *thermal* or *vacuum evaporation*. In this process, the coating material (evaporant) is generally placed in a crucible and heated until it changes to the gas phase. Because the process takes place in vacuum, or at least reduced pressure environment, the atoms ejected from the surface move in a steady stream towards the substrate, upon which they condense. There is a great diversity in the methods used for heating the evaporant. These include heating the crucible by RF induction, conduction or radiation. An electron beam directed at the crucible may also be used, or a laser. In these kinds of processes care must be taken to ensure the cleanliness of the substrate (as is the case with all the processes discussed here). Finally, because the evaporant is held in a crucible while it is being heated care must be taken to ensure that there is no reaction between the evaporant or the crucible material, or at least that this reaction is slowed as much as possible.

A second class of deposition methods is use of *gas phase chemical* techniques. Here a chemical process is used to apply the film rather than a physical one. Example of such techniques are chemical vapour deposition or thermal oxidation. Thermal oxidation is a technique where the surface of the substrate is oxidised to form a protective layer. For example, silicon may be oxidised to silica. This is useful in protecting sensitive silicon electronics, e.g. p-n junctions as well as for device purposes. Chemical vapour deposition (or CVD) involves a mixture of constituents in a vapour phase which then react at or close to the substrate. The chemical and physical composition of the thin film can be tailored since the chemical reaction can be finely controlled. Examples of chemical reactions used in this technique include thermal decomposition, oxidation, reduction, hydrolysis and carbide and nitride formation: this list is

not, however, exhaustive.

Liquid phase chemical film formation includes electrochemical plating (for example, anodisation or electroplating) and chemical deposition, for example reduction plating or displacement deposition.

The final type of thin film deposition we will discuss is use of *glow discharge* techniques. This class includes two main methods, sputtering and plasma processes. Plasma processes use the presence of a cloud of energetic ions to accelerate certain chemical deposition techniques such as oxidation, nitriding and carburizing.

Sputtering is the most basic and widely used glow discharge technique. It involves momentum transfer from a stream of ions which bombards the surface of the coating material. This causes ejection of atoms of the material which condense on the substrate; it appears in this respect very similar to thermal evaporation and is indeed used in its place.

We shall now discuss one particular form of sputtering, ion beam sputtering.

3.2.3 Ion Beam Sputtering

A simple arrangement of ion beam sputtering is shown in figure 3.2. Here the ion beam traverses the evacuated chamber to the target which then ejects atoms towards the substrate. The ions themselves are generally formed in a plasma which itself can either be generated solely within the ion gun itself or, more usually, within the entire chamber. An example of this arrangement, using DC current, is shown in figure 3.3.

In this setup the electric field accelerates the electrons in the argon gas which

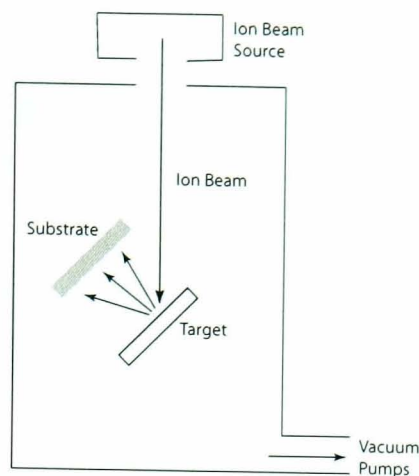


Figure 3.2: *A simple sputtering setup*[2]

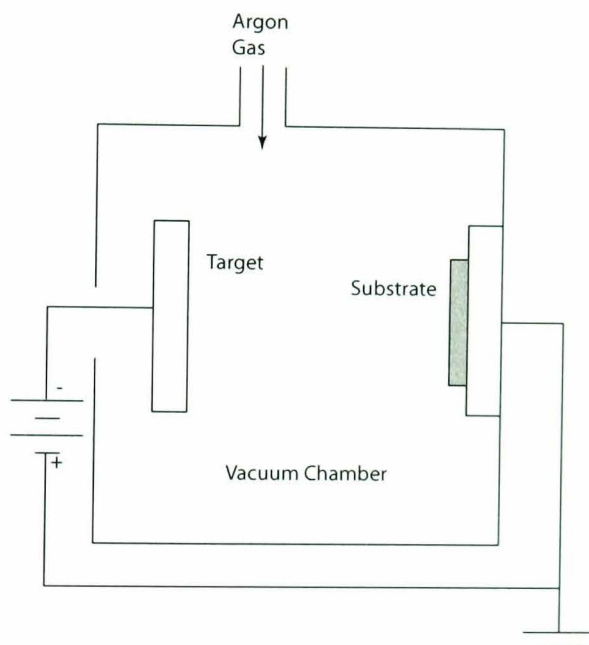


Figure 3.3: *A DC glow discharge sputtering scheme*[2]

ionize the atoms; argon is commonly used as a source of sputtering ions. The positive ions consequently formed are accelerated to the cathode which will then be sputtered, assuming the energy of the bombardment ions is high enough. Note that this arrangement works if the target material is conductive. In the case of an insulating target material an RF power source is used. The target is given a negative potential which attracts positive ions until the consequent positive charging causes the target to repel any further positive ions. The potential is then reversed so that the target is bombarded with negative

electrons which neutralise the charge of the ions. The current is then reversed again and the process continues. A final variant of sputtering is to use a conductive target material but mix reactive gas ions with the inert gas sputtering ions. This is primarily used to produce metallic oxide coatings and is known as “reactive” sputtering.

3.2.4 Ion Assisted Deposition and Dual Ion Beam Sputtering

Another use of an ion source (argon or reactive gas) in thin film deposition is to direct it at the substrate while the target atoms are generated independently. This is known as *ion assisted deposition*; when the target atoms are generated using ion beam sputtering, the combined process is known as *dual ion beam sputtering* (DIBS). The second source is used to improve the material properties of the coating layer. It energises the ejected target atoms before they reach the substrate which gives them greater mobility which in turn leads to a coating with better composition or stoichiometry. In addition, the ions from the second source drive the target atoms into the substrate which again improves the properties of the coating. The alterations to the initial simple sputtering scheme required to allow dual ion beam sputtering are shown in figure 3.4

3.2.5 Properties of Ion Sputtered Coatings

Due to the high energy of the sputtered atoms of film material, ion sputtered coatings tend to exhibit both a denser structure and a greater adhesion. In addition, they have been shown to have better optical properties than equiv-

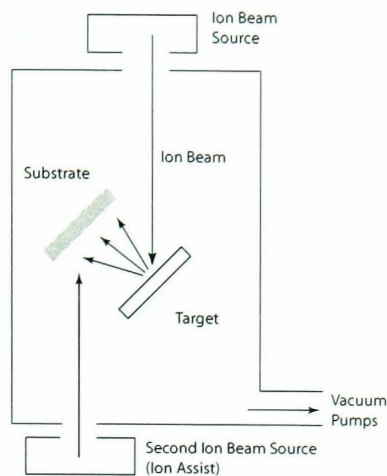


Figure 3.4: *A dual ion beam sputtering setup*

alent coatings created using electron beam thermal evaporation techniques. Electron beam coatings have an optical power absorption in excess of 1000 ppm[88] (parts per million) while sputtered coatings have an absorption of less than 30 ppm[89]. This is especially important in Fabry-Perot type interferometers where extremely high reflectivity/ very low optical absorption mirrors are required (less than a few parts per million).

3.3 Dielectric Coating as Source of Mechanical Loss

Possible sources of mechanical dissipation (and hence possible contributions to the thermal noise level) were discussed with chapter 2. In particular it was noted that alterations to the test mass might lead to an additional source of dissipation; a source of excess loss. The purpose of the remainder of this thesis is to determine initially the existence of such excess loss due to dielectric coatings. Subsequently the possible root cause of such a loss will be investigated (at least phenomenologically). In the next section a possible model of how such a loss might be described analytically will be constructed, followed by a

discussion of a modeshape determination experiment. In the remaining section possible sources of the coating loss will be considered.

3.4 Analysis technique

3.4.1 Loss Parameterisation

The total level of loss attributable to a suspension system can be calculated by adding all the separate loss factors due to different sources of dissipation. If the intrinsic dissipation in the substrate and a loss due to the coating are thought to be the only sources of loss, we may therefore describe the loss of a coated test mass in the following way:

$$\phi(\omega_0)_{coated} = \phi(\omega_0)_{substrate} + \phi(\omega_0)_{coating_{mode\ dependent}} \quad (3.6)$$

where we assume frequency independent damping in the intrinsic term and a general mode dependent form for the coating loss. Hence we may separate the $\phi(\omega_0)_{coating_{mode\ dependent}}$ term into the products of two terms, one of which is mode dependent and one of which is mode *independent*. This gives a loss of the form $R(\omega_0)\phi(\omega_0)_{coating}$ where $R(\omega_0)$ is mode dependent but $\phi(\omega_0)_{coating}$ is mode independent. We wish to establish the form that the factor $R(\omega_0)$ takes. Recall the following definition of $\phi(\omega_0)$;

$$\phi(\omega_0) = \frac{E_{dissipated\ per\ cycle}}{2\pi E_{stored}} \quad (3.7)$$

Now consider the case of two sources of dissipation, the substrate and the

coating. Equation 3.7 then becomes;

$$\phi(\omega_0)_{coated} = \frac{E_{dissipated_{substrate}} + E_{dissipated_{coating}}}{2\pi E_{stored_{total}}} \quad (3.8)$$

Substituting with equation 3.7 into the numerator gives;

$$\begin{aligned} \phi(\omega_0)_{coated} &= \frac{2\pi E_{stored_{substrate}} \phi(\omega_0)_{substrate} + 2\pi E_{stored_{coating}} \phi(\omega_0)_{coating}}{2\pi E_{stored_{total}}} \\ &= \frac{E_{stored_{substrate}}}{E_{stored_{total}}} \phi(\omega_0)_{substrate} + \frac{E_{stored_{coating}}}{E_{stored_{total}}} \phi(\omega_0)_{coating} \end{aligned} \quad (3.9)$$

This may be simplified to

$$\phi(\omega_0)_{coated} = \phi(\omega_0)_{substrate} + \frac{E_{stored_{coating}}}{E_{stored_{substrate}}} \phi(\omega_0)_{coating} \quad (3.10)$$

if $E_{stored_{substrate}} \gg E_{stored_{coating}}$. This is likely since the substrate is of scale \sim cm while the coating is of scale $\sim \mu m$. This consequently defines the mode dependent factor R as:

$$R(\omega_0) = \frac{E_{stored_{coating}}}{E_{stored_{substrate}}} \quad (3.11)$$

It is possible to extend this to other sources of loss. In particular, if coating is present on the barrel of a test mass the following would be appropriate, where from now on we use $E_{stored_{coating}} = E_{coating_{on\ face}}$, $E_{stored_{substrate}} = E_{substrate}$ for simplicity;

$$\phi(\omega_0)_{coated} \approx \phi(\omega_0)_{substrate} + \frac{E_{coating\ on\ face}}{E_{substrate}} \phi(\omega_0)_{coating\ on\ face} + \frac{E_{coating\ on\ barrel}}{E_{substrate}} \phi(\omega_0)_{coating\ on\ barrel} \quad (3.12)$$

where the quantity $E_{coating\ on\ barrel}$ is introduced which is equivalent to $E_{coating\ on\ face}$ for a coating on the barrel of the mass. Hence if we have knowledge of $\phi(\omega_0)_{coated}$ (the loss of the coated test mass), $\phi(\omega_0)_{substrate}$ (the intrinsic loss of the test mass) and $\frac{E_{coating\ on\ face}}{E_{substrate}}$ (the fraction of energy stored in the coating), we can in principle evaluate $\phi(\omega_0)_{coating}$ in the case of coating present on the front surface of the sample only. For the case where coating is also present on the barrel, $\frac{E_{coating\ on\ barrel}}{E_{substrate}}$ would also be required. In particular, if we know a range of these values, for example a set for each resonant mode of the test mass, linear regression could be used to provide not only a value for $\phi(\omega_0)_{coating}$ but also a measure of the accuracy of the model.

3.4.2 Analysis Requirements

We may use equation 3.12 as a multi-parameter linear fitting function to determine values for $\phi(\omega_0)_{coating\ on\ face}$ and $\phi(\omega_0)_{coating\ on\ barrel}$ where appropriate. The value for $\phi(\omega_0)_{coated}$ may be determined for a number of modes, along with the value of $\phi(\omega_0)_{substrate}$, using the experimental technique described in appendix A: the energy ratios $\frac{E_{coating\ on\ face}}{E_{substrate}}$ and $\frac{E_{coating\ on\ barrel}}{E_{substrate}}$ are then calculated for each of the modes measured.

The energy stored in the substrate and coating will depend on the shape of the mode at each resonant frequency. The stored energy arises from the strain induced in the coating/ substrate by this deformation. The calculation of the energy as a function of strain using finite element analysis will be discussed in

chapter 4, along with the subsequent energy ratio calculation.

Finally a further experimental technique is required to link the experimental observations of the loss of the samples with the energy ratios derived through finite element analysis. Assuming that each of the required terms is calculated for several modes (and hence mode shapes in the latter case), a method is needed to ensure that the mode identification in each case is correct; the technique used here to determine the loss of the test mass yields little about the shape of the resonant mode although it gives accurate information about the mode frequency. Hence a second experimental technique is used to connect the mode frequency with the shape generated by finite element analysis. This be presented in the next section.

3.5 Establishing Resonant Mode Shapes

Having obtained loss factors for the samples, the next important stage in the analysis is to establish a link between the mode frequencies and the resonant modes of the mass as determined by a finite element package (see section 4.3). The loss measurement system itself provides a certain amount of information on this subject. The interferometer can be used to sense displacement either at the center of a mass or off centre; indeed this is carried out as a matter of course. Thus modes which have little motion at the centre but greater motion elsewhere (or vice versa) can be determined.

The matter of mode identification may be relatively straightforward where there is a close concordance between the measured frequency of the mode and the modelled frequency, or where there is a large gap in frequencies indicating that there is only one possible candidate for the mode. Where there are a

number of candidates, however, or generally where there is a question of the mode identification, a further technique to determine the modeshape of a mode at a particular frequency would be invaluable. This section will discuss such a technique.

3.5.1 Experimental Setup (Direct Modeshape)

The experimental arrangement is shown in figure 3.5.

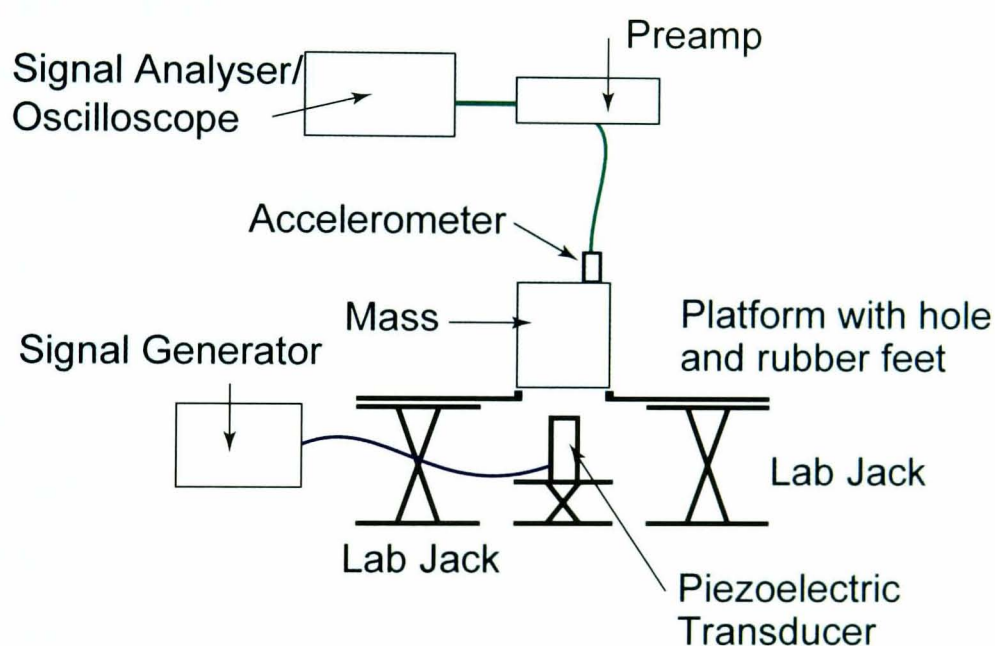


Figure 3.5: *Experimental arrangement used to determine the modeshapes of test masses*

The mass is mounted upon rubber grommets on a metal plate with a circular hole cut in the centre. A piezo transducer is then raised on a lab jack until it touches the lower surface of the mass. This transducer is then used to drive the mass. The motion of various points on the surface of the mass are measured using very small accelerometers (Brüel & Kjaær 4374 accelerometers [90] which have a mass of less than a gram). These accelerometers are attached to the surface of the mass with double sided tape. For this reason this technique is

not suitable for all masses and indeed was only used here with a mass which would not be used in any future interferometer development.

There are two methods of modeshape determination. The first was to use an oscilloscope with the drive signal superimposed with the signal of an accelerometer placed at different sites around the surface of the mass. As the frequency of the drive was increased, the resonances were noted along with the phase difference between the drive and accelerometer signal. By repeating this using different sites around the surface at 45° angular intervals around the edge of the mass, a picture could be obtained of the motion of the surface of the mass and from this the nature of the shape of the mode could be determined.

The difficulty of this method is that the motion is necessarily discretised into separate accelerometer sites, and the accuracy with which the phase difference could be measured is not great since it was measured by eye. In addition since only the motion of the front surface is being measured distinction can only be made between modes which have a different surface motion; it would be difficult to distinguish between modes with the same surface motion but different barrel motion, for example different orders of drum modes.

Nonetheless this method works well in basic mode shape identification. The second method is very similar but uses a spectrum analyser in place of the oscilloscope; for each accelerometer siting a swept sine output is used to determine the transfer function between the accelerometer and the drive. This again gives phase information about the surface motion.

An example of the usage of this technique will be given in chapter 5. In the next section we will discuss where the possible sources of mechanical loss within coating may be.

3.6 Potential Source of Coating Loss

In this final section we will discuss briefly some possible sources of loss due to a coating, and how they might be manifested in a loss measurement scheme such as that outlined above.

Coating/ Substrate Interface

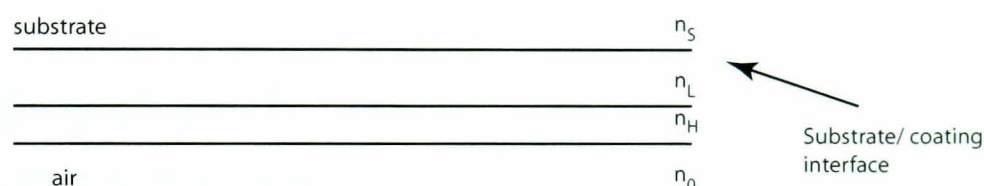


Figure 3.6: *Location of substrate/ coating interface*

One possible source of loss would be the interface between the substrate and the coating itself. This could be due to rubbing between the two objects or damage done to the substrate surface by the deposition technique. If this were the dominant source of loss, then if a number of coatings were tested each with different thicknesses/ layer composition it is likely that the loss would remain essentially constant as the loss arises primarily from the deposition of the initial layer.

Intracoating Interfaces

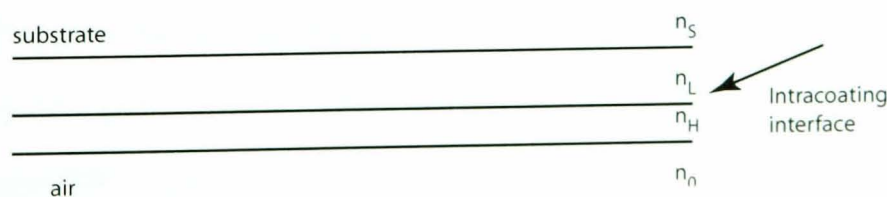


Figure 3.7: *Location of coating/ coating interface*

A similar source of loss might be the interface between each layer in the coating: again this could be due to discontinuities at the edges of each layer caused by the coating process itself. A method of detecting this type of loss would be to measure the loss of a number of coated masses, each with the same coating composition in terms of material and total thickness but with a varying layer thickness thus changing the number of intracoating interfaces.

Intrinsic Coating Material Loss

Finally, the third possible source of loss would be the intrinsic loss of the materials used in the coating. This is perhaps the most likely a priori source of loss, as there will in any case be an intrinsic loss associated with each thin film material. The question is whether this will be dominant compared to other potential loss sources. This loss could be determined by using a number of coatings with the same materials and number of layers but different proportions of materials, for example 1:3, 1:1 and 3:1.

3.7 Conclusions

There are a number of techniques suitable for the deposition of dielectric coatings, of which the most suitable for mirror coatings is ion beam sputtering since it leads to lower optical absorption than, for example, electron beam evaporation. Electron beam coatings have an optical absorption in excess of 1000 ppm[88] (parts per million) while sputtered coatings have an absorption of less than 30 ppm[89]. Sputtered dielectric coatings are themselves used as they are more sturdy and have a better optical performance than metal coatings.

We have established a possible model for the loss due to such a dielectric

coating and the experimental and analytical steps required to determine both the presence and potential source of the loss.

In the next chapter the experimental techniques used in this thesis will be outlined.

Chapter 4

Numerical Calculation of Strain Energy

At the end of chapter 3, the parameterisation and calculation of loss was discussed. This calculation uses the ratio of the strain energy (that due to deformation) stored in the coating of a mirror to that stored in the substrate of the mirror. The purpose of this chapter is to deal with the subject of strain, its definition and consequent use in a strain energy definition. Thereafter the finite element program used to calculate the natural modes of the test mass samples, Algor, will be described along with actual models used.

Finally, the strain energy calculation program Ocean will be examined in each of its stages. We begin, however, with a simple definition of strain.

4.1 Definition of strain

4.1.1 One dimension

Consider a one dimensional bar such as that in figure 4.1. If a force is exerted

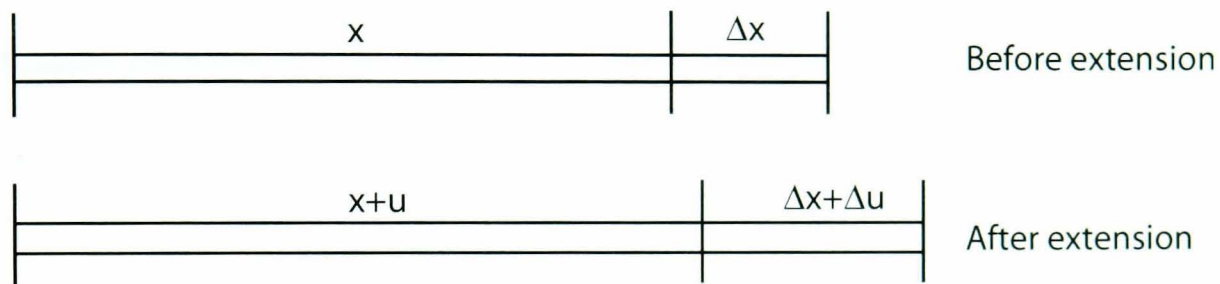


Figure 4.1: *Typical one dimensional shear deformation*

on the bar causing it to extend, x becomes $x + u$ and Δx becomes $\Delta x + \Delta u$ where u is a displacement. *Strain* is defined as the change in length over the original length. Thus we have

$$\begin{aligned} \text{strain} &= \frac{\text{change in length}}{\text{original length}} \\ &= \frac{\Delta u}{\Delta x} \end{aligned} \quad (4.1)$$

which tends to $\frac{du}{dx}$ as $\Delta x \rightarrow 0$. This may be described as an extension per unit length

4.1.2 Two dimensions

To extend this to 2 dimensions, consider a plate with two orthogonal vectors defined upon it, $P\vec{Q}_1$ and $P\vec{Q}_2$. These are shown in figure 4.2. If this plate is then distorted, $P\vec{Q}_1$ will become $P'\vec{Q}'_1$ and $P\vec{Q}_2$ will become $P'\vec{Q}'_2$. Using the notation in the figure, we have the extension per unit length parallel to x_1 as

$\frac{du_1}{dx_1}$ and that parallel to x_2 as $\frac{du_2}{dx_2}$. However there are also two cross terms, $\frac{du_1}{dx_2}$ and $\frac{du_2}{dx_1}$.

4.1.3 Rotation and symmetry

If a pure rotation is considered, such as that shown in figure 4.2, we see that

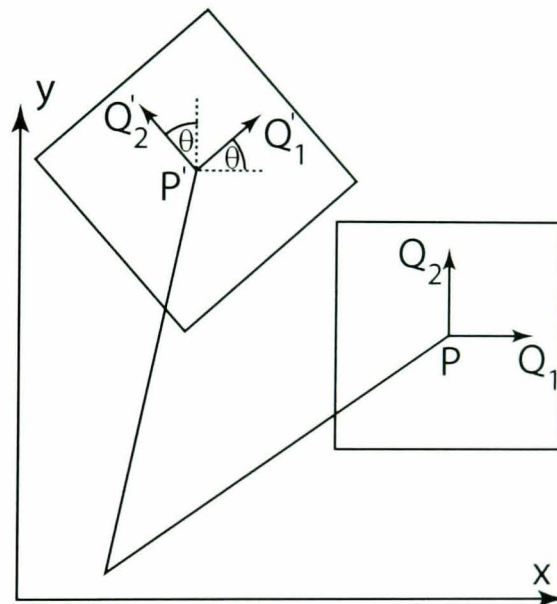


Figure 4.2: *Rotation of square plate*

$$\begin{aligned}
 \tan\theta &= \frac{du_2}{dx_1} \\
 &= -\frac{du_1}{dx_2} \\
 &\approx \theta
 \end{aligned}
 \tag{4.2}$$

for small displacements. A notional “strain” tensor of the form

$$\begin{pmatrix} \frac{du_1}{dx_1} & \frac{du_1}{dx_2} \\ \frac{du_2}{dx_1} & \frac{du_2}{dx_2} \end{pmatrix}$$

would be similar to the form for a pure rotation;

$$\begin{pmatrix} 0 & -\theta \\ \theta & 0 \end{pmatrix}$$

Thus $\frac{du_1}{dx_2}$ and $\frac{du_2}{dx_1}$ signify not only strain but also rotation. Since for a pure rotation there will be no strain a more accurate definition of strain is required which will not confuse rotation with strain. The tensor above is an antisymmetric tensor. So a new definition of a strain tensor can be defined;

$$\begin{pmatrix} \frac{du_1}{dx_1} & \frac{du_1}{dx_2} + \frac{du_2}{dx_1} \\ \frac{du_2}{dx_1} + \frac{du_1}{dx_2} & \frac{du_2}{dx_2} \end{pmatrix}$$

which is symmetric and zero for a pure rotation, as required. [91]

The full definition of strain is as follows;

$$u_{ij} = \frac{1}{2} \left(\frac{du_i}{dx_j} + \frac{du_j}{dx_i} \right) \quad (4.3)$$

which is valid for small displacements. It is this version that will be used for the remainder of the study [92].

4.2 Strain energy

The energy density due to the deformation of an isotropic body is [92]

$$\rho_E = \frac{Y}{2(1+\sigma)} \left(u_{ij}^2 + \left(\frac{\sigma}{1-2\sigma} \right) u_{ll}u_{mm} \right) \quad (4.4)$$

where Einstein summation is implied (e.g. $u_{ij}^2 = u_{ij}u_{ij}$ which means multiply each component of the tensor together and then sum over i and j), Y is the Young's modulus and σ is the Poisson's ratio of the substance being studied. To obtain the energy stored in the whole body, this expression is integrated over the volume of the body [92]. It is instructive to look at the terms in this equation with respect to their physical relevance. Two sources of energy may be introduced, the bulk and shear energies.

4.2.1 Bulk Energy

Consider a small cuboidal volume with sides of length L_x , L_y and L_z . Then the volume V will be $L_xL_yL_z$. If this volume is then deformed, the principal strains (those in the x , y and z direction) will be;

$$u_{xx} = \frac{\Delta x}{L_x} \quad (4.5)$$

$$u_{yy} = \frac{\Delta y}{L_y} \quad (4.6)$$

$$u_{zz} = \frac{\Delta z}{L_z} \quad (4.7)$$

Then the new volume V' will be;

$$\begin{aligned} V' &= (L_x + \Delta x)(L_y + \Delta y)(L_z + \Delta z) \\ &= (L_x + L_x u_{xx})(L_y + L_y u_{yy})(L_z + L_z u_{zz}) \\ &= L_x(1 + u_{xx})L_y(1 + u_{yy})L_z(1 + u_{zz}) \\ &= V + Vu_{ii} \end{aligned} \quad (4.8)$$

where higher order terms are disregarded. Then, since $\Delta V = V' - V$, $\frac{\Delta V}{V} = u_{ii}$. So it is clear that the second term in equation 4.4 refers to the volume change

of the object; this is described as the bulk energy as it refers to a volume change. The term u_{ll} may be referred to as the bulk strain.

4.2.2 Shear energy

The first term, that involving u_{ij} , includes off diagonal terms (those of the form u_{xy}, u_{yz} and so on). These refer to shear strain, for example that shown in figure 4.3. So it would appear that the first term corresponds to shear.

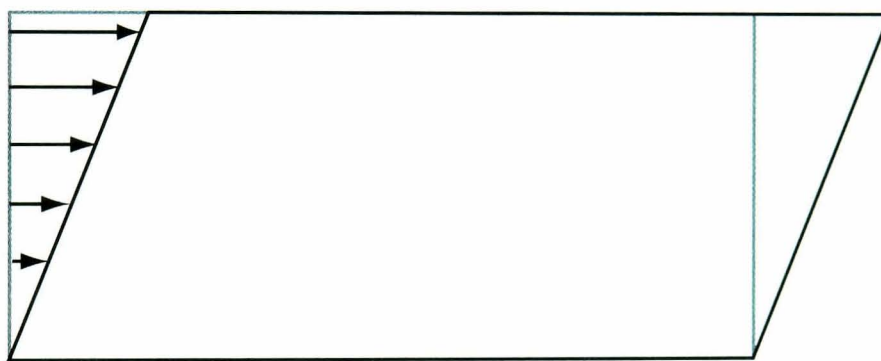


Figure 4.3: *Typical shear deformation*

However, this term also has a contribution from the diagonal elements of the strain tensor because it sums over the entire tensor. So it would appear that it is not possible to completely separate the two terms in the context of their physical representation. However a new object can be defined;

$$S_{ij} = u_{ij} - \frac{1}{3}\delta_{ij}u_{ll} \quad (4.9)$$

which is traceless (see equation 4.10, where S_{mm} is the trace of this tensor), and thus represents strains where the volume of the object does not change. This is described as *pure shear*[92].

$$\begin{aligned}
S_{mm} &= S_{mj} \cdot \delta_{jm} \\
&= \left(u_{mj} - \frac{1}{3} \delta_{mj} u_{ll} \right) \delta_{jm} \\
&= u_{mj} \delta_{jm} - \frac{1}{3} u_{ll} \delta_{mj} \delta_{jm} \\
&= u_{mm} - \frac{1}{3} u_{ll} \delta_{mm} \\
&= u_{mm} - \frac{1}{3} u_{ll} \cdot 3 \\
&= u_{mm} - u_{ll} \\
&= 0
\end{aligned} \tag{4.10}$$

We may rewrite the energy density (equation 4.4) in terms of the bulk and shear strains using the definitions discussed above[92];

$$\rho_E = \frac{1}{2} K u_{ll} u_{mm} + \mu S_{ij} S_{ij} \tag{4.11}$$

where K is the bulk modulus and μ is the shear modulus. These can be related to the Young's modulus and Poisson's ratio as follows;

$$K = \frac{1}{3} \left(\frac{Y}{1 - 2\sigma} \right) \tag{4.12}$$

$$\mu = \frac{1}{2} \left(\frac{Y}{1 + \sigma} \right) \tag{4.13}$$

This definition is due to Landau and Lifshitz [92].

4.3 Finite element analysis (FEA) and Algor

Once the definition of strain energy is known, the next task is to find the strains in the desired mass (or substrate) for each of its natural mode frequencies. This is extremely difficult to do analytically for all but the simplest of modes. Hence finite element analysis (FEA) was used. Finite element analysis essentially involves constructing a model divided into “elements” and “nodes”. A set of equations is then constructed which describes the behaviour of these elements; these equations are then solved simultaneously to derive the behaviour of the body as a whole. The solution of a natural mode problem involves the solution of an eigenvalue problem[93]. A FEA program called Algor was used to generate the displacement values for the nodes of each mode of the substrate. In this section we will discuss the construction of a typical model.

4.3.1 Model Construction and Assumptions

All the test masses in use in current detectors are essentially cylindrical with the exception of the flats used, for example, in GEO600 to attach the silica ears to which the suspension fibres will be welded. However the effect of these was thought to be small and so for ease of calculation were not considered in the model. Hence the model of the test mass was a basic right cylinder. In order to model the coating, three assumptions were made. Firstly it was assumed that the coating does not affect the shape of the surface of the mass on which it lies. The second assumption was that the coating follows that surface exactly. This is valid as long as the coating is not much stiffer than the substrate. These assumptions then allow us to simply model the substrate and then use the displacements of the front flat surface of the substrate as the displacements of the coating. The reason for making these assumptions is that it would be

impractical to model with finite element analysis a thin coating ($\approx 10\mu m$) on top of a thick mass ($\approx 10cm$) accurately in any reasonable length of time - the computational power required would be huge. Thus until computer power increases, compromises must be made between accuracy and practicability. The final assumption was that the coating material was isotropic in nature - this allowed an isotropic material type to be used in Algor. The question of materials which have properties which differ in different axes, which are said to be anisotropic, will be dealt with in chapter 6.

To begin the model, a line is drawn which is the length of the diameter of the mass. This line is then divided into a number of sections as shown in figure 4.4. Note that this figure is an isometric view with the axes as marked. This divided line is then rotated and copied around the z axis to give a meshed disc in the xy plane as shown in figure 4.5. This is a view looking onto the xy plane as marked with $z = 0$. This is then copied a number of times in the positive z direction to give the correct height as shown in figure 4.6, which is also an isometric view. The presence of the suspension loop is ignored so the mass is said to be unconstrained. Algor then proceeds to find the natural modes of the mass by finding the equations of motion of each of the nodes in the model and then solving the associated eigenvalue problem. It also calculates the maximum displacements of each of the nodes at the peak of one cycle.

The lack of constraints means that Algor must be told that there exist the 6 rigid body modes.

The output of the analysis can be seen in graphical form inside Algor itself, or the data can be extracted from a file created by Algor called `modelname.ml`.

Now that we have assembled the model and used Algor to obtain the natural modes, a method is required to calculate from the displacements the amount

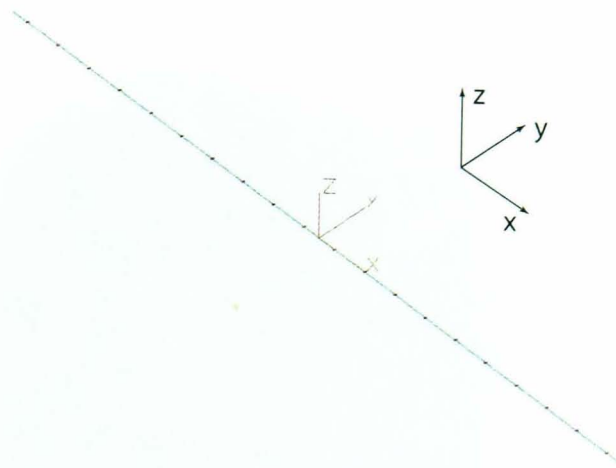


Figure 4.4: *Diameter of cylindrical mass divided into sections*

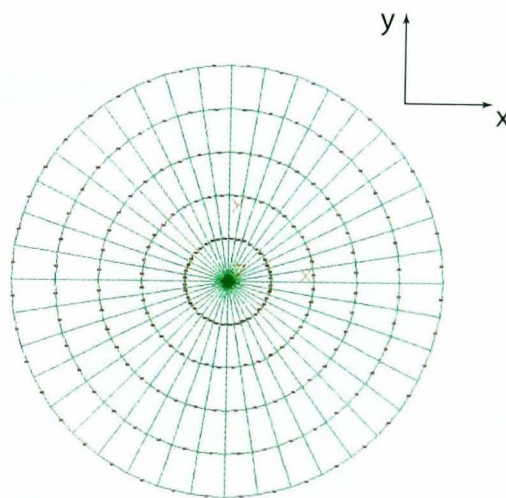


Figure 4.5: *One radially meshed disc*

of strain energy stored within the coating and substrate. For this, a program was written called Ocean. We must first, however, be sure that the output of Algor gives the information that we require. In the next section this will be briefly investigated.

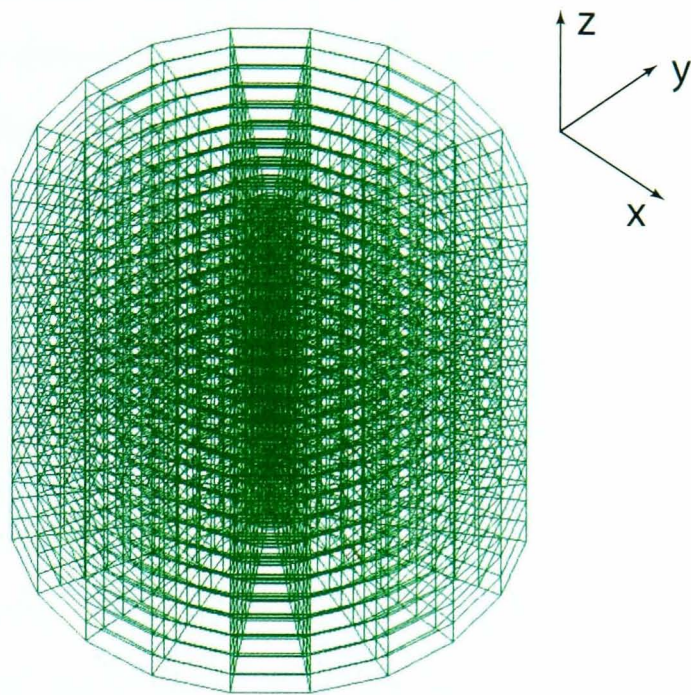


Figure 4.6: *Full cylinder*

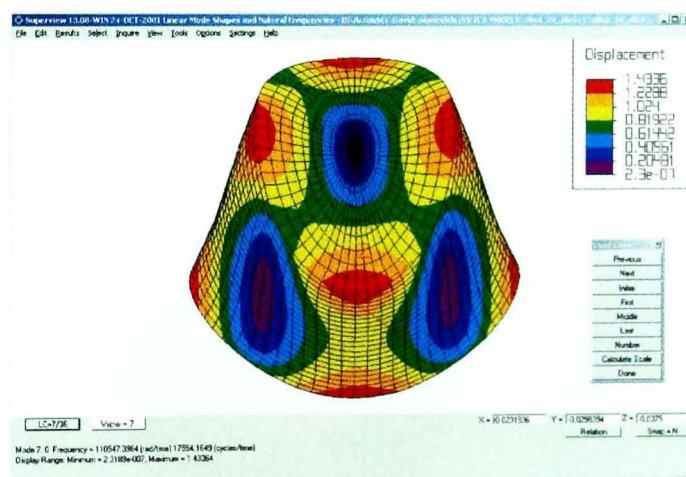


Figure 4.7: *Algor screenshot showing typical deformation of substrate in one of its natural modes*

4.3.2 Verification of Algor Displacements

We require to make sure that the output of Algor gives the information that we require, in particular that it gives the displacements of each node. To do this, we will look at a simple modeshape and show that Algor gives the displacements as required. The model of the initial mass used in chapter

5 was used for this test. Consider the fundamental longitudinal mode of a cylindrical mass as shown in figure 4.8 (and again in appendix B for reference), in particular the centreline of the mass (the line through the origin of each disc). At the peak of one oscillation cycle, the topmost point will have moved in the positive z direction and the lowest point will have moved in the negative z direction. The centre point will have remained motionless. The displacements of the remainder of the nodes down the centreline will follow a sinusoidal curve from one extreme to the other.

A graph of displacement in the z direction against its position on the z axis for the fundamental mode of the Algor model is shown in figure 4.9. We may observe that the displacements follow the pattern described above. However, while the height of the model is 10.2 cm, the displacements shown range from ~ -1 to ~ 1 . This indicates that Algor does not give the *absolute* displacements, but instead *relative* displacements. Since we require the ratios of energies for the same mode in each case, this presents no difficulty.

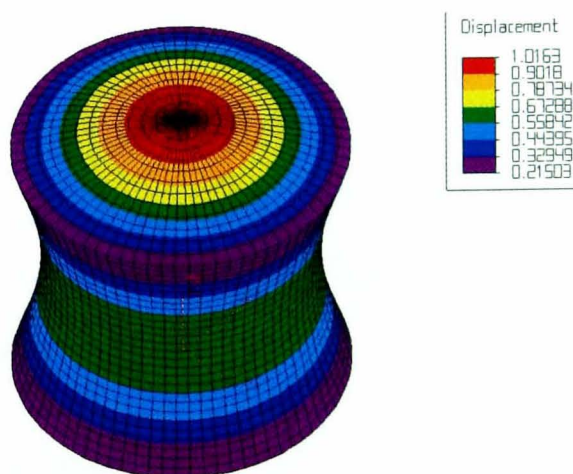


Figure 4.8: Screenshot from Algor showing the fundamental longitudinal mode used in the displacement graph in figure 4.8

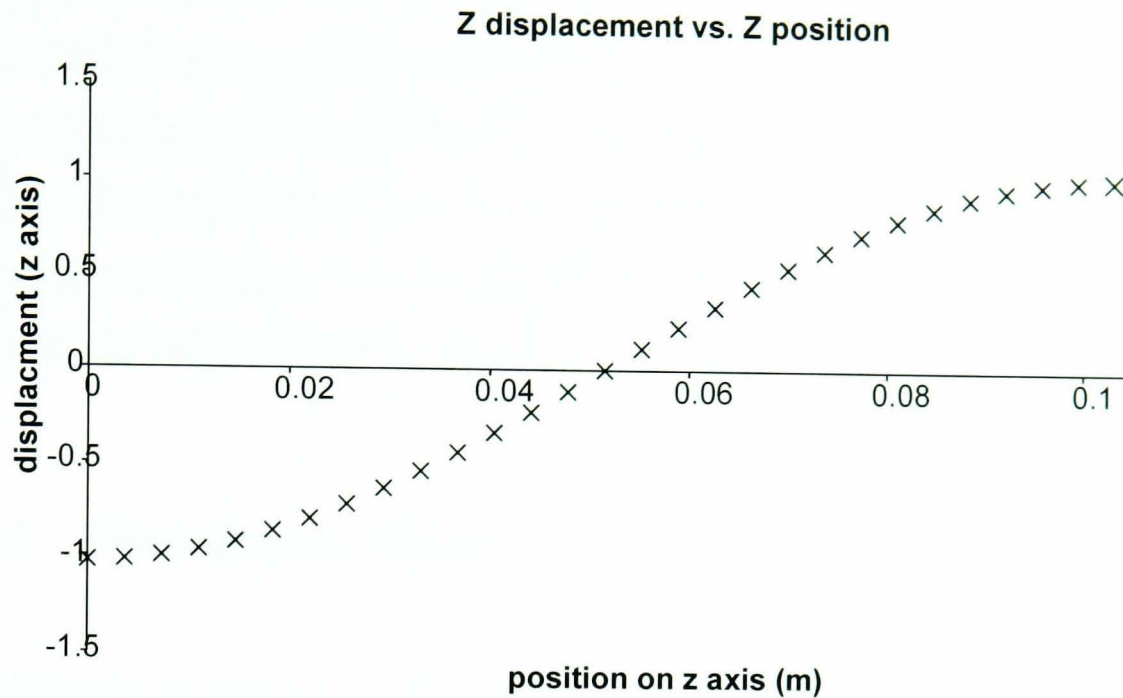


Figure 4.9: Graph of displacements in the z direction vs. the original positions of the nodes on the z axis for the fundamental longitudinal mode of a cylindrical mass

4.4 Ocean

To continue, the strains associated with each node must be calculated. This is the task of *Ocean*¹, a program developed using the *C* language specifically for this purpose. The purpose of this section is to deal with the requirements of *Ocean* and their implementation.

As part of the output of *Algor*, there exists a text file which contains all the node positions and displacements from each of the natural modes. We need to use these in concert with equations 4.3 and 4.4. The tasks required of *Ocean* are to extract this information, read in the particular material properties and calculation options and then calculate and output the relevant strains, strain energies and strain energy ratios.

¹The name of which is a partial acronym of Coating Energy Analysis

In the following section the operation of Ocean will be discussed. Consequently, the numerical scheme used to calculate the strains from the displacement values taken from Algor will be described in section 4.4.1. Thereafter, we will examine a typical Ocean session in section 4.4.2. In the subsequent sections we will look at the various stages of the running of the program. Initially, however, we will examine the method used by Ocean to calculate the strains.

4.4.1 Numerical scheme

The difficulty in calculating the strains lies largely in the arrangement of nodes within the model. We have cartesian forms for calculating the strains, yet the model is essentially in cylindrical polar format, for ease of construction. There are therefore two options open to us: firstly to recast the strain formulae in polar form, or secondly to establish a method of using the cartesian displacements within a polar framework. The second option was chosen as this allows the most natural coordinate system to be used for each task - node identification and strain calculation.

To proceed, each node is firstly assigned a set of co-ordinates in cylindrical polar space, as demonstrated in figure 4.10 in which a single disc is partially indexed. A third co-ordinate was used for the z direction, in which the lowest disc was set as $z = 0$ (hence the origin of the lowest disc would have co-ordinates $(0, 0, 0)$).

Calculation of strain

We are now in a position to calculate the strains for individual nodes. The general case will be described first, followed by individual special cases. The

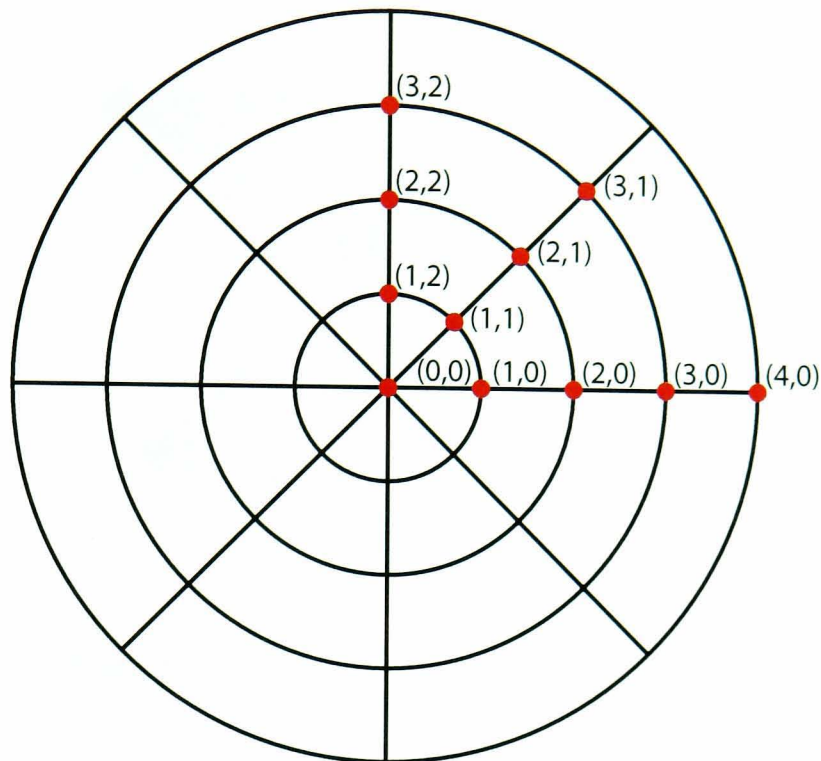


Figure 4.10: *Local cartesian coordinates*

early discussion will use only the xy plane for clarity; the calculation will be extended to the z direction at the end.

The first step is to take one node and define a local *neighbourhood* of 4 nodes around that point; an example of this is shown in figure 4.11. This is because we will take the average of the strains over three nodes in each axis; this provides a more accurate value than would be achieved with two nodes. To understand this scheme, consider figure 4.11. For clarity, only the u_x components are shown.

Consider the following, where u_x is the x component of displacement in the reference co-ordinates of an entire disc, d_x is the x component of the vector \mathbf{d} and so on:

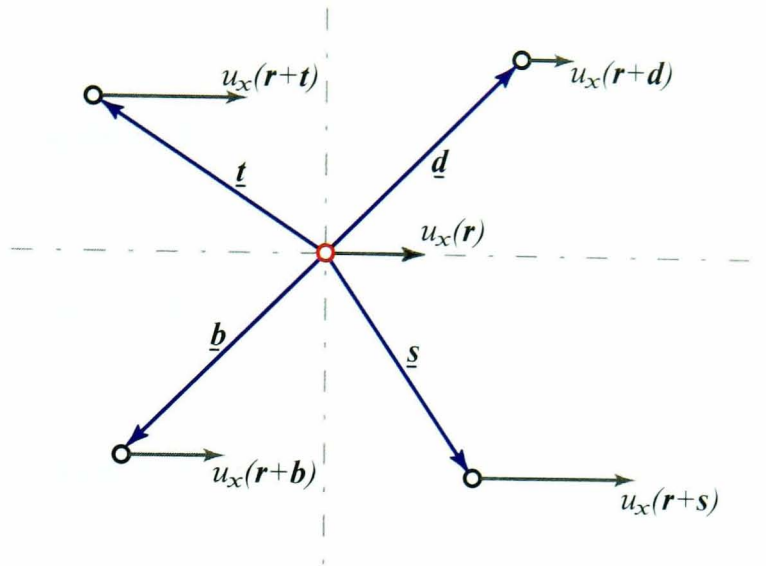


Figure 4.11: *Typical node neighbourhood. \mathbf{r} refers to the centre point*

$$u_x(\mathbf{r} + \mathbf{d}) - u_x(\mathbf{r}) = \frac{\partial u_x}{\partial x} d_x + \frac{\partial u_x}{\partial y} d_y \quad (4.14)$$

$$u_x(\mathbf{r} + \mathbf{b}) - u_x(\mathbf{r}) = \frac{\partial u_x}{\partial x} b_x + \frac{\partial u_x}{\partial y} b_y \quad (4.15)$$

Now, recall from equation 4.3 that $\frac{\partial u_x}{\partial x}$ and $\frac{\partial u_x}{\partial y}$ are exactly the terms we need for the strain tensor. To obtain *average* strain values we can define new quantities which are given in table 4.1.

Quantity	Definition
$\partial_x u_x^+$	$\frac{\partial u_x}{\partial x}$ in positive x
$\partial_x u_x^-$	$\frac{\partial u_x}{\partial x}$ in negative x
$\partial_y u_x^+$	$\frac{\partial u_x}{\partial y}$ in positive x
$\partial_y u_x^-$	$\frac{\partial u_x}{\partial y}$ in negative x

Table 4.1: *Partial strain values used to calculate strain components in local cartesian frame*

We may now recast and expand 4.14-4.15 as:

$$u_x(\mathbf{r} + \mathbf{d}) - u_x(\mathbf{r}) = \partial_x u_x^+ d_x + \partial_y u_x^+ d_y \quad (4.16)$$

$$u_x(\mathbf{r} + \mathbf{b}) - u_x(\mathbf{r}) = \partial_x u_x^- b_x + \partial_y u_x^- b_y \quad (4.17)$$

$$u_x(\mathbf{r} + \mathbf{t}) - u_x(\mathbf{r}) = \partial_x u_x^- t_x + \partial_y u_x^+ t_y \quad (4.18)$$

$$u_x(\mathbf{r} + \mathbf{s}) - u_x(\mathbf{r}) = \partial_x u_x^+ s_x + \partial_y u_x^- s_y \quad (4.19)$$

Hence we have 4 equations and 4 unknowns. It is also clear that

$$\frac{\partial u_x}{\partial x} = \frac{\partial_x u_x^+ + \partial_x u_x^-}{2} \quad (4.20)$$

$$\frac{\partial u_x}{\partial y} = \frac{\partial_y u_x^+ + \partial_y u_x^-}{2} \quad (4.21)$$

Hence we can now calculate both strain components using u_x in the xy plane. The case for u_y is identical.

For practical reasons related to the computation of the strain, it is useful to consider a local cartesian frame defined around each node, for example that shown in figure 4.12.

Here we have two sets of strain values (again consider just the u_x case). $\frac{\partial u_x}{\partial x'}$ and $\frac{\partial u_x}{\partial y'}$ for the local frame and $\frac{\partial u_x}{\partial x}$ and $\frac{\partial u_x}{\partial y}$ for the reference frame. These are related;

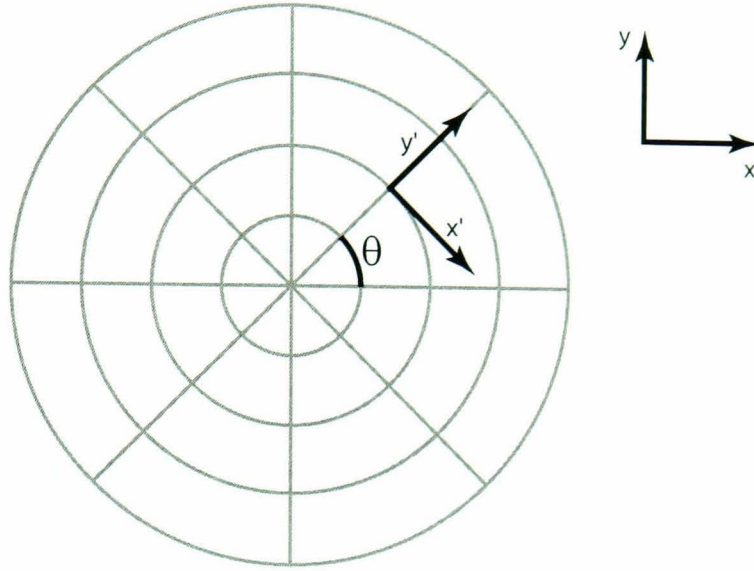


Figure 4.12: *Local cartesian coordinates*

$$\frac{\partial u_x}{\partial x} = \frac{\partial u_x}{\partial x'} \frac{\partial x'}{\partial x} + \frac{\partial u_x}{\partial y'} \frac{\partial y'}{\partial x} \quad (4.22)$$

$$\frac{\partial u_x}{\partial y} = \frac{\partial u_x}{\partial x'} \frac{\partial x'}{\partial y} + \frac{\partial u_x}{\partial y'} \frac{\partial y'}{\partial y} \quad (4.23)$$

Since $\frac{\partial x'}{\partial x} = \cos \theta$, $\frac{\partial y'}{\partial x} = -\sin \theta$, $\frac{\partial x'}{\partial y} = \sin \theta$ and $\frac{\partial y'}{\partial y} = \cos \theta$, we have :

$$\begin{pmatrix} \frac{\partial u_x}{\partial x} \\ \frac{\partial u_x}{\partial y} \end{pmatrix} = \begin{pmatrix} \cos \theta & -\sin \theta \\ \sin \theta & \cos \theta \end{pmatrix} \begin{pmatrix} \frac{\partial u_x}{\partial x'} \\ \frac{\partial u_x}{\partial y'} \end{pmatrix} \quad (4.24)$$

Although this is the most general case, there are some simplifications which can be made to ease calculation. If the $x'y'$ frame is defined such that the y' axis lies along a radius of the disc, then we may simplify our previous strain calculations; think of the neighbourhood of nodes in terms of the $x'y'$ plane, with reference to figure 4.13 and also figure 4.10.

Then $d_x = t_x = 0$ and we now have three instances of $\partial_y u_x^-$. Hence equations 4.16-4.19 become

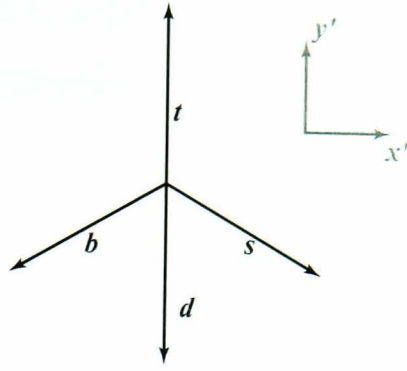


Figure 4.13: *Local neighbourhood of points for one node in a meshed disc*

$$u_x(\mathbf{r} + \mathbf{d}) - u_x(\mathbf{r}) = \partial_y u_x^- d_y \quad (4.25)$$

$$u_x(\mathbf{r} + \mathbf{b}) - u_x(\mathbf{r}) = \partial_x u_x^- b_x + \partial_y u_x^- b_y \quad (4.26)$$

$$u_x(\mathbf{r} + \mathbf{t}) - u_x(\mathbf{r}) = \partial_y u_x^+ t_y \quad (4.27)$$

$$u_x(\mathbf{r} + \mathbf{s}) - u_x(\mathbf{r}) = \partial_x u_x^+ s_x + \partial_y u_x^- s_y \quad (4.28)$$

These equations are equivalent to the original set (4.16-4.19) in terms of accuracy but they make for a simpler calculation which therefore makes the coding simpler.

Thus our general scheme will be to calculate the local strain components then rotate them to the reference frame. It is interesting at this point to note that this single rotation does not, apparently, comply with the standard form for rotation of tensors between co-ordinate systems. In the case of a second order tensor, two rotation tensors would be required;

$$u'_{ij} = \Lambda_{ik} \Lambda_{jl} u_{kl} \quad (4.29)$$

where each tensor Λ_{ik} is a rotation. The reason for this is that this would apply

had the *displacements* been in polar co-ordinates as well as the node positions. However because the displacements were left in cartesian co-ordinates, only one rotation is required.

z direction

The z direction calculations are straightforward in comparison. All that we require is, for example,

$$\frac{\partial u_x}{\partial z} = \frac{\partial_z u_x^+ + \partial_z u_x^-}{2} \quad (4.30)$$

with nodes on three consecutive layers of the cylinder.

Special Cases

We now have a full treatment of the general case of the strain calculation. There are, however, a number of special cases. At the edge of one disc, the neighbourhood is reduced to 3 nodes, one in the radial direction and 2 in the ϕ direction. Thus the ∂'_y strain value will not be an average but take only one value. Similarly, at the top or bottom of the cylinder there will only be one value used for the ∂_z component of strain. This will be discussed further in section 4.5.1.

4.4.2 Typical Ocean Usage (ocean.ini)

Having discussed the calculation of strain in some detail, it now remains to discuss the workings of the program itself. This will be done by considering a

typical usage of the program and describing the steps that take place as the program runs.

An Ocean session begins by configuring the `ocean.ini` file, a sample of which is shown below:

```
model_name: silicacoin_1.ml
mode_number: 7
coating_thickness: 4.4e-6
barrel_thickness: 4.4e-6
substrate_E: 7.2e10
substrate_sigma: 0.17
coating_E: 2.6e11
coating_sigma: 0.26
barrel_E: 2.6e11
barrel_sigma: 0.260
barrel_extent: -1
surface_locn: 0.0
append: 1
mode_print: 0
point_data: 0
```

The function of the majority of these descriptions are straightforward; the first two point Ocean to the correct file (which for the moment should reside in the same directory as the Ocean executable) and indicate the mode of interest; in every case the first possible mode is mode 7 because of the six rigid body modes². The next two lines allow for different front coating and barrel coating thicknesses (both in metres). The following 6 lines describe the material properties of the substrate (`substrate_`), front and barrel coatings - `_E` refers to the Young's modulus in standard units and `_sigma` the Poisson's ratio.

The last 4 lines refer to the location of the barrel and front coating. **barrel_extent:**

²Using Algor. This is not generally the case when other finite element analysis packages are used; see chapter 6.

-1 indicates that the barrel coating covers the entire barrel³ and `surface_locn`: 0.0 indicates that the front surface should be used to calculate the coating energy. These allow for a partial barrel coating and for the energy to be calculated further down the mass. This does not have relevance to the coating problem but is instead present to extend the scope of the program; this will be discussed later. `append` takes two values, 0 and 1. 0 indicates that the energy values calculated will not be appended to the current results file, 1 indicates that they will. If `mode_print` is set to 1, the mode number will be printed before the energy values, otherwise it will not. The purpose of these two settings is to allow a number of different models to be included under one mode heading; this will be discussed later in section 4.5.2. Finally the `point_data` setting allows individual displacements and strain components to be extracted for particular points for testing purposes.

Once `ocean.ini` is setup correctly, Ocean is then called from the command line. It will then run, picking up the settings given above. The results appear in a file called `energy_ratios.csv`, an example of which is shown below. The CSV format is used to allow easy importing into a spreadsheet, for example Microsoft Excel.

```
Mode Number = 14
```

```
Number of nodes,Substrate Energy,Surface Energy,Surface Ratio,...
6545,7.326055e-03,1.198903e-06,1.636492e-04,...

...,Barrel Energy, Barrel Ratio
...,1.423757e-05,1.943415e-03
```

We will now look at the stages carried out by Ocean, having read in the settings file. A copy of the source code for Ocean is in appendix E which has been commented into these sections.

³The negative here has no physical significance and is simply a coding convenience.

4.4.3 Ocean Stages - Data Import

The first task of Ocean is to read in the values from the .ml file. The important step here was to convert the node position values to polar co-ordinates. The dimensions of the mass are then calculated by Ocean (one of the long term goals of the Ocean development is to remove as much non-essential user intervention as possible) and the radial, angular and z step sizes are calculated. Using these values the nodes are sorted into the co-ordinate scheme discussed earlier; although the node scheme used by Algor is known, this sorting made fast calculation possible as it allows loops to be used. In addition it means that any future FEA package can be used as long as it employs the same mass construction model. The relevance of this design choice will be seen in chapter 6.

The cartesian displacement values are then read in and assigned to each node. The strain calculation then proceeds using the principles discussed in section 4.4.1.

4.4.4 Model used for different parameters

Ocean then uses these strain values to calculate the energy density associated with each node (which is assigned a volume as a fraction of the whole) using equation 4.4. For the substrate, the volume assigned to each node is a fraction of the surface area of the front surface multiplied by the increment in the z direction of the mesh. The energy is thus integrated over the whole mass. For the surface coating there are two changes; firstly the volume for each node is given by a fraction of the surface area as before but this time multiplied by the thickness of the coating. Secondly, the actual physical properties of the coating are used here for the first time. For the barrel the volume is found in

a similar way. The formulae for the different parameters that Ocean currently calculates are given below.

1. *Substrate, surface and barrel energy* $\rho_E = \frac{Y}{2(1 + \sigma)} \left(u_{ij}^2 + \left(\frac{\sigma}{1 - 2\sigma} \right) u_{ll}u_{mm} \right)$
2. *Surface Shear Energy* $\rho_E = \mu S_{ij}S_{ij}$
3. *Surface Bulk Energy* $\rho_E = \frac{1}{2}K u_{ll}u_{mm}$
4. *Kinetic Energy* $\rho_E = (2\pi f)^2 \rho V (\Delta x^2 + \Delta y^2 + \Delta z^2)$

Each of these is integrated over the appropriate volume.

4.5 Verification

An important stage in the use of this (and, indeed, any) program is to test the validity of its output. In the case of Ocean, this was done using a test file where the strains and consequent energies are well known. The form of displacement chosen for this test was a cylindrical bar of length L , starting at the origin and bent in a parabola (i.e. as shown in figure 4.14). This is an unphysical displacement but was chosen for simple and transparent analysis. Without volume conservation, the equation of the centre line would be $F(z) = \frac{1}{2}cz^2$ with c the curvature. However to include volume conservation an additional term is required.

Consider the length of a curve. In general this will be (in the co-ordinate system used here);

$$l(z) = \int_0^z \sqrt{dz^2 + dx^2} \quad (4.31)$$

Now $x = F(z)$ and so $dx = F' dz = cz dz$. Substituting this into equation

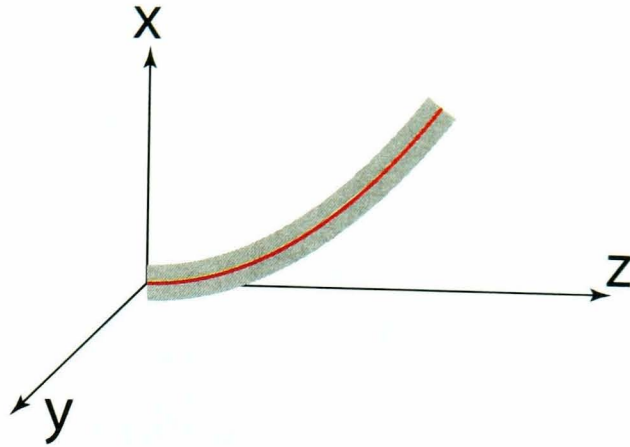


Figure 4.14: *Bar bent into half parabola*

4.31 gives,

$$\begin{aligned}
 l(z) &= \int_0^z \sqrt{1 + c^2 z^2} dz \\
 &= \frac{1}{c} \int_0^{cz} \sqrt{1 + \eta^2} d\eta
 \end{aligned} \tag{4.32}$$

where $\eta = cz$. Using the approximation $\sqrt{1 + x^2} \approx (1 + \frac{x^2}{2})$ we obtain:

$$\begin{aligned}
 l(z) &\approx \frac{1}{c} \int_0^{cz} (1 + \frac{\eta^2}{2}) d\eta \\
 &= z + \frac{c^2 z^3}{6}
 \end{aligned} \tag{4.33}$$

Now $l(z)$ is the length of an element of original length z after the bar has been bent into a parabola. Consider a point \mathbf{r} on the centreline of the undeformed bar at co-ordinates $(0, z)$. We now bend the bar into a parabola and examine the co-ordinates of this point \mathbf{r}' , assuming it retained its position on the centreline (see figure 4.15).

The z co-ordinate of this point will have changed by an amount

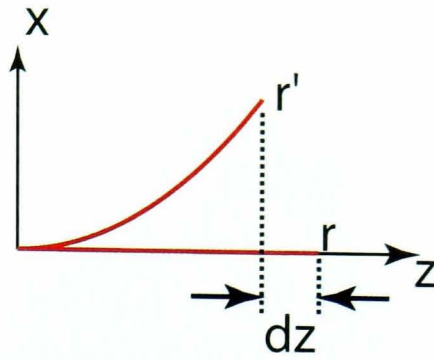


Figure 4.15: *Displacement of point on the centreline of the bar after bar is bent into a parabola*

$$l(z) - z = \frac{c^2 z^3}{6} \quad (4.34)$$

in the negative z direction.

Now the cylindrical bar has non zero radius. Recall that we will convert this model into a form suitable for use with Ocean which will therefore use a stack of radially distributed nodes. Hence the displacement of each point on the cross section is needed as well. This can be calculated with full generality using the point at the highest x value for any particular cross section. The displacement of this cross section can be represented as a combination of a translation in the x direction and a rotation in the xz plane.

The translation is simply $\frac{1}{2}cz^2$ and only contributes to the x displacement. To calculate the displacement contributions of the rotation, consider figure 4.16. The angle θ will be the gradient of the bar at that point, or $\frac{dF}{dz}$ where $F = \frac{1}{2}cz^2$ here.

The value of dz will hence be $-x \sin \theta$. Similarly, $dx = x - x \cos \theta = x(1 - \cos \theta)$.

Combining the displacement of the centre line, the displacement due to volume conservation and the displacements due to the rotation of each cross section

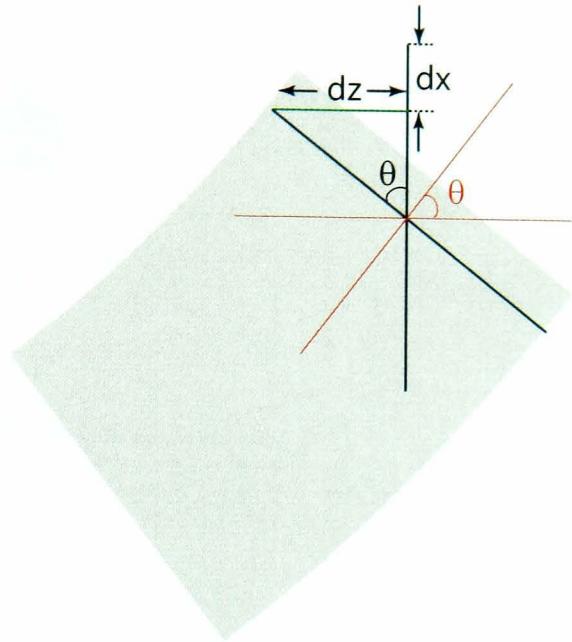


Figure 4.16: *Rotation of cross section*

we obtain the following displacement vector:

$$\mathbf{u} = \left(\frac{1}{2}cz^2 + x(1 - \cos \theta), 0, -\frac{c^2z^3}{6} - x \sin \theta \right) \quad (4.35)$$

Now $\theta = \frac{dF}{dz} = cz$ in this case. Hence equation 4.35 becomes;

$$\mathbf{u} = \left(\frac{1}{2}cz^2 + x(1 - \cos(cz)), 0, -\frac{c^2z^3}{6} - x \sin(cz) \right) \quad (4.36)$$

We are now in a position to calculate the strain tensor. Using equation 4.3 we obtain the following:

$$\begin{aligned}
u_{ij} &= \frac{1}{2} \left(\frac{du_i}{dx_j} + \frac{du_j}{dx_i} \right) \\
&= \begin{pmatrix} 1 - \cos(cz) & 0 & \frac{1}{2} [cz + cx \sin(cz) - \sin(cz)] \\ 0 & 0 & 0 \\ \frac{1}{2} [cz + cx \sin(cz) - \sin(cz)] & 0 & -\frac{c^2 z^2}{2} - cx \cos(cz) \end{pmatrix}
\end{aligned} \tag{4.37}$$

Using the small angle approximations $\sin(x) \approx x$ and $\cos(x) \approx 1 - \frac{x^2}{2}$ this becomes;

$$\begin{aligned}
u_{ij} &= \begin{pmatrix} \frac{c^2 z^2}{2} & 0 & \frac{1}{2} [cz + c^2 xz - cz] \\ 0 & 0 & 0 \\ \frac{1}{2} [cz + c^2 xz - cz] & 0 & -\frac{c^2 z^2}{2} - cx \left(1 - \frac{c^2 z^2}{2} \right) \end{pmatrix} \\
&= \begin{pmatrix} \frac{c^2 z^2}{2} & 0 & \frac{1}{2} c^2 xz \\ 0 & 0 & 0 \\ \frac{1}{2} c^2 xz & 0 & -\frac{c^2 z^2}{2} - cx \left(1 - \frac{c^2 z^2}{2} \right) \end{pmatrix}
\end{aligned} \tag{4.38}$$

In addition, we can calculate the energy using equation 4.4:

$$E_{substrate} = \int_V \frac{Y}{2(1+\sigma)} \left(u_{ij}^2 + \frac{\sigma}{1-2\sigma} u_{ll} u_{mm} \right) \tag{4.39}$$

If we set $\sigma = 0$, u_{ij}^2 becomes,

$$u_{ij}^2 = \frac{c^4 z^4}{4} + \frac{1}{2} c^4 x^2 z^2 + \left[-\frac{c^2 z^2}{2} - cx \left(1 - \frac{c^2 z^2}{2} \right) \right]^2 \quad (4.40)$$

$$= \frac{c^4 z^4}{2} - \frac{c^4 x^2 z^2}{2} + \frac{c^6 x^2 z^4}{4} - \frac{c^5 x z^4}{2} + c^3 x z^2 + c^2 x^2 \quad (4.41)$$

We set $\sigma = 0$ for ease of calculation; it removes the second term from the energy density equation 4.4. We are not in a physical situation with the bar bent into a parabola: the deformation imposed is consistent with a material having sigma equal to zero so there are no adverse consequences to making this assumption. In particular we must use all the strain tensor components in the remaining term of the strain energy density calculation and so we are still testing the strain calculation of Ocean completely. A further test, not detailed here, found agreement between the analytical energy and the Ocean derived energy for a pure longitudinal deformation for a bar where Poisson's ratio was *not* set to zero. After conversion to polar co-ordinates and integrating the z terms from 0 to L , the length of the bar, the total energy $E_{substrate}$ is finally calculated as:

$$E = \frac{Y c^2 \pi R^2 L}{4} \left[\frac{c^2 L^4}{5} - \frac{c^2 R^2 L^2}{12} + \frac{c^4 R^2 L^4}{40} + \frac{R^2}{2} \right] \quad (4.42)$$

If we only integrate z over the range $L - \delta$ to L , where δ is a nominal coating thickness, we obtain the following:

$$E_{coating} = \frac{Y c^2 \pi R^2 [L - (L - \delta)]}{4} \times \left[\frac{c^2 [L^4 - (L - \delta)^4]}{5} - \frac{c^2 R^2 [L^2 - (L - \delta)^2]}{12} + \frac{c^4 R^2 [L^4 - (L - \delta)^4]}{40} + \frac{R^2}{2} \right] \quad (4.43)$$

We now have a complete scheme to test Ocean; we have an analytical model for which the displacements, strains and strain energy are known accurately.

4.5.1 Results

Figure 4.17 shows a graph of the calculated bar energies using various mesh sizes with Ocean. The test values used are shown in table 4.2. Recall that there is an approximation whereby nodes at the top and bottom of the cylinder use only two points to calculate the z components of strain; there is a similar approximation around the rim of each disc. Hence the test value may be slightly inaccurate unless a sufficiently large number of nodes is used thus decreasing the contribution of the top and bottom layers and the rim of each disc. Figure 4.17 shows the test values as a function of the number of nodes. In these test values the product of the number of radial nodes and the number of angle increments ranges from 8 to 400. From this it can be seen that a few thousand nodes are required to obtain accurate results.

Constant	Value
curvature	1.00×10^{-4}
L	$1.00 \times 10^{-1}\text{m}$
Y	$7.20 \times 10^{10} \text{ kg/ms}^2$
R	$1.00 \times 10^{-1}\text{m}$
δ	$1.00 \times 10^{-6}\text{m}$

Table 4.2: *Test constants*

This shows that there is a convergence to a steady value of the calculated energy. This graph would indicate that Ocean does quickly converge to a steady value. However it would suggest that any actual FEA models used should have a few thousand nodes at least to be confident of the Ocean derived ratio. Table 4.3 shows the comparison of the analytical energies and ratios, that were obtained by Ocean with a mesh of 6416 nodes (the highest number

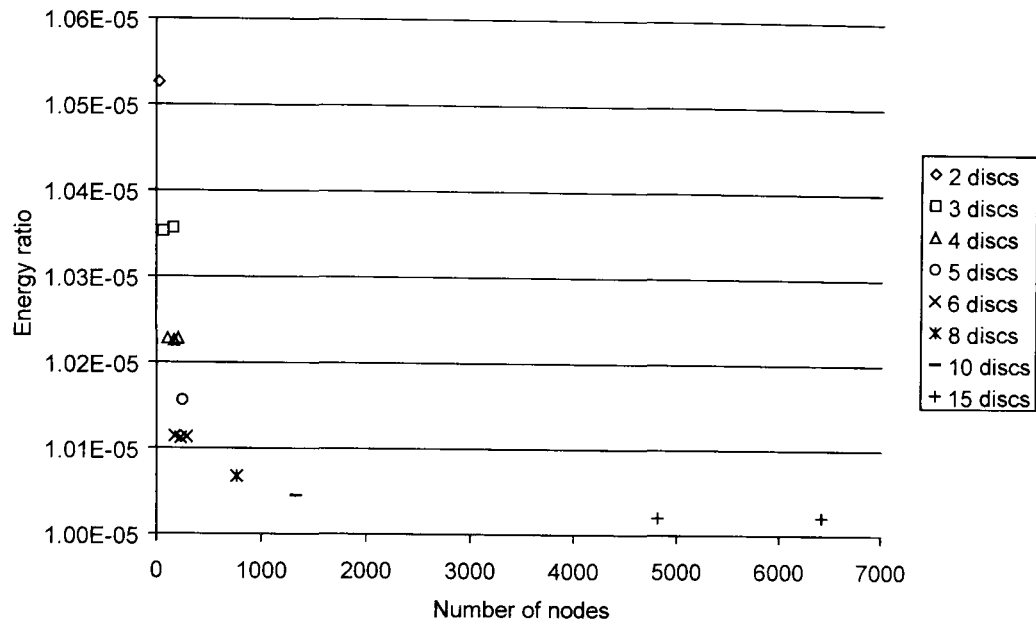


Figure 4.17: *Convergence of energy values calculated by Ocean*

shown on the graph) and that obtained by Ocean using a mesh of 29791 nodes.

	Analytical	Ocean(6416)	Ocean(29791)
Substrate energy	2.8274×10^{-3}	2.8314×10^{-3}	2.829056×10^{-3}
Surface energy	2.8274×10^{-8}	2.8373×10^{-8}	2.830572×10^{-8}
Ratio	1.0000×10^{-5}	1.0021×10^{-5}	1.000536×10^{-5}

Table 4.3: *Comparison between analytical and Ocean test energies*

This indicates that Ocean is accurate to within 1% for the test model chosen.

4.5.2 Convergence

We have discussed now the component parts of Ocean, its running and methodology. There remains one further feature of its use, which is the subject of convergence. It is not *a priori* clear how accurate a finite element mesh is in terms of the energies that it yields (indeed, an example of this was seen in the last section). Experimental tests (see chapter 5, table 5.1) show that the frequency agreement of the FEA models with experiment is good, but it would be prudent to use a number of models to ensure that an accurate reading of

the energy was employed. To this end, a number of models were used for any one sample with increasing mesh densities. The number of nodes in the radial, angular and z directions were increased in proportion to keep the ratio of the individual mesh cell dimensions approximately the same. The consequent energy ratios were plotted in Excel and the Solver package was used to fit an exponential curve to the data. The asymptotic value of the curve was then used as the final ratio value since this would approximate to an infinite number of points. Although this would not give a completely accurate answer - numerical accuracy issues would prevent this - it would nonetheless allow a common procedure to be used for each case. An example of such a convergence can be seen in figure 4.18, with data from chapter 5. The data were found to be well fitted using an exponential.

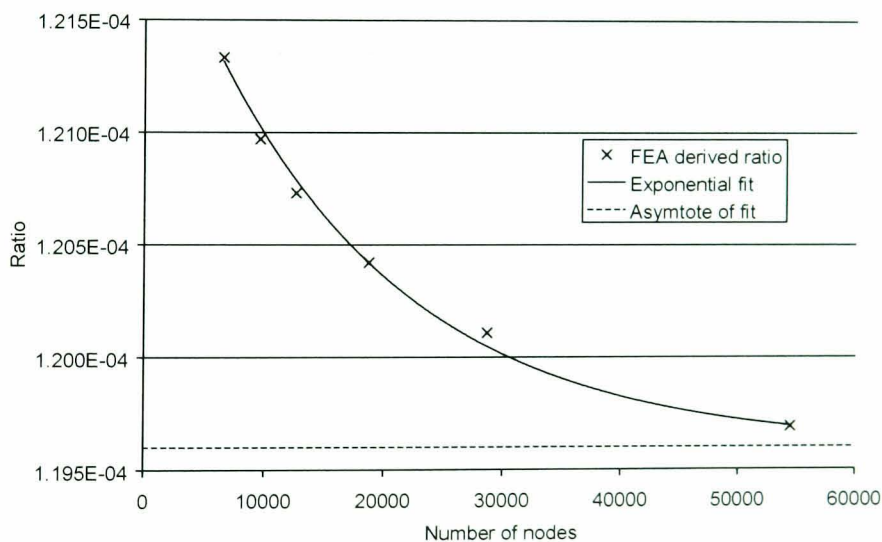


Figure 4.18: *Example convergence*

4.6 Conclusion

In this chapter we have introduced the topic of strain and the subsequent calculation of strain energy. The use of finite element analysis to obtain the nodal

displacements of a variety of natural modes of a mass has been discussed, along with the use of these displacements to numerically calculate the strain energy stored in this mass. To do this, a program called Ocean was written which has been discussed both in terms of its usage and in terms of its conceptual working. Finally, the output of this program has been verified using analytically derived strain energies and limits have been placed on the mesh densities which should be used with Ocean to ensure accuracy.

Chapter 5

Analysis of Coated Silica Test Masses

5.1 Introduction

The previous chapters have dealt with the theory and methodology necessary to assess the presence and determine the level of losses due to dielectric coatings on test masses. In this chapter these concepts will be used in practice.

The study will comprise two parts. The first will describe the initial efforts made to determine the existence of an excess loss due to a coating and to obtain an initial level for that loss. This work has also been published separately[94]. The second part will extend that work to investigate different types of coating to determine the primary source or sources of loss and thus potential ways to reduce that loss. This investigation covers both the composition of the coatings and the materials used. The extended investigation forms part of an updated coating loss paper, currently in preparation.

5.2 Initial Study - 10m Prototype Masses

5.2.1 Nature of samples

The initial investigation employed two fused silica masses originally used in the 10m prototype detector at the University of Glasgow. Each was a right circular cylinder with a diameter of 0.127 m and a height of 0.103 m. The first sample was manufactured from Corning[95] 7980 fused silica (grade 0C) and the second from Corning 7940 fused silica (3G). The faces of both masses were super-polished to sub-angstrom roughness levels and the barrels were inspection polished. The polishing in all cases was carried out by Wave Precision ¹ [96] who also applied dielectric coatings to each sample. One face of each mass was given a coating designed to be highly reflective at 1064 nm, although the reflectivities of each coating were slightly different. The rear face of each mass was given a coating designed to be anti-reflective at the same wavelength.

X-ray fluorescence[97] was carried out on the coatings to determine their material constituents. The outcome of this indicated that the highly reflective coatings on the 7980 and 7940 masses consisted of aluminium oxide (alumina) and tantalum pentoxide (tantala). Subsequent calculations using equations 3.4 and 3.5 suggested that the highly reflective coating on the 7980 mass consisted of approximately 43 alternating quarter wavelength layers, giving a physical thickness of 6.3 μm . It is similarly believed that the highly reflective coating on the 7940 mass used 59 layers giving a geometrical thickness of 8.6 μm .

An initial assumption was made that the loss in the coating was proportional to the total thickness and that the loss was basically homogeneous throughout the coating. It was assumed that the anti-reflection coating, which had sig-

¹previously General Optics

nificantly fewer layers (≈ 2 layers) would not add a significant amount to the total loss and was thus not considered.

The losses of seven modes were obtained using the method described in appendix A. The modeshapes for these modes are shown in appendix B

5.2.2 Results

The lowest loss factors measured for each of the seven modes of the coated 7940 and 7980 masses can be seen in table 5.1.

Mode	Modelled frequency (Hz)	Corning 7980		Corning 7940	
		Measured frequency (Hz)	Measured loss ($\times 10^{-7}$)	Measured frequency (Hz)	Measured loss ($\times 10^{-7}$)
1. Bending (8, $n = 1$)	22401	22105	1.37 ± 0.04	22361	1.6 ± 0.01
2. Asymmetric drum (1, $n = 0$)	23238	22977	1.16 ± 0.02	23004	1.23 ± 0.05
3. Fundamental (1, $n = 2$)	24671	25378	0.65 ± 0.01	25404	0.5 ± 0.02
4. Clover-4 (16, $n = 2$)	25490	26176	1.61 ± 0.03	26193	1.89 ± 0.04
5. Symmetric drum (4, $n = 0$)	27723	28388	3.1 ± 0.12	28395	3.6 ± 0.29
6. Expansion	31397	31710	1.09 ± 0.01	31731	1.01 ± 0.01
7. 2nd Asymmetric drum (3, $n = 0$)	35133	36045	0.86 ± 0.01	36072	0.94 ± 0.03

Table 5.1: *Experimental losses with mode classification (due to McMahon[4]) and modelled and measured frequencies*

The first observation that may be made is that there is a great deal of variation in the losses between the different modes; differences of up to a factor of 4 can be seen. It is postulated that these variations are due to the coating. Previous studies of an uncoated sample manufactured from 7980 fused silica yielded loss factors of between 0.87×10^{-7} and 1×10^{-7} . The spread of these losses is less than 14%. From this we believe that the suspension losses do not contribute significantly to the measured loss values and hence that the variation in the losses seen in the modes of the coated sample arises from the dielectric coatings themselves. Additionally, however, it may be noted that these existing *uncoated* losses are higher in some cases than the coated losses

tabulated above. Hence the uncoated losses cannot be used in this analysis as it would appear that the previous sample had a higher intrinsic loss than the samples in use here. It is now sensible to proceed with the analysis to determine the *level* of the excess loss due to the coatings. Before this, however, it should be noted that in each sample a small amount of the coating had spilled over onto the barrel of the masses during the coating process. The importance of this effect will become clear presently.

5.2.3 Analysis

Recall the form of parameterisation of loss assuming only intrinsic loss and coating loss to be significant but including coating on both the face and barrel:

$$\phi(\omega_0)_{coated} \approx \phi(\omega_0)_{substrate} + \frac{E_{coating\ on\ face}}{E_{substrate}} \phi(\omega_0)_{coating\ on\ face} + \frac{E_{coating\ on\ barrel}}{E_{substrate}} \phi(\omega_0)_{eff} \quad (5.1)$$

where as before $\frac{E_{coating\ on\ face}}{E_{substrate}}$ is the fraction of the energy of the mode stored in the coating and $\frac{E_{coating\ on\ barrel}}{E_{substrate}}$ is that stored in the barrel.

$\phi(\omega_0)_{eff}$ represents the overall effect of the barrel on the loss of the sample. The spillage of coating down the barrel was not part of the coating specification and therefore the exact thickness is unknown. Also, it is possible that it is not of even thickness down the barrel and hence may not have constant loss throughout the layer. Thus to model this precisely is impossible. As a somewhat simplistic approximation it is assumed that the coating has the same thickness as the coating on the face of the sample and is essentially even throughout the coating. It is also assumed that the coating extends down the entire barrel. This assumption is made in case there exist patches of coating further down the barrel which are invisible to the eye but would still have

an effect on the overall loss of the mass. This assumption will be dealt with further later.

The mechanism for obtaining the energy ratios was dealt with in chapter 4. The mode shapes used are given in appendix B. The effective Young's modulus and Poisson's ratio were calculated according to equations 3.4 and 3.5 in chapter 3. The final values used are shown in table 5.2. The citations given in the table indicate the source of the original value. Note that although the thickness of the different coatings were given above, the energy ratios were calculated for a coating thickness of $1 \mu m$. This was because the two coatings had different thicknesses; this allows a single calculation of energy ratios which may then be scaled appropriately.

Material	Young's modulus (Pa)	Poisson's Ratio
Aluminium oxide	3.6×10^{11} [98]	0.27[99]
Tantalum pentoxide	1.4×10^{11} [84]	0.23[84]
Calculated multilayer[84]	2.6×10^{11}	0.26
Fused silica	7.2×10^{10} [99]	0.17[99]

Table 5.2: *Material properties used for coatings and substrate*

In section 4.5.2 we dealt with the necessary convergence of the energy ratios using a number of FEA models with different mesh densities. Figure 5.1 shows a typical convergence; in this case that of the asymmetric drum. Figure 5.2 shows the calculated energy ratios.

5.3 Analytical Ratio Calculation

Recall that in chapter 4 we developed a method to check that Ocean agreed with an analytical model of a bent bar. It would be an instructive final step to directly compare the energy ratios calculated from Algor results with analytical

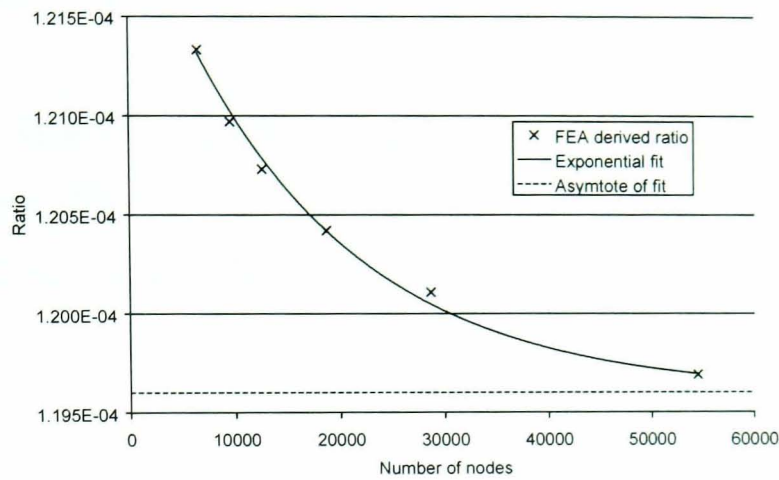


Figure 5.1: *Convergence of energy ratio for the asymmetric drum, fitted with an exponential curve*

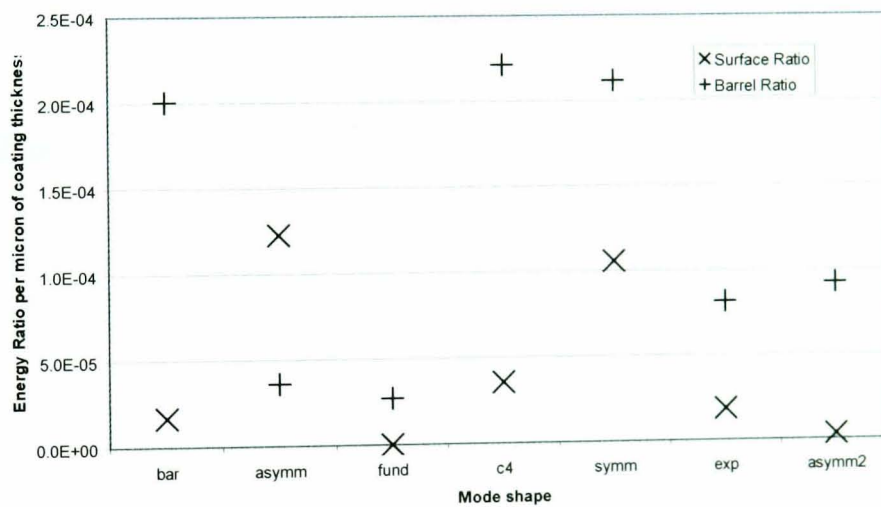


Figure 5.2: *Graph plotting all the relevant energy ratios per μm of coating material. Points \times are those of the surface ratio and those marked $+$ are those of the barrel*

results. Indeed, the best case would be to do this for the cylindrical mass in use in this analysis. It has been established, however, that the analytical solution of the energy ratio for the modes of a cylindrical mass is difficult in many cases (hence the use of Ocean in the first place). One mode where this is not the case (at least to an appropriate level) is the asymmetric drum. We now derive the energy ratio for the asymmetric drum, using first the problem of a bar of rectangular cross section.

5.3.1 Initial Case - Bar

Consider a bar, length L , height D and width b . As shown in figure 5.3, one face has a coating of thickness ΔR . The energy stored in the coating as it is stretched by ΔL as a result of the bar being bent as in figure 5.3 is;

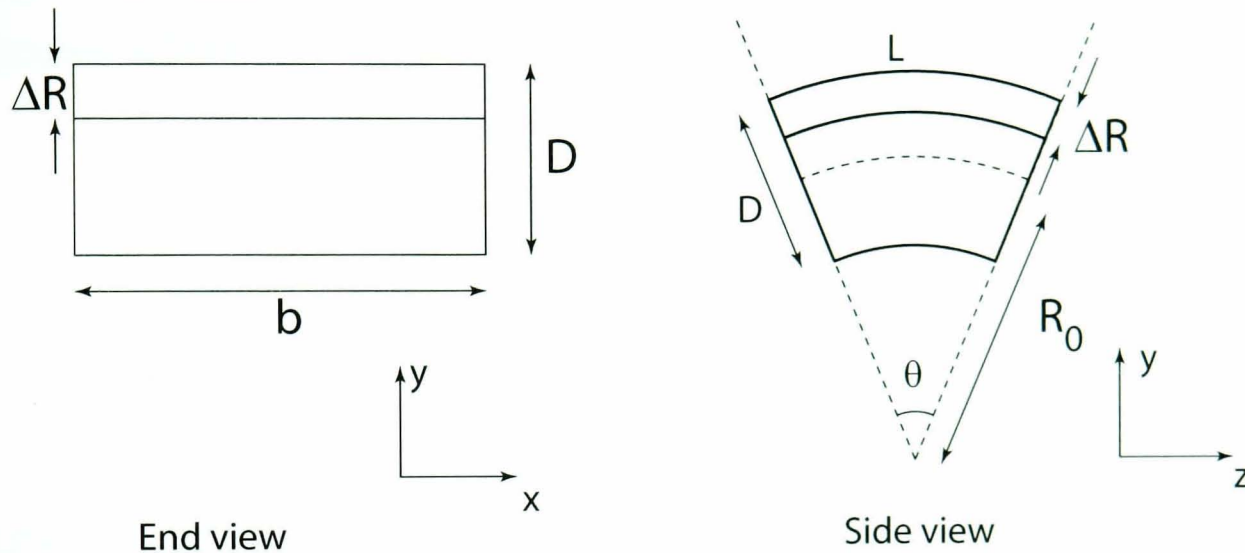


Figure 5.3: *Diagram of a bent bar*

$$\begin{aligned}
 E &= \frac{1}{2}k(\Delta L)^2 = \frac{1}{2}\frac{Y_c A}{L}(\Delta L)^2 \\
 &= \frac{1}{2}\frac{Y_c \Delta R b}{L}(\Delta L)^2
 \end{aligned} \tag{5.2}$$

where $k = Y_c A/L$ is the spring constant, Y_c is the Young's modulus of the coating and $A = \Delta R b$ is the cross sectional area over which the force F is applied. All these values are known except ΔL . Recall, however, that $L = R_0 \theta$, with θ small, and that $L + \Delta L = (R_0 + \frac{D}{2})\theta$. Hence,

$$\Delta L = \left(R_0 + \frac{D}{2}\right)\theta - R_0\theta = \frac{D}{2}\theta \tag{5.3}$$

Thus we have the following expression for the energy stored in the coating:

$$E_{coating} = \frac{Y_c \Delta R b D^2 \theta^2}{8L} \quad (5.4)$$

We now require the energy stored in the bar. Consider a thin section of the bar, dr , at distance r from the origin greater than R_0 . Then the energy of this element will be

$$\begin{aligned} dE &= \frac{1}{2} k dL^2 \\ &= \frac{1}{2} \frac{Y_b b dr}{L} dL^2 \end{aligned} \quad (5.5)$$

with $k = Y_b A/L = Y_b b dr/L$. Y_b is the Young's modulus of the bar and the cross-sectioned area $A = bdr$. Now, $L = R_0 \theta$ as before but $L + dL = r\theta$, so $dL = (r - R_0)\theta$. Hence the energy stored in stretching a thin element of the bar is

$$dE = \frac{1}{2} \frac{Y_b b dr}{L} (r - R_0)^2 \theta^2 \quad (5.6)$$

This expression can now be integrated over the total thickness D of the bar. Note that we have derived dE for an element "above" the neutral axis, where the bar is being stretched. Below the neutral axis an equal amount of energy is stored in the compression of the bar.

So, the total energy stored in the bar is twice the integral of dE from R_0 to $R_0 + \frac{D}{2}$. Consequently we have

$$\begin{aligned}
E_{bar} &= 2 \frac{Y_b b \theta^2}{2L} \int_{R_0}^{R_0+D/2} (r - R_0)^2 dr \\
&= \frac{Y_b b \theta^2}{L} \frac{1}{3} \left(\frac{D}{2} \right)^3 \\
&= \frac{Y_b b \theta^2 D^3}{24L} \tag{5.7}
\end{aligned}$$

In conclusion, therefore, we have the ratio of energy stored in the coating to that stored in the bar as:

$$\frac{E_{coating}}{E_{bar}} = 3 \frac{Y_c \Delta R}{Y_b D} \tag{5.8}$$

5.4 Second Case: Cylinder

Having examined the simple case of a bar, we now extend the analysis to a cylindrical mass excited to its asymmetric drum mode. We will do this by considering the cylinder to be constructed from a number of layers, each of which is deformed radially as the cylinder is bent.

With reference to figures 5.4 and 5.5, consider the mass, or substrate, to be made up of a number of segments reaching almost, but not quite, to the centre of the substrate. The initial stage is to calculate the energy associated with radially stretching such a segment of the substrate above the neutral axis.

Let a segment be divided into a number of elements each with dimensions $r d\theta$ by dr as shown in figure 5.6. Each segment would have thickness ΔR . Thus the cross sectional area $A = r d\theta \Delta R$. So the individual radial spring constant

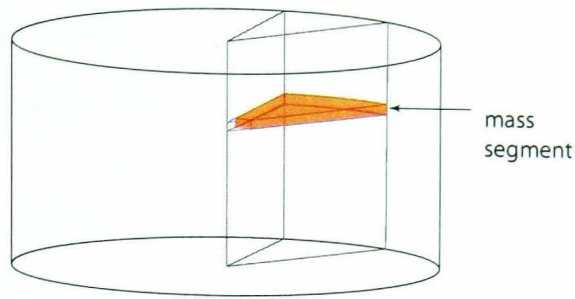


Figure 5.4: *A segment of a cylindrical mass*

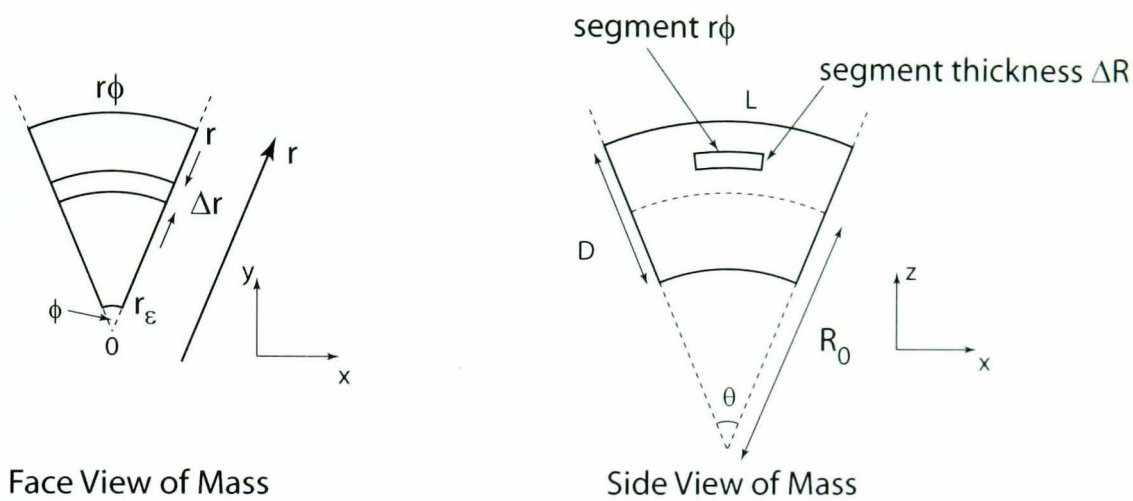


Figure 5.5: *Diagram of a mass distorted into its asymmetric drum mode*

k_n for each element will be

$$\begin{aligned}
 k_n &= \frac{Y_s A}{L} \\
 &= \frac{Y_s r d\phi \Delta R}{dr}
 \end{aligned} \tag{5.9}$$

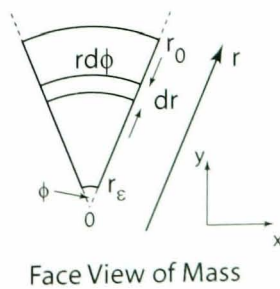


Figure 5.6: *Close up of segment*

where $L = dr$ and Y_s is again the Young's modulus of the substrate. The

spring constant for the entire segment will be the summation of these spring constants over all elements in that segment.

The reciprocal of the spring constant k_{tot} is the sum of the reciprocals of the individual spring constants as follows:

$$\frac{1}{k_{total}} = \frac{1}{k_1} + \frac{1}{k_2} + \frac{1}{k_3} + \dots \quad (5.10)$$

The inverse of k is known as the compliance C ; we thus add the values of C_n where

$$C_n = \frac{1}{k_n} = \frac{dr}{Y_s r d\phi \Delta R} \quad (5.11)$$

Hence the total compliance C_{tot} is;

$$\begin{aligned} C_{tot} &= \frac{1}{Y_s d\phi \Delta R} \int_{r_\epsilon}^{r_0} \frac{1}{r} dr \\ &= \frac{1}{Y_s d\phi \Delta R} \ln \left(\frac{r_0}{r_\epsilon} \right) \end{aligned} \quad (5.12)$$

Hence,

$$dE = \frac{1}{2} Y_s \phi \Delta R \left[\ln \left(\frac{r_0}{r_\epsilon} \right) \right]^{-1} (\Delta x)^2 \quad (5.13)$$

Here, $L = R_0 \theta$ and $L + \Delta x = R \theta$ giving $\Delta x = (R - R_0) \theta$. Therefore,

$$dE = \frac{1}{2} Y_s d\phi \Delta R \left[\ln \left(\frac{r_0}{r_\epsilon} \right) \right]^{-1} (R - R_0)^2 \theta^2 \quad (5.14)$$

To find the energy stored in a segment the thickness of the substrate (a slice). we integrate this expression from R_0 to $R_0 + R_0 + \frac{D}{2}$, then multiply by 2 as before;

$$\begin{aligned}
 dE_{slice} &= 2 \int_{R_0}^{R_0+D/2} dE \\
 &= Y_s d\phi \left[\ln \left(\frac{r_0}{r_\epsilon} \right) \right]^{-1} \theta^2 \int_{R_0}^{R_0+D/2} (R - R_0)^2 dR \\
 &= \frac{1}{24} Y_s d\phi D^3 \left[\ln \left(\frac{r_0}{r_\epsilon} \right) \right]^{-1} \theta^2
 \end{aligned} \tag{5.15}$$

To find the total energy stored we now integrate over ϕ from 0 to 2π . Hence the total energy stored in the substrate is;

$$E_{substrate} = \frac{\pi}{12} Y_s D^3 \left[\ln \left(\frac{r_0}{r_\epsilon} \right) \right]^{-1} \theta^2 \tag{5.16}$$

Finally we wish to calculate the energy stored in a coating. To do this, consider a segment located on the surface of the mass. Then the Δx term in the energy stored $dE = \frac{1}{2}k(\Delta x)^2$ will be $\Delta x = (R_0 + D/2)\theta - R_0\theta = (D/2)\theta$. By comparison with equation 5.13 and considering ΔR to be the total thickness of coating, the energy stored in a segment of coating is;

$$dE = \frac{1}{2} Y_c d\phi \Delta R \left[\ln \left(\frac{r_0}{r_\epsilon} \right) \right]^{-1} \frac{D^2}{4} \theta^2 \tag{5.17}$$

with Y_c the Young's modulus of the coating. Equation 5.17 is integrated over ϕ to give the total energy stored in the coating, giving;

$$E_{coating} = \frac{\pi}{4} Y_c \Delta R D^2 \theta^2 \left[\ln \left(\frac{r_0}{r_\epsilon} \right) \right]^{-1} \tag{5.18}$$

Then, finally the ratio of energy stored in the coating to that in the substrate is equation 5.18 over equation 5.16 giving

$$\frac{E_{coating}}{E_{substrate}} = 3 \frac{Y_c}{Y_s} \frac{\Delta R}{D} \quad (5.19)$$

which is equivalent to the case for the bar (equation 5.8).

In order to test the output from Algor & Ocean, the energy ratio was found for a coating thickness $1 \mu\text{m}$ on a substrate 10.3 cm thick in the situation where both have the same Young's modulus for simplicity. The analytical value is 2.91×10^{-5} . The Algor/ Ocean value (for a model using 28681 nodes) is 2.97×10^{-5} , an agreement to within 2%. This is very encouraging as far as the accuracy of the Algor/ Ocean technique is concerned.

5.4.1 Regression Analysis

Insignificant Barrel Loss

Having obtained the relevant energy ratios, we are now in a position to begin the analysis proper. Reference will be made throughout this section to equation 5.1. First, consider the case where ϕ_{eff} in equation 5.1 is zero, i.e. there exists no barrel coating, or at least the losses associated with such a coating are not significant for these measurements. We may then plot the ratios against experimental loss to obtain the coating loss as gradient. Figure 5.7 shows the results of this plot, wherein the "front surface energy ratio" refers to the energy ratio for the coating only on the front surface. The experimental errors are highest for the two points for each mass at the right-hand side of the figure and the size of these errors (1 standard deviation level for the best suspension length in each case) is indicated by the bars on the points for the 7940 mass.

The numbering of the points refers to the mode numbering in table 5.1.

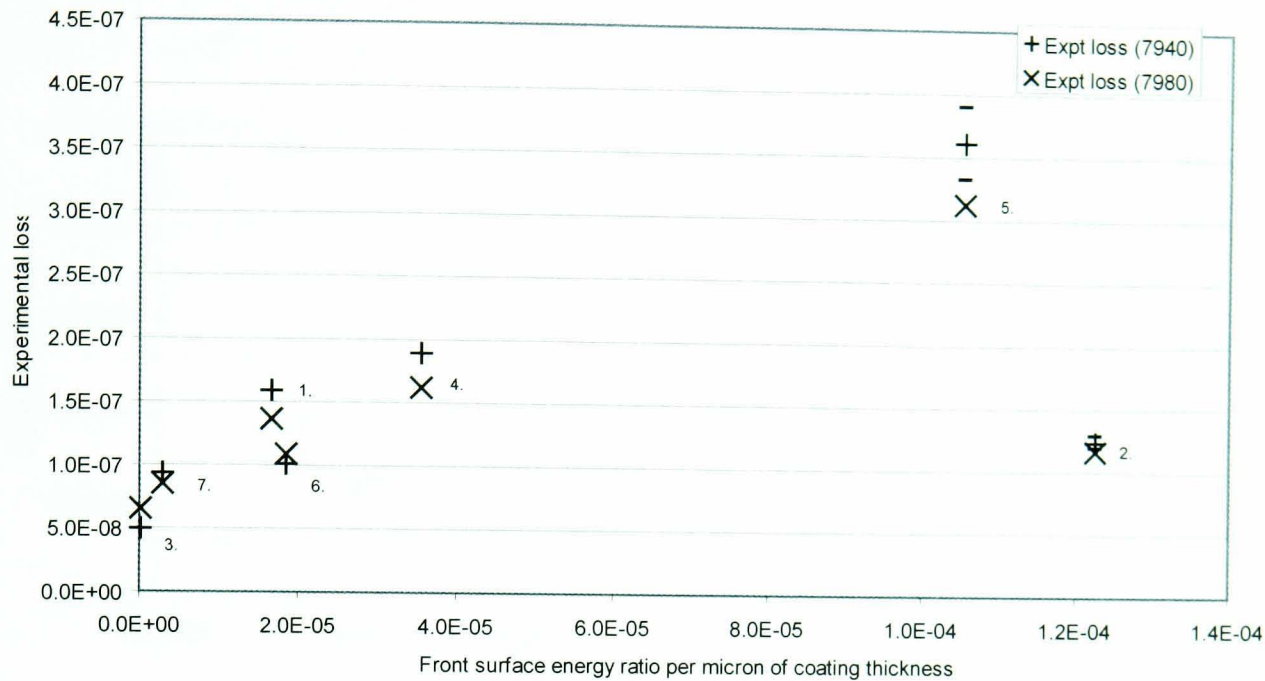


Figure 5.7: Variation of measured loss factor against front surface energy ratio per micron thickness of coating for each mode of the 7940 and 7980 silica test masses

It can be seen from figure 5.7 that if the last point in each of the 7940 and 7980 cases is removed, the straight line fit becomes excellent. However, the point in case is the asymmetric drum, which has a low experimental loss. Confidence in the validity of this point is high because it is unlikely that experimental measurements would yield a loss which was significantly too low. Thus a more detailed analysis is required.

Multi Regression Analysis

We now replace the ϕ_{eff} term from equation 5.1 and perform a multiregression fit for the coating losses. A simple 2D comparison such as that used in figure 5.7 is no longer possible (or relevant) and thus we proceed from now on to plot the experimental loss against the fitted or *predicted* loss. The results of such a fit are shown in figure 5.8. Mode numbers are shown on the first plot only.

A perfect fit would be shown by the data points following the line $y = x$; this line is given for reference in each case.

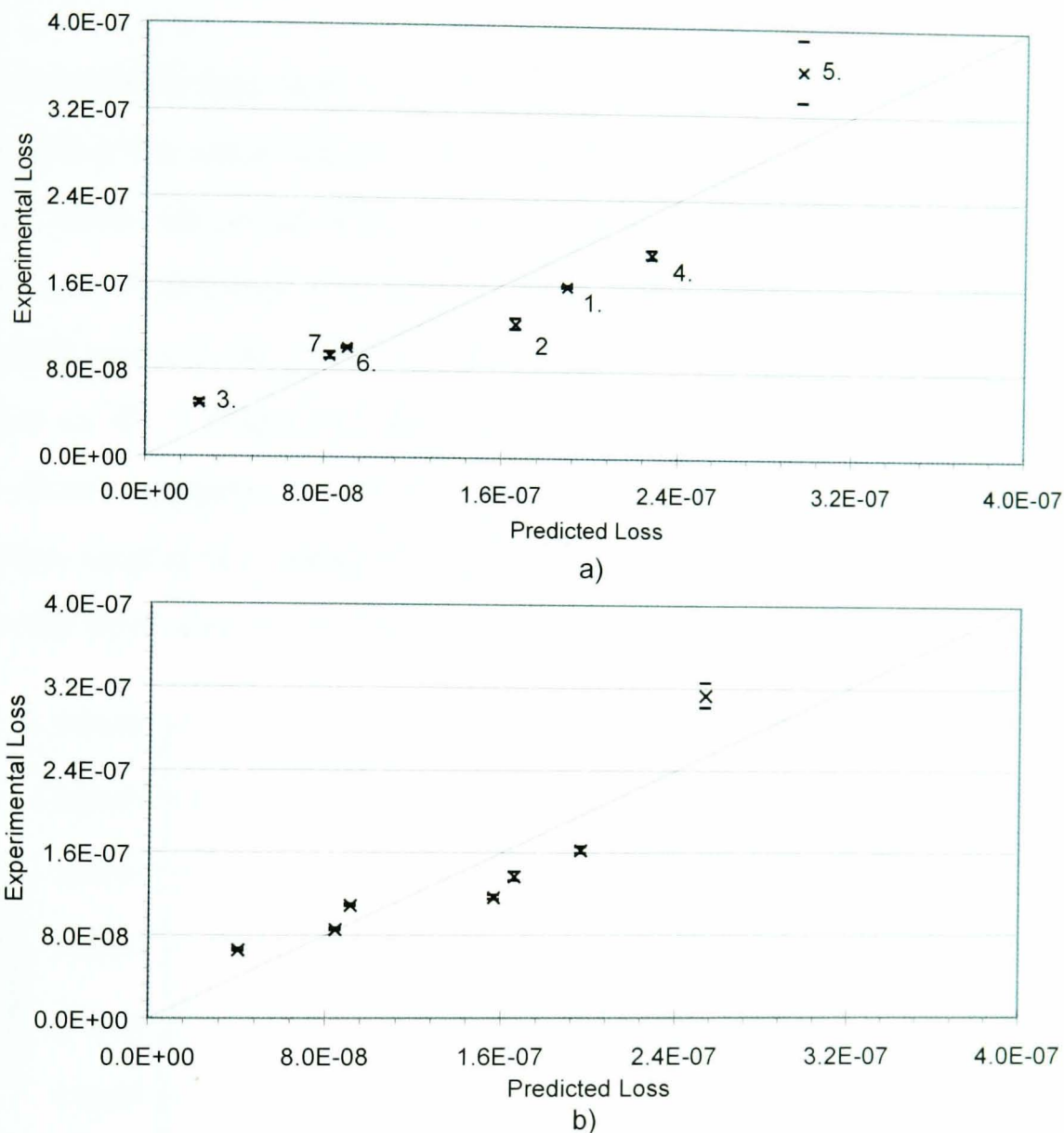


Figure 5.8: Comparison of the experimental loss with that predicted using a three-parameter multiregression analysis for (a) the 7940 and (b) the 7980 mass, assuming that the barrel is completely covered in coating.

Again, as in the single regression case, there is one point in each case which does not follow the otherwise good fit. In this case, we observe that the symmetric drum has a significantly higher loss than that required for an acceptable fit, which is more believable physically than the asymmetric drum having too low a loss. This effect is seen on both the 7940 and 7980 plots and so appears to

be real.

Other Possibilities

It is possible that this is an artifact of the assumption concerning barrel loss covering the entire barrel. It is possible that the barrel coating does not in fact cover the entire barrel, but instead only the ~ 2 cm coating visible to the eye. A fit of all 7 values of coated loss against the front surface ratio and barrel ratio (2 cm only) was carried out to check this. This fit was found to give an $R^2 = 0.52$ in the 7980 case and 0.57 in the 7940 case. The 7980 plot is shown in figure 5.9. The experimental errors have been omitted from this graph (and in the remainder of this section) as they are insignificant compared to the error due to the fitting procedure.

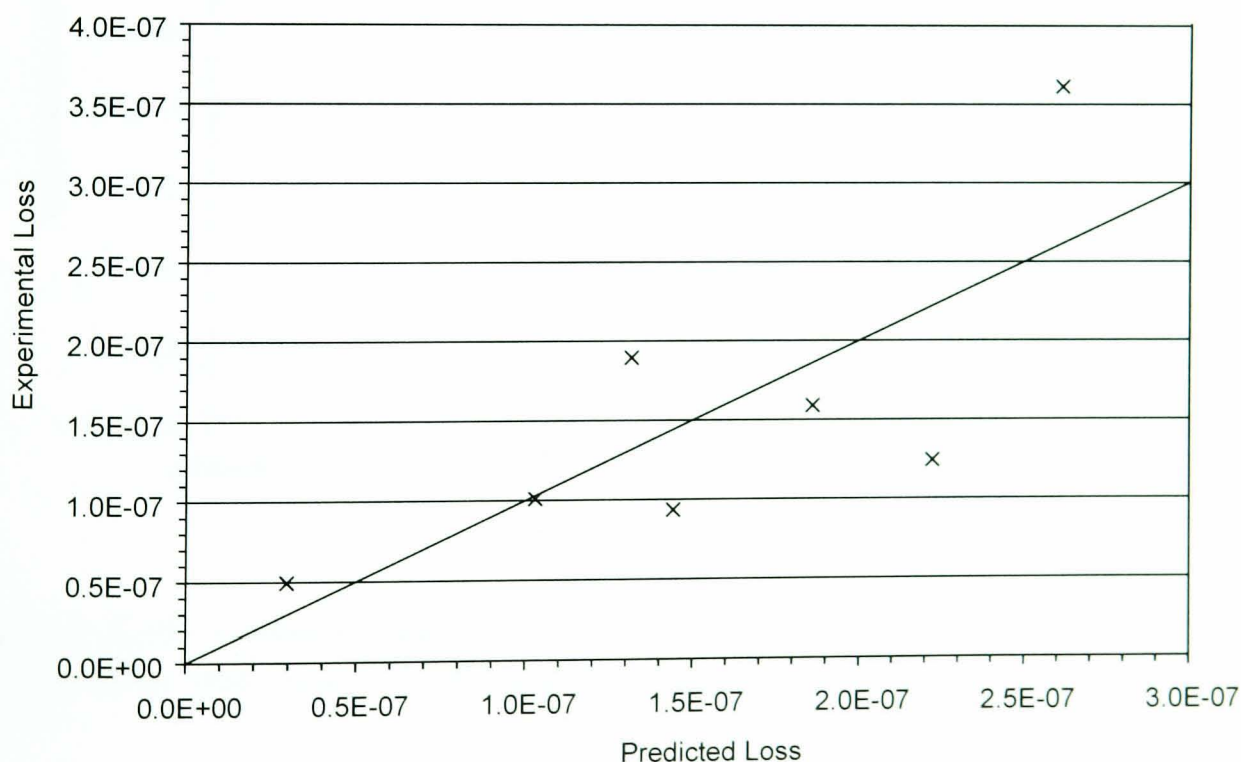


Figure 5.9: Graph of experimental loss against predicted loss for 7980 mass using a partial barrel coating

Another possibility is that there is a split between shear and bulk strain in the coating; recall the discussion of sections 4.2.1 and 4.2.2. A regression analysis

was carried out using equation 5.20.

$$\begin{aligned} \phi(\omega_0)_{coated} \approx \phi(\omega_0)_{substrate} &+ \frac{E_{on\ face\ shear}^{coating}}{E_{substrate}} \phi(\omega_0)_{on\ face\ shear}^{coating} \\ &+ \frac{E_{on\ face\ bulk}^{coating}}{E_{substrate}} \phi(\omega_0)_{on\ face\ bulk}^{coating} \end{aligned} \quad (5.20)$$

As can be seen from figure 5.10 the fit is not good (the 7980 results only are again shown; the 7940 results are similar).

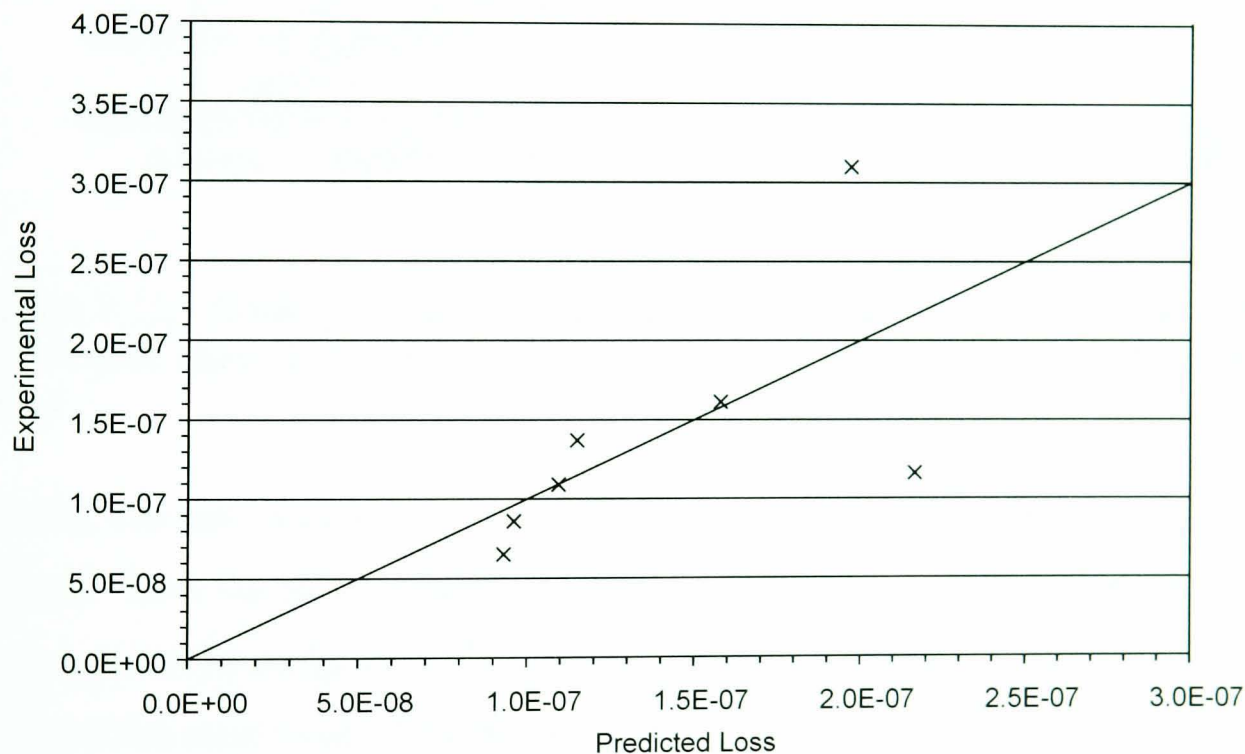


Figure 5.10: Graph of experimental loss against predicted loss for 7980 mass using shear and bulk front surface energy ratios

If, however, the surface shear, surface bulk and total barrel losses are used in the analysis, the fit is rather better ($R^2 = 0.88$, figure 5.11) but the surface shear loss calculated is $(-2 \pm 2) \times 10^{-4}$ which would indicate that this fit is not very physical. One might expect there to be a loss dependence on some combination of shear plus bulk energy; indeed they add to give the total front

surface energy. However there is not enough evidence here to suggest what such a dependence may be.

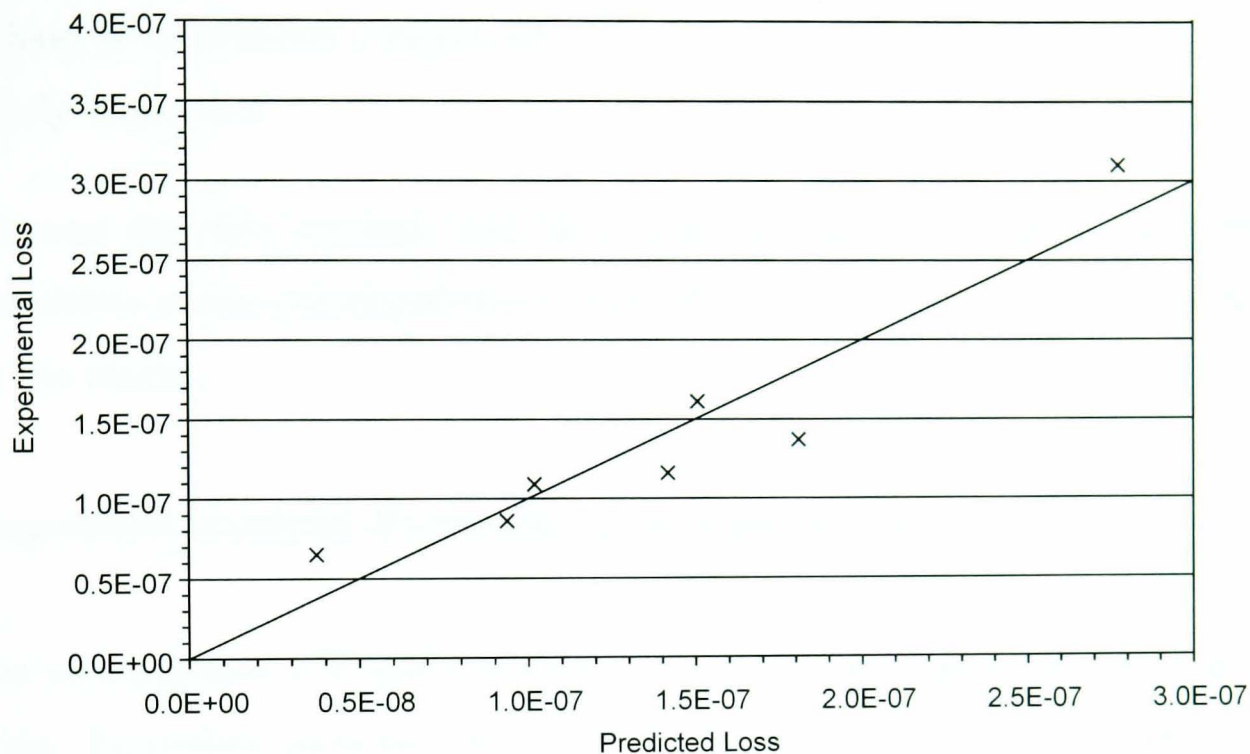


Figure 5.11: *Graph of experimental loss against predicted loss for the 7980 mass using shear and bulk front surface energy ratios and total barrel energy ratios*

Finally, the last possibility considered was that there was a loss arising from friction. Thus the ratio of the kinetic energy of a band the width of the coating layer around the midpoint of the barrel to the strain energy of the substrate was obtained for each mode. The form of energy density mentioned in section 4.4.4 was used to calculate ratios for both the radial ($\Delta x + \Delta y$) and longitudinal (Δz) directions; these led by linear addition to the total kinetic ratio. The ratios obtained were of the order $10^{-10} - 10^{-8}$ and were multiplied by 10^4 to make them of the same order as the other ratios (the regression program, Analyse-IT[100] failed using the original magnitudes because they were too small); this is reasonable since we are not interested at this stage about the actual value of any friction loss, only whether it may reasonably exist. It was found that there was no combination of variables (using front surface ratios,

longitudinal, radial and total kinetic ratios) which yielded a better fit than was obtained using the front surface and barrel ratios except for a fit of loss against the front surface ratio and longitudinal kinetic ratio. This was found to have $R^2 = 0.98$ but a longitudinal kinetic loss of $(-2 \pm 0.2) \times 10^{-3}$ which is clearly unphysical.

We must therefore conclude that there does exist some unmodelled loss in the symmetric drum; one possibility is edge effects associated with the chamfers on the masses.

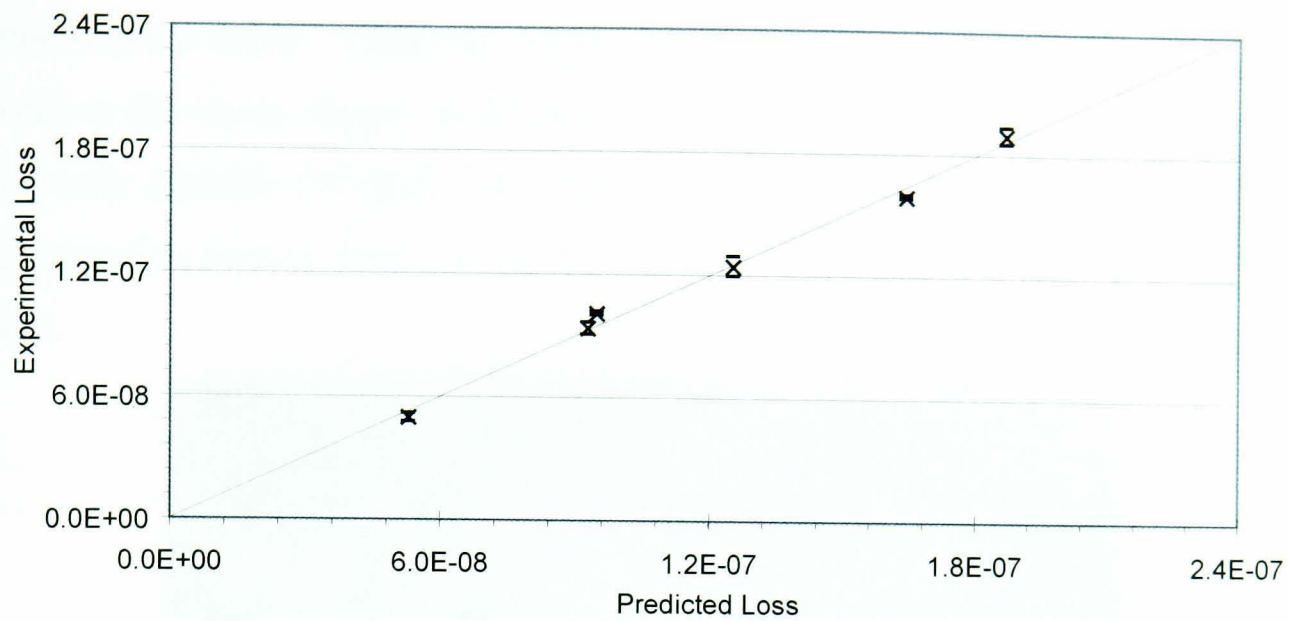
Regression Analysis Excluding Symmetric Drum

The multiregression fit was repeated but with the exclusion of the symmetric drum. Equivalent plots to those shown in figure 5.8 are shown in figure 5.12. We can observe that this time the fit is excellent, with $R^2 = 0.9$. Coating losses derived from this analysis are shown in table 5.3.

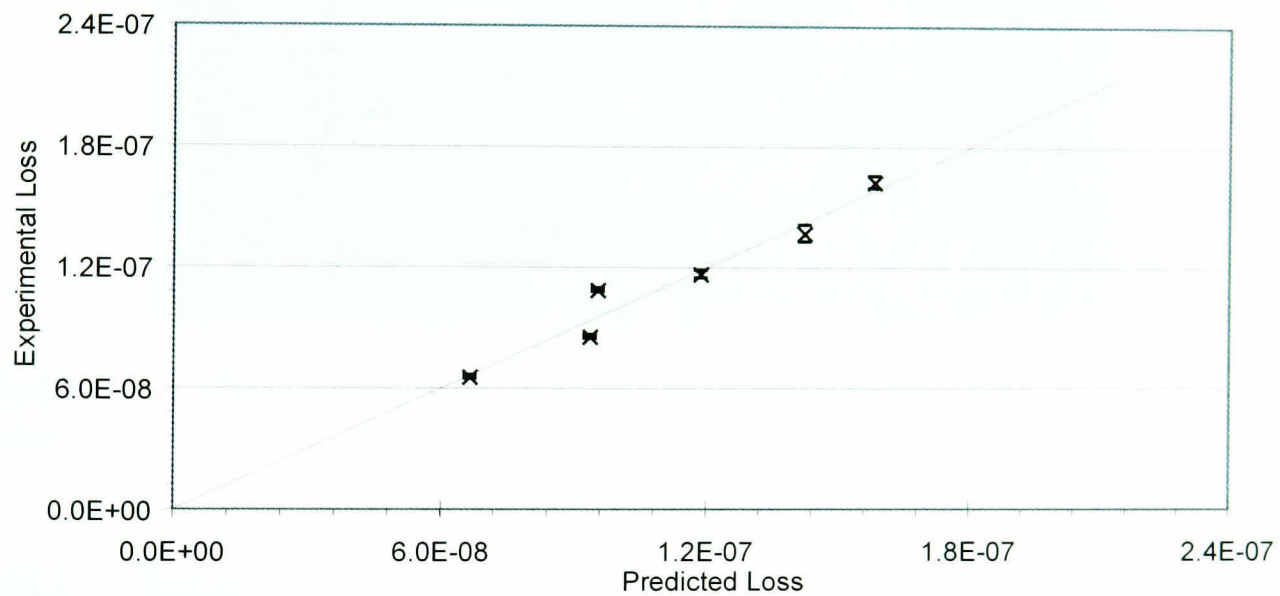
For the Corning 7940 mass:	$\phi(\omega_0)_{substrate}$	$= (3.7 \pm 0.5) \times 10^{-8}$
	$\phi(\omega_0)_{coating}$	$= (6.4 \pm 0.6) \times 10^{-5}$
	$\phi(\omega_0)_{eff}$	$= (6.9 \pm 0.4) \times 10^{-5}$
For the Corning 7980 mass:	$\phi(\omega_0)_{substrate}$	$= (5.6 \pm 0.9) \times 10^{-8}$
	$\phi(\omega_0)_{coating}$	$= (6.3 \pm 1.6) \times 10^{-5}$
	$\phi(\omega_0)_{eff}$	$= (6.3 \pm 0.9) \times 10^{-5}$

Table 5.3: *Coating loss results for the 7980 and 7940 masses. Errors are at the 1 standard deviation level*

The results for $\phi(\omega_0)$ are comparable with the current best results for bulk samples for these types of fused silica[101]. While we do not directly require these results, it is nonetheless a useful check that the predicted value of intrinsic loss is not substantially different from the accepted experimental level.



a)



b)

Figure 5.12: Comparison of the experimental loss with that predicted using a three-parameter multiregression analysis for (a) the 7940 and (b) the 7980 mass, with the symmetric drum removed

5.5 Mode Identification Confirmation

During this investigation, there was one experimentally determined mode which was not used in the analysis due to uncertainty in its identification. This mode was measured to have a frequency of 25787 Hz. This placed it in between the

fundamental mode, 25378 Hz, and the c4 mode, 26176 Hz. It was decided to confirm the mode shapes of the fundamental and c4 modes and consequently correctly identify the mode at 25787 Hz using the direct modeshape method discussed in section 3.5.1. A photograph of the experiment is shown in figure 5.13.

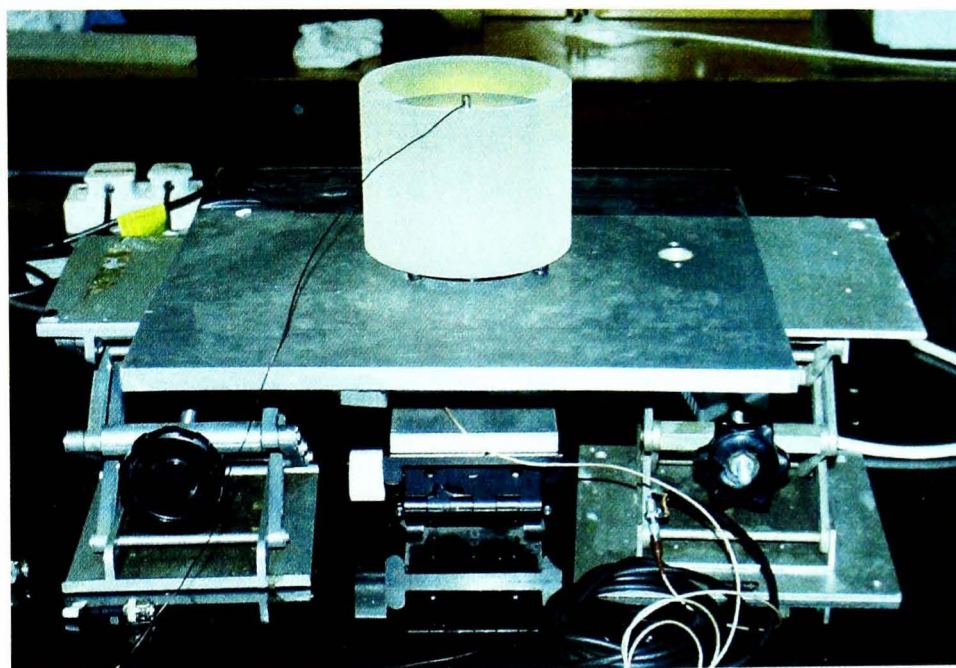


Figure 5.13: *Photograph of experiment to determine modeshapes of cylindrical mass*

5.5.1 Results

The results will be presented in two stages, showing both the oscilloscope and spectrum analyser data which essentially demonstrate the same results. The oscilloscope results will be indicated by a matrix of phase angles, which refer to the site diagram shown in figure 5.14. The results themselves are shown in table 5.4. In this table the phase measurements are given except where the accelerometer signal was too small to discern. This is consistent with location of the accelerometer being a node of that mode; this is indicated in the table accordingly.

The first of these would indicate a situation where the entire front face of the

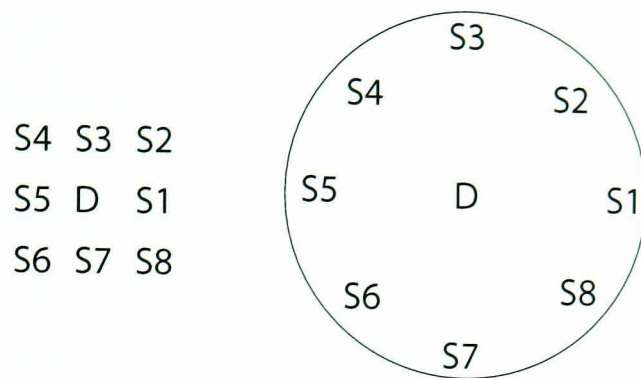


Figure 5.14: *Diagram showing the various accelerometer sites on the front surface of a cylindrical mass*

Frequency (kHz)	Phase Distribution		
25.555	225	225	225
	225	180	225
	225	255	225
25.9	90	90	45
	node	node	node
	-90	-90	-90
26.3	node	-90	node
	90	node	90
	node	-90	node

Table 5.4: *Results of oscilloscope modeshape experiment showing phase and node position*

mass is essentially moving in phase (there is a limit to the accuracy of the phases measured of 45°). This is reminiscent of the fundamental longitudinal mode (see appendix B). The second suggests a mode where one half of the surface is moving out of phase with the other half. This might suggest a mode like the bar mode shown in appendix B. Finally, the third mode would appear to suggest a mode where points on the surface opposite each other are in phase but points 90° apart are out of phase. This would suggest the clover 4 mode shown in appendix B.

These results would tend to support the ordering of the fundamental and clover 4 modes and indicate that the central mode is bar-like.

The equivalent results from the spectrum analyser version of this experiment are detailed below. Firstly, the transfer function between the centre of the surface and the drive is shown in figure 5.15

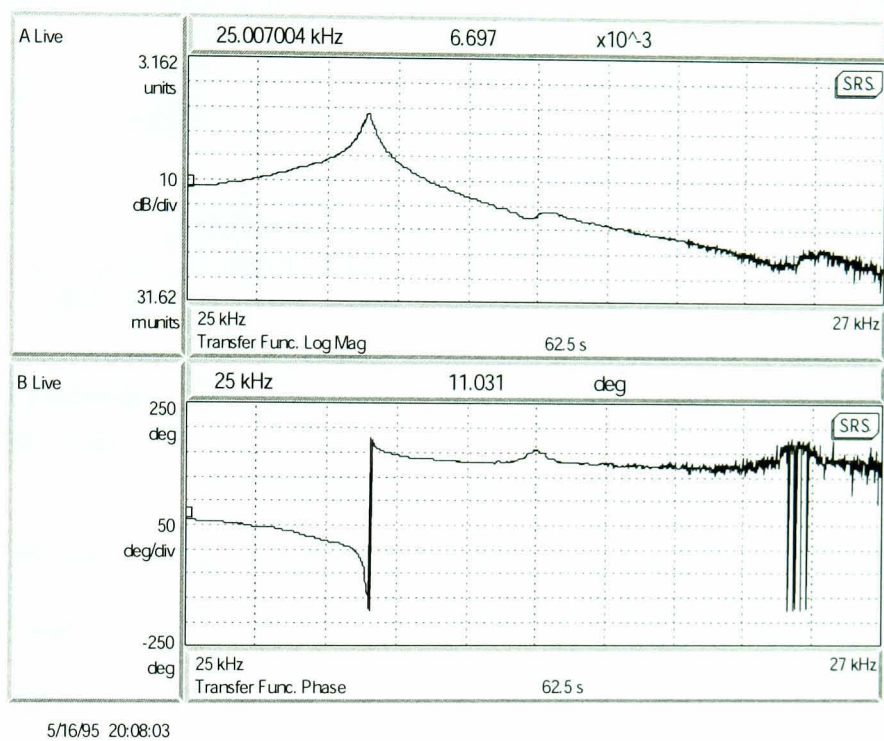


Figure 5.15: *Transfer function between the centre of the surface and the drive*

From this we can see that there is a mode at 25.5 kHz and some form of resonance at 26 kHz. The lower mode is very strong which again is consistent with the fundamental longitudinal mode.

In figure 5.16 we can see the transfer function between the drive and a point on the edge of the surface, where we can again see the 25.5 kHz mode but now also ones at 25.8 and 26.3 kHz. The fact that these two modes appear only when the accelerometer is placed at the edge of the mass is consistent with the fact that the bar and c4 modes indicate little displacement at their centre points.

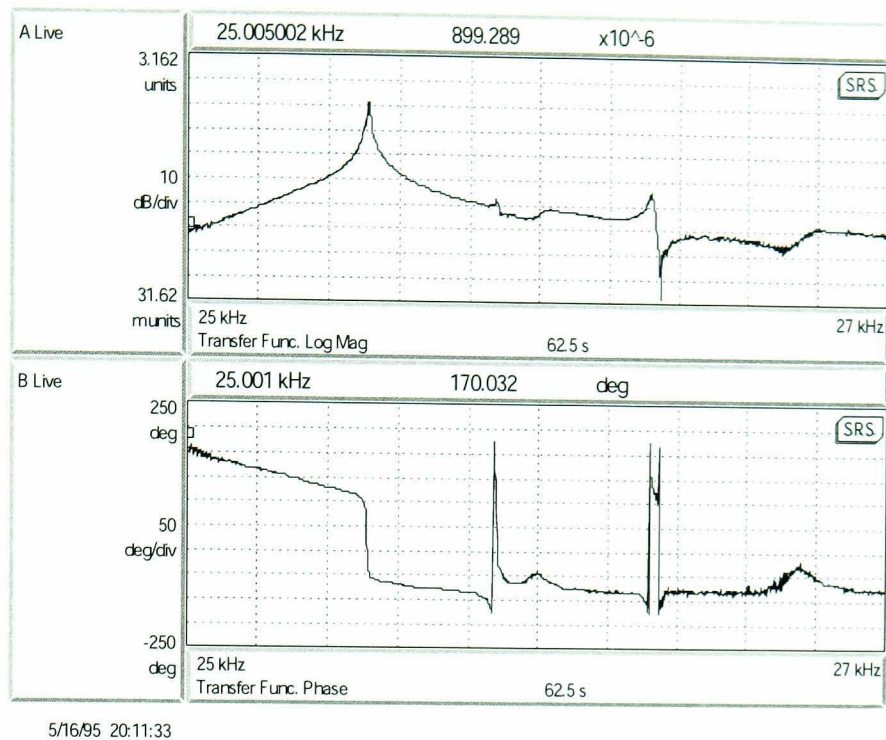


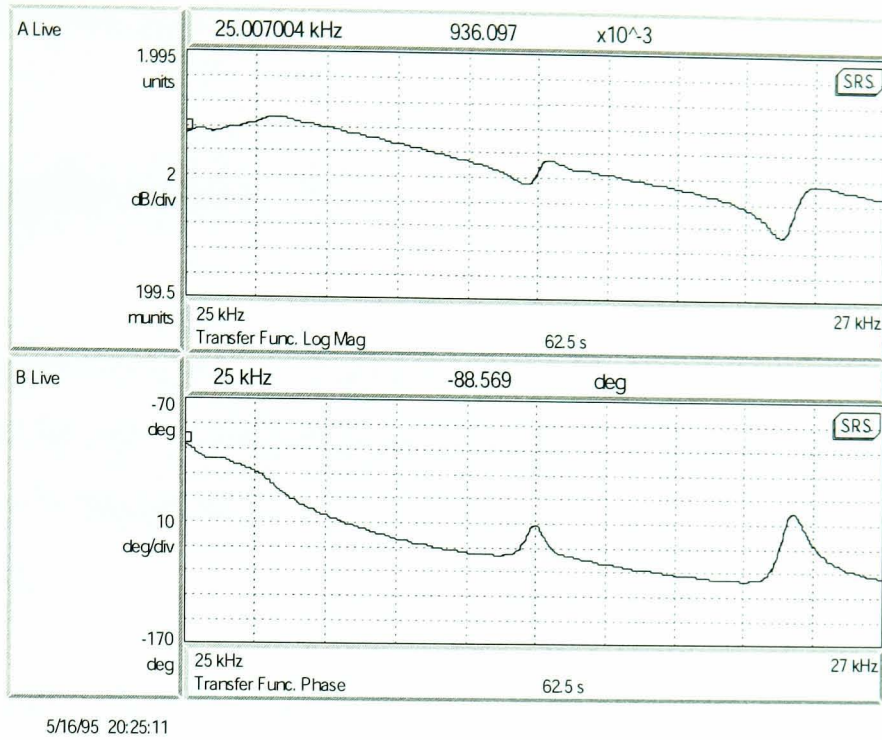
Figure 5.16: *Transfer function between the drive and accelerometer placed at the edge of the mass*

The matter of the small resonance at 26 kHz is interesting since it is not predicted by any of the other experiments and indeed was not seen by the oscilloscope version experiment. The explanation is that it is a resonance of the accelerometer itself; figure 5.17 shows the transfer function between the drive and the accelerometer itself with no mass present.

Here this extra resonance can be clearly be seen. Hence it would appear that this is not, in fact, a mass resonance.

5.5.2 Effect of Extra Mode on Analysis

The mode order confirmation provided another reliable mode identification, the “bar” mode. In order to check that the presence of this mode did not affect the outcome of the foregoing analysis, the fit of loss against front surface coating energy ratio and barrel coating energy ratio was repeated with the addition of this mode. The fit for the 7980 mass may be seen in figure 5.18



5/16/95 20:25:11

Figure 5.17: *Transfer function between accelerometer and drive with no mass present*

(again without the experimental errors); the fit for the 7940 mass is similar.

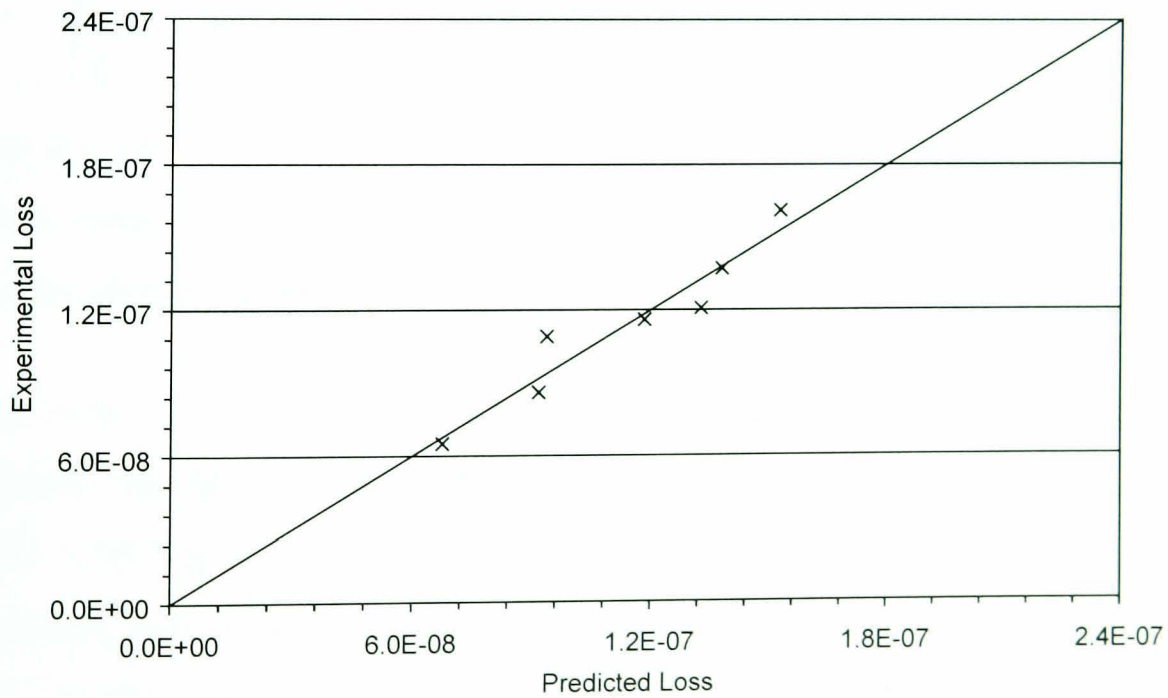


Figure 5.18: *Graph of experimental losses against predicted losses for the 7980 mass using front surface and total barrel energy ratios, including the new mode*

It can be seen that the addition of this mode has no effect of the goodness of

fit; the fitted losses remain as they were before.

5.6 Implications For Advanced Detectors

In chapter 2, the presence and possible sources of thermal noise were discussed. To give more context to the results presented here an estimate of the predicted thermal noise increase which would result from the measured value of coating loss is presented.

Recall equation 2.27 which gives the increase in thermal noise which would result from a slab of excess loss of different material properties to the substrate being placed on a substrate:

$$R = 1 + \left\{ \frac{1}{\sqrt{\pi}} \frac{(1 + \sigma_{coating})}{(1 - \sigma_{substrate}^2)(1 - \sigma_{coating})} \frac{\phi_{coating}}{\phi_{substrate}} \frac{Y_{substrate}}{Y_{coating}} \right\} \times \quad (5.21)$$

$$\left\{ \left[(1 - 2\sigma_{coating}) + (1 - 2\sigma_{substrate})^2 \frac{(1 + \sigma_{substrate})^2}{(1 + \sigma_{coating})^2} \left(\frac{Y_{coating}}{Y_{substrate}} \right)^2 \right] \left(\frac{d}{w} \right) \right\}$$

where d is the coating thickness, w is the radius of the laser beam incident on the test mass, σ is the relevant Poisson's ratio of the test mass or coating and Y is the relevant Young's modulus of the test mass or coating.

Using values for the substrate and coating physical properties from table 5.2. the mean coating thicknesses for the 7980 and 7940 masses, a laser beam of spot size 5.5×10^{-2} m[13], a loss for the substrate of 5×10^{-8} and using the mean of the coating loss values for the 7980 and 7940 masses in table 5.3, the predicted power spectral density of the thermal noise is increased by a factor 1.27. Thus the amplitude spectral density of the thermal noise is increased by a factor of 1.13 over that which would have been found without the presence of the coating layer. It should be noted that it is assumed that the losses in both the substrate and coating are structural, i.e. they do not vary with frequency. This

seems reasonable since calculations[102] suggest that thermoelastic damping, which is frequency dependent, is at a lower level than the losses presented here. The goal for Advanced LIGO is an increase of a factor of 1.1 in the thermal noise power spectral density due to the coating loss. This is consistent with an alumina/ tantala coating loss of $\sim 2.5 \times 10^{-5}$ (the equivalent loss for a silica/ tantala coating is $\sim 3 \times 10^{-5}$). Thus the results here indicate that, while not increasing the noise by a prohibitive amount, nonetheless further investigation is required to characterise and reduce the loss due to the dielectric coatings. In the next section the first stage in this extended investigation will be discussed.

5.7 Extended Investigation (Silica/ Tantala)

Having established the existence of an excess loss due to the coatings, a further investigation was instigated to determine the nature of this loss and its major source. To this end, two directions were pursued. Firstly, different coating dimensions were used and secondly different materials were used in the coatings.

5.7.1 Nature of samples

Initially, coatings made up of layers of silica and tantala were studied. This type of coating was chosen because it is used in current gravitational wave detectors as a result of its optical properties. The next section will deal with other materials used. The samples in this instance were right cylindrical, 76.2 mm in diameter and 25.4 mm in height. All were manufactured from Corning 7980 fused silica (grade 0A). Table 5.5 shows the different samples used. The coatings were applied by SMA, Lyon[103]. The masses were polished to a sub-Angstrom surface roughness by Wave Precision (formerly General Optics)

Run	Number of samples	Effect being investigated	Layer Thicknesses ($SiO_2\lambda, Ta_2O_5\lambda$)	Total number of layers
0	1	Cleaning/ annealing	No coating	N/A
1	2	substrate/ coating interface + 30 coating layers	1/4,1/4	30
2	1	substrate/ coating interface + 2 coating layers	1/4,1/4	2
3a	2	Differential effect of materials	1/8,3/8	30
3a	2	Layer thickness vs. number of layer/layer interfaces	1/8,1/8	60
4	2	Reverse differential effect	3/8,1/8	30

Table 5.5: *Table showing different coating compositions used in investigation of the source of the coating loss*

Unlike in the original experiment described above, these samples were accessible from their original, that is uncoated, state. This allowed a full range of loss measurements to be made. The experimental technique was the same as that used for the original samples.

5.7.2 Results

Losses from each of the coating types are shown in figure 5.19. Where losses are not shown they have not been measured; for example, note in particular the absence of the symmetric drum in some of the samples. This will be mentioned further in the next section.

The analysis of these samples differed slightly from the previous analysis. The biggest difference was that these masses had been coated so that they specifically did not have barrel coating: hence that term was removed from the loss parameterisation.

In the majority of samples 5 modes were measured; in some instances however it was not possible to detect all the modes as the coupling to the sensing was too low. The modeshapes for these modes are given in appendix C

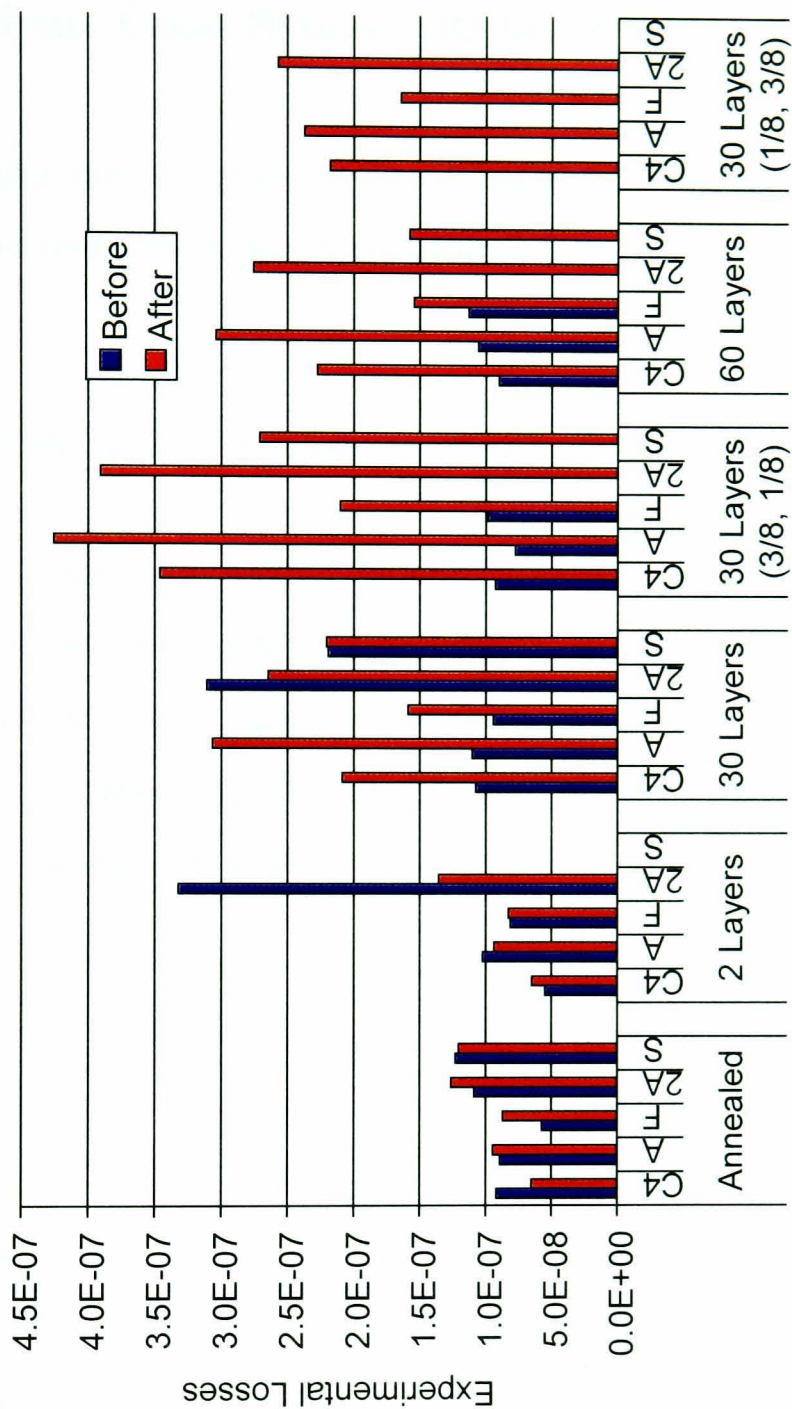


Figure 5.19: Representative losses for each of the coating types, including the annealed mass. “Before” indicates the loss before the sample has been treated/coated and “After” refers to the loss after coating/ treatment. The different modes are “c4” - clover-4, “a” - asymmetric drum, “f” - fundamental, “2a” - second asymmetric drum and “s” - symmetric drum. Pictures of these modes may be found in appendix C.

The analysis, or strictly the development of analysis, of these results was somewhat involved. Consequently, a case study of a typical analysis will be given for the 30 layer $\lambda/4, \lambda/4$ coating.

5.7.3 Analysis Case Study (30 layer $\lambda/4, \lambda/4$)

Since we no longer are concerned with the barrel coating, a new loss parameterisation will be used, as shown in equation 5.22.

$$\phi(\omega_0)_{coated} \approx \phi(\omega_0)_{substrate} + \frac{E_{coating\ on\ face}}{E_{substrate}} \phi(\omega_0)_{coating\ on\ face} \quad (5.22)$$

As already mentioned, the second difference in this new set of masses was that the losses of the samples were measured both before and after they were coated. Hence the simplest analysis now is to plot $\phi(\omega_0)_{coated} - \phi(\omega_0)_{substrate}$ against $\frac{E_{coating\ on\ face}}{E_{substrate}}$; the resulting straight line plot should yield $\phi(\omega_0)_{coating\ on\ face}$ as its gradient. The resulting plot is shown in figure 5.20

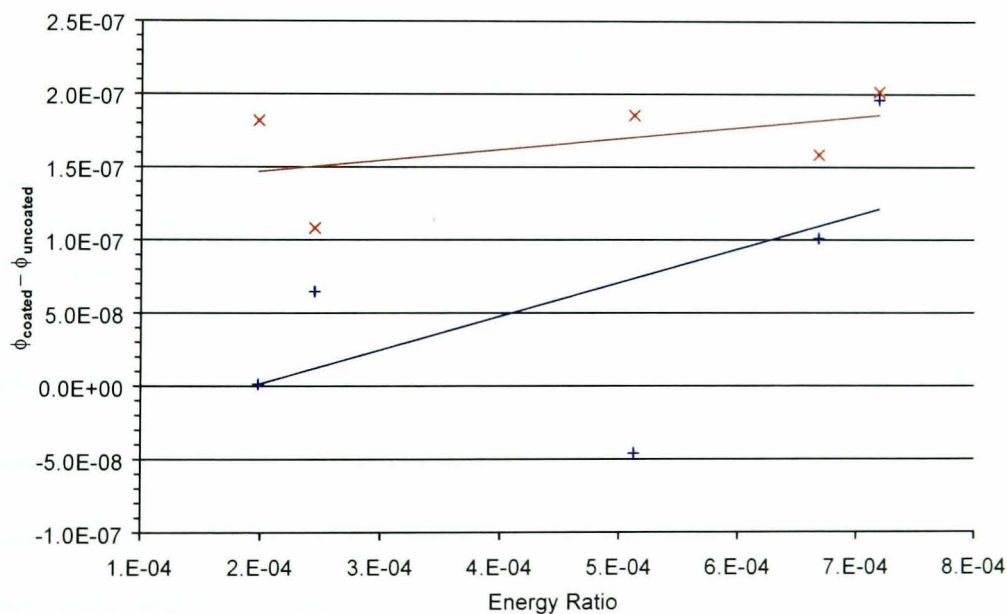


Figure 5.20: Graph of experimental coated loss minus measured intrinsic loss against predicted loss for two masses, each with a 30 layer $\lambda/4, \lambda/4$ coating. The blue set of data corresponds to that shown in figure 5.19.

With an R^2 value of 0.24 for the red sample and $R^2 = 0.35$ for the blue sample, these are not acceptable fits. Given that previous fits were excellent, what could the problem be? One possibility concerns the coating process itself. In one part of the process, the samples are heated to anneal the coatings. The

temperatures used are not high enough to anneal the substrate as silica has an annealing temperature of $\sim 1000^{\circ}\text{C}$ [104] while the samples here were heated to 600°C . An uncoated sample which was “quasi-annealed”, however, was found to have losses for each of its modes which changed by different amounts from the losses measured originally (see figure 5.21).

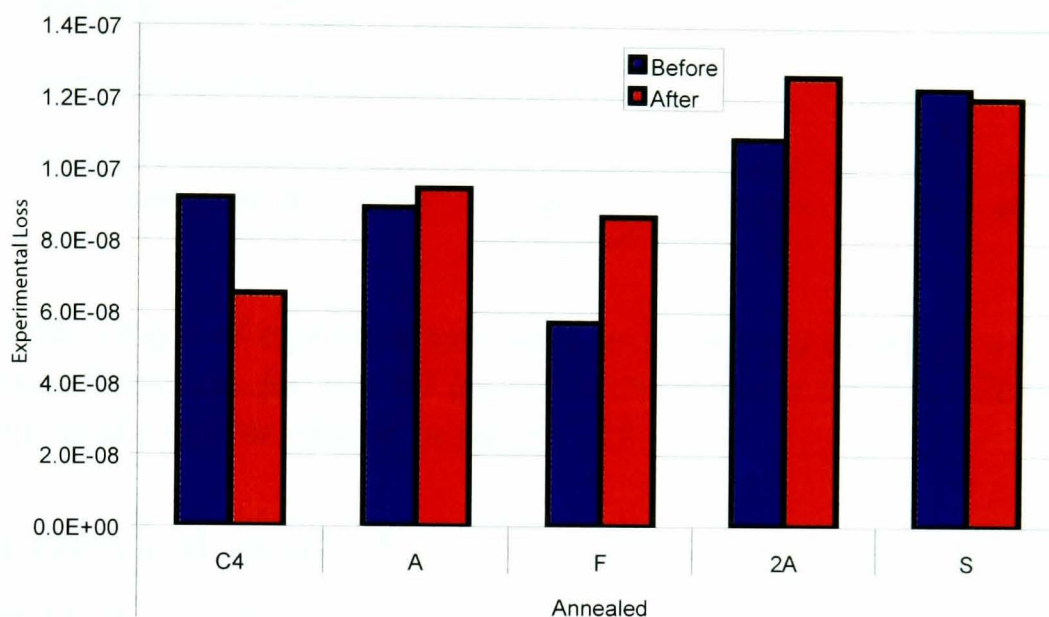


Figure 5.21: *The losses measured before and after an uncoated sample had been heated to the temperature used to anneal the coatings on other samples. This data is the same as the annealed sample in figure 5.19*

It is possible that this was due to stress being introduced into the sample as it was heated and cooled. Previous work has noted that the true annealing of a mass may affect its intrinsic loss[105, 104]. Thus, it would be instructive to neglect the uncoated or *substrate* values and instead fit using the losses taken from the quasi-annealed mass discussed earlier. The outcome of this is shown in figure 5.22.

It can be seen that the fit with the red sample is not very good ($R^2=0.19$), certainly in comparison to the fit for the blue sample for which $R^2=0.78$. It should be noted that there is a significant difference in the loss of the leftmost mode, the symmetric drum mode, between the two samples. If this mode is

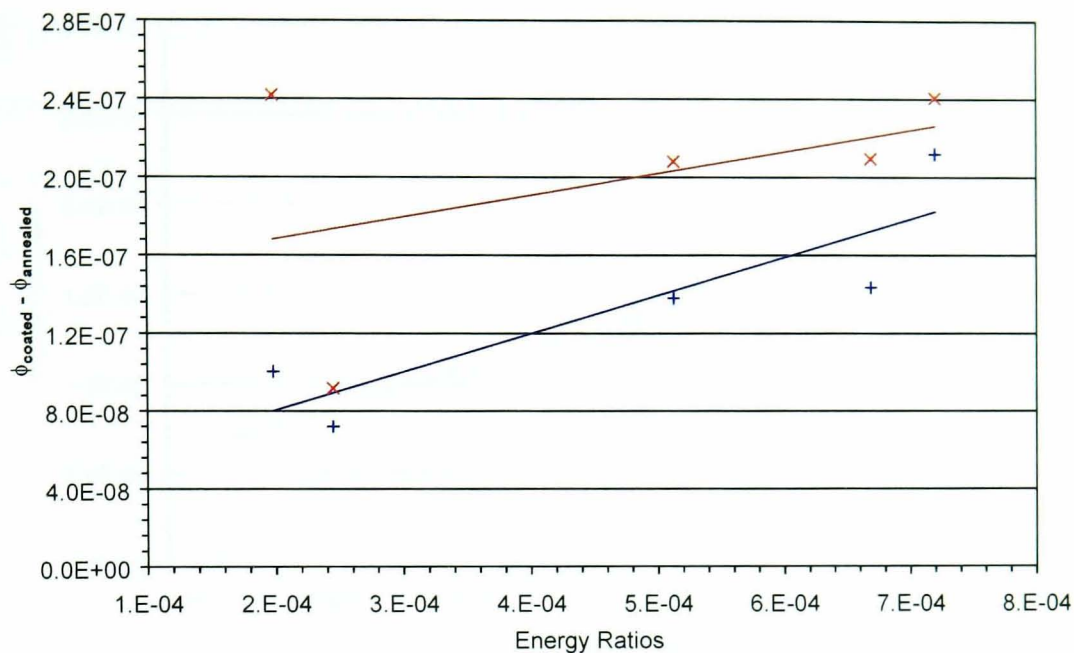


Figure 5.22: Graph of experimental coated loss minus appropriate annealed loss against predicted loss for two 30 layer $\lambda/4, \lambda/4$ coated masses. The blue data set refers to the sample shown in figure 5.19

removed (from both samples for consistency) and the data refitted, the graph shown in figure 5.23 is obtained in which the fit for the red data has $R^2 = 0.91$ and the fit for the blue data has $R^2 = 0.84$. From this we can see firstly that the fit for the red sample is significantly improved and secondly that the two data sets are now consistent in their gradient; the intercept does vary between the two sets but this could perhaps indicate a slight difference in the intrinsic losses of the individual samples. The coating losses yielded from this fit are $(2.9 \pm 0.7) \times 10^{-4}$ for the red data set and $(2.5 \pm 0.8) \times 10^{-4}$ for the blue. These are in agreement within error. This would suggest (in similar way to the original study) that the removal of one mode improves the analysis. Throughout the investigation, it proved difficult in the experimental work to obtain repeatable loss values for the symmetric drum for all the samples [106]; indeed in later work it proved impossible.

In addition, a graph was plotted of the radial displacement along the barrel, normalised to the maximum displacement of the front surface, of each of the

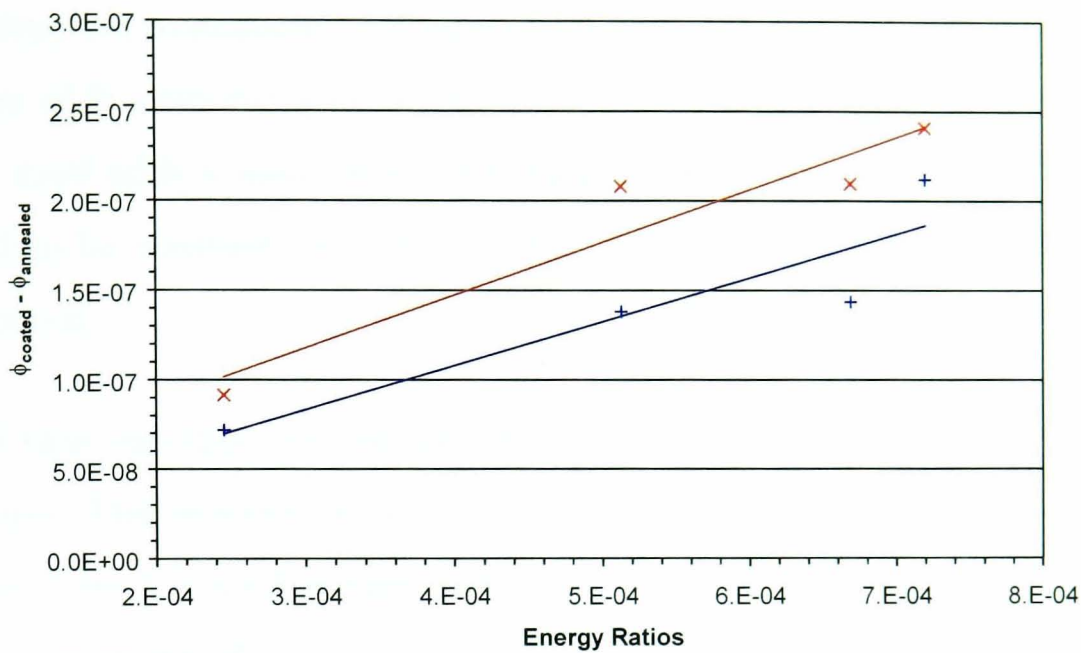


Figure 5.23: Graph of experimental coated loss minus appropriate annealed loss against predicted loss using only 4 modes for two 30 layer $\lambda/4, \lambda/4$ coated samples, where the blue data set corresponds to the data in figure 5.19

modes. The maximum radial displacement for the c4 mode was used as it is not axisymmetric. This graph is shown in figure 5.24. It is possible that the significantly greater curvature noticeable in the symmetric drum is leading to a currently unmodelled loss. Work in this area continues.

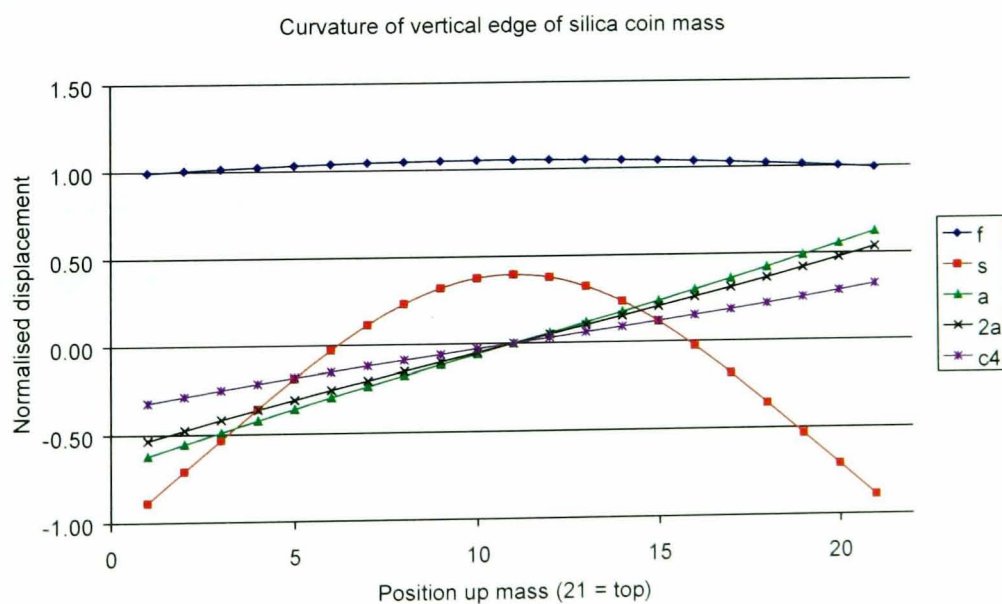


Figure 5.24: Graph of the magnitudes of displacements of the edge of the sample in various modes. Note the particularly large curvature of the symmetric drum

It is instructive to examine the implications of the remarkable improvement in goodness of fit demonstrated in figure 5.23. This suggests that the annealing process itself adds a *mode dependent* element to the intrinsic loss, previously believed to be constant (see chapter 3). This interesting result is still under investigation.

We will thus use this analysis for the remainder of the study, with one final addendum. This was that a similar procedure was carried out using the results from the 2 layer coated sample. The parameterisation is a little less obvious than for the annealed case:

$$\begin{aligned}\phi_{30 \text{ coated}} &= \phi_{30 \text{ intrinsic}} + R_{30}\phi_{30 \text{ coating}} \\ \phi_{2 \text{ coated}} &= \phi_{2 \text{ intrinsic}} + R_2\phi_{2 \text{ coating}}\end{aligned}\tag{5.23}$$

where $\phi_{30 \text{ coated}}$ refers to the 30 layer coated loss, $\phi_{30 \text{ intrinsic}}$ to the intrinsic loss of the 30 layer mass, R_{30} the energy ratio for the 30 layer coating and $\phi_{30 \text{ coating}}$ the loss of the 30 layer coating. Similarly for the 2 layer coating

If $\phi_{30 \text{ intrinsic}} = \phi_{2 \text{ intrinsic}}$ then we have

$$\phi_{30 \text{ coated}} - \phi_{2 \text{ coated}} = R_{30}\phi_{30 \text{ coating}} - R_2\phi_{2 \text{ coating}}\tag{5.24}$$

Now, $R_{30} = 15R_2$. If we assume that $\phi_{30 \text{ coating}} = \phi_{2 \text{ coating}}$, i.e. that there loss dependence on the intra-coating interfaces, then we are left with:

$$\phi_{30 \text{ coated}} - \phi_{2 \text{ coated}} = R_{30}\phi_{30 \text{ coating}} - R_2\phi_{2 \text{ coating}}\tag{5.25}$$

$$= 15R_2\phi_{30 \text{ coating}} - R_2\phi_{2 \text{ coating}}\tag{5.26}$$

$$= R_2(15\phi_{30 \text{ coating}} - \phi_{2 \text{ coating}})\tag{5.27}$$

$$= R_2(15\phi_{2 \text{ coating}} - \phi_{2 \text{ coating}})\tag{5.28}$$

$$= 14R_2\phi_{\text{coating}}\tag{5.29}$$

$$= R_{28}\phi_{\text{coating}}\tag{5.30}$$

So a fit of $\phi_{30 \text{ coated}} - \phi_{2 \text{ coated}}$ against R_{28} should yield a straight line, gradient ϕ_{coating}

The results of a fit using these results in place of the annealed results is shown in figure 5.25

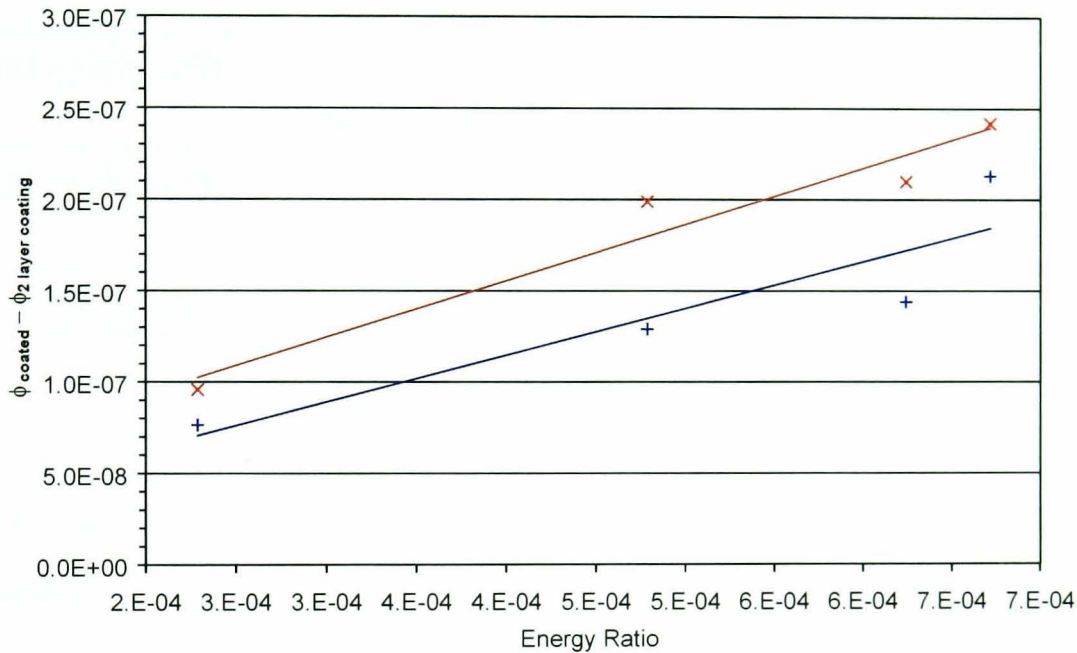


Figure 5.25: Graph of experimental coated loss minus appropriate 2 layer loss against predicted loss using only 4 modes for two 30 layer $\lambda/4, \lambda/4$ coated masses. Again, the blue data set refers to the sample shown in figure 5.19

where $R^2 = 0.95$ for the red data set and $R^2 = 0.82$ for the blue data set. Again, the losses agree within error. This indicates that we are again removing the problem of the substrate. Secondly, it would also appear to confirm our assumption that the loss of the 2 layer coating is the same as that of the 30 layer coating.

5.7.4 Results of Analysis

The losses obtained from the analysis carried out on the silica/tantala coated masses are shown in table 5.6. The column headed $c - a$ indicates that the analysis was carried out with the removal of the (quasi)-annealed mass losses.

The column marked $c - 2$ indicates that the 2 layer coated mass losses.

Coating type	Sample	c-a fit	c-2 fit
30 ($\lambda/4, \lambda/4$)	1	$(2.5 \pm 0.8) \times 10^{-4}$	$(2.6 \pm 0.8) \times 10^{-4}$
	2	$(2.9 \pm 0.7) \times 10^{-4}$	$(3.1 \pm 0.5) \times 10^{-4}$
60 ($\lambda/8, \lambda/8$)	1	$(2.7 \pm 0.5) \times 10^{-4}$	$(2.8 \pm 0.5) \times 10^{-4}$
	2	$(2.5 \pm 1.1) \times 10^{-4}$	$(2.6 \pm 1.1) \times 10^{-4}$
30 ($3\lambda/8, \lambda/8$)	1	$(3.7 \pm 0.4) \times 10^{-4}$	$(3.6 \pm 0.5) \times 10^{-4}$
	2	$(3.8 \pm 0.5) \times 10^{-4}$	$(3.6 \pm 0.5) \times 10^{-4}$
30 ($\lambda/8, 3\lambda/8$)	1	$(1.7 \pm 0.3) \times 10^{-4}$	$(1.7 \pm 0.3) \times 10^{-4}$
	2	$(2.1 \pm 0.2) \times 10^{-4}$	$(2.1 \pm 0.2) \times 10^{-4}$
2 ($\lambda/4, \lambda/4$)	1	$(0.9 \pm 2.8) \times 10^{-4}$	-

Table 5.6: *Results of coating analysis*

For each coating type, the loss used was the lowest loss calculated from the two samples. The reason for this is that it is always possible to measure a loss which is higher than its true value due to additional damping factors present in the experiment. The only way to measure a loss *lower* than its true value, however, is through measurement error.

We may make a number of deductions from these losses. Firstly, compare the 2 layer and 30 layer ($\lambda/4, \lambda/4$) samples. These have losses of $(0.9 \pm 2.8) \times 10^{-4}$ and $(2.5 \pm 0.7) \times 10^{-4}$ respectively. These agree within error. The measured values of loss for the 2 and 30 layer samples (see figure 5.19) suggest that the 2 layer coating has a much smaller effect than the 30 layer coating. So immediately it is implied that it is the coating itself which has the major effect and not, say, the substrate/ coating interface.

Secondly, consider the 30 and 60 layer coatings of the same overall thickness. These have losses of $(2.5 \pm 0.8) \times 10^{-4}$ and $(2.5 \pm 0.7) \times 10^{-4}$ respectively. These are the same, to within error. Hence we may deduce that the intra-coating interfaces are not a significant source of loss.

Thirdly, we have the $3\lambda/8, \lambda/8$ vs $\lambda/4, \lambda/4$ coatings. These yield losses of $(3.7 \pm 0.5) \times 10^{-4}$ and $(2.5 \pm 0.8) \times 10^{-4}$. Recall that the $3\lambda/8, \lambda/8$ coating has 3 times as much tantala as silica. The higher loss shown by the coating which did not have equal amounts of each material therefore indicates that tantala, at least in this coating formulation, has a higher loss than silica.

Finally, we may compare the $\lambda/8, 3\lambda/8$ coatings with the $3\lambda/8, \lambda/8$ and $\lambda/4, \lambda/4$ coatings. Recall that these coatings have the opposite composition to the $3\lambda/8, \lambda/8$ coatings; while the latter had 3 times as much tantala as silica, the $\lambda/8, 3\lambda/8$ coatings have 3 times as much silica. The $\lambda/8, 3\lambda/8$ losses of $(1.7 \pm 0.2) \times 10^{-4}$ agree with the suggestion that tantala has a higher loss than silica.

This trend is repeated if, instead of using the lowest losses the average values are used instead. Furthermore, the findings presented here are corroborated by independent work done at Syracuse University and MIT using much thinner substrates. A joint publication on this work is currently in preparation.

5.7.5 Coating split analysis

Since we now have a number of loss values for different silica/tantala coating compositions we are in a position to evaluate the losses due to each material.

We wish to use the loss due to the total coating to obtain the loss due to each material. To do this we will use the total loss term for the entire front surface coating,

$$\frac{E_{coating}}{E_{substrate}} \Phi_{coating} \quad (5.31)$$

and those of the individual materials which we will define in the same way as;

$$\frac{E_{coating\ layer\ i}}{E_{substrate}} \phi_{coating\ layer\ i} \quad (5.32)$$

where i ranges from 1 to 2. This gives the following relation if we assume that all the loss arises from the intrinsic loss of the constituent materials of the coating:

$$\frac{E_{coating}}{E_{substrate}} \phi_{coating} = \frac{E_{coating\ layer\ 1}}{E_{substrate}} \phi_{coating\ layer\ 1} + \frac{E_{coating\ layer\ 2}}{E_{substrate}} \phi_{coating\ layer\ 2} \quad (5.33)$$

Note immediately that the $E_{substrate}$ term may be cancelled. We may also simplify the $E_{coating}$ terms. These are essentially of the form $E_{coating} = VF$ where V is the volume of the coating and F is the energy density. Recall equation 4.4 for the energy density due to strain:

$$\rho_E = \frac{Y}{2(1+\sigma)} \left(u_{ij}^2 + \left(\frac{\sigma}{1-2\sigma} \right) u_{ll} u_{mm} \right) \quad (5.34)$$

Note that to a first approximation the energy density depends on the Young's modulus of the material times u_{ij}^2 . If we are comparing like modes in each term of equation 5.33 then the u_{ij}^2 term cancels. Finally, since each layer of the coating will have the same surface area as the entire coating, a comparison of volume requires only specification of the thickness t of the layer. Hence it is possible to approximate the term $E_{coating}$ to $Y_{coating} t_{coating}$ when carrying out a comparison such as that we are considering.

Using these approximations we may write the following:

Optical Thickness	Young's Modulus (kg/ms ²)	Thickness (μm)
$\lambda/4, \lambda/4$	1.0×10^{11}	4.7
$3\lambda/8, \lambda/8$	1.2×10^{11}	4.3
$\lambda/8, 3\lambda/8$	8.5×10^{10}	5.1

Table 5.7: Values used in the simultaneous equations involved in the calculation of individual losses due to different coating materials

$$Y_{\text{coating}} t_{\text{coating}} \phi_{\text{coating}} = Y_1 t_1 \phi_1 + Y_2 t_2 \phi_2 \quad (5.35)$$

where Y_1 , t_1 and ϕ_1 refer to the properties of the first coating layer and similarly for Y_2 etc.

Recall that we have loss information for several different coating compositions, in particular one with an equal amount of silica and tantala, one with 3 times as much tantala as silica and one with 3 times as much silica as tantala. We may therefore construct equations as follows:

$$Y_{\text{coating}}^{\lambda/4, \lambda/4} t_{\text{coating}}^{\lambda/4, \lambda/4} \phi_{\text{coating}}^{\lambda/4, \lambda/4} = Y_{\text{silica}} t_{\text{silica}}^{\lambda/4} \phi_{\text{silica}} + Y_{\text{tantala}} t_{\text{tantala}}^{\lambda/4} \phi_{\text{tantala}} \quad (5.36)$$

$$Y_{\text{coating}}^{3\lambda/8, \lambda/8} t_{\text{coating}}^{3\lambda/8, \lambda/8} \phi_{\text{coating}}^{3\lambda/8, \lambda/8} = Y_{\text{silica}} t_{\text{silica}}^{\lambda/8} \phi_{\text{silica}} + Y_{\text{tantala}} t_{\text{tantala}}^{\lambda/8} \phi_{\text{tantala}} \quad (5.37)$$

$$Y_{\text{coating}}^{\lambda/8, 3\lambda/8} t_{\text{coating}}^{\lambda/8, 3\lambda/8} \phi_{\text{coating}}^{\lambda/8, 3\lambda/8} = Y_{\text{silica}} t_{\text{silica}}^{3\lambda/8} \phi_{\text{silica}} + Y_{\text{tantala}} t_{\text{tantala}}^{3\lambda/8} \phi_{\text{tantala}} \quad (5.38)$$

Table 5.7 gives a list of the relevant values for the Young's Modulus and thickness for the different coatings used in these equations. Table 5.8 gives the different (total) thicknesses for silica and tantala depending on the optical thickness of each. Note that the Young's Modulus for silica and tantala are assumed not to change depending on their thickness. $Y_{\text{silica}} = 7.2 \times 10^{10}$ kg/ms² and $Y_{\text{tantala}} = 1.4 \times 10^{11}$ kg/ms².

Using the lowest results for the 30 layer $\lambda/4$ and 30 layer $3\lambda/8, \lambda/8$ coatings.

Material	Optical Thickness	Thickness (μm)
silica	$\lambda/4$	2.8
	$\lambda/8$	1.4
	$3\lambda/8$	4.1
tantala	$\lambda/4$	2.0
	$\lambda/8$	1.0
	$3\lambda/8$	3.0

Table 5.8: *Physical thicknesses associated with different optical thicknesses of silica and tantala coating layers*

equations 5.36 can be solved for the individual losses of silica and tantala to give $\phi_{silica} = (-1.0 \pm 1.7) \times 10^{-4}$ and $\phi_{tantala} = (4.9 \pm 0.5) \times 10^{-4}$. Using the previously obtained loss for an alumina/tantala coating, $(6.3 \pm 1.6) \times 10^{-5}$ (section 5.4.1) we obtain for the loss of an alumina coating of $\phi_{alumina} = (-8 \pm 3) \times 10^{-5}$.

The equivalent coating loss splitting using the $3\lambda/8$ silica $\lambda/8$ tantala coating yields the following losses: $\phi_{silica} = (0.7 \pm 0.1) \times 10^{-4}$ and $\phi_{tantala} = (3.6 \pm 0.2) \times 10^{-4}$, giving a calculated value for the loss of an alumina coating as $\phi_{alumina} = (-4 \pm 2) \times 10^{-5}$.

Finally, solving the simultaneous equations using the $\lambda/8$ silica, $3\lambda/8$ tantala and $3\lambda/8$ silica, $\lambda/8$ tantala coatings gives the following losses: $\phi_{silica} = (0.4 \pm 0.1) \times 10^{-4}$ and $\phi_{tantala} = (4.6 \pm 0.1) \times 10^{-4}$, which results in a calculated value for the loss of an alumina coating as $\phi_{alumina} = (-7 \pm 2) \times 10^{-5}$.

The errors in this section were calculated with the assumption that the errors in the silica and tantala losses were the same in each of the two simultaneous equations. This is not necessarily true, and indeed it is possible that the errors quoted here are too small. Hence to give final values of the losses discussed here we take the mean of the calculated values, using the error calculated from the spread. Table 5.9 gives the values of the different coating losses.

Material	Loss ($\times 10^{-4}$)
silica	0.3 ± 0.6
tantala	4.4 ± 0.5
alumina	-0.6 ± 0.1

Table 5.9: *Mean values of individual coating losses using errors from spread rather than those calculated*

Although the loss determined for the alumina is not a particularly physical result, we can still make some observations using this loss. Firstly, it suggests that the alumina loss is very low. Secondly, it should be noted that we have no information about the tantala loss from the original Wave Precision coating. One possible explanation for the negative alumina loss calculated here is that the tantala loss derived using the current coatings is in fact *higher* than that of the tantala in the original alumina/ tantala coatings. This would imply that the alumina loss calculated here is too low because it is balancing a higher loss due to the tantala than was really the case. However, a more extensive investigation of alumina/tantala coatings is required to make further deductions. The initial stage of this study is presented in the next section.

5.8 Alumina/ Tantala Coatings

The next phase of testing involved using different materials for the coating; this time alumina and tantala as were used in the original coatings on the 10m prototype masses. The choice of alumina was made because it had a similarly low index of refraction to silica and because the earlier work suggested that alumina might have a low loss.

The samples used were the same as those used in the tantala/ silica study. This time, however, the coating work was carried out by MLD[107]. The initial coatings were $\lambda/4\lambda/4$ alumina/ tantala. The overall optical thickness

was the same as the 30 layer silica/ tantala $\lambda/4\lambda/4$ coating, resulting in a 47 layer alumina/ tantala coating, physical thickness $6.8 \mu\text{m}$.

Using the same experimental and analysis techniques as those used previously, the $c - a$ derived loss, averaged over two samples, was $(3.61 \pm 0.01) \times 10^{-4}$. Since there is no equivalent 2 layer coating, there is no $c - 2$ result.

This is an interesting results since it is much higher than the original loss measured on the 10 m prototype masses with a coating of the same composition (although manufactured by a different company, it is likely that a similar process was used). Further studies on this with more coatings from the supplier of the original alumina/tantala coatings (WavePrecision[96]) are underway.

5.9 Conclusions

Following an initial investigation it would appear that there is indeed a mechanical loss due to the dielectric coatings used to turn the silica test masses used in current ground based interferometric detectors into mirrors. A subsequent study, carried out using a significantly greater number of samples, extended this finding to give a potential source for this mechanical loss. The results suggest that the major source of loss due to the dielectric coating is attributable to the intrinsic loss of the individual coating materials. Furthermore, the tests have set limits on the losses of the individual materials used in the coatings. Finally, a second extended investigation has now been initiated which will determine the mechanical losses of coatings using different materials, such as hafnium oxide, niobium oxide and titanium oxide. This study will also allow comparisons to be made between different coating vendors.

Chapter 6

Analysis of Coated Sapphire Substrates

6.1 Introduction

The previous chapter discussed the presence of a mechanical loss mechanism associated with the dielectric mirror coatings used with test masses in interferometric gravitational wave detectors. Such a mechanical loss was shown to exist and an extensive investigation of possible sources of the loss was carried out. However, all the experiments used silica test masses. As was discussed in chapter 1 (section 1.7), the upgrade to LIGO, Advanced LIGO, is likely to use sapphire test masses. This is primarily due to sapphire's lower intrinsic loss.

Hence it would be useful to be able to carry out similar coating investigations on sapphire substrates. A difference is that sapphire is anisotropic; its material properties are not the same in each axial direction and thus conditions at the coating/substrate interface will be different. The anisotropy also affects the analysis; the FEA model and Ocean itself both assume that the substrate and coating are isotropic in their calculations. In particular they both use only the Young's modulus and Poisson's ratio of the substrate/ coating in the energy

calculation

One of the purposes of this chapter is to introduce sapphire as a material and give a summary of its crystal nature and properties. Thereafter the changes to the FEA model and Ocean required to deal with anisotropic materials will be discussed. This will involve the use of a separate FEA analysis package, I-DEAS, and modifications both to the energy calculation section of Ocean and the methods it uses to import data. Finally, the results of an experiment and associated analysis to determine the mechanical loss associated with a coating on a sapphire mass will be presented. However before these topics can be discussed it is necessary to introduce the stiffness tensor.

6.2 The Stiffness Tensor

6.2.1 Hooke's Law & the Stress Tensor

The one dimensional Hooke's Law with τ the stress (force per unit area), c the Young's modulus and u the strain, is defined by[91],

$$\tau = cu \tag{6.1}$$

Recall that in 3 dimensions we have the strain tensor u_{ij} . Equivalently we may define a *stress* tensor, τ_{ij} . Consider a body such as that shown in figure 6.1.

Then we may define the stress as $\tau = \mathbf{F}/\mathbf{S}$ where \mathbf{F} is an applied force and \mathbf{S} is the area over which a force is applied. Then the magnitudes of the individual components of τ will be

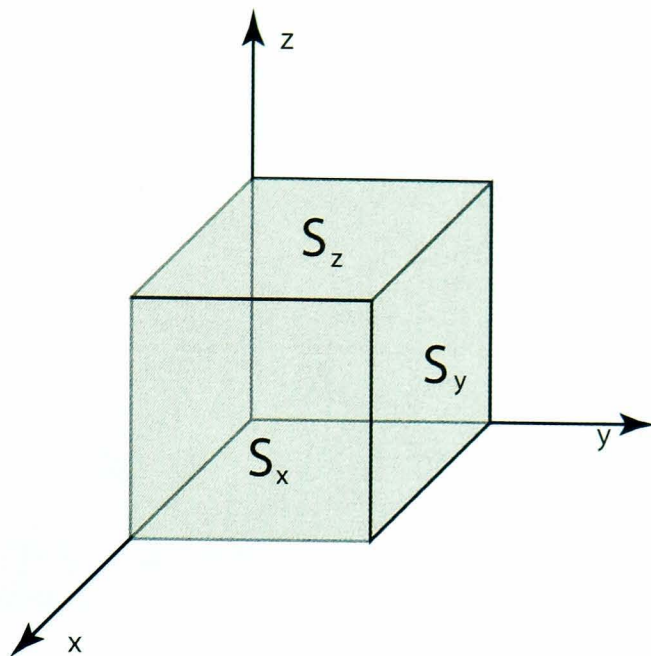


Figure 6.1: A small body which we may use to define the terms of the stress tensor

$$\tau_{ij} = \frac{F_i}{S_j} \quad (6.2)$$

where i and j range over x, y and z , and the *direction* of the surfaces is defined as the normal to each surface. We may make two interesting observations about the stress tensor. The first is that stress is symmetric. Consider the body in figure 6.1 which we will denote as a cube of side l . The torque at the point marked in red around the point marked in green in figure 6.2, which is a view down onto the xy plane of the body, is:

$$T = [\tau_{xy}l^2 - \tau_{yx}l^2] l \quad (6.3)$$

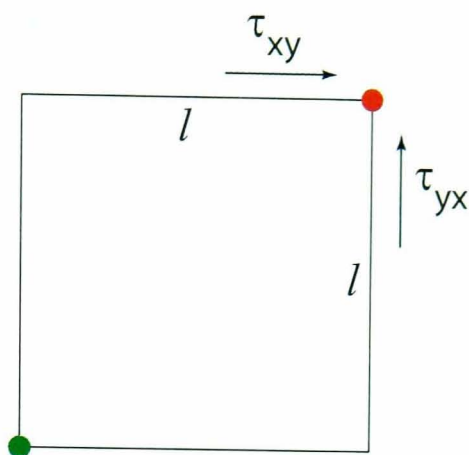


Figure 6.2: View onto the xy plane showing the relevant stress components for the torque as described in the text

Hence, the angular velocity of that point is:

$$\begin{aligned}
 \dot{\omega} &= \frac{T}{I} \\
 &\propto \frac{[\tau_{xy}l^2 - \tau_{yx}l^2] l}{ml^2} \\
 &\propto \frac{[\tau_{xy}l^2 - \tau_{yx}l^2] l}{\rho l^3 l^2} \\
 &\propto \frac{[\tau_{xy} - \tau_{yx}] l^3}{\rho l^5}
 \end{aligned}$$

In order that $\dot{\omega}$ remain finite as $l \rightarrow 0$, $(\tau_{xy} - \tau_{yx}) \propto l^2$ at least. That is, in the limit that $l \rightarrow 0$, $\tau_{xy} = \tau_{yx}$. Or, in other words, the stress tensor is symmetric.

Secondly, we may observe that the stress tensor is continuous. Consider the body in figure 6.1, which we will again define as having length l . This time consider a force F_z following our definition above:

$$F_z = \tau_{zz}(z)S - \tau_{zz}(z+l)S \quad (6.4)$$

Now, the acceleration a_z will be:

$$\begin{aligned}
 a_z &= \frac{F_z}{m} \\
 &= \frac{[\tau_{zz}(z) - \tau_{zz}(z+l)] l^2}{\rho l^3} \\
 &= \frac{\Delta\tau_{zz}}{\rho l}
 \end{aligned} \tag{6.5}$$

where ρ is the density of the material. For a_z to remain finite as $l \rightarrow 0$, we must have that $\Delta\tau_{zz} \propto l$. That is, τ_{zz} is continuous.

6.2.2 The Stiffness Tensor

We may now extend our 1 dimensional version of Hooke's law as follows:

$$\tau_{ij} = c_{ijkl} u_{kl} \tag{6.6}$$

where c_{ijkl} is a fourth order tensor. We would normally expect such an object to have 81 independent components, but both τ and u are symmetric and so c is cyclic, i.e.

$$c_{ijkl} = c_{jkli} = c_{klij} = c_{lijk} \tag{6.7}$$

This means that we instead only have 36 independent components. Thus it is customary to refer to the stiffness tensor using a reduced notation as follows to give a stiffness *matrix* (no longer a tensor as it will not transform as a tensor):

$$c_{ij} = \begin{pmatrix} c_{11} & c_{12} & c_{13} & c_{14} & c_{15} & c_{16} \\ c_{21} & c_{22} & c_{23} & c_{24} & c_{25} & c_{26} \\ c_{31} & c_{32} & c_{33} & c_{34} & c_{35} & c_{36} \\ c_{41} & c_{42} & c_{43} & c_{44} & c_{45} & c_{46} \\ c_{51} & c_{52} & c_{53} & c_{54} & c_{55} & c_{56} \\ c_{61} & c_{62} & c_{63} & c_{64} & c_{65} & c_{66} \end{pmatrix} \quad (6.8)$$

where the following key should be used to translate between the reduced notation and the tensor components:

$$1 \equiv xx \quad (6.9)$$

$$2 \equiv yy \quad (6.10)$$

$$3 \equiv zz \quad (6.11)$$

$$4 \equiv yz \quad (6.12)$$

$$5 \equiv xz \quad (6.13)$$

$$6 \equiv xy \quad (6.14)$$

We will be comparing the energy calculations done using isotropic materials as a consistency check. Hence the stiffness tensor for isotropic materials, in terms of Y the Young's modulus and σ the Poisson's ratio is required. We have the isotropic stiffness tensor in terms of the Lamé coefficients λ and μ [92];

$$c_{ij} = \begin{pmatrix} \lambda + 2\mu & \lambda & \lambda & 0 & 0 & 0 \\ \lambda & \lambda + 2\mu & \lambda & 0 & 0 & 0 \\ \lambda & \lambda & \lambda + 2\mu & 0 & 0 & 0 \\ 0 & 0 & 0 & \mu & 0 & 0 \\ 0 & 0 & 0 & 0 & \mu & 0 \\ 0 & 0 & 0 & 0 & 0 & \mu \end{pmatrix} \quad (6.15)$$

where the relationships between λ , Y , μ and σ are[92];

$$\lambda = -\frac{\sigma Y}{2\sigma^2 + \sigma - 1} \quad (6.16)$$

$$\mu = \frac{1}{2} \frac{Y}{1 + \sigma} \quad (6.17)$$

6.2.3 Stiffness Matrix Rotation

If we have the stiffness tensor (or matrix) for a particular direction of a material, we may well wish to know the stiffness tensor in a different direction.

In general the transformation of a 4th order tensor by a rotation takes the following form:

$$T_{ijkl} = \Lambda_{im}\Lambda_{jn}\Lambda_{ko}\Lambda_{lp}T_{mnop} \quad (6.18)$$

However we have reduced the 4th order stiffness tensor to a matrix. Although in general matrices will not transform as tensors, there is a method which can be used in this instance, developed by W. L. Bond[108]. The stiffness matrix is fully transformed by the expression[109]:

$$\mathbf{c}' = \mathbf{M}\mathbf{c}\widetilde{\mathbf{M}} \quad (6.19)$$

where $\widetilde{\mathbf{M}}$ is the transpose of \mathbf{M} which is in turn defined as:

$$\mathbf{M} = \begin{pmatrix} a_{xx}^2 & a_{xy}^2 & a_{xz}^2 & 2a_{xy}a_{xz} & 2a_{xz}a_{xx} & 2a_{xx}a_{xy} \\ a_{yx}^2 & a_{yy}^2 & a_{yz}^2 & 2a_{yy}a_{yz} & 2a_{yz}a_{yx} & 2a_{yx}a_{yy} \\ a_{zx}^2 & a_{zy}^2 & a_{zz}^2 & 2a_{zy}a_{zz} & 2a_{zz}a_{zx} & 2a_{zx}a_{zy} \\ a_{yx}a_{zx} & a_{yy}a_{zy} & a_{yz}a_{zz} & a_{yy}a_{zz} + a_{yz}a_{zy} & a_{yx}a_{zz} + a_{yz}a_{zx} & a_{yy}a_{zx} + a_{yx}a_{zy} \\ a_{zx}a_{xx} & a_{zy}a_{xy} & a_{zz}a_{xz} & a_{xy}a_{zz} + a_{xz}a_{zy} & a_{xz}a_{zx} + a_{xx}a_{zz} & a_{xx}a_{zy} + a_{xy}a_{zx} \\ a_{xx}a_{yx} & a_{xy}a_{yy} & a_{xz}a_{yz} & a_{xy}a_{yz} + a_{xz}a_{yy} & a_{xz}a_{yx} + a_{xx}a_{yz} & a_{xx}a_{yy} + a_{xy}a_{yx} \end{pmatrix} \quad (6.20)$$

where \mathbf{a} is the transformation tensor use to transform from the first axis to the second; in general to transform between two sets of 3 dimensional cartesian co-ordinates by rotation \mathbf{a} would be:

$$\mathbf{a} = \begin{pmatrix} \cos(x'x) & \cos(x'y) & \cos(x'z) \\ \cos(y'x) & \cos(y'y) & \cos(y'z) \\ \cos(z'x) & \cos(z'y) & \cos(z'z) \end{pmatrix} \quad (6.21)$$

where, for example, $x'x$ is the angle between the rotated x axis and the original x axis. This technique will be important if the sample of sapphire in use is not grown along the c axis, which is the main symmetry axis (as is indeed the case here; see section 6.7).

6.2.4 Full Energy Description

The most general form of the energy density in a body due to a deformation will be[92]:

$$\begin{aligned}\rho_E &= \frac{1}{2}\tau_{ij}u_{ij} \\ &= \frac{1}{2}c_{ijkl}u_{kl}u_{ij}\end{aligned}\tag{6.22}$$

It is this form of the energy that we will use in a modified, anisotropic version of Ocean.

6.3 Sapphire

6.3.1 Crystal Nature

Sapphire has a hexagonal (rhombohedral) crystallographic system and hence has 3-fold symmetry. It has three crystallographic axes, the c , m and a axes. A diagram showing these axes is shown in figure 6.3.

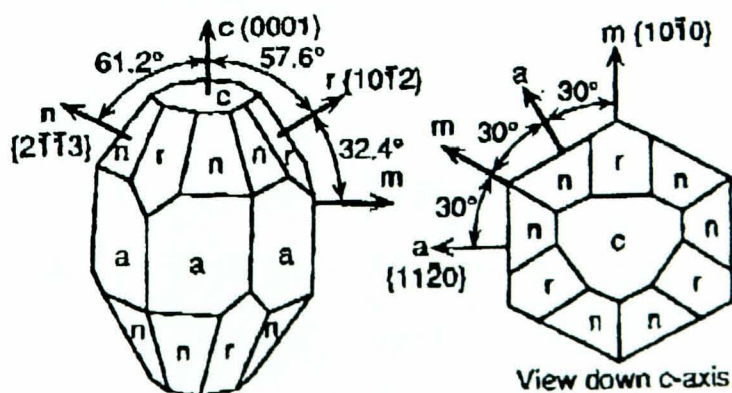


Figure 6.3: *Diagram of crystal axes of sapphire[3]*

Sapphire is *trigonal* (a crystal class which is a subset of the hexagonal class)

and has the following form for the stiffness matrix (this refers to the c -axis properties by convention);

$$c_{ij} = \begin{pmatrix} c_{11} & c_{12} & c_{13} & c_{14} & 0 & 0 \\ c_{12} & c_{11} & c_{13} & -c_{14} & 0 & 0 \\ c_{13} & c_{13} & c_{33} & 0 & c_{35} & 0 \\ c_{14} & -c_{14} & 0 & c_{44} & c_{45} & 0 \\ 0 & 0 & 0 & 0 & c_{44} & c_{14} \\ 0 & 0 & 0 & 0 & c_{14} & \frac{1}{2}(c_{11} - c_{12}) \end{pmatrix} \quad (6.23)$$

6.3.2 Conversion from c - to m - axis

An important application of the transformation technique discussed in section 6.2.3 is the conversion between sapphire c -axis coefficients (those normally quoted in literature) and m - or a - axis coefficients. In this case we shall transform between the c - and m - axis co-ordinates. If we consider a 3 dimensional set of cartesian axes, then the c -axis would lie along the z axis while the m axis would lie along the y axis. Thus, the transformation from c - to m - axis involves a rotation of the co-ordinates 90° clockwise around the x axis. Thus \mathbf{a} is formed as follows, using equation 6.21;

$$\mathbf{a} = \begin{pmatrix} \cos(0) & \cos(90) & \cos(90) \\ \cos(90) & \cos(90) & \cos(180) \\ \cos(90) & \cos(0) & \cos(90) \end{pmatrix} \quad (6.24)$$

$$= \begin{pmatrix} 1 & 0 & 0 \\ 0 & 0 & -1 \\ 0 & 1 & 0 \end{pmatrix} \quad (6.25)$$

This will in turn yield an \mathbf{M} of the following form;

$$\mathbf{M} = \begin{pmatrix} 1 & 0 & 0 & 0 & 0 & 0 \\ 0 & 0 & 1 & 0 & 0 & 0 \\ 0 & 1 & 0 & 0 & 0 & 0 \\ 0 & 0 & 0 & -1 & 0 & 0 \\ 0 & 0 & 0 & 0 & 0 & 1 \\ 0 & 0 & 0 & 0 & -1 & 0 \end{pmatrix} \quad (6.26)$$

The final stage in the conversion is to use equation 6.19 to calculate the new properties.

6.3.3 Manufacture

Small samples of sapphire may be grown using the horizontal oriented crystallisation method [55]. However for larger samples, for example those required for future gravitational wave detectors, the Heat Exchanger Method (HEM)[110] is required. This process was pioneered by Crystal Systems Inc.[111]. In this method the entire crystal is annealed as part of the growth process and so the defect density is reduced.

6.4 I-DEAS

Algor has a limitation that it will not perform a natural frequency analysis on a fully anisotropic material (at least not in the same manner as for isotropic materials). Thus a second option is required. The new package that was chosen was *I-DEAS*[112]. This was because of availability and experience, gained after the acquisition of Algor and its use in the isotropic case.

There were necessarily complications involved with employing a further FEA package when Ocean had already been written to work with the output from Algor. The most important problem was to ensure that I-DEAS could perform the same calculation as Algor and give the same result. The second problem arises from the fact that Ocean uses the specific mesh pattern used in Algor (which will be referred to as a *radial* mesh from now on; see figure 4.6 for an example of this type of mesh). The default mesh pattern used by I-DEAS, however, is *tetrahedral* as shown in figure 6.4. Note that in this and the other screenshots of I-DEAS the colours have been reversed for clarity; normally I-DEAS has a black background. This raises a question - is it better to adapt Ocean to use a tetrahedral mesh, or discover a method to create a radial mesh in I-DEAS? There is naturally no correct or incorrect answer; clearly either would be sufficient.

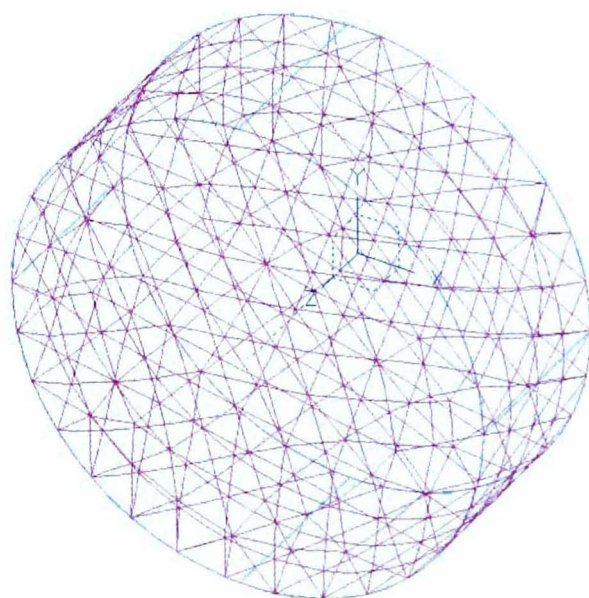


Figure 6.4: *Tetrahedral mesh as used in I-DEAS*

However, adapting Ocean would involve potentially changing the calculation scheme which is, as was seen in chapter 4, intimately tied to the radial mesh scheme. A possible route might be to take in an arbitrary mesh (tetrahedral for example) and then interpolate to a radial mesh. This would allow any possible

mesh configuration to be used while still maintaining the radial calculation engine used in Ocean.

The method of using I-DEAS to create a radial mesh was the one which was chosen. The reason for this was that it was more efficient given the time constraints to create a specific mesh pattern in I-DEAS than to allow Ocean to read any possible mesh. The interpolation scheme is however on the list of future alterations to Ocean; the intention is to allow Ocean to work with any suitable program with the minimum of compatibility problems. Removing the radial mesh dependency is a key stage in this upgrade process.

6.4.1 I-DEAS Radial Mesh Construction

The method of construction of the radially meshed cylinder in I-DEAS is slightly different to that used in Algor. Essentially the steps are to first create a rectangle of length the radius of the cylinder and height the height of the cylinder (figure 6.5).

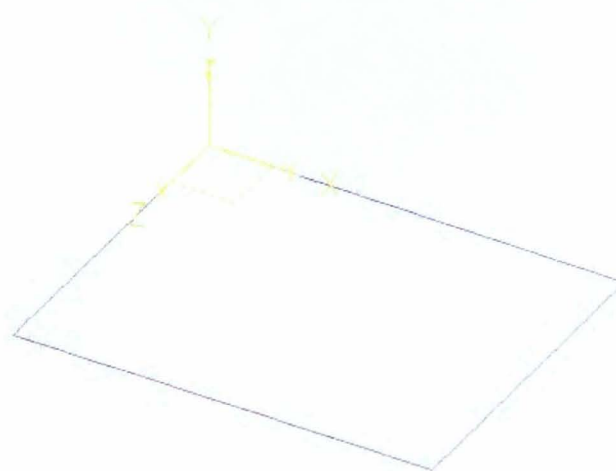


Figure 6.5: *Initial stage of radial meshing in I-DEAS*

Next this is meshed (figure 6.6) and rotated around the z axis to make the

completed cylinder; see figure 6.7.

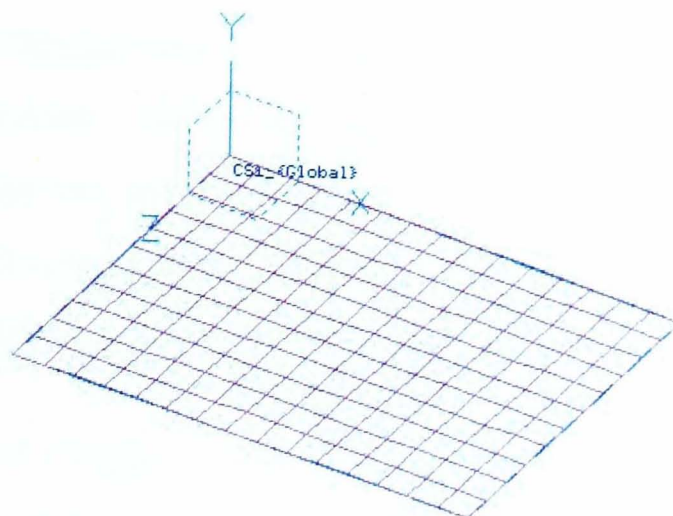


Figure 6.6: *Meshed rectangle*

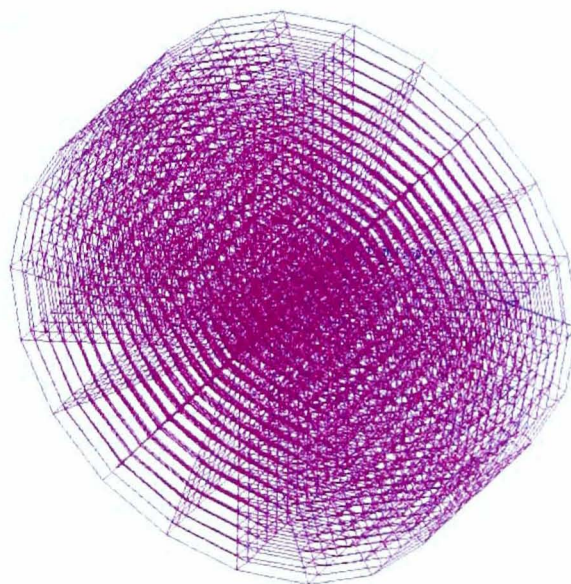


Figure 6.7: *Final radial mesh in I-DEAS*

Note that although the cylinder here appears to be oriented at ninety degrees to that in Algor they do in fact have the same orientation. This would not be a problem in any case using isotropic materials; it is very relevant when using anisotropic materials however.

6.5 Necessary Changes to Ocean

In this section the changes made to Ocean to take account of the anisotropic models will be discussed. There are essentially 3 changes to be made; Ocean must be able to read the full stiffness matrix material properties, it must be able to read I-DEAS output files, and it must be able to use the stiffness matrix properties to correctly calculate the strain energies.

To illustrate the first change, a sample .ini file is given below. Note that the Anisotropic version of Ocean is called Aocean; the isotropic and anisotropic versions currently reside in separate programs, although a combined version is currently being tested.

```
model_name sapp_296.unv
mode_number 1
coating_thickness 5.11E-06
barrel_thickness 5.11E-06

substrate_properties c11 4.89E+11 c12 1.12E+11 c13 1.57E+11 c14
2.31E+10 ... c64 0.00E+00 c65 -2.31E+10 c66 1.45E+11 ]

coating_properties
c11 1.12E+11
c12 2.86E+10
c13 2.86E+10
...
c64 0.00E+00
c65 0.00E+00
c66 4.17E+10
]

barrel_properties
c11 1.12E+11
c12 2.86E+10
c13 2.86E+10
...
c64 0.00E+00
```

```
c65 0.00E+00
c66 4.17E+10
]
```

```
barrel_extent -1
surface_locn 0
append 1
mode_print 1
```

The dots indicate the remainder of the stiffness matrix components. In reality, only the non-zero components need be specified as all components are set to zero by default. The changes to the original .ini file are fairly self evident; the major change apart from the fully specified properties is the range of file types the program will take. Previously, Ocean would only accept .ml data files, i.e. those from Algor. Now, however, Aocean will accept .ml files from Algor or (slightly modified) .unv files from I-DEAS. Aocean uses the file extension to decide which file type is in use and thus changes its file reading routines accordingly. The .unv files from I-DEAS are similar to those of the .ml files of Algor but some pre-processing is required, essentially to remove extraneous data and add the textual switches Aocean uses to locate nodal and modal data. The source code for Aocean is given in appendix F.

Aocean takes the stiffness matrix properties provided by the .ini file and converts them to the stiffness tensor form; although this represents a duplication of information, it allows the energy calculation to be performed in the simplest way. The actual energy calculation involves the summation of the energy density given in equation 6.22 and its consequent integration in the same way as for the isotropic case. It can be seen from this that the anisotropic method is in fact somewhat more powerful than the isotropic method and has greater scope for detailed evaluation of strain component contributions to the energy. However for a study of that nature to be carried out a large number of modes would be required.

6.6 Testing of Aocean & I-DEAS Models

As with the original version of Ocean, it is a very important stage to test both model production using I-DEAS and the energy ratios calculated using Aocean. This testing will take the steps shown in table 6.1, with explanation of what is achieved in each case to form a logical progression from the tested output of Algor/ Ocean to the untested output of I-DEAS/ Aocean. The section in which each test is carried out is given at the left hand side. The term “Full” under the heading “Material Description” indicates that the full stiffness matrix was used (thus allowing anisotropy while not excluding isotropy) as opposed to the Young’s modulus and Poisson’s ratio.

Section	Purpose	Program	Material Description
6.6.1	Algor isotropic behaviour known; link to equivalent I-DEAS behaviour	Algor	Isotropic
		I-DEAS	Full
6.6.2	FEA models now believed, need to check that the new energy calculations also behave correctly	Algor/Ocean	Isotropic
		I-DEAS/Aocean	Full

Table 6.1: *Stages of verification of I-DEAS derived energy ratios*

6.6.1 Comparison of Algor (Isotropic) and I-DEAS (Full) Models

A radial model of a fused silica cylinder with dimensions 7.62cm diameter by 2.54cm height was constructed in Algor and I-DEAS to compare the frequencies they yielded. The modes used in the extended silica mass investigation (section 5.7) were used for the comparison. The results are shown in table 6.2. The value of Young’s modulus that was used in the Algor model was $Y = 7.2 \times 10^{10}$ kg/ms² and the Poisson’s ratio was $\sigma = 0.17$. The number of nodes used in

Algor (Hz)	I-DEAS (Hz)
Frequencies	Frequencies
20008	20028
28339	28621
47359	47367
72628	73294

Table 6.2: *Comparison of Algor and I-DEAS FEA models*

the Algor model was 10897.

The same mass was modelled in I-DEAS using the full description of isotropic silica. The properties used were calculated using equation 6.15 and are given below (all values have units 10^{10} kg/ms²):

$$\mathbf{c} = \begin{pmatrix} 7.74 & 1.59 & 1.59 & 0 & 0 & 0 \\ 1.59 & 7.74 & 1.59 & 0 & 0 & 0 \\ 1.59 & 1.59 & 7.74 & 0 & 0 & 0 \\ 0 & 0 & 0 & 3.08 & 0 & 0 \\ 0 & 0 & 0 & 0 & 3.08 & 0 \\ 0 & 0 & 0 & 0 & 0 & 3.08 \end{pmatrix} \quad (6.27)$$

The number of nodes used in the I-DEAS model was 10320.

The results are shown in table 6.2.

We can see that Algor and I-DEAS do in fact identify the same modes at equivalent frequencies. The slight differences can be accounted for by the slightly different number of nodes and the slight numerical differences in the material properties caused by the different description method used in each

Algor Iso	I-DEAS Full
Ratio	Ratio
1.43×10^{-4}	1.46×10^{-4}

Table 6.3: *Comparison of Algor and I-DEAS generated energy ratios*

case.

6.6.2 Comparison of Algor Energy Ratios (Isotropic) and I-DEAS Energy Ratios (Full)

Finally the isotropic description Algor model was used to generate the energy ratio for the clover 4 mode of a silica cylinder 0.0254 m in height and 0.0381 m radius (essentially the same as mode “i” in appendix D). The I-DEAS full description model was then used to calculate the same ratios. The coating modelled was a 1 μm thick sample of quarter wave silica/ tantalum pentoxide. This has a Young’s modulus of 1.0×10^{11} kg/ms² and a Poisson’s ratio of 0.2. The equivalent stiffness matrix is shown below (units are 10^{11} kg/m²),

$$\mathbf{c} = \begin{pmatrix} 1.12 & 0.29 & 0.29 & 0 & 0 & 0 \\ 0.29 & 1.12 & 0.29 & 0 & 0 & 0 \\ 0.29 & 0.29 & 1.12 & 0 & 0 & 0 \\ 0 & 0 & 0 & 0.42 & 0 & 0 \\ 0 & 0 & 0 & 0 & 0.42 & 0 \\ 0 & 0 & 0 & 0 & 0 & 0.42 \end{pmatrix} \quad (6.28)$$

The result is shown in table 6.3

These are the same to within $\sim 2\%$, which means that we can believe that the

Algor and I-DEAS models with different methods of material description are in fact performing the same calculation adequately.

6.7 Loss Measurement of a Coated M -axis Sapphire Sample

The theory used to describe material properties has now been described, along with the changes necessary to calculate the natural modes and energy ratios of materials with anisotropic properties. The programs used to perform these calculations have now been tested. We are now in a position to use these calculations to measure the coating loss on a sapphire sample with a dielectric coating. The sample used was made by Crystal Systems[111]. It was grown along the m -axis and had a diameter of 0.0762 m. It had a wedge on one surface, giving a height at one end of the wedge of 0.0290 m and at the other 0.0302 m. The sample was coated by Wave Precision with 39 quarter wave layers of alternating silica and tantalum pentoxide layers.

6.7.1 Experimental Losses

The experimental losses of 5 modes were measured in the same manner as that used in chapter 5. The losses found are shown in table 6.4

6.7.2 Analysis

The c axis stiffness matrix for sapphire was taken from [113], as suggested by Crystal Systems. The m -axis properties derived using the method in section

Mode Number	Frequency (Hz)	Uncoated measured loss $\times 10^{-8}$	Coated measured loss $\times 10^{-8}$
1	35679	3.47 ± 0.08	8.33 ± 0.07
2	54855	4.52 ± 0.08	15.02 ± 0.22
3	68629	11.14 ± 0.20	13.81 ± 0.44
4	82987	1.91 ± 0.04	6.41 ± 0.08
5	87275	3.65 ± 0.11	9.43 ± 0.18

Table 6.4: *Experimental losses measured on m-axis sapphire sample*

6.3.2 are shown below (all values are in units 10^{11} kg/ms²):

$$\mathbf{c}_{\mathbf{m-axis}} = \begin{pmatrix} 4.9730 & 1.1600 & 1.6280 & 0.2190 & 0 & 0 \\ 1.1600 & 5.0090 & 1.1600 & 0 & 0 & 0 \\ 1.6280 & 1.1600 & 4.9730 & -0.2190 & 0 & 0 \\ 0.2190 & 0 & -0.2190 & 1.4680 & 0 & 0 \\ 0 & 0 & 0 & 0 & 1.6725 & 0.2190 \\ 0 & 0 & 0 & 0 & 0.2190 & 1.4680 \end{pmatrix} \quad (6.29)$$

The major difficulty with this sample was mode identification. The first, second and fourth modes agree reasonably well with experiment. However, the third and fifth modes proved more difficult. The ratios and frequencies for all modes up to 95kHz are shown in table 6.5; the barrel ratios assume a coating over the entire barrel as before. These were created using an I-DEAS model with 18020 nodes.

The next problem is to identify the modes correctly. In this case the direct drive experiment could not be used since it would be too harsh on the sample. The identification is straightforward for the first two modes: the frequencies of these

Mode number	Measured Mode	Measured (Hz) Frequency	Modelled (Hz) Frequency	Front surface Energy ratio	Barrel Energy ratio
i	1	35679	35201	1.19E-04	2.26E-05
ii	2	54855	55209	1.00E-04	8.42E-06
iii	3	68629	67324	1.02E-04	3.80E-05
iv	3		68289	1.00E-04	3.85E-05
v	3		68423	3.67E-05	2.37E-06
vi	3		68818	4.03E-05	3.50E-05
vii	3		73467	4.10E-05	3.16E-05
viii	4	82987	86021	3.24E-05	1.08E-05
ix	5	87275	89186	7.13E-05	5.78E-06

Table 6.5: *Mode candidates for m axis sapphire sample. Modeshapes are given in appendix D*

comply with the first two experimental modes reasonably well. The last two modes are also identifiable; the second last mode is likely to be the fundamental mode because the experimentally determined loss results indicate that it has a low loss and a strong signal, which might be expected of a fundamental mode[106]. Also the last mode is the only mode with a frequency in the region of the last experimental mode.

This leaves two difficulties. The first is that the frequency agreement between the measured and modelled modes is not uniformly good. Of the modes already “identified”, the modelled frequency lies within 1 kHz of the measured frequency except for the fundamental which appears to lie up to 3 kHz from its measured value. However the experimental evidence would suggest that this identification was good. Hence, one might believe that the material properties were slightly different from those used to make the model. The second difficulty is the range of possible candidates for the third mode.

Hence calculations were carried out to discover whether it were possible to match the frequencies of the first, second and fundamental modes by altering the stiffness matrix slightly, and then use the results from this to determine whether the choice of candidate for the third mode became easier.

However, these models did not prove fruitful. Essentially it proved impossible to fit all three modes within the time devoted to the study. Recall that there are 6 independent stiffness coefficients. It is not a priori clear how any one of these affects any one of the modes. Hence an element of trial and error is required to ascertain whether a better fit can be obtained. This is an extremely difficult task, made more difficult by the length of time taken to run any one model.

Hence this element of the investigation was delayed until, perhaps, actual measurements of the material properties could be made from this sample.

Thus finally it was decided to accept the mode identifications of the first, second, fourth and last modes and then use the regression analysis to decide which mode candidate to use for the third mode.

6.7.3 Regression

Regression analysis was used to fit the losses of the coated sapphire mass to the front surface ratios and the barrel ratios. As in chapter 5, if all 5 modes are used the fits were not good, with values of R^2 less than 0.5.

However, if in each case the first mode was removed, two fits emerged which were good, with R^2 greater than 0.9

The first was a fit using the first or second candidates for the third experimental

mode, with front surface ratios only. The fit curve is shown in 6.8. The R^2 value is 0.94. This gives a coating loss of $(9.5 \pm 3.0) \times 10^{-4}$.

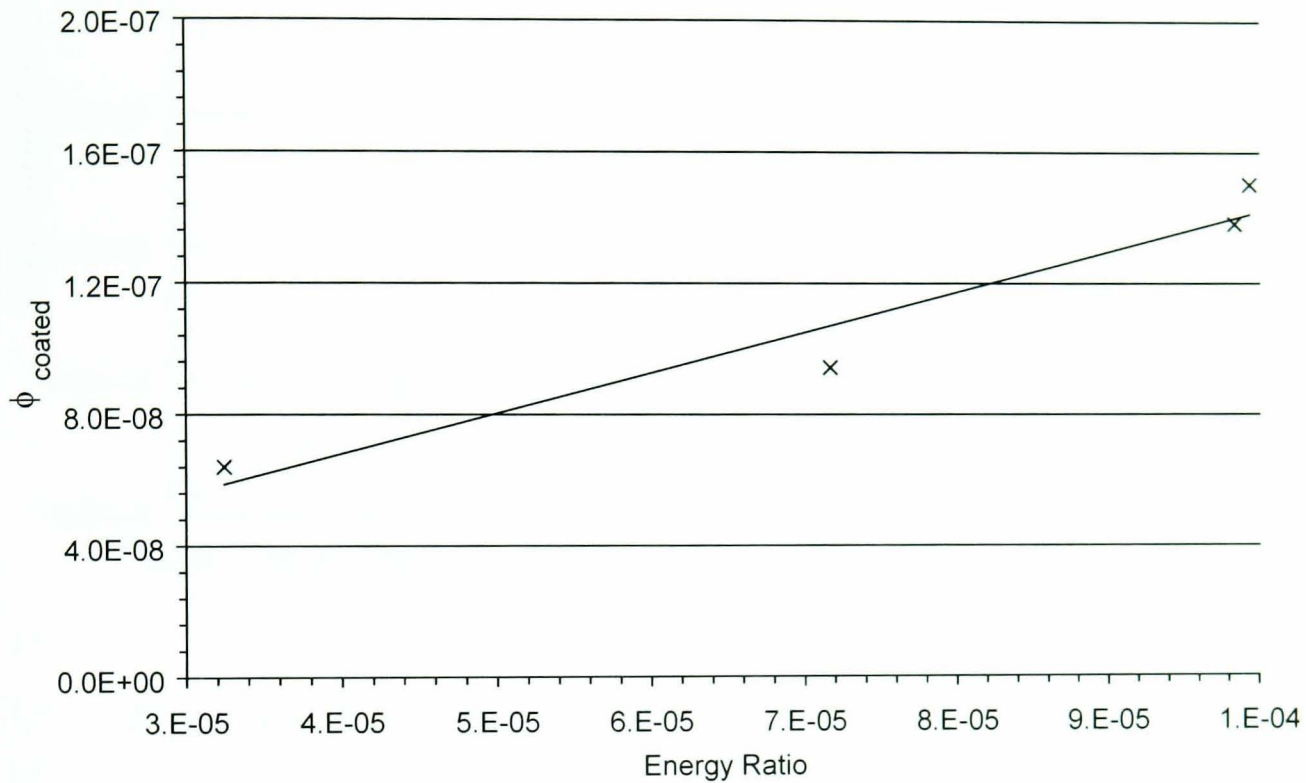


Figure 6.8: *Fit of experimental coated loss against energy ratio*

The reason that the fit can use either the first or second candidates is that these are in fact split modes; the same modeshape but rotated 90° .

The second working fit uses the third/ fourth candidates (again, these are split modes) and *both* the front surface ratios and the barrel ratios. The fit is shown in figure 6.9. The R^2 value is 0.99 and the coating loss was found to be $1.1 \pm 0.1 \times 10^{-3}$

It thus remains to decide which of these fits is the correct one. There are two aspects to this decision; statistical and physical. The statistical decision would be to choose the first; you might have more confidence in a fit using 2 parameters (intrinsic loss and coating loss) and 4 modes than you would in one using 4 modes and 3 parameters. This, however, assumes a zero barrel loss. On closer inspection of the sapphire mass it became clear that there was a

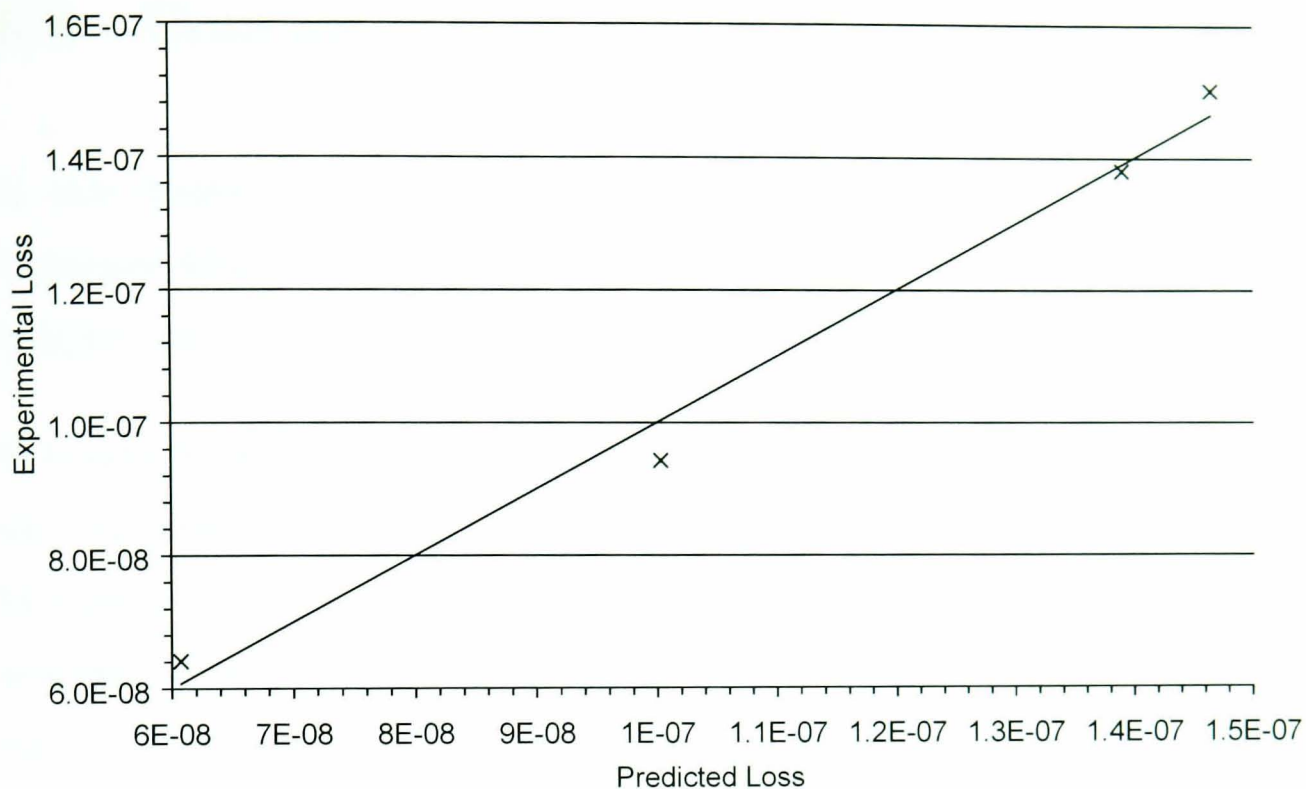


Figure 6.9: *Fit of experimental coated loss against energy ratio*

significant level of coating on the barrel; hence according to the investigations made thus far the barrel loss should certainly not be zero.

Hence the physical aspect overrules any decision made on statistical grounds: if the physical reality does not match the model, then the model must be changed. Accordingly, we may now state the coating loss due to a dielectric coating on a sapphire mass to be at a level of $1.1 \pm 0.1 \times 10^{-3}$. Although this is high compared to the losses mentioned in chapter 5, it should be considered as an upper limit on the coating loss on a sapphire substrate. Further work is required in this area and a more comprehensive study, similar to that carried out for the silica samples, is currently in the planning stages.

6.8 Conclusions

In this chapter we have developed an extension to the strain energy ratio technique which allows it to be used with anisotropic materials. The first analysis using this technique has been completed successfully.

New samples will allow further work to be carried out in this area. In particular, samples without coating on the barrel would allow a simpler analysis to be used such as that employed in the latter sections of chapter 5. A similar program of different coating compositions/ material construction as initiated with the work in chapter 5 would also give further definition to the differences between the use of silica and sapphire as a test mass substrate. For example, it may be the case that the substrate/coating interface may be more significant in the sapphire test mass case.

Throughout this study coatings have been treated as being isotropic. This may well not be the case. The new version of Ocean provides an analytical framework for an investigation of anisotropic coatings to be carried out. In parallel with this, a study of the crystal and phase nature of the applied coatings would provide useful insight now that a phenomenological study of their contribution to the excess loss of their substrates has been carried out.

Chapter 7

Conclusions

One of the most important limits to sensitivity in current interferometric gravitational wave detectors is thermal noise. Hence investigations into its nature are very important. One aspect of this investigation is the determination of the contribution to the total level of thermal noise of the dielectric coatings used on the faces of the test masses used in current detectors as mirrors.

This study requires both experimental work and considerable analytical effort. This thesis gives an account of the preliminary and extended studies carried out to establish the presence of a mechanical loss factor associated with the dielectric coatings and to subsequently determine its source. Emphasis is given to the analytical work involved which forms the majority of the thesis.

The initial findings of the investigation using silica substrates with alumina/tantala coatings were that the coatings do present a source of excess loss which will be important in the design of upgraded interferometric detectors such as Advanced LIGO. The extended study of silica/ tantala coatings, also using silica substrates, suggested that the principal source of the excess loss was

the intrinsic loss of the coating materials. In addition, tantala was found to have a higher loss than silica, at least for the coatings used. The initial stage of an investigation into different coating materials was presented which gave interesting results for an alumina/ tantala coatings which suggested that the coatings tested had a higher loss than the coatings used in the first study, which used the same materials. Further samples of coatings of this type are currently under investigation.

Finally, as might have been expected, preliminary results using a sapphire substrate suggest a similar damping effect in the coating as that noticed using silica substrates. The loss of a coating using the same materials as those used in the extended silica investigation, silica and tantala, was found to be significantly higher than in the silica case. However this should be best regarded as an upper limit to the loss. Perhaps more importantly, the sapphire investigation has confirmed the ability of the analytical framework used, which is now fully capable of dealing with both substrates and coatings which are either isotropic or anisotropic.

The work in this thesis has provided a complete analytical framework suitable for the investigation of mechanical losses associated with a variety of coatings and substrates. Considerable work in this area lies in the future. For example, coatings from different vendors with different materials in the layers will be tested in the near future. In addition, coatings on sapphire substrates, important for Advanced LIGO, may now be fully analysed; a careful investigation of these has been planned and will be carried out in the next months.

Appendix A

Low Suspension Loss Measurement

Recall that a technique is required to measure the loss associated with a test mass. This method must be capable of measuring this loss without the presence of excess loss such as that due to the suspension system. Such a technique will be presented here. The work done to devise this technique in its current form is given in [114].

Initially, consider a mass which has been excited to one of its natural resonances by some means. When the excitation is removed, the amplitude decay of a point in the mass will be given by[63];

$$A(t) = x_0 e^{-\frac{1}{2}\phi_{total}(\omega_0)\omega_0 t} \quad (\text{A.1})$$

If the time taken for the amplitude of the excitation to fall to a level $A(t) = x_0/c$ is measured (the relaxation time, τ), this reduces to:

$$\phi_{total}(\omega_0) = \frac{2}{\omega_0\tau} \quad (\text{A.2})$$

We may rearrange equation A.1 to give the following:

$$\phi_{total}(\omega_0) = \frac{2 \ln(x_0/A(t))}{\omega_0 t} \quad (\text{A.3})$$

This may in turn be expressed in terms of $A(t)$ and t , the observed variables in this experiment:

$$\ln(A(t)) = -\frac{\phi_{total}(\omega_0)\omega_0}{2}t + \ln(x_0) \quad (\text{A.4})$$

which in turn gives the loss at the resonant mode from the gradient of a graph of $\ln(A(t))$ against t . This may then be repeated for all resonant modes desired.

A.1 Experimental Setup

The experimental setup used is shown in figure A.1. The mass is suspended by a wire or silk loop from a clamp to provide isolation from external noise sources. The helium neon laser interferometer is locked to the low frequency pendulum motion of the suspension by using the piezoelectric transducer on which the mirror for the reference arm of the interferometer is mounted. The signal from the interferometer is fed through a lock-in amplifier which beats the high frequency displacement signal down to a level suitable for the data acquisition system. The vacuum tank is evacuated to the 10^{-5} mb level. The electrostatic drive plate is a comb of wire, mounted off the central axis of the

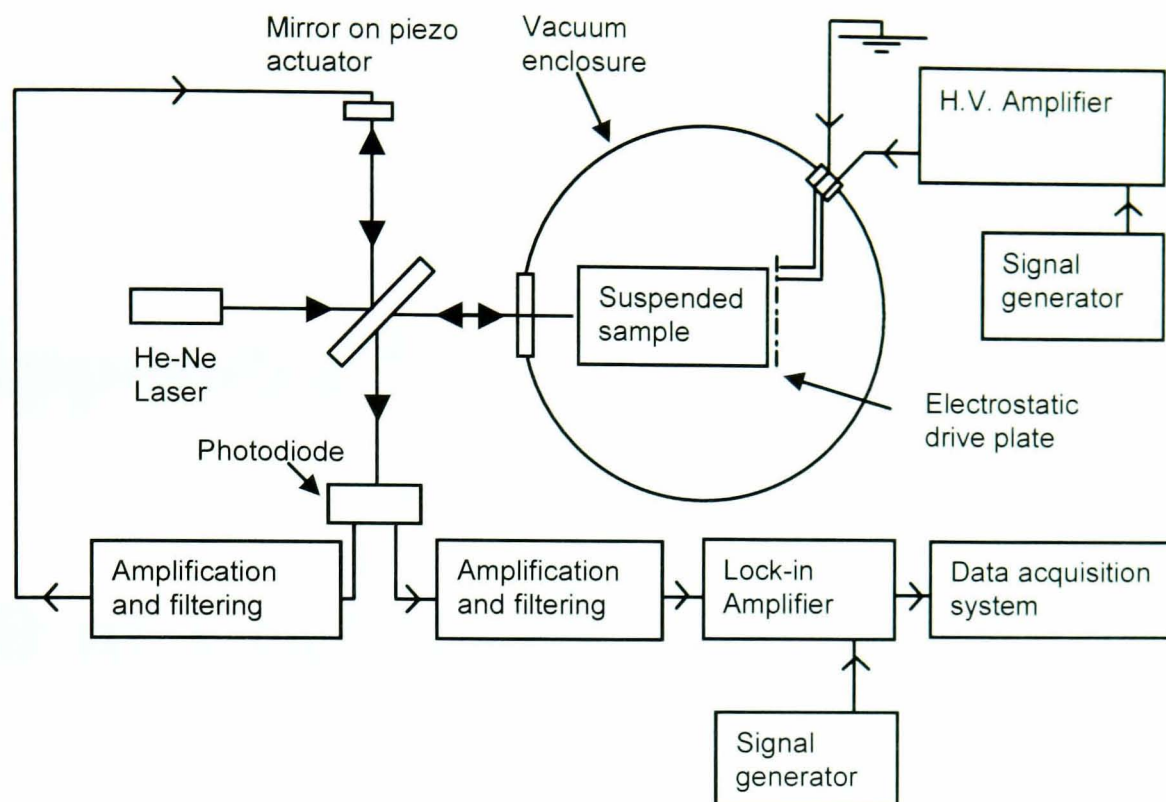


Figure A.1: *Experimental arrangement used to measure the loss factors of suspended test masses*

mass to increase the effectiveness of the drive in exciting as many modes as possible.

For each mass, the loss measurements are repeated a number of times. On each occasion, small adjustments are made to the experimental setup. In particular, the length of the suspension loop is altered, to remove the possibility of a coupling between the resonance of the mass and a resonance of the suspension loop. In addition, various different loop materials may be employed, for example polished tungsten wire or silk. Animal based grease is also used to polish the suspension loop. This is to minimise frictional effects which may be present between the mass and the suspension wire.

The loss taken for each mode of each mass is taken to be the lowest measured over a number of suspensions. Thus the measurement of losses takes a considerable period to ensure that the best results are obtained.

Appendix B

10 m Prototype Modeshapes

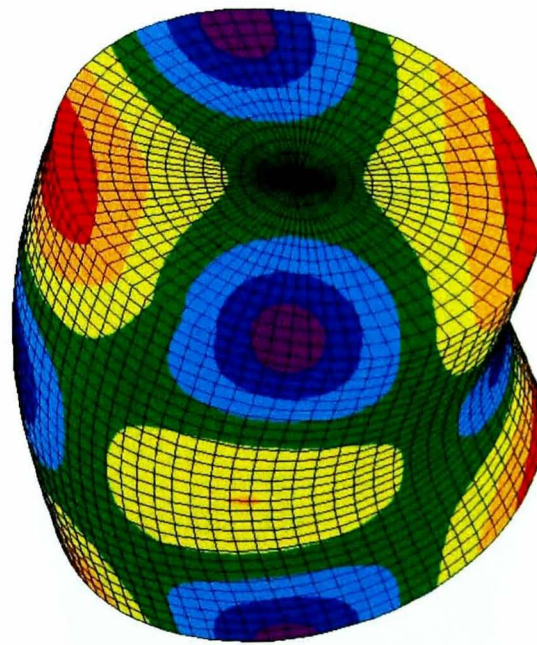


Figure B.1: *“Bending” mode*

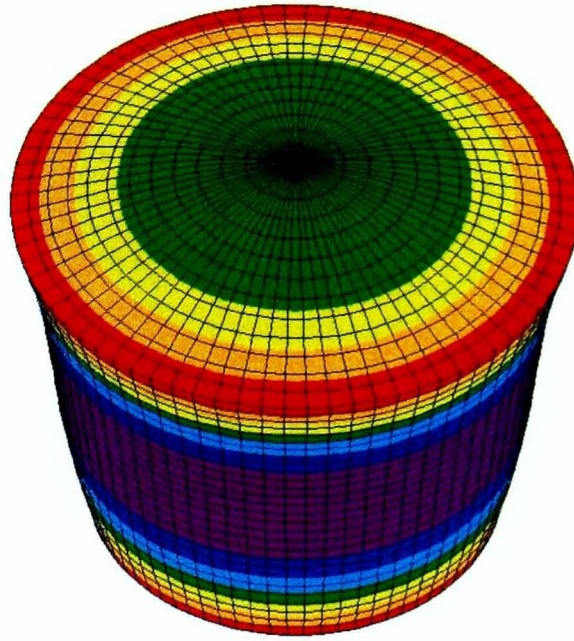


Figure B.2: *“Asymmetric Drum” mode*

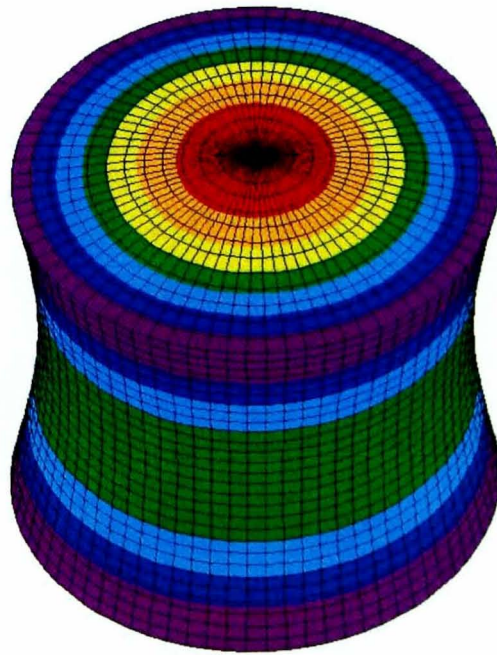


Figure B.3: *“Fundamental” mode*

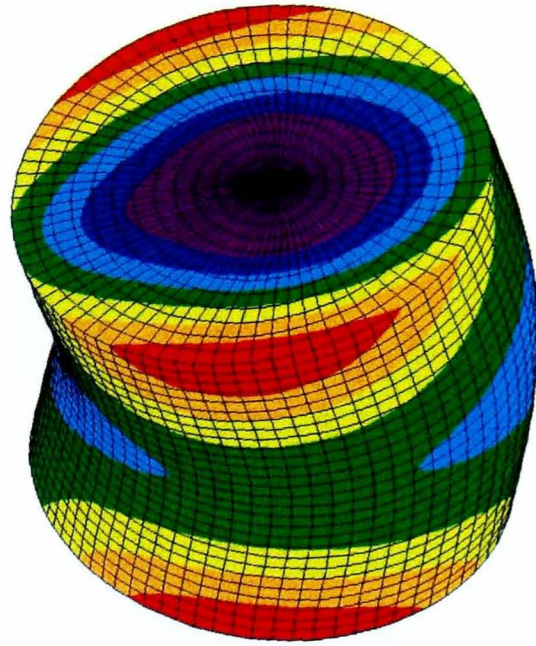


Figure B.4: "Bar" mode

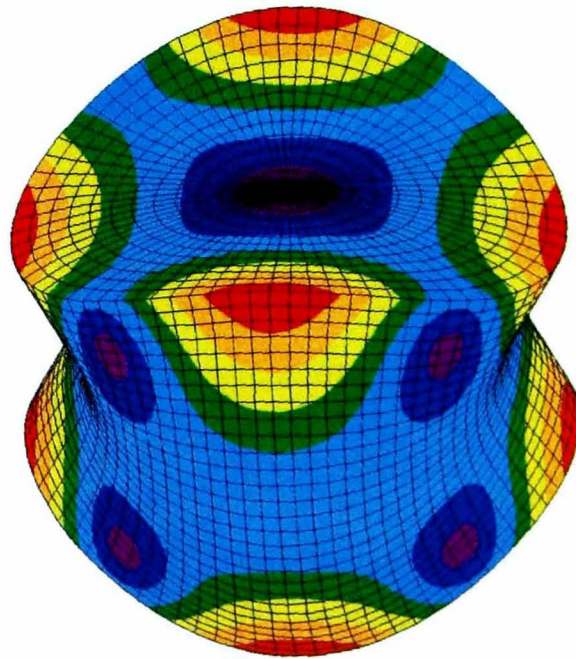


Figure B.5: "Clover-4" mode

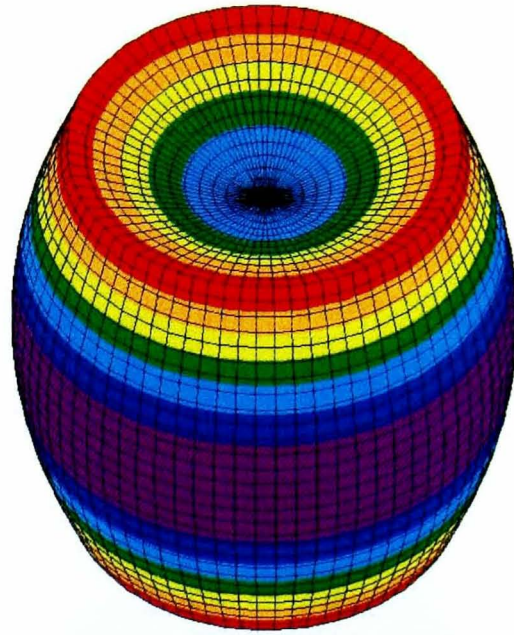


Figure B.6: *“Symmetric Drum” mode*

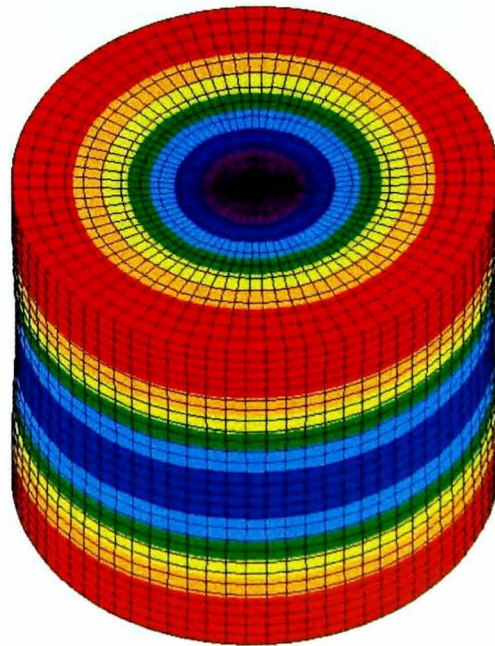


Figure B.7: *“Expansion” mode*

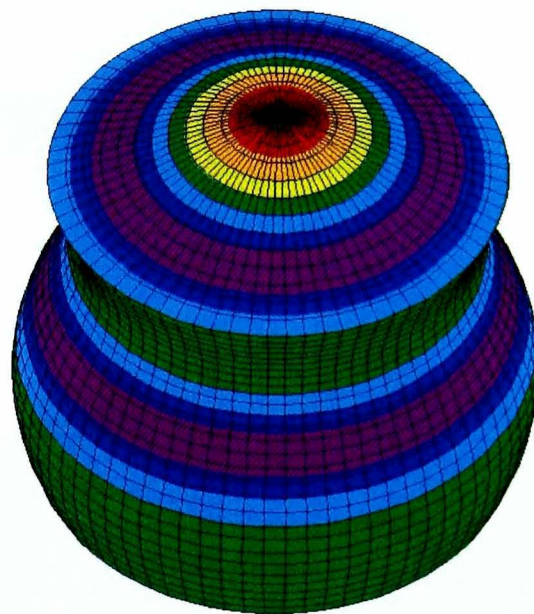


Figure B.8: *"2nd Asymmetric Drum" mode*

Appendix C

Extended Study Silica Modeshapes

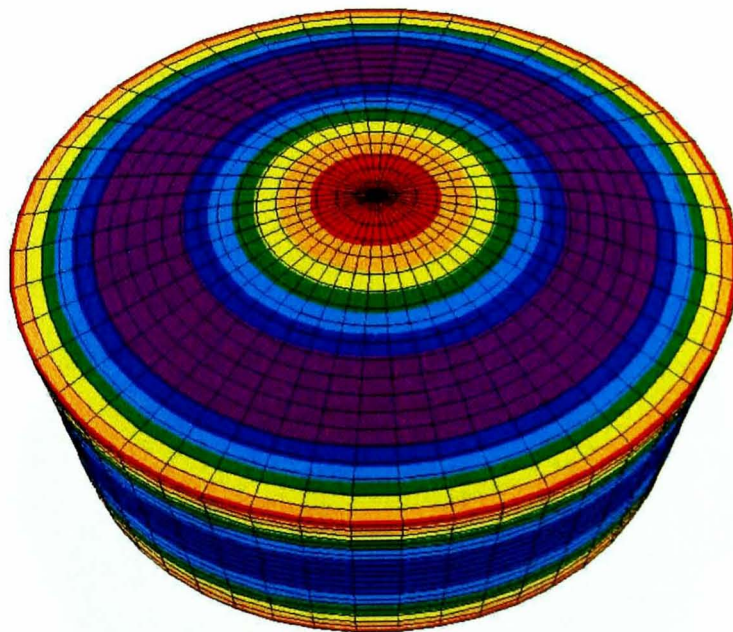


Figure C.1: *“Asymmetric Drum” mode*

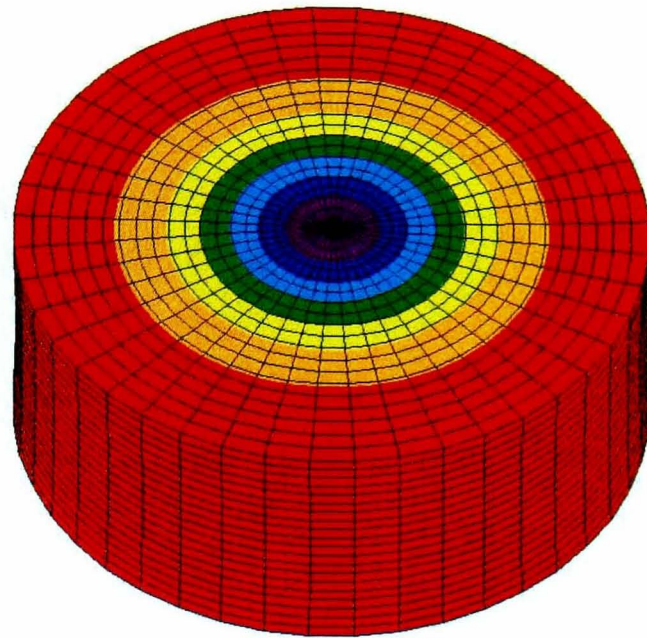


Figure C.2: *"Fundamental" mode*

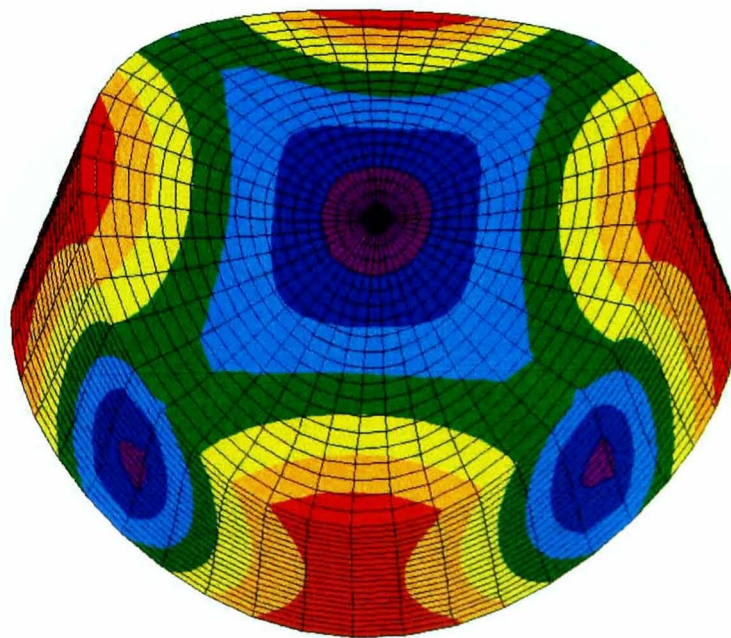


Figure C.3: *"Clover-4" mode*

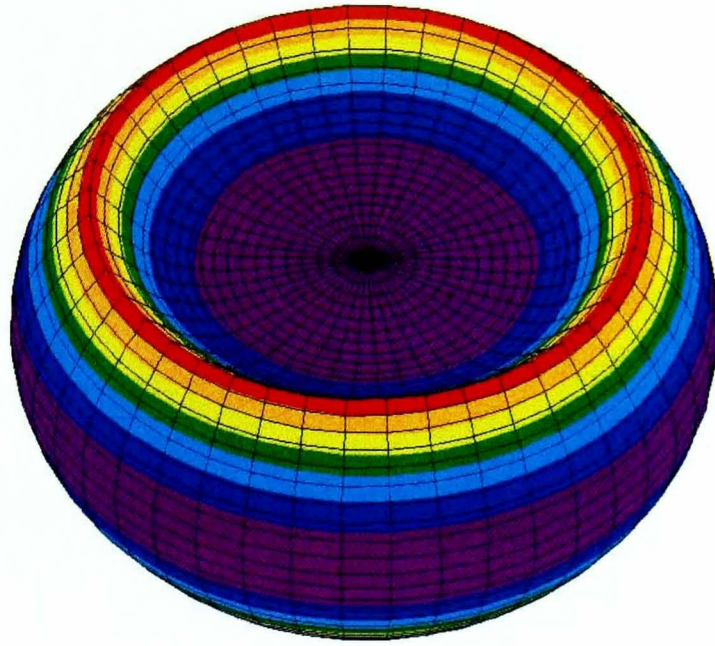


Figure C.4: *“Symmetric Drum” mode*

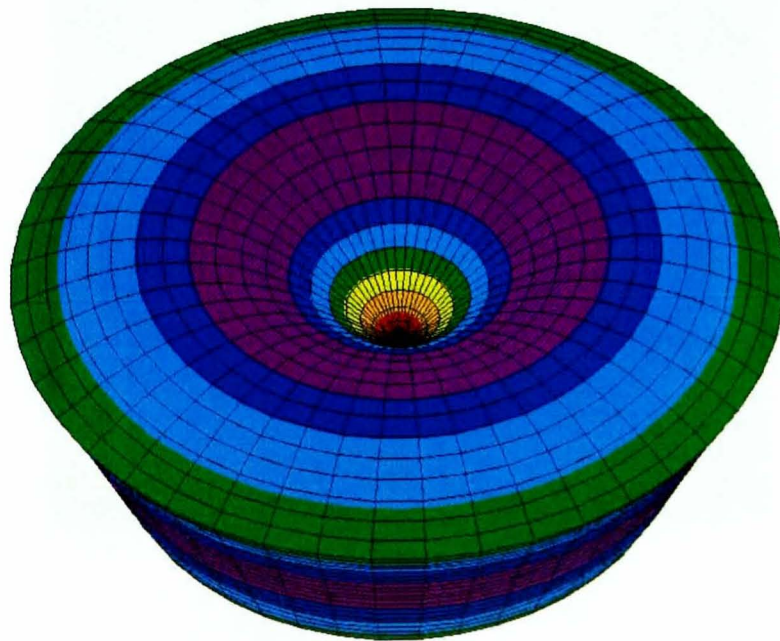


Figure C.5: *“2nd Asymmetric Drum” mode*

Appendix D

Sapphire Modeshapes

Note that the rectangle protruding from these modeshapes is part of the construction process and is not part of the actual modeshape.

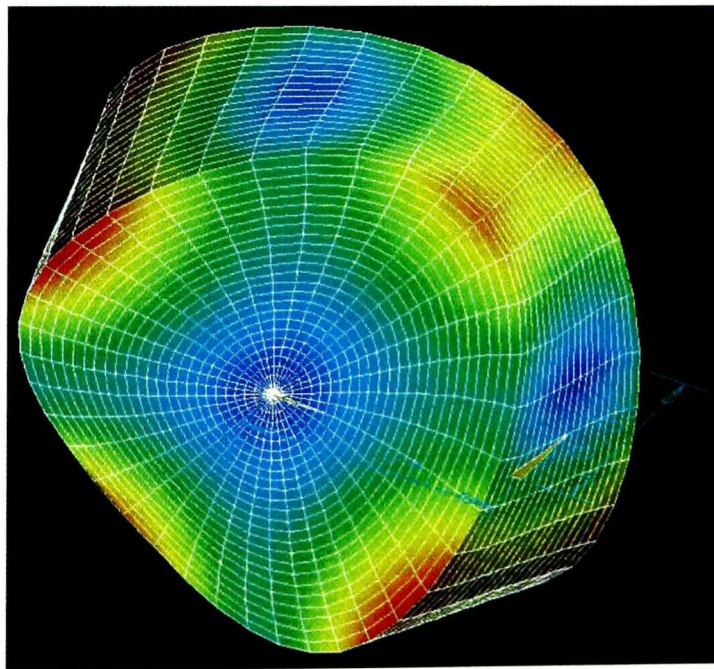


Figure D.1: *Mode "i"*

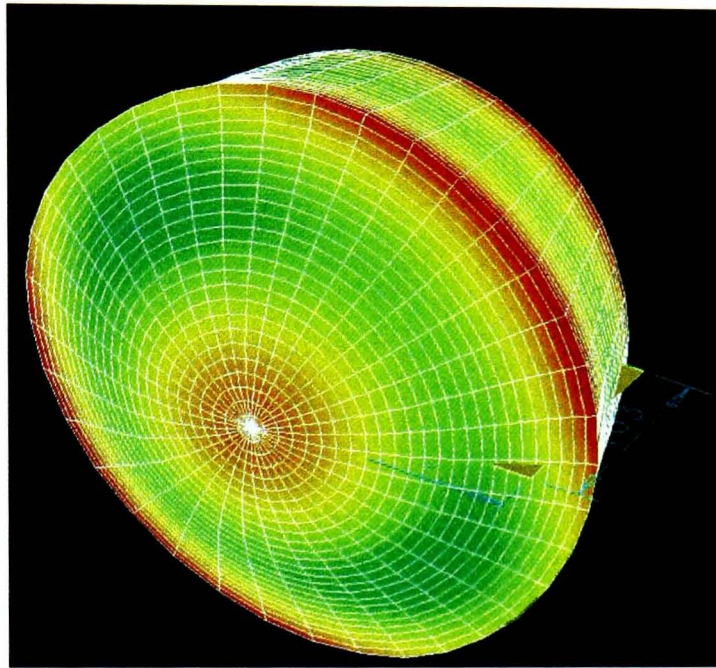


Figure D.2: *Mode "ii"*

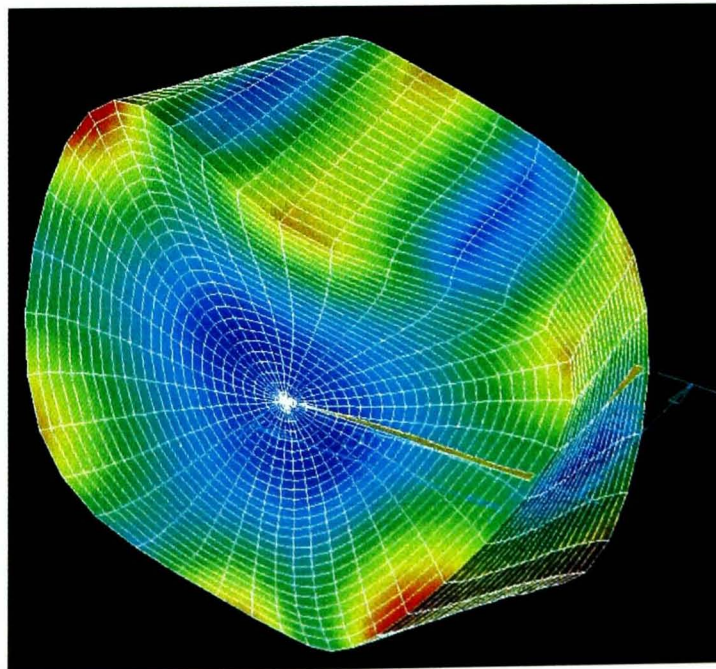


Figure D.3: *Modes "iii" & "iv"*

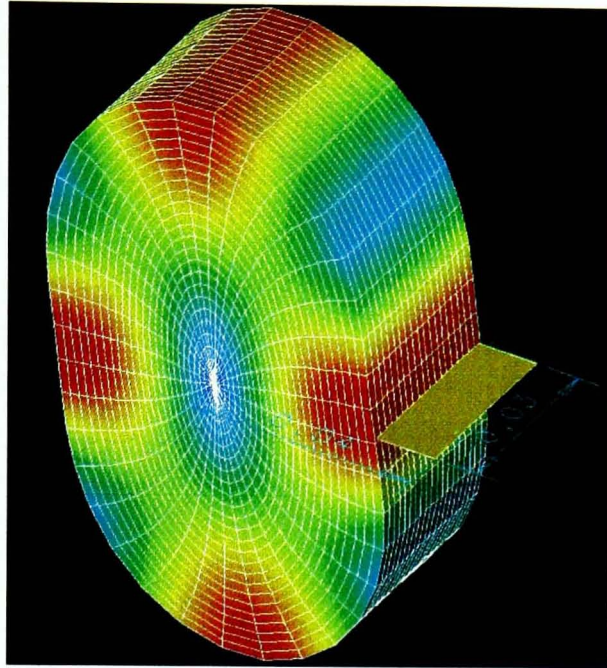


Figure D.4: *Mode v*

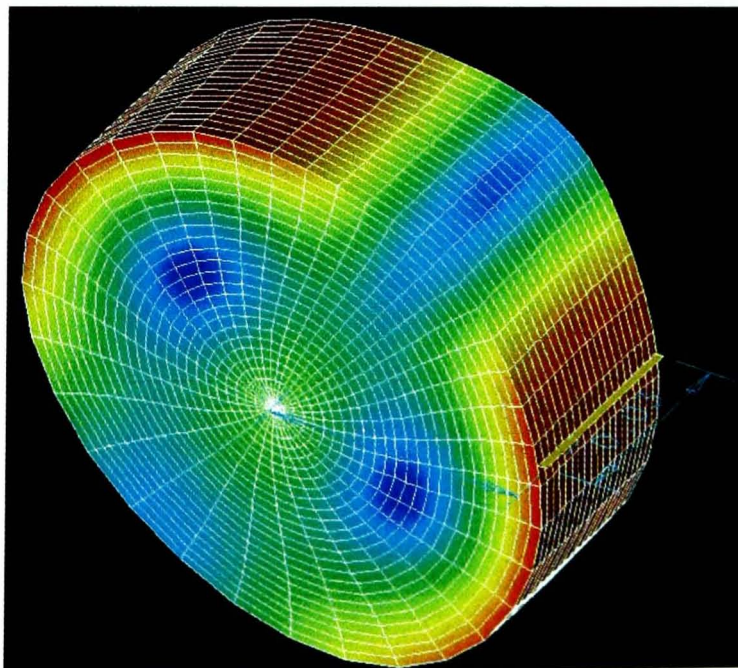


Figure D.5: *Modes " vi " & " vii "*

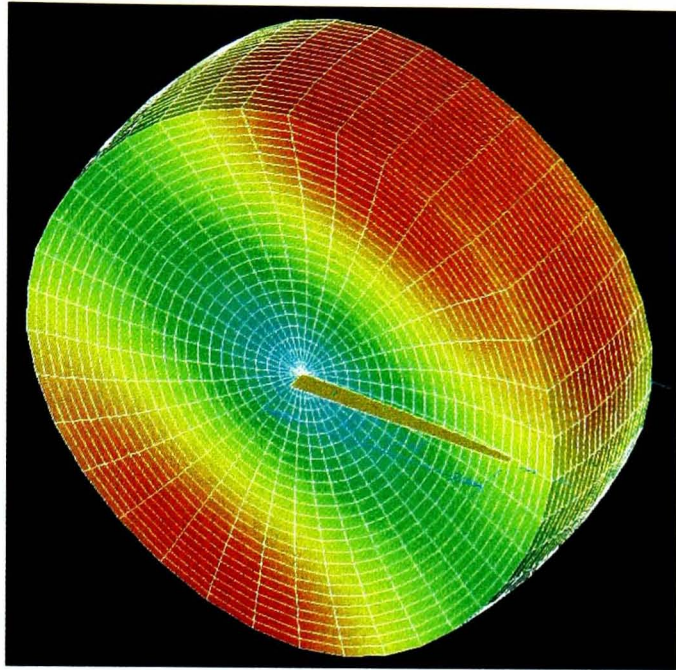


Figure D.6: *Mode "viii"*

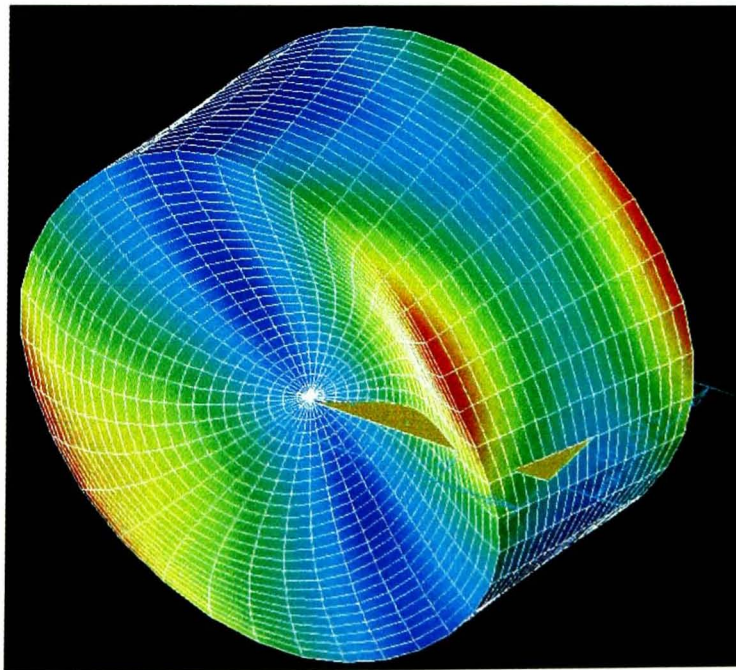


Figure D.7: *Mode "ix"*

Appendix E

Ocean Source Code

```
/*
Isotropic Ocean. Required files are:

ocean.exe
ocean.ini
*.ml file(s)

Generated files:

ocean.log
*_str.csv
*_str.map
energy_ratios.csv
*/

#include <stdio.h>
#include <stdlib.h>
#include <math.h>
#include <string.h>

#define MAXLENGTH 80 // Maximum length of word

#define X 0 // Define array labels
#define Y 1 // so that it is clear
#define Z 2 // which co-ordinate is being
#define DX 3 // manipulated at any one
#define DY 4 // time.
```

```
#define DZ 5
#define R 0
#define PHI 1
#define DR 3
#define DPHI 4
#define U_RR 0
#define U_RPHI 1
#define U_RZ 2
#define U_PHIR 3
#define U_PHIPHI 4
#define U_PHIZ 5
#define U_ZR 6
#define U_ZPHI 7
#define U_ZZ 8
#define PI 3.141592 //PI

int round( double );

FILE * settings_file; //Settings File
FILE * log_file; //Log file
FILE * mode_file; // File pointer
FILE * mapping_file; //Mapping file pointer.
FILE * strain_file; //Strain tensor file.
FILE * ratio_file; //Ratios file
FILE * details_file; //Useful file

int main(int argc, char *argv[]) {
    char word[MAXLENGTH]; // General String array used to
read in position data.

    int number; // General integer variable used
to read position.
    int z_no, r_no, phi_no; // Number of z values, etc.
    int disc_size; // Size of disc in number of
points.
    int desired_mode; // Mode number on which info is
wanted.
    double data, trace=0.0; // Used to collect data;
temporary storage.
    double substrate=0.0, surface=0.0, barrel=0.0, coating_h=0.0,
barrel_h=0.0; // Energies.
    double x,y,r,phi; // Used for polar conversion.
    double z_max, z_increment, r_max, r_increment, phi_increment, ax,
bx, ay;
    double du_dyplus, du_dyneg, du_dxplus, du_dxneg, du_dzplus,
du_dzneg;
```

```

double du_dydash, du_dxdash, disp_max, disp_reduction;
double ** node_data;           // Pointer to node data array.
double ** polar_node_data;     // Pointer to node data
characterised as polars.
double * frequency;           // Pointer to frequency array.
int * p;                       // Point details for point file.
double **** point;            // Pointer to integer mapped
description;
char * map_extension=".map";    // Make result file into .map
file.
char * str_extension="_str.csv"; // Make result file into .str
file.
char * help_string="help";
char model_name[MAXLENGTH];    // To store name of model
char * map_file;               // To store filename of .map file
char * str_file;               // To store filename of .str file
char * rat_file="energy_ratios.csv"; // To store
filename of .rat file
char * det_file="point_details.csv"; // To store point info.
char switches[10]="\n";
double ***** u;              // Strain tensor
double ***** du;             // Used to construct strain
tensor components.
double *** vol;

double *** area;

int number_of_nodes;           // Obvious
int number_of_modes;          // Ditto
int count,i,j,k,l,m;          // Useful integers.

int append=0, mode_print=0, verbose=0, point_data=0, centre=0,
coating_thickness=0; //switches
int barrel_thickness=0, help=0, moduli=0, coating_moduli=0,
barrel_moduli=0, suspension_barrel_extent=0;

int z_start=0, z_finish=0, discs=0, slices=0; // switch
dependent variables
double r_large, r_small, substrate_E=0.0, substrate_sigma=0.0,
coating_E=0.0, coating_sigma=0.0;
double density=2202.0, G = 0.0, K = 0.0;
double barrel_E=0.0, barrel_sigma=0.0, barrel_extent=0.0,
surface_locn=0.0;

int r_count, phi_count, z_count, phi_total, z_disc=0;

```

```

// SET DEFAULT VALUES

coating_h=1e-5;                // Coating Thickness
barrel_h=coating_h;            // Barrel Thickness
substrate_E=7.2e10;             // substrate Young's modulus
substrate_sigma=0.17;          // substrate Poisson's ratio
coating_E=2.5e11;              // Coating Young's modulus
coating_sigma=0.25;            // Coating Poisson's Ratio
barrel_E=coating_E;            // Barrel Young's modulus
barrel_sigma=coating_sigma;    // Barrel Poisson's Ratio

// READ SETTINGS FILE OCEAN.INI

settings_file = fopen("ocean.ini", "r");
if ( !settings_file ) {
    printf("Settings file not found. Please find ocean.ini");
    return 0;
}

if ( (log_file=fopen("ocean.log", "w+")) == NULL) {
    printf("Error opening log file");
    return 0;
}

do { // Get model name
    fscanf(settings_file,"%s",word);
    i = strcmp(word,"model_name:");
} while ( i != 0 );

fscanf(settings_file,"%s",word);
strcpy ( model_name , word);
fprintf(log_file,"Model Name: %s\n",model_name);

mode_file = fopen(model_name, "r");
if ( !mode_file ) { // Checks whether file exists.
    fprintf(log_file,"File %s not found\n", model_name);
    printf("File %s not found.\n",model_name);
    return 0;
}

do { //Get mode numbers
    fscanf(settings_file,"%s",word);
    i = strcmp(word,"mode_number:");
} while ( i != 0 );

```

```

fscanf(settings_file,"%d",&number);
fprintf(log_file,"Mode number = %d\n",number);

desired_mode = number;

do { //Get coating thickness
    fscanf(settings_file,"%s",word);
    i = strcmp(word,"coating_thickness:");
} while ( i != 0 );

fscanf(settings_file,"%lf",&data);
fscanf(settings_file,"%s",word);
if ( strcmp(word,"barrel_thickness:")!=0 ) {
    printf("\nSettings file corrupted; check it out, please.
\nWord found=%s",word);
    return 0;
}

fprintf(log_file,"Coating thickness = %1.0e m\n",data);

coating_h = data;

// Get Barrel thickness

fscanf(settings_file,"%lf",&data);
fscanf(settings_file,"%s",word);
if ( strcmp(word,"substrate_E:")!=0 ) {
    fprintf(log_file,"Settings file corrupted
(substrate_E missing);
check it out, please. See help files for details");
    return 0;
}

fprintf(log_file,"Barrel thickness = %1.0e m\n",data);

barrel_h = data;

// Get substrate Young's Modulus

fscanf(settings_file,"%lf",&data);
fscanf(settings_file,"%s",word);
if ( strcmp(word,"substrate_sigma:")!=0 ) {
    fprintf(log_file,"Settings file corrupted (substrate_sigma
missing); check it out, please. See help files for details");

```

```

return 0;
}

fprintf(log_file,"substrate Young's modulus
= %1.3e m\n",data);

substrate_E = data;

//Get substrate Poisson's Ratio

fscanf(settings_file,"%lf",&data);

substrate_sigma = data;

fprintf(log_file,"substrate Poisson's Ratio = %0.2lf m\n",data);

do { //Get coating E
    fscanf(settings_file,"%s",word);
    i = strcmp(word,"coating_E:");
} while ( i != 0 );

fscanf(settings_file,"%lf",&data);
fscanf(settings_file,"%s",word);
if ( strcmp(word,"coating_sigma:")!=0 ) {
    printf("\nSettings file corrupted (coating_sigma missing);
check it out, please. \nWord found=%s",word);
    return 0;
}

fprintf(log_file,"Coating Young's modulus = %1.3e m\n",data);

coating_E = data;

//Get coating Poisson's Ratio

fscanf(settings_file,"%lf",&data);

coating_sigma = data;

fprintf(log_file,"Coating Poisson's Ratio = %1.2lf m\n",data);

do { //Get barrel E
    fscanf(settings_file,"%s",word);
    i = strcmp(word,"barrel_E:");
} while ( i != 0 );

```

```

fscanf(settings_file,"%lf",&data);
fscanf(settings_file,"%s",word);
if ( strcmp(word,"barrel_sigma")!=0 ) {
    printf("\nSettings file corrupted (barrel_sigma missing);
check it out, please. \nWord found=%s",word);
    return 0;
}

fprintf(log_file,"Barrel Young's modulus = %1.3e m\n",data);

barrel_E = data;

//Get coating Poisson's Ratio

fscanf(settings_file,"%lf",&data);

barrel_sigma = data;

fprintf(log_file,"Barrel Poisson's Ratio = %1.2lf m\n",data);

do { //Get number of barrel slices
    fscanf(settings_file,"%s",word);
    i = strcmp(word,"barrel_extent:");
} while ( i != 0 );

fscanf(settings_file,"%lf",&data);
fprintf(log_file,"Slices down barrel = %lf\n",data);

barrel_extent = data;

do { //Location down mass for surface
    fscanf(settings_file,"%s",word);
    i = strcmp(word,"surface_locn:");
} while ( i != 0 );

fscanf(settings_file,"%lf",&data);
fprintf(log_file,"Fraction down mass for surface = %lf\n",data);

surface_locn = data;

do { //Get append switch
    fscanf(settings_file,"%s",word);
    i = strcmp(word,"append:");
} while ( i != 0 );

```

```

fscanf(settings_file,"%d",&number);
fprintf(log_file,"Append (0 = No, 1=Yes) = %d\n",number);

append = number;

do { //Get mode_print switch
    fscanf(settings_file,"%s",word);
    i = strcmp(word,"mode_print:");
} while ( i != 0 );

fscanf(settings_file,"%d",&number);
fprintf(log_file,"Print Mode Number (0 = No, 1=Yes) =
%d\n",number);

mode_print = number;

do { //Get point_data switch
    fscanf(settings_file,"%s",word);
    i = strcmp(word,"point_data:");
} while ( i != 0 );

printf("!");
fscanf(settings_file,"%d",&number);
fprintf(log_file,"Request Co-ordinate data (0 = No, 1=Yes) =
%d\n",number);

point_data = number;

if ( point_data ) {
    p = (int *) malloc ( 21 * sizeof ( int ));
    fprintf(log_file,"\nCo-ordinates of point of interest
(r,phi,z):\n");

    do { //Get r co-ord
        fscanf(settings_file,"%s",word);
        i = strcmp(word,"");
    } while ( i != 0 );
    fscanf(settings_file,"%d",&number);
    fprintf(log_file,"%d",number);
    p[0]=number;

    do { //Get phi co-ord
        fscanf(settings_file,"%s",word);

```

```

        i = strcmp(word, ".");
    } while ( i != 0 );
    fscanf(settings_file, "%d", &number);
    fprintf(log_file, "%d", number);
    p[1]=number;

    do { //Get z co-ord
        fscanf(settings_file, "%s", word);
        i = strcmp(word, ".");
    } while ( i != 0 );
    fscanf(settings_file, "%d", &number);
    fprintf(log_file, "%d", number);
    p[2]=number;
}

if( fclose(log_file)!=0 )          // Don't need log file
now.                               printf("Error closing file \n" );

if( fclose(settings_file)!=0 )     // Don't need
settings file now.                printf("Error closing file \n" );

// FINISHED READING SETTINGS FILE

printf("Isotropic Ocean (c) 2001 University of Glasgow, all
rights reserved\nView ocean.log for details of run\n");

// BEGIN READING MODEL FILE

// Get number of nodes

do {
    fscanf(mode_file, "%s", word);          // Looks for
(NUMNP)                                  i = strcmp(word, "(NUMNP)");
    } while ( i != 0 );

    fscanf(mode_file, "%s", word);          // Looks for
"="                                       fscanf(mode_file, "%d", &number);
number of nodes                          // To get
number_of_nodes=number;

```

```

    if ( verbose ) printf("\nNumber of nodes is: %d",
number_of_nodes);

    // Get number of modes

    do {
        fscanf(mode_file, "%s", word);          // Looks for
(NF)                                       i = strcmp(word, "(NF)");
    } while ( i != 0 );

    fscanf(mode_file, "%s", word);          // Looks for
"="                                       fscanf(mode_file, "%d", &number);
number of modes                          // To get
number_of_modes=number;

    if ( verbose ) printf("\nNumber of modes is: %d",
number_of_modes);

// Set up necessary arrays/ perform error traps on settings

if ( desired_mode>number_of_modes || desired_mode<=0 ) {
    if ( (log_file=fopen("ocean.log", "a+")) == NULL) {
        printf("Error opening log file");
        return 0;
    }
    fprintf(log_file, "Mode number out of bounds");
    return 0;
    if( fclose(log_file)!=0 )
        printf("Error closing file \n" );
}

node_data = (double **) malloc (number_of_nodes *
sizeof(double*)); // Initialise data
for ( i=0 ; i<number_of_nodes ; i++ ) {
// array.
    node_data[i] = (double *) malloc (6*sizeof(double));
}

polar_node_data = (double **) malloc (number_of_nodes *
sizeof(double*)); // Initialise
for ( i=0 ; i<number_of_nodes ; i++ ) {

```

```

// polar co-ord array.
polar_node_data[i] = (double *) malloc (6*sizeof(double));
}

frequency = (double * ) malloc ( number_of_modes *
sizeof(double)); // Init freq array

for ( i=0 ; i<4 ; i++ ){
do {
fscanf(mode_file,"%s",word); // Looks
for underline
j = strcmp(word,"-----");
} while ( j != 0 );
}

for ( count=0 ; count<number_of_nodes ; count++ ) {
// Main node data
i=0;
// loop.
do { // Pass over node number
and boundary condns.
fscanf(mode_file,"%d",&number); //

i++; //
} while ( i<7 );
for ( i=0 ; i<3 ; i++ ) { // Actually take data.
fscanf(mode_file,"%lf",&data);
node_data [count][i] = data;
}
fscanf(mode_file,"%lf",&data); // Passes over time value
}

//Mode search

if ( verbose ) printf("\nLooking for mode %d\n",desired_mode);

do {
fscanf(mode_file,"%s",word); // Looks for
mode 1
i = strcmp(word,"Displacements/Rotations(degrees)");
} while ( i != 0 );

```

```

for ( i=0 ; i<3 ; i++ ) { //Looks for rotation 3
times
do {
fscanf(mode_file,"%s",word);
j = strcmp(word,"rotation");
} while ( j != 0 );
}

if ( desired_mode!=1 ) {
do {
do {
fscanf(mode_file,"%s",word); //
Looks for ANALYSIS
i = strcmp(word,"ANALYSIS");
} while ( i != 0 );

do {
fscanf(mode_file,"%s",word); //
Looks for number
i = strcmp(word,"number");
} while ( i != 0 );
fscanf(mode_file,"%s",word); //
"="

fscanf(mode_file,"%d", &number);
for ( i=0 ; i<3 ; i++ ) { //Looks for
rotation 3 times
do {
fscanf(mode_file,"%s",word);
j = strcmp(word,"rotation");
} while ( j != 0 );
}
} while ( number!=desired_mode );
}

if ( verbose ) printf("\nReading Data from Mode number:
%d\n",number);

for ( count=0 ; count<number_of_nodes ; count++ ) { // Main
displacement data loop
fscanf(mode_file,"%d",&number);

```

```

    for ( i=3 ; i<6 ; i++ ) {
Values          // Actual
        fscanf(mode_file,"%lf",&data);
        node_data[count][i] = data;
    }

    x=node_data[count][X];          // Polar
conv.           // done on
    y=node_data[count][Y];
the fly...
    r=sqrt(x*x + y*y);
    phi=atan2(y,x);
    if ( phi<0 ) phi += ( 2.0*PI );          // Want all
phi's to be +ve
    if ( fabs(phi-( 2.0*PI ))<=1e-6 ) phi=0.0; // Different dps
mean might not be the same
    polar_node_data[count][R]=r;
    polar_node_data[count][PHI]=phi;
    polar_node_data[count][Z]=node_data[count][Z];
    polar_node_data[count][DX]=node_data[count][DX];
    polar_node_data[count][DY]=node_data[count][DY];
    polar_node_data[count][DZ]=node_data[count][DZ];

    if ( verbose && count%((int)(number_of_nodes/20))==0)
printf(".");

    for ( i=0 ; i<3 ; i++ ) {
        fscanf(mode_file,"%lf",&data);          //Skip over
rotation values (constrained)
    }

}

// End of displacement entry

// Find modal frequency

for ( count=0 ; count<4 ; count++ ) {
    do {
        fscanf(mode_file,"%s",word);
//"-----"*4
        j = strcmp(word,"-----");
    } while ( j != 0 );
}

```

```

for ( count=0 ; count<number_of_modes ; count++ ) {
    fscanf(mode_file,"%lf",&data);
    fscanf(mode_file,"%lf",&data);
    fscanf(mode_file,"%lf",&data);
    frequency[count] = data;
    fscanf(mode_file,"%lf",&data);
    fscanf(mode_file,"%lf",&data);
}

if ( (log_file=fopen("ocean.log", "a+")) == NULL) {
    printf("Error opening log file");
    return 0;
}
fprintf(log_file,"Mode frequency: %1.0lf
Hz\n",frequency[desired_mode-1]);
if( fclose(log_file)!=0 )
    printf("Error closing file \n" );

for ( count=0 ; count<number_of_nodes ; count++ ) { // We no
longer require node_data
    free(node_data[count]);
}
free(node_data);

if( fclose(mode_file)!=0 )          // Don't need
mode_file now.
    printf("Error closing file %s\n",mode_file );

// Determine useful quantities like z_max, z_increment and so
on...

z_max=polar_node_data[number_of_nodes-1][Z];
count=0;
do {
    z_increment=polar_node_data[count++][Z];
}
while(z_increment==0.0);

disc_size=count-1;

r_max=polar_node_data[count][R];          //Find r_max
within disc.
for ( count=0 ; count<disc_size ; count++ ) {
    if ( polar_node_data[count][R]>r_max )
r_max=polar_node_data[count][R];
}

```

```

    r_increment=r_max;
    for ( count=0 ; count<disc_size; count++ ) { //Find increment
of r.
        if ( fabs(polar_node_data[count][R]-0.0)>1e-7 ) {
            if ( polar_node_data[count][R]<r_increment )
r_increment=polar_node_data[count][R];
        }
    }

    phi_increment=PI;
    for ( count=0 ; count<disc_size; count++ ) { // Increment of
phi.
        if ( fabs(polar_node_data[count][PHI]-0.0)>1e-7 ) {
            if ( polar_node_data[count][PHI]<phi_increment )
phi_increment=polar_node_data[count][PHI];
        }
        //printf("%lf %lf\n",polar_node_data[count][PHI],
phi_increment);
    }

    if ( (log_file=fopen("ocean.log", "a+")) == NULL) {
        printf("Error opening log file");
        return 0;
    }
    fprintf(log_file,"r increment: %lf m\n",r_increment);
    fprintf(log_file,"phi increment: %lf m\n",phi_increment);
    fprintf(log_file,"z increment: %lf m\n",z_increment);
    if( fclose(log_file)!=0 )
        printf("Error closing file \n" );

    z_no = round(z_max/z_increment)+1; // Determine no of z points
    r_no = round(r_max/r_increment)+1; // Ditto r
    phi_no = round(2*PI/phi_increment); // Ditto phi
    phi_total = phi_no-1; // Useful for cyclic angles
later.
    z_disc = z_no-1;

    if ( (log_file=fopen("ocean.log", "a+")) == NULL) {
        printf("Error opening log file");
        return 0;
    }
    fprintf(log_file,"r points: %d\n",r_no);
    fprintf(log_file,"phi points: %d\n",phi_no);

```

```

fprintf(log_file,"discs: %d\n",z_no);
if( fclose(log_file)!=0 )
    printf("Error closing file \n" );

    if ( point_data ) {
        if ( p[0]<0 || p[0]>r_no-1 ) {
            fprintf(log_file,"\nPoint co-ordinates out of bounds:
r");
            point_data = 0;
        }
        if ( p[1]<0 || p[1]>phi_no-1 ) {
            fprintf(log_file,"\nPoint co-ordinates out of bounds:
phi");
            point_data = 0;
        }
        if ( p[2]<0 || p[2]>z_no-1 ) {
            fprintf(log_file,"\nPoint co-ordinates out of bounds:
z");
            point_data = 0;
        }
    }

    // Begin translation to point[] [] [] integer mapped points.

    point = (double ****) malloc (r_no * sizeof(double****)); //
Initialise
    for ( i=0 ; i<r_no ; i++ ) { //
co-ord array.
        point[i] = (double ***) malloc ( phi_no * sizeof(double**));
        for ( j=0 ; j<phi_no ; j++ ) {
            point[i][j] = (double **) malloc ( z_no * sizeof(double
*));
            for ( k=0 ; k<z_no ; k++ ) {
                point[i][j][k] = (double *) malloc ( 6 *
sizeof(double));
            }
        }
    }

```

```

}
for ( i=0 ; i<r_no ; i++ ) { //
co-ord array.
for ( j=0 ; j<phi_no ; j++ ) {
for ( k=0 ; k<z_no ; k++ ) {
for ( l=0 ; l<6 ; l++ ) {
point[i][j][k][l] = 0.0;
}
}
}
}

for ( count=0 ; count<number_of_nodes ; count++ ) { // Convert
polar_node_data to point; new structure.
i = round (polar_node_data[count][R]/r_increment);
j = round (polar_node_data[count][PHI]/phi_increment);
k = round (polar_node_data[count][Z]/z_increment);
if ( i==0 ) j=0; // Defines
phi=0 for r=0 (convention).
for ( l=0 ; l<6 ; l++ ) {

point[i][j][k][l]=polar_node_data[count][l];

}

}

for ( count=0 ; count<number_of_nodes ; count++ ) { // Free up
polar node data as well.
free(polar_node_data[count]);
}
free(polar_node_data);

// Begin strain tensor calculation.

u = (double *****) malloc (r_no * sizeof(double****)); //
Initialise
for ( i=0 ; i<r_no ; i++ ) { // strain
tensor.
u[i] = (double ****) malloc ( phi_no * sizeof(double****));
for ( j=0 ; j<phi_no ; j++ ) {
u[i][j] = (double ***) malloc ( z_no * sizeof(double
**));
for ( k=0 ; k<z_no ; k++ ) {

```

```

u[i][j][k] = (double **) malloc ( 3 *
sizeof(double*));
for ( l=0 ; l<3 ; l++ ) {
u[i][j][k][l] = (double *) malloc ( 3 *
sizeof(double));
}
}
}

for ( i=0 ; i<r_no ; i++ ) { // strain
tensor components tensor.
for ( j=0 ; j<phi_no ; j++ ) {
for ( k=0 ; k<z_no ; k++ ) {
for ( l=0 ; l<3 ; l++ ) {
for ( m=0 ; m<3 ; m++ ) {
u[i][j][k][l][m] = 0.0;
}
}
}
}
}

du = (double *****) malloc (r_no * sizeof(double****)); //
Initialise
for ( i=0 ; i<r_no ; i++ ) { // partial strain
tensor components tensor.
du[i] = (double ****) malloc ( phi_no * sizeof(double****));
for ( j=0 ; j<phi_no ; j++ ) {
du[i][j] = (double ***) malloc ( z_no * sizeof(double
**));
for ( k=0 ; k<z_no ; k++ ) {
du[i][j][k] = (double **) malloc ( 3 *
sizeof(double*));
for ( l=0 ; l<3 ; l++ ) {
du[i][j][k][l] = (double *) malloc ( 3 *
sizeof(double));
}
}
}
}

for ( i=0 ; i<r_no ; i++ ) { // strain
tensor components tensor.
for ( j=0 ; j<phi_no ; j++ ) {
for ( k=0 ; k<z_no ; k++ ) {

```

```

        for ( l=0 ; l<3 ; l++ ) {
            for ( m=0 ; m<3 ; m++ ) {
                du[i][j][k][l][m] = 0.0;
            }
        }
    }
}

disp_max=0.0;          //Find disp_max within surface.
z_count = z_no-1;
for ( r_count=0 ; r_count<r_no ; r_count++ ) {
    for ( phi_count=0 ; phi_count<phi_no ; phi_count++ ) {
        for ( i=3 ; i<6 ; i++ ) {
            if (
fabs(point[r_count][phi_count][z_count][i])>disp_max )
disp_max=fabs(point[r_count][phi_count][z_count][i]);
        }
    }
}

if ( verbose ) printf("\nCalculating strain tensor
derivatives.\n");

for ( z_count=0 ; z_count<z_no ; z_count++ ) {          // Strain
tensor component calculation

    if ( verbose &&
r_count*phi_count*z_count%((int)r_no*phi_no*z_no)/20000==0 )
printf(".");

    for ( r_count=0 ; r_count<r_no ; r_count++ ) {
        ax = (r_count*r_increment)*(double)sin(phi_increment);
        bx = -(r_count*r_increment)*(double)sin(phi_increment);
        ay = -(r_count*r_increment) * (1 -
(double)cos(phi_increment));
        for ( phi_count=0 ; phi_count<phi_no ; phi_count++ ) {
            if ( !(r_count==0 && phi_count!=0) ) {
                if ( z_count==0 ) {
                    for ( count=3 ; count<6 ; count++ ) {
                        du[r_count][phi_count][z_count][count-3][
Z] =
(point[r_count][phi_count][1][count]-point[r_count][phi_count][0][
count])/z_increment;

```

```

                if ( point_data && r_count==p[0] &&
phi_count==p[1] && z_count==p[2] ) {
                    p[3]=r_count;
                    p[4]=phi_count;
                    p[5]=1;
                }
            }
        } else if ( z_count==z_no-1 ) {
            for ( count=3 ; count<6 ; count++ ) {
                du[r_count][phi_count][z_count][count-3][
Z] =
(point[r_count][phi_count][z_count][count]-point[r_count][phi_count][
z_count-1][count])/z_increment;
                if ( point_data && r_count==p[0] &&
phi_count==p[1] && z_count==p[2] ) {
                    p[3]=r_count;
                    p[4]=phi_count;
                    p[5]=z_count-1;
                }
            }
        } else {
            for ( count=3 ; count<6 ; count++ ) {
                du_dzplus =
(point[r_count][phi_count][z_count+1][count]-point[r_count][phi_count
][z_count][count])/z_increment;
                du_dzneg =
(point[r_count][phi_count][z_count-1][count]-point[r_count][phi_count
][z_count][count])/z_increment;
                du[r_count][phi_count][z_count][count-3][
Z] = 0.5*( du_dzplus + du_dzneg );
                if ( point_data && r_count==p[0] &&
phi_count==p[1] && z_count==p[2] ) {
                    p[3]=r_count;
                    p[4]=phi_count;
                    p[5]=z_count+1;
                    p[6]=r_count;
                    p[7]=phi_count;
                    p[8]=z_count-1;
                }
            }
        }
    }

if ( r_count==0 ) {

        for ( count=3 ; count<6 ; count++ ) {

```

```

                du_dyplus =
(point[r_count+1][phi_no/4][z_count][count]-point[r_count][0][z_count
][count])/r_increment;
                du_dyneg =
(point[r_count+1][(3*phi_no)/4][z_count][count]-point[r_count][0][
z_count][count])/r_increment;
                du[r_count][0][z_count][count-3][Y] =
0.5*( du_dyplus + du_dyneg );

                if ( point_data && r_count==p[0] &&
phi_count==p[1] && z_count==p[2] ) {
                    p[9]=r_count+1;
                    p[10]=phi_no/4;
                    p[11]=z_count;
                    p[12]=r_count+1;
                    p[13]=(3*phi_no)/4;
                    p[14]=z_count;
                }
                du_dxplus =
((point[1][0][z_count][count]-point[0][0][z_count][count])/
r_increment);
                du_dxneg =
((point[1][phi_no/2][z_count][count] -
point[0][0][z_count][count])/r_increment);
                du[r_count][0][z_count][count-3][X] =
0.5*( du_dxplus + du_dxneg );

                if ( point_data && r_count==p[0] &&
phi_count==p[1] && z_count==p[2] ) {
                    p[15]=1;
                    p[16]=0;
                    p[17]=z_count;
                    p[18]=1;
                    p[19]=phi_no/2;
                    p[20]=z_count;
                }
            }
        } else if ( r_count==1 ){
            for ( count=3 ; count<6 ; count++ ) {
                du_dyplus =
(point[2][phi_count][z_count][count]-point[r_count][phi_count][
z_count][count])/r_increment;
                du_dyneg =
(point[0][0][z_count][count]-point[r_count][phi_count][z_count][count

```

```

])/r_increment;
                du_dydash = 0.5*( du_dyplus + du_dyneg );

                if ( point_data && r_count==p[0] &&
phi_count==p[1] && z_count==p[2] ) {
                    p[9]=2;
                    p[10]=phi_count;
                    p[11]=z_count;
                    p[12]=0;
                    p[13]=0;
                    p[14]=z_count;
                }

                du_dxplus =
(point[r_count][(phi_count-1+phi_no)%phi_no][z_count][count] -
point[r_count][phi_count][z_count][count]-(du_dyneg*ay))/ax;
                du_dxneg =
(point[r_count][(phi_count+1)%phi_no][z_count][count] -
point[r_count][phi_count][z_count][count] - (du_dyneg*ay))/bx;
                du_dxdash = 0.5*( du_dxplus + du_dxneg );

                if ( point_data && r_count==p[0] &&
phi_count==p[1] && z_count==p[2] ) {
                    p[15]=r_count;
                    p[16]=(phi_count-1+phi_no)%phi_no;
                    p[17]=z_count;
                    p[18]=r_count;
                    p[19]=(phi_count+1)%phi_no;
                    p[20]=z_count;
                }
                du[r_count][phi_count][z_count][count-3][
X] = cos((phi_count*phi_increment)-(PI/2))*du_dxdash -
sin((phi_count*phi_increment)-(PI/2))*du_dydash;
                du[r_count][phi_count][z_count][count-3][
Y] = sin((phi_count*phi_increment)-(PI/2))*du_dxdash +
cos((phi_count*phi_increment)-(PI/2))*du_dydash;
            }
        } else if ( r_count==r_no-1 ) {
            for ( count=3 ; count<6 ; count++ ) {
                du_dyneg =
(point[r_count-1][phi_count][z_count][count]-point[r_count][phi_count
][z_count][count])/r_increment;
                du_dydash = du_dyneg;

                if ( point_data && r_count==p[0] &&

```

```

phi_count==p[1] && z_count==p[2] ) {
    p[9]=r_count-1;
    p[10]=phi_count;
    p[11]=z_count;
}
du_dxplus =
(point[r_count][phi_count-1+phi_no][z_count][count] -
point[r_count][phi_count][z_count][count]-(du_dyneg*ay))/ax;
du_dxneg =
(point[r_count][phi_count+1+phi_no][z_count][count] -
point[r_count][phi_count][z_count][count] - (du_dyneg*ay))/bx;
du_dxdash = 0.5*( du_dxplus + du_dxneg );

if ( point_data && r_count==p[0] &&
phi_count==p[1] && z_count==p[2] ) {
    p[15]=r_count;
    p[16]=(phi_count-1+phi_no)%phi_no;
    p[17]=z_count;
    p[18]=r_count;
    p[19]=(phi_count+1)%phi_no;
    p[20]=z_count;
}
du[r_count][phi_count][z_count][count-3][
X] = cos(phi_count*phi_increment-PI/2)*du_dxdash -
sin(phi_count*phi_increment-PI/2)*du_dydash;
du[r_count][phi_count][z_count][count-3][
Y] = sin(phi_count*phi_increment-PI/2)*du_dxdash +
cos(phi_count*phi_increment-PI/2)*du_dydash;
}
} else {
for ( count=3 ; count<6 ; count++ ) {
du_dyplus =
(point[r_count+1][phi_count][z_count][count]-point[r_count][phi_count
][z_count][count])/r_increment;
du_dyneg =
(point[r_count-1][phi_count][z_count][count]-point[r_count][phi_count
][z_count][count])/-r_increment;
du_dydash = 0.5*( du_dyplus + du_dyneg );

if ( point_data && r_count==p[0] &&
phi_count==p[1] && z_count==p[2] ) {
    p[9]=r_count+1;
    p[10]=phi_count;
    p[11]=z_count;
    p[12]=r_count-1;

```

```

    p[13]=phi_count;
    p[14]=z_count;
}
du_dxplus =
(point[r_count][phi_count-1+phi_no][z_count][count] -
point[r_count][phi_count][z_count][count]-(du_dyneg*ay))/ax;
du_dxneg =
(point[r_count][phi_count+1+phi_no][z_count][count] -
point[r_count][phi_count][z_count][count] - (du_dyneg*ay))/bx;
du_dxdash = 0.5*( du_dxplus + du_dxneg );

if ( point_data && r_count==p[0] &&
phi_count==p[1] && z_count==p[2] ) {
    p[15]=r_count;
    p[16]=(phi_count-1+phi_no)%phi_no;
    p[17]=z_count;
    p[18]=r_count;
    p[19]=(phi_count+1)%phi_no;
    p[20]=z_count;
}
du[r_count][phi_count][z_count][count-3][
X] = cos(phi_count*phi_increment-PI/2)*du_dxdash -
sin(phi_count*phi_increment-PI/2)*du_dydash;
du[r_count][phi_count][z_count][count-3][
Y] = sin(phi_count*phi_increment-PI/2)*du_dxdash +
cos(phi_count*phi_increment-PI/2)*du_dydash;
}
}
}
}
}
for ( z_count=0 ; z_count<z_no ; z_count++ ) { //Strain tensor
calculation.
for ( r_count=0 ; r_count<r_no ; r_count++ ) {
for ( phi_count=0 ; phi_count<phi_no ; phi_count++ ) {
for ( i=0 ; i<3 ; i++ ) {
for ( j=0 ; j<3 ; j++ ) {
u[r_count][phi_count][z_count][i][j] =
0.5*(du[r_count][phi_count][z_count][i][j] +
du[r_count][phi_count][z_count][j][i]);
}
}
}
}
}
}

```

```

    }
}

area = (double ***) malloc (r_no * sizeof(double**)); //
Initialise
for ( i=0 ; i<r_no ; i++ ) { // volume
tensor.
    area[i] = (double **) malloc ( phi_no * sizeof(double*));
    for ( j=0 ; j<phi_no ; j++ ) {
        area[i][j] = (double *) malloc ( z_no * sizeof(double ));
    }
}

vol = (double ***) malloc (r_no * sizeof(double**)); //
Initialise
for ( i=0 ; i<r_no ; i++ ) { // volume
tensor.
    vol[i] = (double **) malloc ( phi_no * sizeof(double*));
    for ( j=0 ; j<phi_no ; j++ ) {
        vol[i][j] = (double *) malloc ( z_no * sizeof(double ));
    }
}

for ( z_count=0 ; z_count<z_no ; z_count++ ) { //Volume
calculation for ( r_count=0 ; r_count<r_no ; r_count++ )
    for ( r_count=0 ; r_count<r_no ; r_count++ ) {
        for ( phi_count=0 ; phi_count<phi_no ; phi_count++ ) {
            r = r_increment*r_count;
            r_large = r_increment*(r_count+0.5);
            r_small = r_increment*(r_count-0.5);

            if ( r_count==0 ) {
                area[r_count][phi_count][z_count] =
PI*r_large*r_large;
            } else if ( r_count==r_no-1 ) {
                area[r_count][phi_count][z_count] = (PI*r*r -
PI*r_small*r_small)/phi_no;
            } else {
                area[r_count][phi_count][z_count] =
(PI*r_large*r_large - PI*r_small*r_small)/phi_no;

```

```

        }
        if ( z_count==0 || z_count==z_no-1 ) {
            vol[r_count][phi_count][z_count] =
area[r_count][phi_count][z_count]*z_increment*0.5;

        } else {
            vol[r_count][phi_count][z_count] =
area[r_count][phi_count][z_count]*z_increment;
        }
    }
}

// substrate ENERGY CALCULATION

data = 0.0;

if ( centre ) {
    printf("\nHow many discs on either side of centre to
calculate energy: (Number of discs inc. z=0:%d)",z_no);
    scanf("%d",&discs);
    z_start=round((z_no-1)/2)-discs;
    z_finish=round((z_no-1)/2)+discs+1;
    printf("Start disc: %d \nFinish disc:
%d",z_start,z_finish-1);
} else {
    z_start=0;
    z_finish=z_no;
}

for ( z_count=z_start ; z_count<z_finish ; z_count++ ) {
//Energy calculation.
    for ( r_count=0 ; r_count<r_no ; r_count++ ) {
        for ( phi_count=0 ; phi_count<phi_no ; phi_count++ ) {
            if ( ! ( r_count==0 && phi_count!=0 ) ) {
                for ( i=0 ; i<3 ; i++ ) { // u_ik^2
                    for ( j=0 ; j<3 ; j++ ) {
                        data +=
u[r_count][phi_count][z_count][i][j]*u[r_count][phi_count][z_count][i
][j];
                    }
                }
            }
        }
    }
}

```

```

        for ( i=0 ; i<3 ; i++ ) {          // trace
            trace +=
u[r_count][phi_count][z_count][i][i];
        }

        substrate += vol[r_count][phi_count][z_count]*
(substrate_E/(2*(1+substrate_sigma)))*(data +
(substrate_sigma/(1-2*substrate_sigma))*trace*trace);

        data = 0.0;
        trace = 0.0;
    }
}

if ( !append ) {
    if( (ratio_file = fopen( rat_file , "w+" )) != NULL ) {
        fprintf(ratio_file,"Mode Number =
%d\n\n",desired_mode);
        fprintf(ratio_file,"Number of nodes,substrate
Energy,Surface Energy,Surface Ratio,Surface L&L Shear Energy,Surface
L&L Shear Ratio,Surface Timo Shear Energy,Surface Timo Shear
Ratio,Surface Hydrostatic Energy,Surface Hydrostatic Ratio,Barrel
Energy, Barrel Ratio, Radial Kinetic Energy, Radial Kinetic Ratio,
Longitudinal Kinetic Energy, Longitudinal Kinetic Ratio\n");
        fprintf(ratio_file,"%d,%e,",number_of_nodes,substrate);
        if( fclose( ratio_file ) ) printf("\n%s not closed
properly",rat_file);
        else if ( verbose ) printf("\n%s closed
correctly.",rat_file);
    }
} else {
    if( (ratio_file = fopen( rat_file , "a+" )) != NULL ) {
        if ( mode_print ) {
            fprintf(ratio_file,"\nMode Number =
%d\n\n",desired_mode);
            fprintf(ratio_file,"Number of nodes,substrate
Energy,Surface Energy,Surface Ratio,Surface L&L Shear Energy,Surface
L&L Shear Ratio,Surface Timo Shear Energy, Surface Timo Shear Ratio,
Surface Hydrostatic Energy,Surface Hydrostatic Ratio,Barrel Energy,
Barrel Ratio, Radial Kinetic Energy, Radial Kinetic Ratio,
Longitudinal Kinetic Energy, Longitudinal Kinetic Ratio\n");
        }

        fprintf(ratio_file,"%d,%e,",number_of_nodes,

```

```

        substrate);
        if( fclose( ratio_file ) ) printf("\n%s not closed
properly",rat_file);
        else if ( verbose ) printf("\n%s closed
correctly.",rat_file);
    }
}

```

```

// SURFACE ENERGY

```

```

data = 0.0;
trace = 0.0;

```

```

if ( surface_locn!=0.0 ) {
    z_count = round((z_no-1)*(1-surface_locn));
} else {
    z_count = z_disc;
}

for ( r_count=0 ; r_count<r_no ; r_count++ ) {
    for ( phi_count=0 ; phi_count<phi_no ; phi_count++ ) {
        if ( ! (r_count==0 && phi_count!=0 ) ) {
            for ( i=0 ; i<3 ; i++ ) {          // u_ik^2
                for ( j=0 ; j<3 ; j++ ) {
                    data +=
u[r_count][phi_count][z_count][i][j]*u[r_count][phi_count][z_count][i
][j];
                }
            }
            for ( i=0 ; i<3 ; i++ ) {          // trace
                trace += u[r_count][phi_count][z_count][i][i];
            }

            surface +=
coating_h*area[r_count][phi_count][z_count]*(coating_E/(2*(1+
coating_sigma)))*(data +
(coating_sigma/(1-2*coating_sigma))*trace*trace);

            data = 0.0;
            trace = 0.0;
        }
    }
}

if( (ratio_file = fopen( rat_file , "a+" )) != NULL ) {

```

```

        fprintf(ratio_file,"%e,%e,", surface, surface/substrate);
        if( fclose( ratio_file ) ) printf("\n%s not closed
properly",rat_file);
        else if ( verbose ) printf("\n%s closed
correctly.",rat_file);
    }

    // SURFACE SHEAR ENERGY

    data = 0.0;
    trace = 0.0;
    surface = 0.0;

    G = (0.5*coating_E)/(1+coating_sigma);

    z_count = z_disc; //Surface energy calculation.
    for ( r_count=0 ; r_count<r_no ; r_count++ ) {
        for ( phi_count=0 ; phi_count<phi_no ; phi_count++ ) {
            if ( ! ( r_count==0 && phi_count!=0 ) ) {
                for ( i=0 ; i<3 ; i++ ) { // u_ik^2
                    for ( j=0 ; j<3 ; j++ ) {
                        data +=
u[r_count][phi_count][z_count][i][j]*u[r_count][phi_count][z_count][i
][j];
                    }
                }

                for ( i=0 ; i<3 ; i++ ) { // trace
                    trace += u[r_count][phi_count][z_count][i][i];
                }

                surface +=
coating_h*area[r_count][phi_count][z_count]*G*(data -
(1/3)*trace*trace);

                data = 0.0;
                trace = 0.0;
            }
        }

        if( (ratio_file = fopen( rat_file , "a+" )) != NULL ) {
            fprintf(ratio_file,"%e,%e,", surface,
surface/substrate);
            if( fclose( ratio_file ) ) printf("\n%s not closed
properly",rat_file);
        }
    }

```

```

        else if ( verbose ) printf("\n%s closed
correctly.",rat_file);
    }

    // SURFACE Hydro ENERGY

    data = 0.0;
    trace = 0.0;
    surface = 0.0;

    K = coating_E/(3*(1-2*coating_sigma));

    if ( (log_file=fopen("ocean.log", "a+")) == NULL ) {
        printf("Error opening log file");
        return 0;
    }
    fprintf(log_file,"K: %lf\n",K);
    if( fclose(log_file)!=0 )
        printf("Error closing file \n" );

    z_count = z_disc; //Surface energy calculation.
    for ( r_count=0 ; r_count<r_no ; r_count++ ) {
        for ( phi_count=0 ; phi_count<phi_no ; phi_count++ ) {
            if ( ! ( r_count==0 && phi_count!=0 ) ) {
                for ( i=0 ; i<3 ; i++ ) { // trace
                    trace += u[r_count][phi_count][z_count][i][i];
                }

                surface +=
coating_h*area[r_count][phi_count][z_count]*0.5*K*trace*trace;

                trace = 0.0;
            }
        }

        if( (ratio_file = fopen( rat_file , "a+" )) != NULL ) {
            fprintf(ratio_file,"%e,%e,", surface,
surface/substrate);
            if( fclose( ratio_file ) ) printf("\n%s not closed
properly",rat_file);
            else if ( verbose ) printf("\n%s closed
correctly.",rat_file);
        }
    }

    // BARREL ENERGY

```

```

data = 0.0;
trace = 0.0;

if ( barrel_extent!=-1 ) {
    slices = round(barrel_extent/z_increment);
    z_start=z_no-1-slices;
} else {
    z_start=0;
}

if ( (log_file=fopen("ocean.log", "a+")) == NULL) {
    printf("Error opening log file");
    return 0;
}
fprintf(log_file,"Start disc: %d \nSlices: %d",z_start,slices);
if( fclose(log_file)!=0 )
    printf("Error closing file \n" );

r_count=r_no-1;
for ( z_count=z_start ; z_count<z_no ; z_count++ ) {
    for ( phi_count=0 ; phi_count<phi_no ; phi_count++ ) {
        for ( i=0 ; i<3 ; i++ ) {          // u_ik^2
            for (j=0 ; j<3 ; j++ ) {
                data +=
u[r_count][phi_count][z_count][i][j]*u[r_count][phi_count][z_count][i
][j];
            }

            for ( i=0 ; i<3 ; i++ ) {          // trace
                trace += u[r_count][phi_count][z_count][i][i];
            }

            if ( z_count==0 || z_count==z_no-1 ) {
                barrel +=
barrel_h*z_increment*0.5*r_max*phi_increment*(barrel_E/(2*(1+
barrel_sigma)))*(data +
(barrel_sigma/(1-2*barrel_sigma))*trace*trace);
            } else {
                barrel +=
barrel_h*z_increment*r_max*phi_increment*(barrel_E/(2*(1+barrel_sigma
)))*(data + (barrel_sigma/(1-2*barrel_sigma))*trace*trace);
            }

```

```

data = 0.0;
trace = 0.0;

}

if( (ratio_file = fopen( rat_file , "a+" )) != NULL ) {
    fprintf(ratio_file,"%e,%e,", barrel,
barrel/substrate);
    if( fclose( ratio_file ) ) printf("\n%s not closed
properly",rat_file);
    else if ( verbose ) printf("\n%s closed
correctly.",rat_file);
}
// RADIAL SUSPENSION POINT KINETIC ENERGY

barrel = 0.0;
data = 0.0;
trace = 0.0;

r_count=r_no-1;
z_count=round((z_no-1)/2);

for ( phi_count=0 ; phi_count<phi_no ; phi_count++ ) {

    for ( i=3 ; i<5 ; i++ ) {
        data +=
point[r_count][phi_count][z_count][i]*point[r_count][phi_count][
z_count][i]; // dx^2 + dy^2
    }

    data =
4*PI*PI*frequency[desired_mode-1]*frequency[desired_mode-1]*data;
// v^2
    barrel += barrel_h*barrel_h*r_max*phi_increment*density*data;
    data = 0.0;
}

if( (ratio_file = fopen( rat_file , "a+" )) != NULL ) {
    fprintf(ratio_file,"%e,%e,", barrel,
barrel/substrate);
    if( fclose( ratio_file ) ) printf("\n%s not closed
properly",rat_file);
    else if ( verbose ) printf("\n%s closed
correctly.",rat_file);
}

```

```

// LONGITUDINAL SUSPENSION POINT KINETIC ENERGY

barrel = 0.0;
data = 0.0;
trace = 0.0;

r_count=r_no-1;
z_count=round((z_no-1)/2);

for ( phi_count=0 ; phi_count<phi_no ; phi_count++ ) {
    data +=
point[r_count][phi_count][z_count][DZ]*point[r_count][phi_count][
z_count][DZ]; // dz^2
    data =
4*PI*PI*frequency[desired_mode-1]*frequency[desired_mode-1]*data;
// v^2

    barrel += barrel_h*barrel_h*r_max*phi_increment*density*data;
    data = 0.0;
}

if( (ratio_file = fopen( rat_file , "a+" )) != NULL ) {
    fprintf(ratio_file,"%e,%e\n", barrel, barrel/substrate);
    if( fclose( ratio_file ) ) printf("\n%s not closed
properly",rat_file);
    else if ( verbose ) printf("\n%s closed
correctly.",rat_file);
}

// OUTPUT FILES
if ( point_data ) {
    if( (details_file = fopen ( det_file , "w+" )) != NULL ) {
        fprintf(details_file,"Point details file\n");
        fprintf(details_file,"Reference Algor/I-DEAS
file:\n%s\n\n",model_name);
        fprintf(details_file,"Co-ordinates,(r phi z) =
(,%d,%d,%d)\n\n",p[0],p[1],p[2]);
        fprintf(details_file,"Node
position: ,r=,%e,x=,%e\n",point[p[0]][p[1]][p[2]][R],point[p[0]][p[1]]
[p[2]][R]*cos(point[p[0]][p[1]][p[2]][PHI]));
        fprintf(details_file," ,phi=,%e,y=,%e\n",point[p[0]][p[1]]
[p[2]][PHI],point[p[0]][p[1]][p[2]][R]*sin(point[p[0]][p[1]][p[2]][
PHI]));
    }
}

```

```

        fprintf(details_file,"z=,%e,z=,%e\n\n",point[p[0]][p[1]]
[p[2]][Z],point[p[0]][p[1]][p[2]][Z]);
        fprintf(details_file,"Displacements: ,dx=,%e\n,dy=,%e\n,dz
=,%e\n\n",point[p[0]][p[1]][p[2]][DX],point[p[0]][p[1]][p[2]][DY],
point[p[0]][p[1]][p[2]][DZ]);
        fprintf(details_file,"Increments: ,r=,%e\n,phi=,%e\n,z=,%e
\n\n",r_increment,phi_increment,z_increment);
        fprintf(details_file,"Neighbours:\n\ndui_dz
direction\n\n(,");

        for ( i=3 ; i<5 ; i++ ) fprintf(details_file,"%d",p[i]);
        fprintf(details_file,"%d,)",p[5]);
        if ( p[2]!=0 && p[2]!=z_no-1 ) {
            fprintf(details_file,"(,");
            for ( i=6 ; i<8 ; i++ )
                fprintf(details_file,"%d",p[i]);
            fprintf(details_file,"%d,)\n",p[8]);
        }
        fprintf(details_file,"\ndui_dydash direction\n\n(,");
        for ( i=9 ; i<11 ; i++ )
            fprintf(details_file,"%d",p[i]);
        fprintf(details_file,"%d,)\n",p[11]);
        if ( p[0]!=r_no-1 ) {
            fprintf(details_file,"(,");
            for ( i=12 ; i<14 ; i++ )
                fprintf(details_file,"%d",p[i]);
            fprintf(details_file,"%d,)\n",p[14]);
        }
        fprintf(details_file,"dui_dxdash direction\n\n(,");
        for ( i=15 ; i<17 ; i++ )
            fprintf(details_file,"%d",p[i]);
        fprintf(details_file,"%d,)\n(,)",p[17]);
        for ( i=18 ; i<20 ; i++ )
            fprintf(details_file,"%d",p[i]);
        fprintf(details_file,"%d,)\n\n",p[20]);
        fprintf(details_file,"dux_dx,dux_dy,dux_dz,duy_dx,duy_dy,
duy_dz,duz_dx,duz_dy,duz_dz\n");
        for ( i=0 ; i<3 ; i++ ) {
            for ( j=0 ; j<3 ; j++ ) {
                fprintf(details_file,"%e",du[p[0]][p[1]][p[2]]
[i][j]);
            }
        }
        fprintf(details_file," \n\nStrain
Tensor:\n\nu_xx,u_xy,u_xz,u_yx,u_yy,u_yz,u_zx,u_zy,u_zz\n");
        for ( i=0 ; i<3 ; i++ ) {

```

```

        for ( j=0 ; j<3 ; j++ ) {
            fprintf(
details_file,"%e,",u[p[0]] [p[1]] [p[2]] [i] [j]);
        }

        if( fclose( details_file ) ) printf("\n%s not closed
properly",det_file);
        else if ( verbose ) printf("\n%s closed
correctly.",det_file);
    }
}

//Output strain tensor to filename.str
str_file=strtok(model_name,".");
strncat(str_file,str_extension,9);

if( (strain_file = fopen( str_file , "w+" )) != NULL ) {

    if ( verbose ) printf("\nFile %s open for input\n",str_file);

    fprintf(strain_file,"Energy program strain tensor\n");
    fprintf(strain_file,"=====\n\n");
    fprintf(strain_file,"Filename: %s\n\n",str_file);
    fprintf(strain_file,"Mode: %d\n\n",desired_mode);
    fprintf(strain_file,"substrate Energy= %e (in appropriate
units)\n\n",substrate);
    fprintf(strain_file,"Surface Energy= %e (in appropriate
units)\n\n",surface);
    fprintf(strain_file,"Co-ords, , , |, Strain tensor
components, , , , , , , , , , , , |, Displacements\n");
    fprintf(strain_file,"r, phi, z, |, u_xx, u_xx^2, u_xy, u_xy^2, u_xz,
u_xz^2, u_yx, u_yx^2, u_yy, u_yy^2, u_yz, u_yz^2, u_zx, u_zx^2, u_zy, u_zy^2,
u_zz, u_zz^2, trace, trace^2 |, x, y, z\n");
    fprintf(strain_file,"-----
-----\n");

    for ( z_count=0 ; z_count<z_no ; z_count++ ) {
        for ( r_count=0 ; r_count<r_no ; r_count++ ) {

            if ( verbose &&
(z_count*r_count*phi_count*1)%((int)((r_no*phi_no*z_no*6)/20))==0 )
printf(".");

```

```

        for ( phi_count=0 ; phi_count<phi_no ; phi_count++) {
            if ( !(r_count==0 && phi_count!=0 ) ) {
                fprintf(
strain_file,"%d,%d,%d), |, ", r_count, phi_count, z_count);
                for ( i=0 ; i<3 ; i++ ) {
                    for ( j=0 ; j<3 ; j++ ) {
                        fprintf(
strain_file,"%e,%e,",u[r_count] [phi_count] [z_count] [i] [j], u[r_count] [
phi_count] [z_count] [i] [j]*u[r_count] [phi_count] [z_count] [i] [j]);
                    }
                }
                fprintf(
strain_file,"%e,%e,",u[r_count] [phi_count] [z_count] [X] [X]+u[r_count] [
phi_count] [z_count] [Y] [Y]+u[r_count] [phi_count] [z_count] [Z] [Z], (u[
r_count] [phi_count] [z_count] [X] [X]+u[r_count] [phi_count] [z_count] [Y] [
Y]+u[r_count] [phi_count] [z_count] [Z] [Z])*(u[r_count] [phi_count] [
z_count] [X] [X]+u[r_count] [phi_count] [z_count] [Y] [Y]+u[r_count] [
phi_count] [z_count] [Z] [Z]));

                fprintf(
strain_file,"|, %e,%e,%e\n",point[r_count] [phi_count] [z_count] [DX],
point[r_count] [phi_count] [z_count] [DY], point[r_count] [phi_count] [
z_count] [DZ]);
            }
        }
    }

    if( fclose( strain_file ) )
        printf("\n%s not closed properly",str_file);
    else if ( verbose ) printf("\n%s closed correctly.",str_file);

//Output mapping data to filename.map

map_file=strtok(model_name,".");
strncat(map_file,map_extension,5);

if( (mapping_file = fopen( map_file , "w+" )) != NULL ) {

    if ( verbose ) printf("\nFile %s open for input\n",map_file);

    fprintf(mapping_file,"Energy program integer mapping
output\n");
    fprintf(mapping_file,"=====\n

```



```

    return 0;
}

int round(double floating_point_number) {
    int result;
    result=(int) (floating_point_number+0.5);
    return result;
}

```

Appendix F

Aocean Source Code

```

/*
Anisotropic Ocean. Required files are:

    aocean.exe
    aocean.ini
    *.ml file(s)

Generated files:

    aocean.log
    *_str.csv
    *_str.map
    ani_energy_ratios.csv
*/

#include <stdio.h>
#include <stdlib.h>
#include <math.h>
#include <string.h>
//#include<conio.h>

#define MAXLENGTH 80 // Maximum length of word

#define X 0 // Define array labels
#define Y 1 // so that it is clear
#define Z 2 // which co-ordinate is being
#define DX 3 // manipulated at any one
#define DY 4 // time.
#define DZ 5

```

```

#define R          0
#define PHI        1
#define DR         3
#define DPHI       4
#define U_RR       0
#define U_RPHI     1
#define U_RZ       2
#define U_PHIR     3
#define U_PHIPHI   4
#define U_PHIZ     5
#define U_ZR       6
#define U_ZPHI     7
#define U_ZZ       8
#define PI         3.141592 //PI

int round( double );
void prop_assign(FILE *, FILE *, double[][4][4][4] );

FILE * settings_file; //Settings File
FILE * log_file;      //Log file
FILE * mode_file;    // File pointer
FILE * mapping_file; //Mapping file pointer.
FILE * strain_file;  //Strain tensor file.
FILE * ratio_file;   //Ratios file
FILE * details_file; //Useful file

int main(int argc, char *argv[]) {
    char word[MAXLENGTH]; // General String array used to
    read in position data.

    int number; // General integer variable used
    to read position.
    int z_no, r_no, phi_no; // Number of z values, etc.
    int EOF_check; // Used to check for EOF
    int disc_size; // Size of disc in number of
    points.
    int desired_mode; // Mode number on which info is
    wanted.
    double data, trace=0.0; // Used to collect data;
    temporary storage.
    double substrate=0.0, surface=0.0, barrel=0.0, coating_h=0.0,
    barrel_h=0.0; // Energies.
    double x,y,r,phi; // Used for polar conversion.
    double z_max,z_min, z_increment, r_max, r_increment,
    phi_increment, ax, bx, ay;
    double du_dyplus, du_dyneg, du_dxplus, du_dxneg, du_dzplus,

```

```

du_dzneg;
double du_dydash, du_dxdash, disp_max, disp_reduction;
double ** node_data; // Pointer to node data array.
double ** polar_node_data; // Pointer to node data
characterised as polars.
double * frequency; // Pointer to frequency array.
int * p; // Point details for point file.
double **** point; // Pointer to integer mapped
description;
char * map_extension=".map"; // Make result file into .map
file.
char * str_extension="_str.csv"; // Make result file into .str
file.
char * help_string="help";
char model_name[MAXLENGTH]; // To store name of model
char * map_file; // To store filename of .map file
char * str_file; // To store filename of .str file
char * rat_file="ani_energy_ratios.csv"; // To
store filename of .rat file
char * det_file="ani_point_details.csv"; // To store point info.
char switches[10]="\n";
char index1,index2,index3,index4; //Index names for printing
out properties
double ***** u; // Strain tensor
double ***** du; // Used to construct strain
tensor components.
double substrate_c[4][4][4][4]; // stiffness matrices for
substrate,
coating and barrel.
double coating_c[4][4][4][4];
double barrel_c[4][4][4][4];
double *** vol;

double *** area;

int number_of_nodes; // Obvious
int number_of_modes; // Ditto
int count,i,j,k,l,m; // Useful integers.

int ideas=0, append=0, mode_print=0, verbose=0, point_data=0,
centre=0, coating_thickness=0; //switches
int barrel_thickness=0, help=0, moduli=0, coating_moduli=0,
barrel_moduli=0, suspension_barrel_extent=0;

int z_start=0, z_finish=0, discs=0, slices=0; // switch
dependent variables

```

```

double r_large, r_small, substrate_E=0.0, substrate_sigma=0.0,
coating_E=0.0, coating_sigma=0.0;
double density=2202.0, G = 0.0, K = 0.0;
double barrel_E=0.0, barrel_sigma=0.0, barrel_extent=0.0,
surface_locn=0.0;

int r_count, phi_count, z_count, phi_total, z_disc=0;

// SET DEFAULT VALUES

for ( i=0 ; i<3 ; i++ ) {
  for ( j=0 ; j<3 ; j++ ) {
    for ( k=0 ; k<3 ; k++ ) {
      for ( l=0 ; l<3 ; l++ ) {
        substrate_c[i][j][k][l]=0;
        coating_c[i][j][k][l]=0;
        barrel_c[i][j][k][l]=0;
      }
    }
  }
}

coating_h=1e-5;           // Coating Thickness
barrel_h=coating_h;      // Barrel Thickness
substrate_E=7.2e10;      // Substrate Young's modulus
substrate_sigma=0.17;    // Substrate Poisson's ratio
coating_E=2.5e11;        // Coating Young's modulus
coating_sigma=0.25;      // Coating Poisson's Ratio
barrel_E=coating_E;      // Barrel Young's modulus
barrel_sigma=coating_sigma; // Barrel Poisson's Ratio

// Define property tensors

// READ SETTINGS FILE AOCEAN.INI
settings_file = fopen("aocean.ini", "r");
if ( !settings_file ) {
  printf("Settings file not found. Please find ocean.ini");
  return 0;
}

if ( (log_file=fopen("aocean.log", "w+")) == NULL ) {
  printf("Error opening log file");

```

```

return 0;
}
do { // Get model name
  EOF_check=fscanf(settings_file,"%s",word);
  if (EOF_check==EOF) {
    fprintf(log_file,"\nEnd of settings file reached\n");
    printf("\nEnd of settings file reached\n");
    return(0);
  }
} while ( strcmp(word,"model_name")!= 0 );

fscanf(settings_file,"%s",word);
strcpy ( model_name , word);
fprintf(log_file,"Model Name: %s\n",model_name);

if ( strstr( model_name, ".ml" )!=NULL ) {
  ideas = 0;
} else if ( strstr( model_name, ".unv" )!=NULL ){
  ideas = 1;
} else {
  fprintf(log_file,"File extension unknown. Should be
.ml(Algor) or .unv(I-DEAS)\n");
  return 0;
}

fprintf(log_file,"Using I-DEAS (1: Yes, 0: No) = %d\n",ideas);

mode_file = fopen(model_name, "r");
if ( !mode_file ) { // Checks whether file exists.
  fprintf(log_file,"File %s not found\n", model_name);
  printf("File %s not found.\n",model_name);
  return 0;
}

do { //Get mode numbers
  fscanf(settings_file,"%s",word);
  i = strcmp(word,"mode_number");
} while ( i != 0 );

fscanf(settings_file,"%d",&number);
fprintf(log_file,"Mode number = %d\n",number);

desired_mode = number;

do { //Get coating thickness

```

```

        fscanf(settings_file,"%s",word);
        i = strcmp(word,"coating_thickness");
    } while ( i != 0 );

    fscanf(settings_file,"%lf",&data);
    fscanf(settings_file,"%s",word);
    if ( strcmp(word,"barrel_thickness")!=0 ) {
        printf("\nSettings file corrupted; check it out, please.
\nWord found=%s",word);
        return 0;
    }

    fprintf(log_file,"Coating thickness = %1.0e m\n",data);

    coating_h = data;

    // Get Barrel thickness

    fscanf(settings_file,"%lf",&data);
    fscanf(settings_file,"%s",word);
    if ( strcmp(word,"substrate_properties")!=0 ) {
        fprintf(log_file,"Settings file corrupted (substrate
properties
may be missing); check it out, please. See help files for details");
        return 0;
    }

    fprintf(log_file,"Barrel thickness = %1.0e m\n",data);

    barrel_h = data;

    // Get substrate properties

    prop_assign(settings_file,log_file,substrate_c);

    fscanf(settings_file,"%s",word);
    if ( strcmp(word,"coating_properties")!=0 ) {
        fprintf(log_file,"Settings file corrupted (coating properties
may be missing); check it out, please. See help files for details");
        return 0;
    }

    prop_assign(settings_file,log_file,coating_c);

    fscanf(settings_file,"%s",word);
    if ( strcmp(word,"barrel_properties")!=0 ) {

```

```

        fprintf(log_file,"Settings file corrupted (barrel properties
may be missing); check it out, please. See help files for details");
        return 0;
    }

    prop_assign(settings_file,log_file,barrel_c);

    fprintf(log_file,"substrate properties\n");
    for ( i=0 ; i<3 ; i++ ) {
        for ( j=0 ; j<3 ; j++ ) {
            for ( k=0 ; k<3 ; k++ ) {
                for ( l=0 ; l<3 ; l++ ) {
                    switch (i) {
                        case 0:
                            index1='x';
                            break;
                        case 1:
                            index1='y';
                            break;
                        case 2:
                            index1='z';
                            break;
                    }

                    switch (j) {
                        case 0:
                            index2='x';
                            break;
                        case 1:
                            index2='y';
                            break;
                        case 2:
                            index2='z';
                            break;
                    }

                    switch (k) {
                        case 0:
                            index3='x';
                            break;
                        case 1:
                            index3='y';
                            break;
                        case 2:
                            index3='z';
                            break;
                    }
                }
            }
        }
    }

```

```

switch (l) {
  case 0:
    index4='x';
    break;
  case 1:
    index4='y';
    break;
  case 2:
    index4='z';
    break;
}

fprintf(log_file,
        "substrate_c[%c] [%c] [%c] [%c]=%1.3e\n"
        ,index1,index2,index3,index4,substrate_c[i][j][k][l]);
}
}
}

```

```

fprintf(log_file,"Coating properties\n");
for ( i=0 ; i<3 ; i++ ) {
  for ( j=0 ; j<3 ; j++ ) {
    for ( k=0 ; k<3 ; k++ ) {
      for ( l=0 ; l<3 ; l++ ) {
        switch (i) {
          case 0:
            index1='x';
            break;
          case 1:
            index1='y';
            break;
          case 2:
            index1='z';
            break;
        }

        switch (j) {
          case 0:
            index2='x';
            break;
          case 1:
            index2='y';

```

```

break;
  case 2:
    index2='z';
    break;
}
switch (k) {
  case 0:
    index3='x';
    break;
  case 1:
    index3='y';
    break;
  case 2:
    index3='z';
    break;
}

switch (l) {
  case 0:
    index4='x';
    break;
  case 1:
    index4='y';
    break;
  case 2:
    index4='z';
    break;
}

```

```

fprintf(log_file,"Coating_c[%c] [%c] [%c] [%c]=%1.3e\n",
        index1,index2,index3,index4,coating_c[i][j][k][l]);
}
}
}

```

```

fprintf(log_file,"Barrel properties\n");
for ( i=0 ; i<3 ; i++ ) {
  for ( j=0 ; j<3 ; j++ ) {
    for ( k=0 ; k<3 ; k++ ) {
      for ( l=0 ; l<3 ; l++ ) {
        switch (i) {
          case 0:
            index1='x';

```

```

        break;
    case 1:
        index1='y';
        break;
    case 2:
        index1='z';
        break;
}

switch (j) {
    case 0:
        index2='x';
        break;
    case 1:
        index2='y';
        break;
    case 2:
        index2='z';
        break;
}

switch (k) {
    case 0:
        index3='x';
        break;
    case 1:
        index3='y';
        break;
    case 2:
        index3='z';
        break;
}

switch (l) {
    case 0:
        index4='x';
        break;
    case 1:
        index4='y';
        break;
    case 2:
        index4='z';
        break;
}

```

```

        fprintf(log_file,"Barrel_c[%c] [%c] [%c] [%c]=%1.3e\
n",index1,index2,index3,index4,barrel_c[i] [j] [k] [l]);
    }
}

do { //Get number of barrel slices
    fscanf(settings_file,"%s",word);
    i = strcmp(word,"barrel_extent");
} while ( i != 0 );

fscanf(settings_file,"%lf",&data);
fprintf(log_file,"Slices down barrel = %lf\n",data);

barrel_extent = data;

do { //Location down mass for surface
    fscanf(settings_file,"%s",word);
    i = strcmp(word,"surface_locn");
} while ( i != 0 );

fscanf(settings_file,"%lf",&data);
fprintf(log_file,"Fraction down mass for surface = %lf\n",data);

surface_locn = data;

do { //Get append switch
    fscanf(settings_file,"%s",word);
    i = strcmp(word,"append");
} while ( i != 0 );

fscanf(settings_file,"%d",&number);
fprintf(log_file,"Append (0 = No, 1=Yes) = %d\n",number);

append = number;

do { //Get mode_print switch
    fscanf(settings_file,"%s",word);
    i = strcmp(word,"mode_print");

```

```

} while ( i != 0 );

fscanf(settings_file,"%d",&number);
fprintf(log_file,"Print Mode Number (0 = No, 1=Yes) =
%d\n",number);

mode_print = number;

do { //Get point_data switch
    fscanf(settings_file,"%s",word);
    i = strcmp(word,"point_data");
} while ( i != 0 );

fscanf(settings_file,"%d",&number);
fprintf(log_file,"Request Co-ordinate data (0 = No, 1=Yes) =
%d\n",number);

point_data = number;

if ( point_data ) {
    p = (int * ) malloc ( 21 * sizeof ( int ));
    fprintf(log_file,"\nCo-ordinates of point of interest
(r,phi,z):\n");

    do { //Get r co-ord
        fscanf(settings_file,"%s",word);
        i = strcmp(word,"");
    } while ( i != 0 );
    fscanf(settings_file,"%d",&number);
    fprintf(log_file,"%d",number);
    p[0]=number;

    do { //Get phi co-ord
        fscanf(settings_file,"%s",word);
        i = strcmp(word,"");
    } while ( i != 0 );
    fscanf(settings_file,"%d",&number);
    fprintf(log_file,"%d",number);
    p[1]=number;

    do { //Get z co-ord
        fscanf(settings_file,"%s",word);
        i = strcmp(word,"");
    } while ( i != 0 );

```

```

    fscanf(settings_file,"%d",&number);
    fprintf(log_file,"%d",number);
    p[2]=number;
}

if( fclose(log_file)!=0 ) // Don't need settings
file now.
    printf("Error closing file \n" );

if( fclose(settings_file)!=0 ) // Don't need
settings file now.
    printf("Error closing file \n" );

// FINISHED READING SETTINGS FILE

printf("Anisotropic Ocean (c)2001 University of Glasgow, all
rights reserved\nView aocean.log for details of run\n");

// BEGIN READING MODEL FILE

// Get number of nodes

do {
    fscanf(mode_file,"%s",word); // Looks for
(NUMNP)
    i = strcmp(word,"(NUMNP)");
} while ( i != 0 );

fscanf(mode_file,"%s",word); // Looks for
"="
fscanf(mode_file,"%d", &number); // To get
number of nodes
number_of_nodes=number;

if ( (log_file=fopen("aocean.log", "a+")) == NULL) {
    printf("Error opening log file");
    return 0;
}
fprintf(log_file,"Number of Nodes is :%d \n",number_of_nodes);
if( fclose(log_file)!=0 ) // Don't need settings
file now.
    printf("Error closing file \n" );

```

```

// Get number of modes
do {
  fscanf(mode_file,"%s",word);
(NF)                                     // Looks for
  i = strcmp(word,"(NF)");
} while ( i != 0 );

fscanf(mode_file,"%s",word);
"="                                     // Looks for
fscanf(mode_file,"%d", &number);
// To get
number of modes
number_of_modes=number;

if ( (log_file=fopen("aocean.log", "a+")) == NULL) {
  printf("Error opening log file");
  return 0;
}
fprintf(log_file,"Number of Modes is :%d \n",number_of_modes);
if( fclose(log_file)!=0 )
file now.                               // Don't need settings
  printf("Error closing file \n" );

if ( (log_file=fopen("aocean.log", "a+")) == NULL) {
  printf("Error opening log file");
  return 0;
}
fprintf(log_file,"Read Nodes and Modes\n");
if( fclose(log_file)!=0 )
  printf("Error closing file \n" );

// Set up necessary arrays/ perform error traps on settings

if ( desired_mode>number_of_modes || desired_mode<=0) {
  if ( (log_file=fopen("aocean.log", "a+")) == NULL) {
    printf("Error opening log file");
    return 0;
  }
  fprintf(log_file,"Mode number out of bounds");
  return 0;
  if( fclose(log_file)!=0 )
    printf("Error closing file \n" );
}

node_data = (double **) malloc (number_of_nodes *

```

```

sizeof(double*)); // Initialise data
for ( i=0 ; i<number_of_nodes ; i++ ) {
  // array.
  node_data[i] = (double *) malloc (6*sizeof(double));
}

polar_node_data = (double **) malloc (number_of_nodes *
sizeof(double*)); // Initialise
for ( i=0 ; i<number_of_nodes ; i++ ) {
  // polar co-ord array.
  polar_node_data[i] = (double *) malloc (6*sizeof(double));
}

frequency = (double * ) malloc ( number_of_modes *
sizeof(double)); // Init freq array

if (!ideas) {
  for ( i=0 ; i<4 ; i++ ){
    do {
      fscanf(mode_file,"%s",word);
Looks for underline                               //
      j = strcmp(word,"-----");
    } while ( j != 0 );
  }
}

if ( (log_file=fopen("aocean.log", "a+")) == NULL) {
  printf("Error opening log file");
  return 0;
}
for ( count=0 ; count<number_of_nodes ; count++ ) {
// Main node data
  i=0;
// loop.
  if ( ideas ) {
    j=4;
  } else {
    j=7;
  }

  do {
and boundary condns.                               // Pass over node number

```

```

        fscanf(mode_file,"%d",&number); //
        i++; //
    } while ( i<j );
    for ( i=0 ; i<3 ; i++ ) { // Actually take data.
        fscanf(mode_file,"%lf",&data);
        node_data [count][i] = data;
    }
    fprintf(log_file,"node %d\n",count);
    if ( !ideas ) {
        fscanf(mode_file,"%lf",&data); // Passes over time
value
    }
}

if( fclose(log_file)!=0 )
    printf("Error closing file \n" );

if ( (log_file=fopen("aocean.log", "a+")) == NULL) {
    printf("Error opening log file");
    return 0;
}
fprintf(log_file,"Read Node values\n");
if( fclose(log_file)!=0 )
    printf("Error closing file \n" );

//Mode search

if ( verbose ) printf("\nLooking for mode %d\n",desired_mode);

do {
    fscanf(mode_file,"%s",word); // Looks for
mode 1
    i = strcmp(word,"Displacements/Rotations(degrees)");
} while ( i != 0 );

for ( i=0 ; i<3 ; i++ ) { //Looks for rotation 3
times
    do {
        fscanf(mode_file,"%s",word);
        j = strcmp(word,"rotation");
    } while ( j != 0 );
}

```

```

if ( desired_mode!=1 ) {
    if ( (log_file=fopen("aocean.log", "a+")) == NULL) {
        printf("Error opening log file");
        return 0;
    }
    fprintf(log_file,"Not mode 1...\n");
    if( fclose(log_file)!=0 )
        printf("Error closing file \n" );
    if ( !ideas ) {
        do {
            do {
                fscanf(mode_file,"%s",word);
// Looks for ANALYSIS
                i = strcmp(word,"ANALYSIS");
            } while ( i != 0 );

            do {
                fscanf(mode_file,"%s",word);
// Looks for number
                i = strcmp(word,"number");
            } while ( i != 0 );
            fscanf(mode_file,"%s",word);
// "="

            fscanf(mode_file,"%d", &number);
            for ( i=0 ; i<3 ; i++ ) { //Looks for
rotation 3 times
                do {
                    fscanf(mode_file,"%s",word);

                    j = strcmp(word,"rotation");
                } while ( j != 0 );
            } while ( number!=desired_mode );
        } else {
            do {
                do {
                    fscanf(mode_file,"%s",word);
// Looks for Shape
                    i = strcmp(word,"Shape");
                } while ( i != 0 );
            }
        }
    }
}

```

```

        fscanf(mode_file,"%d", &number);
        if ( (log_file=fopen("aocean.log", "a+")) == NULL) {
            printf("Error opening log file");
            return 0;
        }
        fprintf(log_file,"Mode number:%d\n",number);
        if( fclose(log_file)!=0 )
            printf("Error closing file \n" );

        do {
            fscanf(mode_file,"%s",word);
            j = strcmp(word,"ds");
        } while ( j != 0 );
    } while ( number!=desired_mode );
}

if ( (log_file=fopen("aocean.log", "a+")) == NULL) {
    printf("Error opening log file");
    return 0;
}
fprintf(log_file,"\nReading Data from Mode number: %d\n",number);

for ( count=0 ; count<number_of_nodes ; count++ ) { // Main
displacement data loop
    fscanf(mode_file,"%d",&number);

    for ( i=3 ; i<6 ; i++ ) { // Actual
Values
        fscanf(mode_file,"%lf",&data);
        node_data[count][i] = data;
    }

    x=node_data[count][X]; // Polar
conv.
    y=node_data[count][Y]; // done on
the fly...
    r=sqrt(x*x + y*y);
    phi=atan2(y,x);
    if ( phi<0 ) phi += ( 2.0*PI ); // Want all
phi's to be +ve
    if ( fabs(phi-( 2.0*PI ))<=1e-6 ) phi=0.0; // Different dps
mean might not be the same
    polar_node_data[count][R]=r;
    fprintf(log_file,"%lf",r);

```

```

        polar_node_data[count][PHI]=phi;
        fprintf(log_file,"%lf",phi);
        polar_node_data[count][Z]=node_data[count][Z];
        fprintf(log_file,"%lf\n",node_data[count][Z]);

        polar_node_data[count][DX]=node_data[count][DX];
        polar_node_data[count][DY]=node_data[count][DY];
        polar_node_data[count][DZ]=node_data[count][DZ];

        if ( verbose && count%((int)(number_of_nodes/20))==0)
        printf(".");

        for ( i=0 ; i<3 ; i++ ) {
            fscanf(mode_file,"%lf",&data); //Skip over
rotation values (constrained)
        }

    }
    if( fclose(log_file)!=0 )
        printf("Error closing file \n" );

    if ( (log_file=fopen("aocean.log", "a+")) == NULL) {
        printf("Error opening log file");
        return 0;
    }
    fprintf(log_file,"Reading Node data successful.\n");
    if( fclose(log_file)!=0 )
        printf("Error closing file \n" );

    // End of displacement entry

    // Find modal frequency

    if (!ideas) {
        for ( count=0 ; count<4 ; count++ ) {
            do {
                fscanf(mode_file,"%s",word);
                //-----"*4
                j = strcmp(word,"-----");
            } while ( j != 0 );
        }
        for ( count=0 ; count<number_of_modes ; count++ ) {
            fscanf(mode_file,"%lf",&data);

```

```

        fscanf(mode_file,"%lf",&data);
        fscanf(mode_file,"%lf",&data);
        frequency[count] = data;
        fscanf(mode_file,"%lf",&data);
        fscanf(mode_file,"%lf",&data);
    }

    if ( (log_file=fopen("aocean.log", "a+")) == NULL) {
        printf("Error opening log file");
        return 0;
    }
    fprintf(log_file,"Mode frequency: %1.0lf
Hz\n",frequency[desired_mode-1]);
    if( fclose(log_file)!=0 )
        printf("Error closing file \n" );
}

    for ( count=0 ; count<number_of_nodes ; count++ ) { // We no
longer require node_data
        free(node_data[count]);
    }
    free(node_data);

    if( fclose(mode_file)!=0 ) // Don't need
mode_file now.
        printf("Error closing file %s\n",mode_file );

    // Determine useful quantities like z_max, z_increment and so
on...

    if (!ideas ) {
        z_max=polar_node_data[number_of_nodes-1][Z];
        count=0;
        do {
            z_increment=polar_node_data[count][Z];
        }
        while(z_increment==0.0);
    } else {
        z_max=fabs(polar_node_data[0][Z]);
        for ( count=0 ; count<number_of_nodes ; count++ ) {
            if ( fabs(polar_node_data[count][Z])>z_max )
z_max=fabs(polar_node_data[count][Z]);
        }

        z_min=polar_node_data[0][Z];

```

```

        for ( count=0 ; count<number_of_nodes ; count++ ) {
            if ( polar_node_data[count][Z]<z_min )
z_min=polar_node_data[count][Z];
        }

        if ( z_min<0.0 ) {
            for ( count=0 ; count<number_of_nodes ; count++ ) {
                polar_node_data[count][Z]+=z_max;
            }
        }

        z_min=polar_node_data[0][Z];
        for ( count=0 ; count<number_of_nodes ; count++ ) {
            if ( polar_node_data[count][Z]<z_min )
z_min=polar_node_data[count][Z];
        }

        z_increment=z_max;
        for ( count=0 ; count<number_of_nodes; count++ ) { //Find
increment of z.
            if ( fabs(polar_node_data[count][Z]-0.0)>1e-7 ) {
                if ( fabs(polar_node_data[count][Z])<z_increment )
z_increment=fabs(polar_node_data[count][Z]);
            }
        }
    }

    if ( (log_file=fopen("aocean.log", "a+")) == NULL) {
        printf("Error opening log file");
        return 0;
    }
    fprintf(log_file,"Found z_max,z_increment.\n");
    fprintf(log_file,"z max: %lf m\n",z_max);
    fprintf(log_file,"z min: %lf m\n",z_min);
    fprintf(log_file,"z increment: %lf m\n",z_increment);
    if( fclose(log_file)!=0 )
        printf("Error closing file \n" );

    disc_size=count-1;
    r_max=polar_node_data[0][R]; //Find r_max within
disc.
    if ( !ideas ) {
        for ( count=0 ; count<disc_size ; count++ ) {
            if ( polar_node_data[count][R]>r_max )
r_max=polar_node_data[count][R];

```

```

    }
  } else {
    for ( count=0 ; count<number_of_nodes ; count++ ) {
      if ( fabs(polar_node_data[count][Z]-0.0)<1e-7 ) {
        if ( polar_node_data[count][R]>r_max )
          r_max=polar_node_data[count][R];
      }
    }
  }

  r_increment=r_max;
  if ( !ideas ) {
    for ( count=0 ; count<disc_size; count++ ) { //Find
increment of r.
      if ( fabs(polar_node_data[count][R]-0.0)>1e-7 ) {
        if ( polar_node_data[count][R]<r_increment )
          r_increment=polar_node_data[count][R];
      }
    }
  } else {
    for ( count=0 ; count<number_of_nodes; count++ ) { //Find
increment of r.
      if ( fabs(polar_node_data[count][Z]-0.0)<1e-7 ) {
        if ( fabs(polar_node_data[count][R]-0.0)>1e-7 ) {
          if ( polar_node_data[count][R]<r_increment )
            r_increment=polar_node_data[count][R];
        }
      }
    }
  }

  phi_increment=PI;
  if ( !ideas ) {
    for ( count=0 ; count<disc_size; count++ ) { // Increment
of phi.
      if ( fabs(polar_node_data[count][PHI]-0.0)>1e-7 ) {
        if ( polar_node_data[count][PHI]<phi_increment )
          phi_increment=polar_node_data[count][PHI];
      }
      //printf("%lf %lf\n",polar_node_data[count][PHI],
phi_increment);
    }
  } else {

```

```

    for ( count=0 ; count<number_of_nodes; count++ ) { //
Increment of phi.
      if ( fabs(polar_node_data[count][Z]-0.0)<1e-7 ) {
        if ( fabs(polar_node_data[count][PHI]-0.0)>1e-7 ) {
          if ( polar_node_data[count][PHI]<phi_increment )
            phi_increment=polar_node_data[count][PHI];
        }
        //printf("%lf %lf\n",polar_node_data[count][PHI],
phi_increment);
      }
    }

    if ( (log_file=fopen("aocean.log", "a+")) == NULL) {
      printf("Error opening log file");
      return 0;
    }
    fprintf(log_file,"r max: %lf m\n",r_max);
    fprintf(log_file,"r increment: %lf m\n",r_increment);
    fprintf(log_file,"phi increment: %lf m\n",phi_increment);
    if( fclose(log_file)!=0 )
      printf("Error closing file \n" );

    z_no = round(z_max/z_increment)+1; // Determine no of z points
    r_no = round(r_max/r_increment)+1; // Ditto r
    phi_no = round(2*PI/phi_increment); // Ditto phi
    phi_total = phi_no-1; // Useful for cyclic angles
later.
    z_disc = z_no-1;

    if ( (log_file=fopen("aocean.log", "a+")) == NULL) {
      printf("Error opening log file");
      return 0;
    }
    fprintf(log_file,"r points: %d\n",r_no);
    fprintf(log_file,"phi points: %d\n",phi_no);
    fprintf(log_file,"discs: %d\n",z_no);
    if( fclose(log_file)!=0 )
      printf("Error closing file \n" );

    if ( point_data ) {

```

```

        if ( p[0]<0 || p[0]>r_no-1 ) {
            fprintf(log_file,"\nPoint co-ordinates out of bounds:
r");
            point_data = 0;
        }

        if ( p[1]<0 || p[1]>phi_no-1 ) {
            fprintf(log_file,"\nPoint co-ordinates out of bounds:
phi");
            point_data = 0;
        }

        if ( p[2]<0 || p[2]>z_no-1 ) {
            fprintf(log_file,"\nPoint co-ordinates out of bounds:
z");
            point_data = 0;
        }
    }
}

```

... as for Ocean until ...

```

// substrate ENERGY CALCULATION

data = 0.0;

if ( centre ) {
    printf("\nHow many discs on either side of centre to
calculate energy: (Number of discs inc. z=0:%d)",z_no);
    scanf("%d",&discs);
    z_start=round((z_no-1)/2)-discs;
    z_finish=round((z_no-1)/2)+discs+1;
    printf("Start disc: %d \nFinish disc:
%d",z_start,z_finish-1);
} else {
    z_start=0;
    z_finish=z_no;
}

for ( z_count=z_start ; z_count<z_finish ; z_count++ ) {
//Energy calculation.

```

```

        for ( r_count=0 ; r_count<r_no ; r_count++ ) {
            for ( phi_count=0 ; phi_count<phi_no ; phi_count++ ) {
                if ( ! ( r_count==0 && phi_count!=0 ) ) {

                    for ( i=0 ; i<3 ; i++ ) {
                        for ( j=0 ; j<3 ; j++ ) {
                            for ( k=0 ; k<3 ; k++ ) {
                                for ( l=0 ; l<3 ; l++ ) {
                                    data +=
substrate_c[i][j][k][l]*u[r_count][phi_count][z_count][i][j]
*u[r_count][
phi_count][z_count][k][l];
                                }
                            }
                        }
                    }

                    substrate +=
vol[r_count][phi_count][z_count]*0.5*data;

                    data = 0.0;

                }
            }
        }

        if ( !append ) {
            if( (ratio_file = fopen( rat_file , "w+" )) != NULL ) {
                fprintf(ratio_file,"Mode Number =
%d\n\n",desired_mode);
                fprintf(ratio_file,"Number of nodes,substrate
Energy,Surface Energy,Surface Ratio,Barrel Energy, Barrel Ratio\n");
                fprintf(ratio_file,"%d,%e,",number_of_nodes,substrate);
                if( fclose( ratio_file ) ) printf("\n%s not closed
properly",rat_file);
                else if ( verbose ) printf("\n%s closed
correctly.",rat_file);
            }
        } else {
            if( (ratio_file = fopen( rat_file , "a+" )) != NULL ) {
                if ( mode_print ) {
                    fprintf(ratio_file,"\nMode Number =
%d\n\n",desired_mode);
                    fprintf(ratio_file,"Number of nodes,substrate

```

```

Energy, Surface Energy, Surface Ratio, Barrel Energy, Barrel Ratio\n");
}
    fprintf(ratio_file, "%d,%e,", number_of_nodes,
    substrate);
    if( fclose( ratio_file ) ) printf("\n%s not closed
properly", rat_file);
    else if ( verbose ) printf("\n%s closed
correctly.", rat_file);
    }
    }

// SURFACE ENERGY

data = 0.0;
trace = 0.0;

if ( surface_locn!=0.0 ) {
    z_count = round((z_no-1)*(1-surface_locn));
} else {
    z_count = z_disc;
}
for ( r_count=0 ; r_count<r_no ; r_count++ ) {
    for ( phi_count=0 ; phi_count<phi_no ; phi_count++ ) {
        if ( ! ( r_count==0 && phi_count!=0 ) ) {
            for ( i=0 ; i<3 ; i++ ) {
                for ( j=0 ; j<3 ; j++ ) {
                    for ( k=0 ; k<3 ; k++ ) {
                        for ( l=0 ; l<3 ; l++ ) {
                            data +=
coating_c[i][j][k][l]*u[r_count][phi_count][z_count][i][j]*u[r_count]
[phi_count][z_count][k][l];
                        }
                    }
                }
            }
            surface +=
coating_h*area[r_count][phi_count][z_count]*0.5*data;
            data = 0.0;
        }
    }
}
}

```

```

if( (ratio_file = fopen( rat_file , "a+" )) != NULL ) {
    fprintf(ratio_file, "%e,%e,", surface,
    surface/substrate);
    if( fclose( ratio_file ) ) printf("\n%s not closed
properly", rat_file);
    else if ( verbose ) printf("\n%s closed
correctly.", rat_file);
    }

// BARREL ENERGY

data = 0.0;
trace = 0.0;

if ( barrel_extent!=-1 ) {
    slices = round(barrel_extent/z_increment);
    z_start=z_no-1-slices;
} else {
    z_start=0;
}

if ( (log_file=fopen("aocean.log", "a+")) == NULL) {
    printf("Error opening log file");
    return 0;
}
fprintf(log_file, "Start disc: %d \nSlices: %d", z_start, slices);
if( fclose(log_file)!=0 )
    printf("Error closing file \n" );

r_count=r_no-1;
for ( z_count=z_start ; z_count<z_no ; z_count++ ) {
    for ( phi_count=0 ; phi_count<phi_no ; phi_count++ ) {
        if ( ! ( r_count==0 && phi_count!=0 ) ) {
            for ( i=0 ; i<3 ; i++ ) {
                for ( j=0 ; j<3 ; j++ ) {
                    for ( k=0 ; k<3 ; k++ ) {
                        for ( l=0 ; l<3 ; l++ ) {
                            data +=
barrel_c[i][j][k][l]*u[r_count][phi_count][z_count][i][j]*u[r_count][
phi_count][z_count][k][l];
                        }
                    }
                }
            }
        }
    }
}
}
}

```

```

        if ( z_count==0 || z_count==z_no-1 ) {
            barrel +=
barrel_h*z_increment*0.5*r_max*phi_increment*0.5*data;
        } else {
            barrel +=
barrel_h*z_increment*r_max*phi_increment*0.5*data;
        }

        data = 0.0;
    }

}

if( (ratio_file = fopen( rat_file , "a+" )) != NULL ) {
    fprintf(ratio_file,"%e,%e\n", barrel,
barrel/substrate);
    if( fclose( ratio_file ) ) printf("\n%s not closed
properly",rat_file);
    else if ( verbose ) printf("\n%s closed
correctly.",rat_file);
}

// RADIAL SUSPENSION POINT KINETIC ENERGY

barrel = 0.0;
data = 0.0;
trace = 0.0;

r_count=r_no-1;
z_count=round((z_no-1)/2);

for ( phi_count=0 ; phi_count<phi_no ; phi_count++ ) {

    for ( i=3 ; i<5 ; i++ ) {
        data +=
point[r_count][phi_count][z_count][i]*point[r_count][phi_count][
z_count][i];// dx^2 + dy^2
    }

    data =
4*PI*PI*frequency[desired_mode-1]*frequency[desired_mode-1]*data;
// v^2

    barrel += barrel_h*barrel_h*r_max*phi_increment*density*data;
    data = 0.0;
}

```

```

}

if( (ratio_file = fopen( rat_file , "a+" )) != NULL ) {
    fprintf(ratio_file,"%e,%e", barrel,
barrel/substrate);
    if( fclose( ratio_file ) ) printf("\n%s not closed
properly",rat_file);
    else if ( verbose ) printf("\n%s closed
correctly.",rat_file);
}

// LONGITUDINAL SUSPENSION POINT KINETIC ENERGY

barrel = 0.0;
data = 0.0;
trace = 0.0;

r_count=r_no-1;
z_count=round((z_no-1)/2);

for ( phi_count=0 ; phi_count<phi_no ; phi_count++ ) {
    data +=
point[r_count][phi_count][z_count][DZ]*point[r_count][phi_count][
z_count][DZ];// dz^2
    data =
4*PI*PI*frequency[desired_mode-1]*frequency[desired_mode-1]*data;
// v^2

    barrel += barrel_h*barrel_h*r_max*phi_increment*density*data;
    data = 0.0;
}

if( (ratio_file = fopen( rat_file , "a+" )) != NULL ) {
    fprintf(ratio_file,"%e,%e\n", barrel,
barrel/substrate);
    if( fclose( ratio_file ) ) printf("\n%s not closed
properly",rat_file);
    else if ( verbose ) printf("\n%s closed
correctly.",rat_file);
}

... as for Ocean until ...

```

```

//end of main() function

void prop_assign(FILE *settings_file, FILE *log, double c[][4][4][4])
{
    char word[MAXLENGTH];
    char character[3];
    int index[4];
    int number, i;
    double data;
    fscanf(settings_file,"%s",word);
    if ( word[0] == 'c' && strlen(word)==3 ) {
        do {
            fprintf(log,"%s\t",word);
            for ( i=1 ; i<3 ; i++ ) {
                sprintf(character,"%c\n",word[i]);
                number=atoi(character);
                switch(number) {
                    case 1:
                        index[2*(i-1)]=0;
                        index[2*i-1]=0;
                        break;
                    case 2:
                        index[2*(i-1)]=1;
                        index[2*i-1]=1;
                        break;
                    case 3:
                        index[2*(i-1)]=2;
                        index[2*i-1]=2;
                        break;
                    case 4:
                        index[2*(i-1)]=1;
                        index[2*i-1]=2;
                        break;
                    case 5:
                        index[2*(i-1)]=0;
                        index[2*i-1]=2;
                        break;
                    case 6:
                        index[2*(i-1)]=0;
                        index[2*i-1]=1;
                        break;
                }
            }
        }
    }
}

```

```

fscanf(settings_file,"%lf",&data);
fscanf(settings_file,"%s",word);

fprintf(log,"%1.3e\n",data);

c[index[0]][index[1]][index[2]][index[3]]=data;

c[index[1]][index[2]][index[3]][index[0]]=data; // C
tensor is cyclic...
c[index[2]][index[3]][index[0]][index[1]]=data;
c[index[3]][index[0]][index[1]][index[2]]=data;

c[index[1]][index[0]][index[2]][index[3]]=data; // ...and
symmetric
c[index[0]][index[1]][index[3]][index[2]]=data;
c[index[1]][index[0]][index[3]][index[2]]=data;
fprintf(log,"c[%d] [%d] [%d] [%d]=%1.3e\n",index[0],index[1]
,index[2],index[3],data);

        } while ( word[0]!='c' );
        if ( strcmp(word,"")!=0) fprintf(log,"Settings file
corrupt");

    }
}

int round(double floating_point_number) {
    int result;
    result=(int) (floating_point_number+0.5);
    return result;
}

```

Appendix G

Additional Papers

1. **“Excess mechanical loss associated with dielectric mirror coatings on test masses in interferometric gravitational wave detectors”**

D.R.M. Crooks, P.H. Sneddon, G. Cagnoli, J. Hough, S. Rowan, M.M. Fejer, E. Gustafson, R. Route, N. Nakagawa, D. Coyne, G.M. Harry and A.M. Gretarsson. *Classical and Quantum Gravity*, 19(5):883-896, 2002

2. **“Thermal noise in interferometric gravitational wave detectors due to dielectric optical coatings”**

G.M. Harry, A.M. Gretarsson, P.R. Saulson, S.E. Kittelberger, S.D. Penn, W.J. Startin, S. Rowan, M.M. Fejer, D.R.M. Crooks, G. Cagnoli, J. Hough and N. Nakagawa. *Classical and Quantum Gravity*. 19(5):897-917, 2002

3. **“The GEO 600 gravitational wave detector”**

B. Willke, P. Aufmuth, C. Aulbert, S. Babak, R. Balasubramanian, B.W. Barr, S. Berukoff, S. Bose, G. Cagnoli, M.M. Casey, D. Churches, D. Clubley, C. N. Colacino, D.R.M. Crooks, C. Cutler, K. Danzmann, R.

Davies, R. Dupuis, E. Elliffe, C. Fallnich, A. Freise, S. Goßler, A. Grant, H. Grote, G. Heinzel, A. Heptonstall, M. Heurs, M. Hewitson, J. Hough, O. Jennrich, K. Kawabe, K. Kötter, V. Leonhardt, H. Lück, M. Malec, P.W. McNamara, S.A. McIntosh, K. Mossavi, S. Mohanty, S. Mukherjee, S. Nagano, G.P. Newton, B.J. Owen, D. Palmer, M.A. Papa, M.V. Plissi, V. Quetschke, D.I. Robertson, N.A. Robertson, S. Rowan, A. Rüdiger, B.S. Sathyaprakash, R. Schilling, B.F. Schutz, R. Senior, A.M. Sintes, K.D. Skeldon, P. Sneddon, F. Stief, K.A. Strain, I. Taylor, C.I. Torrie, A. Vecchio, H. Ward, U. Weiland, H. Welling, P. Williams, W. Winkler, G. Woan, and I. Zawischa. *Classical and Quantum Gravity*. 19(7):1377. 2002

4. **“Quadruple suspension design for Advanced LIGO”**

N.A. Robertson, G. Cagnoli, D.R.M. Crooks, E. Elliffe, J.E. Faller, P. Fritschel, S. Goßler, A. Grant, A. Heptonstall, J. Hough, H. Lück, R. Mittleman, M. Perreux-Lloyd, M.V. Plissi, S. Rowan, D.H. Shoemaker, P.H. Sneddon, K.A. Strain, C.I. Torrie, H. Ward and P. Willems. *Classical and Quantum Gravity*, 19(15):4043-4058, 2002

5. **“Silica research in Glasgow”**

B.W. Barr, G. Cagnoli, M.M. Casey, D. Clubley, D.R.M. Crooks, K. Danzmann, E.J. Elliffe, S. Goßler, A. Grant, H. Grote, A. Heptonstall, J. Hough, O. Jennrich, H. Lück, S.A. McIntosh, G.P. Newton, D.A. Palmer, M.V. Plissi, D.I. Robertson, N.A. Robertson, S. Rowan, K.D. Skeldon, P.H. Sneddon, K.A. Strain, C.I. Torrie, H. Ward, P.A. Willems, B. Willke and W. Winkler. *Classical and Quantum Gravity*. 19(7):1655-1662. 2002

Excess mechanical loss associated with dielectric mirror coatings on test masses in interferometric gravitational wave detectors

D R M Crooks¹, P Sneddon¹, G Cagnoli¹, J Hough¹, S Rowan²,
M M Fejer², E Gustafson², R Route², N Nakagawa³, D Coyne⁴,
G M Harry^{5,6} and A M Gretarsson⁶

¹ Department of Physics and Astronomy, University of Glasgow, Glasgow G12 8QQ, UK

² Edward L Ginzton Laboratory, Stanford University, Stanford, CA 94305-4085, USA

³ Centre for Nondestructive Evaluation, Institute for Physical Research and Technology,
Iowa State University, Ames, IA 50011, USA

⁴ LIGO Laboratory, California Institute of Technology, Pasadena, CA 91125, USA

⁵ LIGO Laboratory, Massachusetts Institute of Technology, Room NW17-161,
175 Albany Street, Cambridge, MA 02139, USA

⁶ Department of Physics, Syracuse University, Syracuse, NY 13244-1130, USA

Received 26 November 2001

Published 12 February 2002

Online at stacks.iop.org/CQG/19/883

Abstract

Interferometric gravitational wave detectors use mirrors whose substrates are formed from materials of low intrinsic mechanical dissipation. The two most likely choices for the test masses in future advanced detectors are fused silica or sapphire (Rowan *S et al* 2000 *Phys. Lett. A* 265 5). These test masses must be coated to form mirrors, highly reflecting at 1064 nm. We have measured the excess mechanical losses associated with adding dielectric coatings to substrates of fused silica and calculated the effect of the excess loss on the thermal noise in an advanced interferometer.

PACS numbers: 0480N, 6240, 7755, 9555Y

1. Introduction

Interferometric gravitational wave detectors use laser interferometry to sense the position of test masses coated as mirrors, suspended as pendulums and highly isolated from external disturbances. Across part of the frequency range of interest for gravitational wave detection, thermal noise from the test masses and their suspensions forms a limit to achievable detector sensitivity [1–6]. To minimize the thermal noise from the test masses, substrate materials of low intrinsic loss are desirable. All the detectors currently under construction use fused

silica as the substrate material, due to a combination of its properties including relatively low mechanical loss, availability in suitably sized pieces and ease of polish. To benefit from the low intrinsic dissipation of the substrates all sources of excess mechanical loss associated with using the substrates as suspended mirrors should be minimized [7, 8]. The multilayer dielectric coatings which are applied to each substrate to form mirror coatings are a potential source of excess dissipation, and we present here measurements of the excess dissipation associated with typical coatings. To assess the level of dissipation, the loss factors of samples of fused silica with dielectric coatings were measured. Similar measurements on substrates of different geometry and with a coating of different constituents were simultaneously carried out by a subset of the authors at Syracuse University and are published in an accompanying paper. From these measurements it is possible to estimate values for the mechanical loss associated with the dielectric coatings. Using the papers of Nakagawa *et al* [9, 10] the effect of this loss on the expected sensitivity of advanced gravitational wave detectors may then be calculated.

For advanced detectors sapphire is also under consideration as a substrate material, since it can have an intrinsic dissipation even lower than fused silica. Mechanical losses associated with adding coatings to sapphire substrates are a subject of ongoing research.

2. Experimental measurements on fused silica samples

Two coated fused silica samples were studied, each being a right circular cylinder of 0.127 m diameter and 0.103 m height. The first sample was made from Corning 7980 fused silica (grade 0C) and the second from Corning 7940 fused silica (3G). Each sample was polished by General Optics Inc.⁷, having faces super-polished to sub-angstrom roughness levels and barrels with an inspection polish. Dielectric coatings were applied to each face of the cylinders by the same company. One face of each sample had a mirror coating designed to be highly reflecting at 1064 nm, and an anti-reflection coat (at 1064 nm) was applied to each rear face. From our analysis we believe that the high reflective coating on the 7980 mass consists of approximately 43 alternating quarter wavelength layers of aluminium oxide and tantalum pentoxide, with a geometrical thickness of 6.3 μm . For the 7940 mass we believe there were approximately 59 layers with a geometrical thickness of 8.6 μm .

We make the assumption that the loss in the coating is proportional to the total coating thickness and that the loss is homogenous throughout the coating, thus we assume that the anti-reflection coating (which has significantly fewer layers ~ 2) does not add appreciably to the total loss. In the accompanying paper describing results obtained by colleagues at Syracuse University the possibility of the coating loss being different depending on whether the coating is deformed perpendicular to the surface, parallel to the surface or in shear, is examined. There will be further discussion of this later.

The loss factors of seven modes of each sample were measured. The experimental arrangement used to measure the loss factors is shown in figure 1.

The samples were suspended using a single sling of lightly greased tungsten wire of 150 μm diameter, with the upper ends of the wires held inside a steel clamp, mounted on a rigid tripod structure. This structure was mounted inside a vacuum tank, evacuated to approximately 10^{-5} mb. The resonant modes of each sample were excited using an electrostatic drive plate mounted behind the samples, and the amplitude of the induced motion of the front face of each sample was sensed using a Michelson interferometer illuminated by light from a helium–neon laser. The mirror in the reference arm of the Michelson was

⁷ General Optics Inc., now WavePrecision Inc., 5390 Kazuko Court, Moorpark, CA 93021, USA.

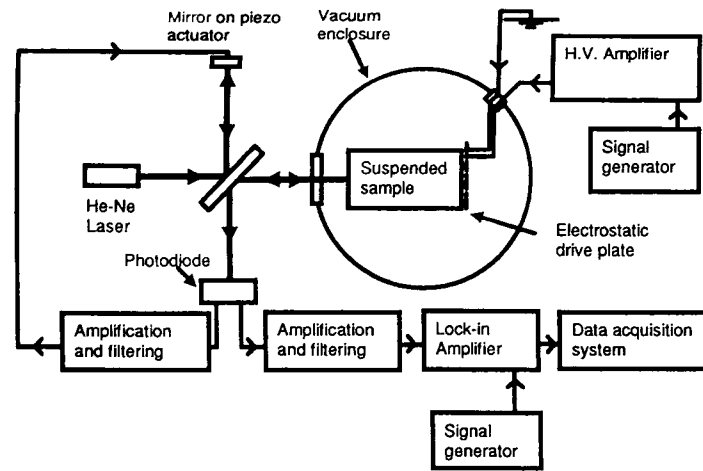


Figure 1. Experimental arrangement for measuring the loss factors of suspended test mass samples.

mounted on a piezoelectric transducer which, using a signal from the photodiode sensing the interference signal, was locked at low frequency to the pendulum motion of the mass on its suspension. The high frequency motion of the front face of the mass, sampled by the laser beam, was obtained from the signal from the photodiode, at frequencies well above the unity gain point of the servo loop. By measuring the rate of decay of the amplitude of the resonant motion of the test masses, the loss factors of the modes of the samples were obtained.

It should be noted that the samples were suspended multiple times, with the lengths of the suspension wires being varied each time, and the lowest measured loss factors for each mode used in our analysis. The reason for this is that previous experiments [8, 11] have shown that the measured loss factors may be too large if the frequency of the resonant mode of the test mass happens to coincide with a frequency of a resonant mode of the suspension wires.

3. Results

The lowest measured loss factors for seven modes of the coated 7940 and 7980 fused silica masses are shown in table 1.

It can be seen that there is a considerable variation in the level of measured loss factor between the modes, with some modes showing a loss factor as much as four times higher than others and we postulate that this difference is due to losses associated with the coating. Previous measurements of an uncoated 7980 test mass of the same dimensions, but different inclusion class, showed a much smaller variation of the loss factor between equivalent modes. The loss factors varied from 0.87×10^{-7} to 1×10^{-7} , lower than the loss factors for most of the modes of the coated masses. The spread in measured loss factors was within 14%. Thus we believe that suspension losses are insignificant and that the substantial variation in loss measurements seen for the modes of the coated samples is predominantly due to the effects of

Table 1. Experimental losses for Corning 7980 and 7940 silica test masses, with dielectric coating as described in section 2. (Errors shown are the 1 standard deviation level for the best suspension length in each case.)

Mode ^a	Corning 7980			Corning 7940	
	Modelled frequency (Hz)	Measured frequency (Hz)	Measured loss ($\times 10^{-7}$)	Measured frequency (Hz)	Measured loss ($\times 10^{-7}$)
1. Bending (8, $n = 1$)	22401	22105	1.37 ± 0.04	22361	1.6 ± 0.01
2. Asymmetric drum (1, $n = 0$)	23238	22977	1.16 ± 0.02	23004	1.23 ± 0.05
3. Fundamental (1, $n = 2$)	24671	25378	0.65 ± 0.01	25404	0.5 ± 0.02
4. Clover-4 (16, $n = 2$)	25490	26176	1.61 ± 0.03	26193	1.89 ± 0.04
5. Symmetric drum (4, $n = 0$)	27723	28388	3.1 ± 0.12	28395	3.6 ± 0.29
6. Expansion	31397	31710	1.09 ± 0.01	31731	1.01 ± 0.01
7. 2nd Asymmetric drum (3, $n = 0$)	35133	36045	0.86 ± 0.01	36072	0.94 ± 0.03

^a Numbering denotes the symmetry classification of the modes following G McMahon [12].

the dielectric coating. In each case a small amount of the coating had spilled over on to the barrel of the mass during the coating process. As will be seen later this is an important effect.

Assuming that all other losses have been reduced to a negligible level, the total measured loss may be expressed as the sum of the intrinsic loss of the substrate material plus any loss associated with having added a coating to the substrate. In the general case of coating both on the face and on the barrel:

$$\phi(\omega_0)_{\text{coated}} = \frac{E_{\text{substrate}}}{E_{\text{total}}} \phi(\omega_0)_{\text{substrate}} + \frac{E_{\text{coating on face}}}{E_{\text{total}}} \phi(\omega_0)_{\text{coating on face}} + \frac{E_{\text{barrel coating}}}{E_{\text{total}}} \phi(\omega_0)_{\text{eff}} \quad (1)$$

and, assuming $E_{\text{coating on face}} \ll E_{\text{substrate}}$ and $E_{\text{barrel coating}} \ll E_{\text{substrate}}$

$$\phi(\omega_0)_{\text{coated}} \approx \phi(\omega_0)_{\text{substrate}} + \frac{E_{\text{coating on face}}}{E_{\text{substrate}}} \phi(\omega_0)_{\text{coating on face}} + \frac{E_{\text{barrel coating}}}{E_{\text{substrate}}} \phi(\omega_0)_{\text{eff}} \quad (2)$$

where $E_{\text{coating on face}}/E_{\text{substrate}}$ is the fraction of the energy of the mode stored in the coating compared with the substrate and $E_{\text{barrel coating}}/E_{\text{substrate}}$ is the fraction of the energy of the mode stored in the barrel compared with the substrate.

$\phi(\omega_0)_{\text{eff}}$ represents the effective loss due to the coating material on the barrel of the sample and it is assumed at this stage that the distribution of the coating on the barrel is essentially even and of the same thickness as the coating on the faces. This assumption will be discussed further at a later stage.

Finite element analysis⁸ was used to model the displacement of the test masses for each of the modes under study—these mode shapes are shown in the appendix. The relevant energy ratios for the faces and for the barrels of the different modes were then calculated. It was assumed that the coating followed the contours of the silica mass below. Using typical bulk values for Young's modulus and Poisson's ratio for aluminium oxide and tantalum pentoxide, an equivalent value for each property was obtained for the multilayer coating as described in [13]. These values were used in calculating the energy associated with the layers of coating, whereas the relevant values for fused silica were used for the substrate. The values used are as in table 2.

⁸ Algor Inc., 159 Beta Drive, Pittsburgh, PA 15238-2932, USA.

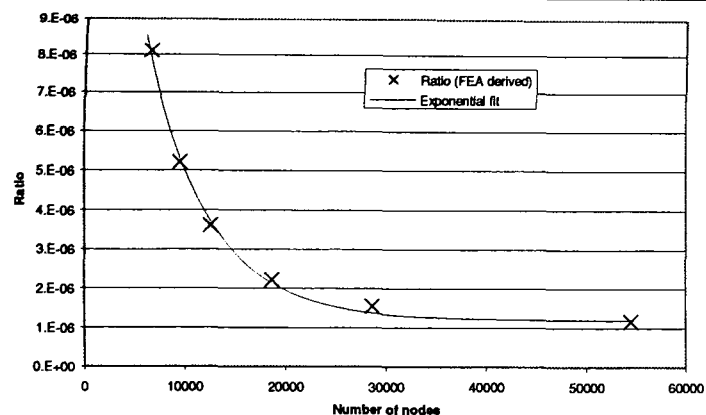


Figure 2. Variation in the computed ratio of energy stored in the dielectric mirror coating on a silica substrate per micron of coating thickness to the total energy stored in the substrate as the number of nodes in the FE model is increased. These data are for the asymmetric drum mode. The convergent value for this ratio is 1.19×10^{-6} .

Table 2. Material properties for coatings and substrate.

Material	Young's modulus (Pa)	Poisson's ratio
Aluminium oxide	3.6×10^{11} [15]	0.27 [14]
Tantalum pentoxide	1.4×10^{11} [13]	0.23 [13]
Calculated multilayer [13]	2.6×10^{11}	0.26
Fused silica	7.2×10^{10} [14]	0.17 [14]

In carrying out this calculation, care was exercised as the ratios obtained depended on the coarseness of the mesh used in the FE analysis. In practice the ratios were computed for a range of grid dimensions and the results extrapolated to the case of an infinitely fine mesh.

The convergence of an energy ratio as a function of the number of nodes used in the FE model for a typical mode is shown in figure 2 and the convergent energy ratios for the different modes are shown in figure 3.

3.1. Regression analysis

As an initial approach it was assumed in equation (2) that $\phi_{\text{eff}} = 0$ (i.e. mechanical losses associated with the coating overspray on the barrel of the sample were of a level which was not significant for these measurements). Then the variation of ϕ_{coated} against front surface energy ratio was examined for the 7940 and 7980 test masses.

It can be seen in figure 4 that if one point in each case is excluded from the data, then for both datasets there is an excellent linear fit of coated loss to the front surface energy ratio. However, the point which is excluded—that for the asymmetric drum mode—is one where the confidence in its value is particularly high since it is unlikely that experimental measurements will result in losses which are significantly too low. Thus it seems that the simple analysis is not

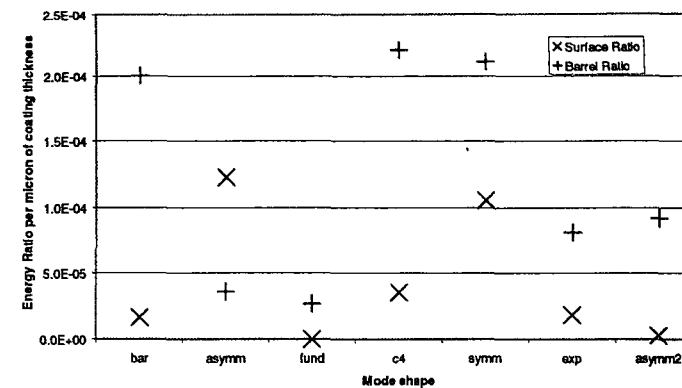


Figure 3. Ratios of energy stored per micron thickness of dielectric coating to total energy in substrate. Points x refer to the front surface and points + refer to the curved barrel.

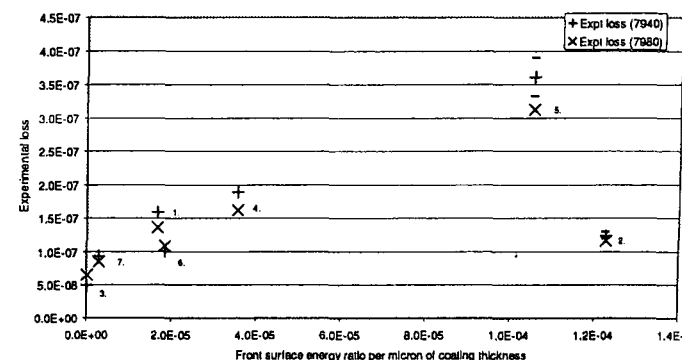


Figure 4. Variation of measured loss factor ϕ_{coated} against front surface energy ratio per micron thickness of coating for each mode of the 7940 and 7980 silica test masses. The experimental errors are highest for the two points for each mass at the right-hand side of the figure and the size of these errors (1 standard deviation level for the best suspension length in each case) is indicated by the bars on the points for the 7940 mass. The numbering of the points refers to the mode numbering in table 2.

adequate and a fuller analysis involving losses due to the coating on the barrels of the masses was carried out. In this case a multivariable linear regression algorithm for three parameters was adopted and it was no longer possible to use the simple graphical representation of figure 4. The fits were now demonstrated by graphs of experimental loss against predicted loss for both the 7940 and the 7980 masses as in figures 5 and 6.

As can be seen the fit is likely to be good in both cases provided the point corresponding to the symmetric drum mode is ignored. This is clear from figure 6 which shows the same results as above with the symmetric drum removed.

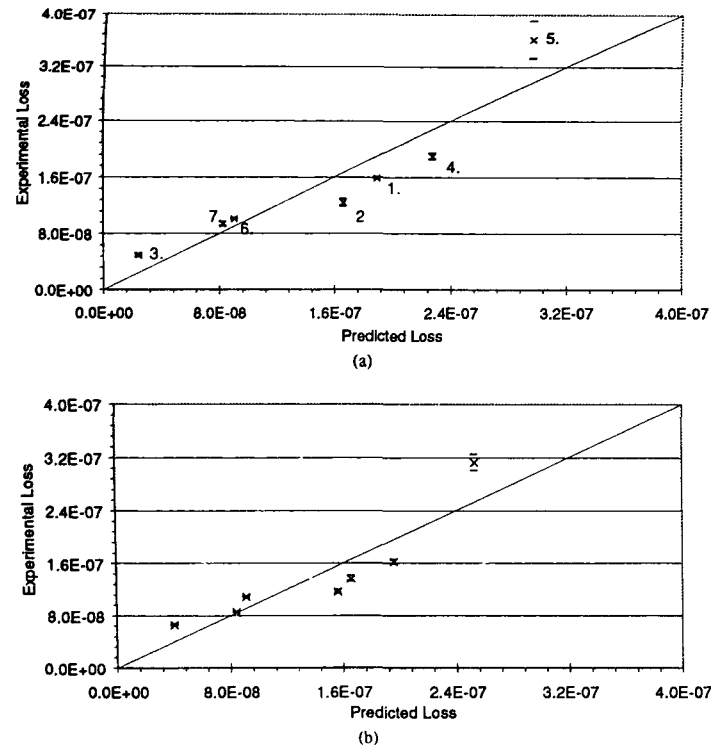


Figure 5. Comparison of the experimental loss with that predicted using a three-parameter multiregression analysis for (a) the 7940 and (b) the 7980 mass. Mode numbers are shown on (a) only. The line $y = x$ is drawn for information in each case.

The loss for the symmetric drum mode is significantly higher than that which is consistent with the best fit. Since this is the case for both the 7940 and 7980 masses it appears to be a real effect. In case this result is an artifact of the assumption of even coating thickness on the barrel a number of possibilities were investigated. For example, situations where the coating effects on the barrel were mainly at one end or mainly in the middle were investigated. However, no improvements were observed for the fitting of the data either with or without the symmetric drum mode included. Also, the possibility of the result being due to differing losses associated with shear and bulk strains was studied. Analysis shows that the ratio of shear to bulk strain is broadly similar for all the modes except for the clover-4 mode (mode number 4) where shear dominates by a large factor. There is no sign that the loss for this clover mode is significantly different from that of the others suggesting that our assumption of a homogeneous loss is well founded. We also checked that the kinetic energy of the symmetric drum mode at the breakaway points of the suspending wire was not particularly high compared with that of the other modes and thus it seems unlikely that frictional loss could explain the observations. It has to be assumed that there is some unmodelled loss associated with the shape

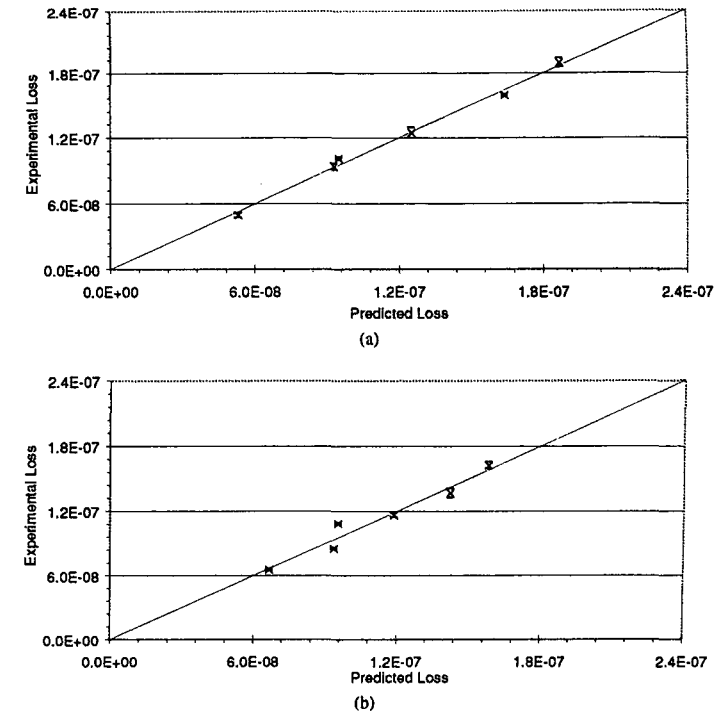


Figure 6. Comparison of the experimental loss with that predicted using a three-parameter multiregression analysis for (a) the 7940 and (b) the 7980 mass, this time with the symmetric drum mode excluded. The line $y = x$ is drawn for information.

of the symmetric drum mode, perhaps due to edge effects at the chamfers between the coated mirror faces and the barrels.

The multivariable regression analysis, with the symmetric drum mode excluded, yields values for the loss parameters as shown in table 3.

Table 3. Fitted values of bulk, coating and barrel losses for the 7940 and 7980 masses. Errors are calculated from the regression analysis at the 1 standard deviation level.

For the Corning 7940 mass:	$\phi(\omega_0)_{\text{substrate}} = (3.7 \pm 0.5) \times 10^{-8}$
	$\phi(\omega_0)_{\text{coating}} = (6.4 \pm 0.6) \times 10^{-5}$
	$\phi(\omega_0)_{\text{eff}} = (6.9 \pm 0.4) \times 10^{-5}$
For the Corning 7980 mass:	$\phi(\omega_0)_{\text{substrate}} = (5.6 \pm 0.9) \times 10^{-8}$
	$\phi(\omega_0)_{\text{coating}} = (6.3 \pm 1.6) \times 10^{-5}$
	$\phi(\omega_0)_{\text{eff}} = (6.3 \pm 0.9) \times 10^{-5}$

The values obtained for $\phi(\omega_0)_{\text{substrate}}$ are comparable with the best results for bulk samples of these types of fused silica [16].

4. Significance of coating results for advanced detectors

Until relatively recently the method of predicting the thermal noise in the test masses of gravitational wave detectors, at frequencies well below the first internal resonant modes of the mirrors, involved a normal mode expansion of the acoustic modes of the mirrors. The expected thermal noise was calculated by adding incoherently, with suitable weighting factors, the noise in the tails of the resonances of the test masses (see for example [2] and [17]). Alternative approaches to the problem have been developed by Levin [18], Nakagawa *et al* [9], Bondu *et al* [19] and Liu and Thorne [20]. Levin has pointed out that in cases where the spatial distribution of the loss in a mirror is non-uniform, using a modal expansion approach may lead to an incorrect estimation of the thermal noise.

Nakagawa *et al* [9] have developed a formalism where the fluctuation dissipation theorem can be expressed in terms of the static Green's function to calculate the distribution of the thermal motion on the front face of a semi-infinite mirror. This study has been extended to allow estimation of the effect of having a coated layer of finite thickness and different material properties on the front face of the mass. It is calculated [10] that the spectral density of the thermal noise, $S_{\phi}^{\text{coated}}(f)$ is increased, over that of the uncoated mass, $S_{\phi}^{\text{substrate}}(f)$, by the factor shown in equation (3)

$$\frac{S_{\phi}^{\text{coated}}(f)}{S_{\phi}^{\text{substrate}}(f)} = \left\{ 1 + \frac{2}{\sqrt{\pi}} \frac{(1-2\sigma)}{(1-\sigma)} \frac{\phi_{\text{coating}}}{\phi_{\text{substrate}}} \left(\frac{d}{w} \right) \right\} \quad (3)$$

where d is the coating thickness, w is the radius of the laser beam interrogating the test mass and σ represents the Poisson's ratio of the substrate material of Young's modulus Y . This assumes that the substrate and coating have the same mechanical properties but different loss factors.

More fully, allowing different values for σ and Y in the coating and substrate the ratio then becomes [21]

$$\left\{ 1 + \frac{1}{\sqrt{\pi}} \frac{(1+\sigma_{\text{coating}})}{(1-\sigma_{\text{substrate}}^2)(1-\sigma_{\text{coating}})} \frac{\phi_{\text{coating}}}{\phi_{\text{substrate}}} \frac{Y_{\text{substrate}}}{Y_{\text{coating}}} \left[\frac{Y_c^2}{Y_s^2} (1-2\sigma_{\text{coating}}) + (1-2\sigma_{\text{substrate}})^2 \frac{(1+\sigma_{\text{substrate}})^2}{(1+\sigma_{\text{coating}})^2} \left(\frac{Y_{\text{coating}}}{Y_{\text{substrate}}} \right)^2 \right] \left(\frac{d}{w} \right) \right\}. \quad (4)$$

Using the moduli of elasticity and Poisson's ratio for the coating material and the substrate listed in table 2, the mean of the bulk and coating losses for the 7940 and 7980 masses listed in table 3 and using the mean of the coating thicknesses for the 7980 and 7940 masses the predicted power spectral density of the thermal noise is found to be increased by a factor $(1 + 1.5 \times 10^{-2}/w)$. For the case of LIGO, where the laser beam has a spot radius of 5.5×10^{-2} m [22], this factor becomes 1.27. This means that the amplitude spectral density of the noise is increased by 1.13 over that which would be predicted without evaluating the effect of the mechanical loss of the coating. It should be noted that we have assumed that the losses in the coating and the substrate are structural in nature, i.e. they have the same value at low frequency as they have at the mode frequencies where they were measured. This seems reasonable as our calculations suggest that thermoelastic damping—often non-structural in nature—is at a lower level than the losses we have measured.

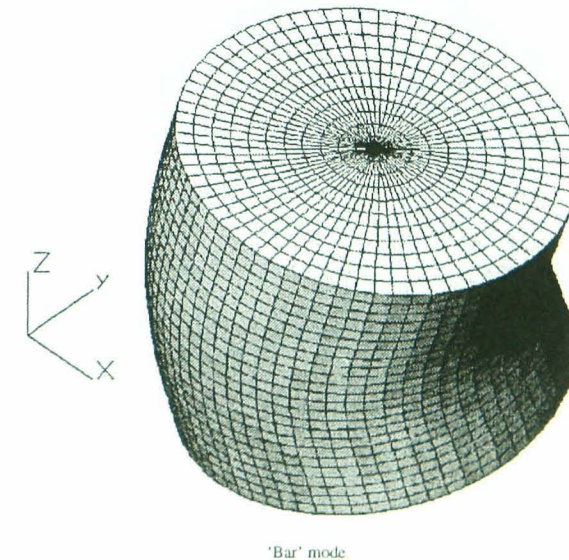
5. Conclusion

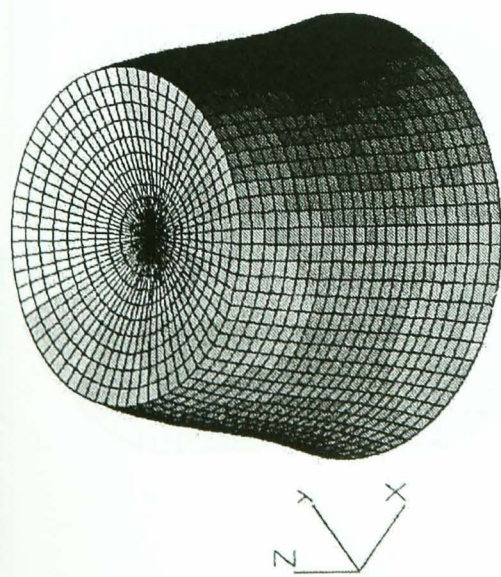
Experiments suggest that the effect of argon-sputtered dielectric coatings on the level of thermal noise associated with silica test masses in advanced interferometric gravitational wave detectors will be significant. Experiments on sapphire substrates are under way and preliminary analysis suggests a similar damping effect by the coating. There is a clear need for a series of experiments to be carried out, in which coating parameters are systematically varied as this will allow the source of the coating losses to be investigated.

Acknowledgments

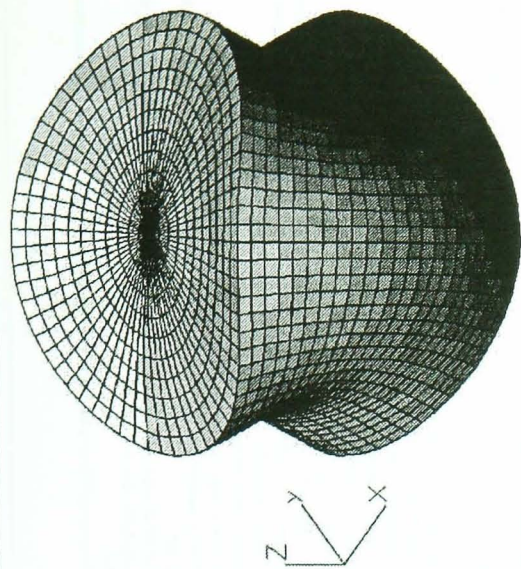
The authors would like to thank their colleagues in the University of Glasgow, the University of Hanover, the Max Planck Institut für Quantenoptik Garching, Stanford University and Syracuse University for their interest in this study. The authors would also like to thank Helena Armandula of Caltech and Dale Ness of REO Inc, for useful discussions on coating. They are also grateful to PPARC in the UK, NSF in the US (grant PHY-99-00793) and their Universities for financial support.

Appendix. Pictures of the test mass modes

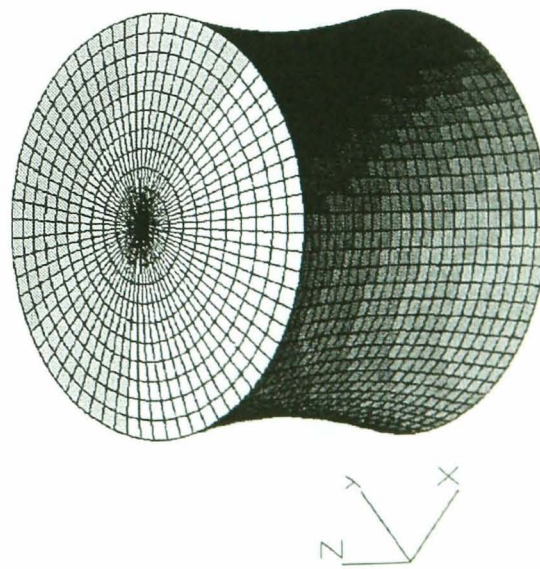




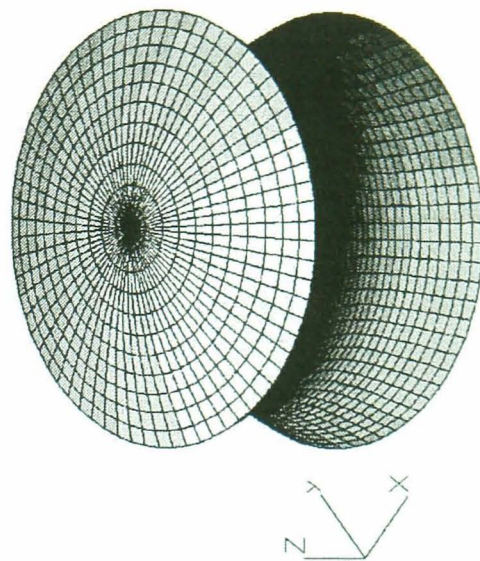
'Asymmetric drum' mode



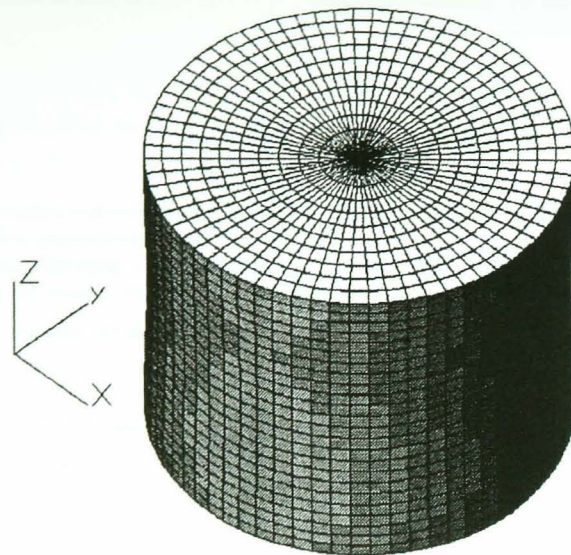
'Clover-4' mode



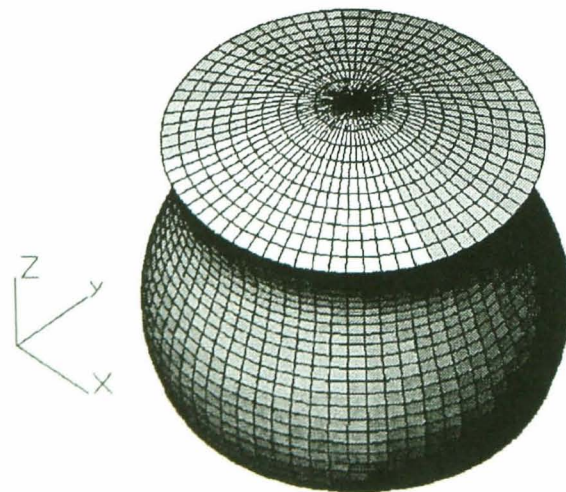
'Fundamental' mode



'Symmetric drum' mode



'Expansion' mode



'Second asymmetric drum' mode

References

- [1] Rowan S, Cagnoli G, Hough J, Sneddon P, Fejer M M, Gustafson E, Route R and Mitrofanov V 2000 *Phys. Lett. A* **265** 5
- [2] Saulson P R 1990 *Phys. Rev. D* **42** 2437
- [3] Gretarsson A M, Harry G M, Penn S D, Saulson P R, Startin W J, Rowan S, Cagnoli G and Hough J 2000 *Phys. Lett. A* **270** 108
- [4] Rowan S, Cagnoli G, McIntosh S, Hough J, Sneddon P, Fejer M, Gustafson E and Route R 2000 *Gravitational Waves Detection II* 1999 (Tokyo: Universal Academy) pp 203–15
- [5] Amico P et al 2001 *Class. Quantum Grav.* **18** 4127
- [6] Yamamoto J K *PhD Thesis* <http://t-munu.phys.s.u-tokyo.ac.jp/theses/yamamoto.d.pdf>
- [7] Twyford S M, Rowan S, Hough J and Gwo D H 1998 *Proc. of the 2nd Edoardo Amaldi Conference on Gravitational Wave Experiments CERN* (Geneva) ed E Coccia, G Veneziano and G Pizzella (Singapore: World Scientific) pp 479–84
- [8] Rowan S, Twyford S M, Hough J, Gwo D H and Route R 1998 *Phys. Lett. A* **246** 471
- [9] Nakagawa N, Auld B A, Gustafson E and Fejer M M 1997 *Rev. Sci. Instrum.* **68** 3553
- [10] Nakagawa N, Gretarsson A M, Gustafson E K and Fejer M M *Phys. Rev. D* **65** 0420XX
- [11] Logan J E, Robertson N A and Hough J 1992 *Phys. Lett. A* **170** 352
- [12] McMahon G W 1964 *J. Opt. Soc. Am.* **36** 85
- [13] Srinivasan K, Coyne D and Vogt R 1997 *LIGO Document* no LIGO-T97016-00-D
- [14] Musikant S 1985 *Optical Materials: An Introduction to Selection and Application* (New York: Dekker)
- [15] Waynant R W and Ediger M N (eds) 1994 *Electro-Optics Handbook* (Optical and Electro-Optical Engineering Series) (New York: McGraw Hill)
- [16] Startin W J, Beilby M A and Saulson P R 1998 *Rev. Sci. Instrum.* **69** 3681
- [17] Gillespie A and Raab F 1995 *Phys. Rev. D* **52** 577
- [18] Levin Y 1998 *Phys. Rev. D* **57** 659
- [19] Bondu F, Hello P and Vinet J-Y 1998 *Phys. Lett. A* **246** 227
- [20] Liu Y T and Thorne K S 2000 *Phys. Rev. D* **62** 12202
- [21] Nakagawa N, Fejer M M and Gustafson E 2002 *Phys. Rev. D* submitted
- [22] Fritschel P (ed) 2001 *Advanced LIGO Systems Design* LIGO-T010075-00-D LIGO Scientific Collaboration

Erratum

Excess mechanical loss associated with dielectric mirror coatings on test masses in interferometric gravitational wave detectors

D R M Crooks, P Sneddon, G Cagnoli, J Hough, S Rowan, M M Fejer, E Gustafson, R Route, N Nakagawa, D Coyne, G M Harry and A M Gretarsson *Class. Quantum Grav.* 19 883–896

On page 891, equation (4) should read as follows:

$$1 + \left\{ \frac{1}{\sqrt{\pi}} \frac{(1 + \sigma_{\text{coating}})}{(1 - \sigma_{\text{substrate}})(1 - \sigma_{\text{coating}})} \frac{\phi_{\text{coating}}}{\phi_{\text{substrate}}} \frac{Y_{\text{substrate}}}{Y_{\text{coating}}} \right\} \times \left\{ \left[(1 - 2\sigma_{\text{coating}}) + (1 - 2\sigma_{\text{substrate}})^2 \frac{(1 + \sigma_{\text{substrate}})^2}{(1 + \sigma_{\text{coating}})^2} \left(\frac{Y_{\text{coating}}}{Y_{\text{substrate}}} \right)^2 \right] \left(\frac{d}{w} \right) \right\}. \quad (4)$$

Thermal noise in interferometric gravitational wave detectors due to dielectric optical coatings

Gregory M Harry^{1,2}, Andri M Gretarsson², Peter R Saulson²,
Scott E Kittelberger², Steven D Penn², William J Startin², Sheila Rowan³,
Martin M Fejer³, D R M Crooks⁴, Gianpietro Cagnoli⁴, Jim Hough⁴
and Norio Nakagawa⁵

¹ LIGO Laboratory, Massachusetts Institute of Technology, Room NW17-161,
175 Albany Street, Cambridge, MA 02139, USA

² Department of Physics, Syracuse University, Syracuse, NY 13244-1130, USA

³ Edward L. Ginzton Lab, Stanford University, Stanford, CA 94305-4085, USA

⁴ Department of Physics and Astronomy, University of Glasgow, Glasgow G12 8QQ,
UK

⁵ Center for Nondestructive Evaluation, Institute for Physical Research and Technology,
Iowa State University, Ames, IA 50011, USA

E-mail: gharry@ligo.mit.edu and andri@physics.syr.edu

Received 26 November 2001

Published 12 February 2002

Online at stacks.iop.org/CQG/19/897

Abstract

We report on thermal noise from the internal friction of dielectric coatings made from alternating layers of Ta₂O₅ and SiO₂ deposited on fused silica substrates. We present calculations of the thermal noise in gravitational wave interferometers due to optical coatings, when the material properties of the coating are different from those of the substrate and the mechanical loss angle in the coating is anisotropic. The loss angle in the coatings for strains parallel to the substrate surface was determined from ringdown experiments. We measured the mechanical quality factor of three fused silica samples with coatings deposited on them. The loss angle, $\phi_l(f)$, of the coating material for strains parallel to the coated surface was found to be $4.2 \pm 0.3 \times 10^{-4}$ for coatings deposited on commercially polished slides, and $1.0 \pm 0.3 \times 10^{-4}$ for a coating deposited on a superpolished disc. Using these numbers, we estimate the effect of coatings on thermal noise in the initial LIGO and Advanced LIGO interferometers. We also find that the corresponding prediction for thermal noise in the 40 m LIGO prototype at Caltech is consistent with the noise data. These results are complemented by results for a different type of coating, presented in a companion paper.

PACS numbers: 0480, 0480N, 6835G, 6860B, 9555Y

1. Introduction

The experimental effort to detect gravitational waves is entering an important phase. A number of interferometric gravitational wave observatories are being built around the world [1–4] and most should be operational in the next few years. Plans are being developed to operate the next generation of interferometers, and crucial research is going on now to ensure that these interferometers will have the sensitivity necessary to reach distances at which multiple events may be detected per year [5–7].

The sensitivity of interferometric gravitational wave observatories is limited by fundamental noise sources. In Advanced LIGO, thermal noise from the internal degrees of freedom of the interferometer test masses is expected to be the limiting noise source in the middle frequency range (~30–500 Hz). This is also the interferometer's most sensitive frequency band. Thus, any additional thermal noise, such as thermal noise associated with optical coatings, will directly reduce the number of events that Advanced LIGO can detect.

The initial LIGO interferometer uses fused silica for the interferometer test masses, the beam splitter and other optics. Fused silica has been shown to have very low internal friction [8–10] and will therefore exhibit very low (off-resonance) thermal noise. This property, coupled with the fact that high quality, large, fused silica optics are commercially available, makes fused silica a natural choice for the initial interferometer. Sapphire, which has even lower internal friction [11, 12] (although higher thermoelastic loss), is currently proposed as the material from which to fabricate the optics for use in Advanced LIGO [5]. In addition to lower thermal noise, sapphire offers benefits due to its superior thermal conductivity, which, in transporting heat from the reflective surface of the test masses, allows a higher power laser to be used.

In order to use the test masses as mirrors, optical coatings must be applied to the surface. To obtain high reflectivities, multi-layer, dielectric coatings are used. Such coatings consist of alternating layers of two dielectric materials with differing refractive indices. The number of layers deposited determines the reflectivity. It is possible to use a number of different dielectric material pairs for reflective coatings, but it has been found that coatings made with alternating layers of Ta₂O₅ and SiO₂ give the necessary reflectivity while at the same time satisfying the stringent limits on optical loss and birefringence required for LIGO [13]. However, the effect of these coatings on thermal noise is only now being studied.

The simplest way to predict the thermal noise is to use the fluctuation–dissipation theorem [14]. It states that the thermal noise power spectrum is proportional to the real part of the mechanical admittance of the test mass. Explicitly

$$S_x(f) = \frac{k_B T}{\pi^2 f^2} \text{Re}\{Y(f)\} \quad (1)$$

where S_x is the spectral density of the thermally induced fluctuations of the test mass surface as read by the interferometer, T is the temperature of the test mass and f is the frequency of the fluctuations. The quantity $Y(f)$ is the mechanical admittance of the test mass to a cyclic pressure distribution having the same form as the interferometer beam intensity profile [15]. For LIGO, the proposed beam profile is Gaussian. $\text{Re}\{Y(f)\}$ can be written in terms of the mechanical loss angle, ϕ_{readout} , of the test mass response to the applied cyclic Gaussian pressure distribution. To calculate the thermal noise we must therefore obtain ϕ_{readout} .

The loss angle ϕ_{readout} depends both on the distribution of losses in the test mass and on the shape of the deformation of the test mass in response to the applied pressure. If the distribution of losses in the test mass were homogeneous, the loss angle ϕ_{readout} would be independent of the deformation of the test mass. In that case, one could obtain ϕ_{readout} by measuring the loss angle associated with a resonant mode of the test mass, $\phi = 1/Q$, where Q is the quality factor

of a resonant mode. However, when the distribution of mechanical losses in the test mass is not homogeneous, this approach does not work.

One way of obtaining ϕ_{readout} would be to measure it directly. This would involve applying a cyclic Gaussian pressure distribution to the test mass face and measuring the phase lag of the response. But such an experiment presents several insuperable technical difficulties and is useful mainly as a thought experiment, in which interpretation of the result would be simple.

In this paper, we give the results of another kind of experiment whose results allow us to calculate ϕ_{readout} using elasticity theory. The measurement process is relatively straightforward: we compare the quality factor, Q , of vibrations of an uncoated sample of fused silica to the quality factor when a coating has been applied. In order to make the effect easier to measure, and to improve the accuracy of the measurements, we used thin pieces of fused silica rather than the relatively thick mirrors used in LIGO. Our measurements show a significant reduction of the Q due to mechanical loss associated with the coating.

In choosing to make the measurements easy to carry out, we necessarily complicated the interpretation of the results. Scaling from the results of our measurements to the prediction of ϕ_{readout} takes some effort. In section 2 we describe the relationship between the measured coating loss angle, ϕ_1 , and the interferometer readout loss angle, ϕ_{readout} . Section 3 describes the measurement process. The results are given in section 4. The implications for LIGO are described in section 5, and a programme of future work is discussed in section 6. This paper is complemented by a companion paper describing similar measurements on $\text{Al}_2\text{O}_3/\text{Ta}_2\text{O}_5$ coatings [16].

2. Theory

To use the fluctuation–dissipation theorem, equation (1), to predict thermal noise in LIGO, we need to calculate the real part of the mechanical admittance of the test mass. The mechanical admittance of the test mass is defined as

$$Y(f) \equiv i2\pi f \frac{x(f)}{F} \quad (2)$$

where F is the (real) amplitude of a cyclic force applied to the test mass at frequency f and $x(f)$ is the amplitude of the steady state displacement response. Choosing the appropriate pressure distribution with which to excite the test mass constitutes the first step in the calculation. Levin [15] has argued that in calculating the thermal noise read by an interferometer, the appropriate pressure distribution has the same profile as the laser beam intensity and should be applied to the test mass face (in the same position and orientation as the beam). In the case of the initial LIGO interferometer, the laser beam has a Gaussian intensity distribution. A Gaussian beam profile is also proposed for Advanced LIGO. The corresponding cyclic pressure distribution is

$$p(\vec{r}, t) = p(r, t) = \frac{2F}{\pi w^2} \exp\left(\frac{-2r^2}{w^2}\right) \sin(2\pi f t) \quad (3)$$

where \vec{r} is a point on the test mass surface, $r = |\vec{r}|$, f is the frequency of interest and w is the field amplitude radius of the laser beam. (At the radius w , the light intensity is $1/e^2$ of maximum.) To simplify the calculation of the response $x(f)$, we make use of the fact that the beam radius is considerably smaller than the test mass radius, and approximate the test mass by an infinite half-space. This allows us to ignore boundary conditions everywhere except on the face of the test mass. For the case of homogeneous loss, Liu and Thorne [17] have shown that this approximation leads to an overestimate of the thermal noise, but that for a test mass of radius 14 cm, the error is about 30% or less for beam field amplitude radii w up to 6 cm.

To calculate the real part of the admittance we follow Levin and rewrite it in the form

$$\text{Re}\{Y(f)\} = \frac{4\pi f U(f)}{F^2} \phi \quad (4)$$

where $U(f)$ is the maximum elastic energy stored in the test mass as a result of the excitation at frequency f and ϕ is the loss angle of the response. Equation (4) holds at frequencies far below the first resonance of the test mass, provided $\phi \ll 1$, and is obtained as follows. Under the conditions stated

$$U(f) = \frac{1}{2} F |x(f)| \quad (5)$$

and the response $x(f)$ to the excitation is

$$x(f) = |x(f)| \exp(-i\phi) \approx |x(f)|(1 - i\phi). \quad (6)$$

Substituting equations (5) and (6) into equation (2) and taking the real part yields equation (4).

The strategy is then to calculate $U(f)$ and ϕ under the pressure distribution in equation (3). Calculation of the loss angle ϕ requires some care since the loss angle is specific to the applied force distribution and to the associated deformation. If the material properties or intrinsic sources of loss are not isotropic and homogeneous throughout the sample, different deformations will exhibit different loss angles. Since interferometer test masses do have inhomogeneous loss due to the dielectric coating on the front surface, the calculation of thermal noise depends on obtaining the value of the loss angle associated with precisely the response to the pressure distribution given in equation (3). Throughout this paper we will assume that losses in the substrate are always homogeneous and isotropic and that the only source of inhomogeneous and anisotropic loss is the coating.

The loss angle $\phi \equiv \phi_{\text{readout}}$ associated with the Gaussian pressure distribution can be written as a weighted sum of coating and substrate losses. We will first obtain an expression for the loss angle in the simple case where the coating loss is homogeneous and isotropic, but quickly generalize to anisotropic coating loss.

If the loss in the coating is homogeneous and isotropic, yet different from that of the substrate, we can write

$$\phi_{\text{readout}} = \frac{1}{U} (U_{\text{substrate}} \phi_{\text{substrate}} + U_{\text{coating}} \phi_{\text{coating}}) \quad (7)$$

where U is the maximum elastic energy stored in the sample as a consequence of the applied pressure, $U_{\text{substrate}}$ is the portion of the energy stored in the substrate, U_{coating} is the portion of the energy stored in the coating, $\phi_{\text{substrate}}$ is the loss angle of the substrate and ϕ_{coating} is the loss angle of the coating. To simplify the calculation of the energies, we make use of the fact that the frequencies where thermal noise dominates interferometer noise budgets are far below the first resonances of the test masses. Thus, the shape of the response of the test mass to a cyclic Gaussian pressure distribution of frequency f is well approximated by the response to an identical Gaussian pressure distribution that is constant in time. Thus, to a good approximation, U , $U_{\text{substrate}}$ and U_{coating} can be calculated from the deformation associated with the static Gaussian pressure distribution

$$p(r) = \frac{2F}{\pi w^2} \exp\left(\frac{-2r^2}{w^2}\right). \quad (8)$$

Since we are in the limit where the coating is very thin compared to the width of the pressure distribution

$$U_{\text{coating}} \approx \delta U d \quad (9)$$

where δU is the energy density stored at the surface, integrated over the surface, and d is the thickness of the coating. Similarly, $U_{\text{substrate}} \approx U$, giving

$$\phi_{\text{readout}} = \phi_{\text{substrate}} + \frac{\delta U d}{U} \phi_{\text{coating}}. \quad (10)$$

If, however, the loss angle of the coating is not isotropic, the second term in equation (10) must be expanded. Since the coatings have a layer structure, we cannot ignore the possibility of anisotropy of structural loss in the calculation of thermal noise.

To address the possible anisotropy of the structural loss we shall use the following model. The energy density ρ_U of a material that is cyclically deformed will generally have a number of terms. We shall associate a different (structural) loss angle with each of these terms. For example, in cylindrical coordinates

$$\rho_U = \rho_{rr} + \rho_{r\theta} + \dots \quad (11)$$

where

$$\begin{aligned} \rho_{rr} &\equiv \frac{1}{2} \sigma_{rr} \epsilon_{rr} \\ \rho_{r\theta} &\equiv \frac{1}{2} \sigma_{r\theta} \epsilon_{r\theta} \\ &\vdots \end{aligned} \quad (12)$$

where σ_{ij} are the stresses and ϵ_{ij} the strains. The associated loss angles are ϕ_{rr} , $\phi_{r\theta}$, etc. In this paper we will assume that the loss angles associated with energy stored in strains parallel to the plane of the coating are all equal. This assumption is motivated by the observation that many isotropic amorphous materials, like fused silica, do not show significantly different quality factors for many modes even though the relative magnitude of the various terms in the elastic energy varies significantly between the modes [18]. The measurements made at Glasgow and Stanford Universities further strengthen this assumption [16]—those measurements show no significant variation of the coating loss as the relative size of the parallel strain energy terms changes from mode to mode.

Since we will always have traction-free boundary conditions for the problems considered here, we shall always have $\epsilon_{rz} = \epsilon_{zr} = 0$. Thus we will have loss angles associated only with the following coating energy density components:

$$\begin{aligned} \rho'_{U\parallel} &= \frac{1}{2} (\epsilon'_{rr} \sigma'_{rr} + \epsilon'_{\theta\theta} \sigma'_{\theta\theta} + \epsilon'_{r\theta} \sigma'_{r\theta}) \\ \rho'_{U\perp} &= \frac{1}{2} \epsilon'_{zz} \sigma'_{zz} \end{aligned} \quad (13)$$

where ϵ'_{ij} are the strains and σ'_{ij} the stresses in the coating. We define the loss angle associated with the energy density in parallel coating strains $\rho'_{U\parallel}$, as ϕ_{\parallel} , and the loss angle associated with the density of energy in perpendicular coating strains, $\rho'_{U\perp}$, as ϕ_{\perp} . The components of the energy density in equation (13) integrated over the surface of the (half-infinite) test mass are

$$\begin{aligned} \delta U_{\parallel} &= \int_S \rho'_{U\parallel} d^2 r \\ \delta U_{\perp} &= \int_S \rho'_{U\perp} d^2 r \end{aligned} \quad (14)$$

so that finally, to account for the anisotropic layer structure of the coating, equation (10) is replaced by

$$\phi_{\text{readout}} = \phi_{\text{substrate}} + \frac{\delta U_{\parallel} d}{U} \phi_{\parallel} + \frac{\delta U_{\perp} d}{U} \phi_{\perp}. \quad (15)$$

To obtain an expression for ϕ_{readout} we need to calculate δU_{\parallel} , δU_{\perp} and U for a coated half-infinite test mass subject to the Gaussian pressure distribution $p(r)$ of equation (8). The quantities δU_{\parallel} and δU_{\perp} involve only the stress and strain in the coating. The total energy involves the stress and strain throughout the substrate,

$$U = \pi \int_0^{\infty} dz \int_0^{\infty} r dr (\epsilon_{rr} \sigma_{rr} + \epsilon_{\theta\theta} \sigma_{\theta\theta} + \epsilon_{zz} \sigma_{zz} + 2\epsilon_{rz} \sigma_{rz}) \quad (16)$$

where ϵ_{ij} are the strains and σ_{ij} the stresses in the substrate. To obtain the stresses and strains in the coating and in the substrate we must solve the axially symmetric equations of elasticity for the coated half-infinite test mass subject to the pressure distribution $p(r)$. The general solution to these equations for an uncoated half-infinite test mass is given by Bondu *et al* [19] (with corrections by Liu and Thorne [17]).

Because the coating is thin, we can, to a good approximation, ignore its presence in the solution of the elastic equations for the substrate. The strains in the coating should also not vary greatly as a function of depth within the coating, and we shall approximate them as being constant. Due to axial symmetry, $\epsilon_{r\theta} = \epsilon_{\theta r} = \epsilon'_{r\theta} = \epsilon'_{\theta r} = 0$. Due to traction-free boundary conditions, $\epsilon'_{rz} = \epsilon'_{zr} = 0$ at the coating surface, and the same must therefore hold (to leading order) for the entire coating. This approximation is valid, provided the Poisson's ratio of the coating is not very different from that of the substrate. To obtain the non-zero stresses and strains in the coating (ϵ'_{rr} , $\epsilon'_{\theta\theta}$ and ϵ'_{zz}) we note that since the coating is constrained tangentially by the surface of the substrate, the coating must have the same tangential strains (ϵ'_{rr} and $\epsilon'_{\theta\theta}$) as the surface of the substrate. Also, the coating sees the same perpendicular pressure distribution (σ'_{zz}) as the surface of the substrate. These conditions, which represent reasonably good approximations for the case of a thin coating, allow us to calculate all the coating stresses and strains in terms of the stresses and strains in the surface of the substrate. See the appendix for the details of this calculation.

Using the solutions for ϵ'_{ij} , σ'_{ij} , ϵ_{ij} and σ_{ij} derived in the appendix, and substituting into equations (13)–(16), we obtain the required quantities,

$$U = \frac{F^2(1-\sigma^2)}{2\sqrt{\pi}wY} \quad (17)$$

$$\delta U_{\parallel}/U = \frac{1}{\sqrt{\pi}w} \frac{Y'(1+\sigma)(1-2\sigma)^2 + Y\sigma'(1+\sigma')(1-2\sigma)}{Y(1+\sigma')(1-\sigma')(1-\sigma)} \quad (18)$$

$$\delta U_{\perp}/U = \frac{1}{\sqrt{\pi}w} \frac{Y(1+\sigma')(1-2\sigma') - Y'\sigma'(1+\sigma)(1-2\sigma)}{Y'(1-\sigma')(1+\sigma)(1-\sigma)} \quad (19)$$

where Y and σ are the Young's modulus and Poisson's ratio of the substrate, and Y' and σ' are the Young's modulus and Poisson's ratio of the coating. In general, the coating Young's modulus and Poisson's ratio are different in the parallel and perpendicular directions. For the Young's modulus, these values can be found by averaging the Young's moduli of the coating materials, and by averaging the reciprocals of the Young's moduli, respectively [20]. However, because the values for SiO_2 and Ta_2O_5 are similar, the Young's moduli and Poisson's ratios in the two directions are similar. This is in contrast to the case for the ϕ where it is not known whether ϕ_{\parallel} is similar in magnitude to ϕ_{\perp} . For simplicity, we have therefore approximated the Young's moduli and Poisson's ratios in the two directions as equal to the value for stresses parallel to the coating. Thus, from equation (15)

$$\begin{aligned} \phi_{\text{readout}} &= \phi_{\text{substrate}} + \frac{1}{\sqrt{\pi}w} \left(\frac{Y'(1+\sigma)(1-2\sigma)^2 + Y\sigma'(1+\sigma')(1-2\sigma)}{Y(1+\sigma')(1-\sigma')(1-\sigma)} \phi_{\parallel} \right. \\ &\quad \left. + \frac{Y(1+\sigma')(1-2\sigma') - Y'\sigma'(1+\sigma)(1-2\sigma)}{Y'(1-\sigma')(1+\sigma)(1-\sigma)} \phi_{\perp} \right). \end{aligned} \quad (20)$$

Substituting equations (17) and (20) into equation (4) and substituting the result into the fluctuation-dissipation theorem, equation (1), gives the power spectral density of interferometer test mass displacement thermal noise as

$$S_x(f) = \frac{2k_B T}{\pi^{3/2} f} \frac{1 - \sigma^2}{wY} \left\{ \phi_{\text{substrate}} + \frac{1}{\sqrt{\pi}} \frac{d}{w} \frac{1}{YY'(1 - \sigma^2)(1 - \sigma'^2)} \right. \\ \times [Y'^2(1 + \sigma)^2(1 - 2\sigma)^2\phi_{\parallel} + YY'\sigma'(1 + \sigma)(1 + \sigma')(1 - 2\sigma)(\phi_{\parallel} - \phi_{\perp}) \\ \left. + Y^2(1 + \sigma')^2(1 - 2\sigma')\phi_{\perp}] \right\}. \quad (21)$$

Equation (21) is valid provided that most of the loss at the coated surface occurs in the coating materials themselves and is not due to interfacial rubbing between the coating and the substrate, or to rubbing between the coating layers. If a large proportion of the loss is due to rubbing, the coating-induced thermal noise will not be proportional to the coating thickness as indicated in equation (21). Rather, it may be proportional to the number of layers and may be very dependent on the substrate preparation.

The limits of equation (21) agree with the previous results. In the limit that $\phi_{\parallel} = \phi_{\perp}$, the YY' term disappears and the result agrees with the result of Nakagawa who has solved the problem for that case by a different method [21]. The limit of equation (21) in the case $Y' = Y$, $\sigma' = \sigma$ and $\phi_{\perp} = \phi_{\parallel}$ agrees with the result obtained previously [22],

$$S_x(f) = \frac{2k_B T}{\pi^{3/2} f} \frac{1 - \sigma^2}{wY} \left\{ \phi_{\text{substrate}} + \frac{2}{\sqrt{\pi}} \frac{(1 - 2\sigma)d}{(1 - \sigma)w} \phi_{\parallel} \right\}. \quad (22)$$

For the case of fused silica or sapphire substrates coated with alternating layers of Ta_2O_5 and SiO_2 , the Poisson's ratio of the coating may be small enough ($\lesssim 0.25$) that, for likely values of the other parameters, equation (21) is reasonably approximated (within about 30%) by the result obtained by setting $\sigma = \sigma' = 0$,

$$S_x(f) = \frac{2k_B T}{\pi^{3/2} f} \frac{1}{wY} \left\{ \phi_{\text{substrate}} + \frac{1}{\sqrt{\pi}} \frac{d}{w} \left(\frac{Y'}{Y} \phi_{\parallel} + \frac{Y}{Y'} \phi_{\perp} \right) \right\}. \quad (23)$$

Equation (23) highlights the significant elements of equation (21). It shows that, in order to estimate the thermal noise performance of a particular coating, we must know all of Y , Y' , ϕ_{\parallel} , and ϕ_{\perp} . It also shows that if $\phi_{\parallel} \approx \phi_{\perp}$, then the lowest coating-induced thermal noise occurs when the Young's modulus of the coating is matched to that of the substrate. If $Y' \neq Y$, one of ϕ_{\parallel} or ϕ_{\perp} will be emphasized and the other de-emphasized. This is particularly worrying for coatings on sapphire substrates, whose high Young's modulus means that for most coatings, ϕ_{\perp} is likely to be the main contributor to the coating thermal noise. Section 3 describes ringdown experiments on coated samples in order to determine ϕ_{\parallel} . Unfortunately, we do not obtain ϕ_{\perp} from ringdown experiments of samples with coatings on the surface. Since the coatings experience free boundary conditions, they are not greatly compressed perpendicular to the surface (there will be some small amount of compression due to Poisson's ratio effects). Therefore ϕ_{\perp} cannot be easily measured in such experiments, and no measurement of ϕ_{\perp} exists at the present time. Because of this, we can only obtain very rough estimates of the coating-induced thermal noise. We will set $\phi_{\perp} = \phi_{\parallel}$, but the accuracy of our thermal noise estimates will remain unknown until ϕ_{\perp} is measured.

3. Method

In order to estimate the coating loss component ϕ_{\parallel} , we made measurements of the loss angles of fused silica samples with and without the $\text{Ta}_2\text{O}_5/\text{SiO}_2$ high reflective coating used in LIGO.

A standard way of determining the loss angle at the frequency of a particular resonant mode is to measure its ringdown time, τ_n . This allows the calculation of the mode's quality factor Q , through

$$Q \equiv \pi f_n \tau_n \quad (24)$$

where f_n is the frequency of the resonant mode. The loss angle at the resonance frequency is the inverse of the mode's quality factor

$$\phi(f_n) = 1/Q. \quad (25)$$

Because of the free boundary conditions no energy is stored in strains with perpendicular components. The loss angle ϕ_{coated} of a resonating sample after coating is therefore related to the loss angle ϕ_{uncoated} of the same sample before coating by

$$\phi_{\text{coated}} = \phi_{\text{uncoated}} + \frac{\delta\bar{U}_{\parallel}d}{\bar{U}} \phi_{\parallel} \quad (26)$$

where \bar{U} is the energy stored in the resonance. Similarly, as in section 2, the quantity $\delta\bar{U}_{\parallel}$ is the resonance energy stored in strains having no component perpendicular to the surface

$$\delta\bar{U}_{\parallel} = \int_S d^2r \sum_{i,j \neq z} \rho'_{ij} \quad (27)$$

where S is the coated surface of the sample, z is the direction perpendicular to the surface and

$$\rho'_{ij} = \frac{1}{2} \epsilon'_{ij} \sigma'_{ij}. \quad (28)$$

Just as in section 2, ϕ_{\parallel} in equation (26) is the loss angle associated with the energy stored in strains in the plane of the coating. Because we assume that all in-plane loss angles are identical, the loss angle ϕ_{\parallel} is the same as in section 2, and once measured, can be substituted directly into equation (21).

For each sample resonance that was found, ϕ_{coated} and ϕ_{uncoated} were measured by recording the Q with and without an optical coating, respectively. The quantity $(\delta\bar{U}_{\parallel}d/\bar{U})$ was then calculated either numerically or analytically, allowing equation (26) to be solved for ϕ_{\parallel} based on the measured values of ϕ_{coated} and ϕ_{uncoated} . The resulting value for ϕ_{\parallel} was then substituted into equation (21) to obtain an interferometer thermal noise estimate.

In order to reduce systematic errors in the Q measurements, we took a number of steps to reduce excess loss (technical sources of loss, extrinsic to the sample) [23, 24]⁶. All Q were measured in a vacuum space pumped down to at least 1×10^{-5} Torr, and more typically 2×10^{-6} Torr. This reduced mechanical loss from gas damping. During the Q measurements, the samples were hung below a monolithic silica suspension made by alternating a massive bob of silica with thin, compliant, silica fibres. The suspensions and samples are shown in figure 1. (The suspension is of the same style used previously in [10, 24, 25].) The piece of fused silica rod at the top of the suspension is held in a collet which is rigidly connected to the underside of a thick aluminium plate supported by three aluminium columns. Between the piece of rod held in the collet and the sample was a single fused silica isolation bob. Its function was to stop vibrations from travelling between the sample and the aluminium optical table from which it was suspended. The size chosen for the isolation bob depended on the sample, with the heavier sample requiring a larger bob. The two fibres in the suspension were monolithically pulled out of the neighbouring parts using a $\text{H}_2\text{-O}_2$ torch. These fibres had a typical diameter of roughly 100–200 μm . The normal modes of the sample were excited using

⁶ In the referenced paper, the more general surface loss parameter d , is used. For coatings, as we have modelled them here, $d, \phi_{\text{bulk}} = dY'\phi_{\parallel}/Y$.

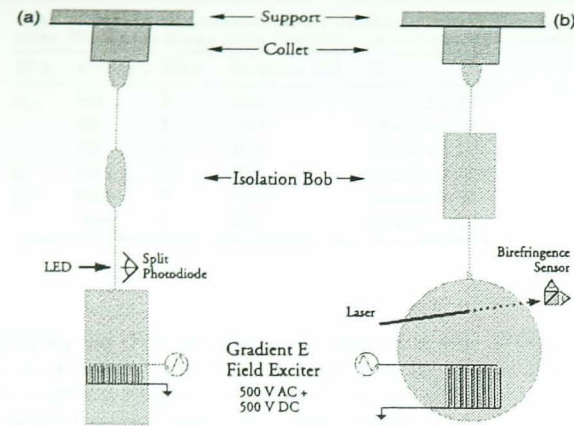


Figure 1. (a) The suspended microscope slide and exciter. (b) The suspended disc and exciter. In both (a) and (b), the entire structure below the steel collet is fused silica.

a comb capacitor [26]. This exciter was made from two copper wires sheathed with Teflon, each having a total diameter of about 1/2 mm. The two wires were then wrapped around a ground plane and placed about 1 mm from the face of the sample. Special care was taken to ensure that the exciter and the sample did not touch at any point. The position of the exciter is shown in figure 1. Alternating wires of the comb capacitor were given a 500 V dc voltage while the other wires were held at ground to induce a polarization in the glass sample. To reduce any eddy current damping [23] and to reduce the probability that polarized dust could span the gap between the sample and the exciter, the exciter was always kept more than 1/2 mm away from the sample. An ac voltage at a resonance frequency of the sample was then added to the dc voltage to excite the corresponding mode. Once the mode had been excited ('rung up') to an amplitude where it could be seen clearly above the noise, both the ac and dc voltages were removed and both exciter wires were held at ground. The sample was then allowed to ring down freely.

The amplitude of excitation in the sample was read out using a birefringence sensor [27, 28] or (in the earliest measurements) by a shadow sensor. For the birefringence sensor, a linearly polarized beam is passed through the sample at or near a node of the resonant mode under study. Modally generated stress at the node induces birefringence in the glass, which couples a small amount of the light into the orthogonal polarization, phase shifted by $\pi/2$. Thus, the light exiting the sample is slightly elliptically polarized. The beam is then passed through a $\lambda/4$ wave-plate aligned with the initial polarization. This brings the phases of the two orthogonal polarization components together, converting the elliptically polarized light to a linear polarization that is rotated slightly compared with the initial polarization. The rotation angle is (to first order) proportional to the modal strain, and is measured by splitting the beam with a polarizing beamsplitter and monitoring the relative intensity of light in the two channels. This was done with two identical photodiodes and a differencing current-to-voltage amplifier. The output voltage oscillates sinusoidally at the resonant frequency in proportion to the modally induced strain. This signal is sent to a lock-in amplifier to demodulate it to a lower frequency and the data is collected on a PC. The ringdown time τ_n was obtained

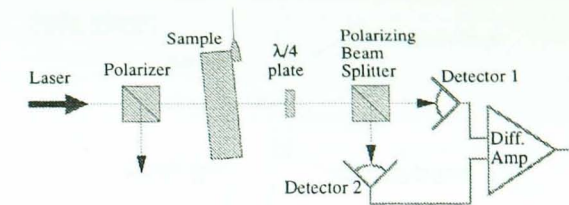


Figure 2. Layout of the birefringence sensor.

by fitting the acquired signal to a damped sinusoid, or by extracting the envelope of the decay. Both approaches yielded the same results, although the accuracy of the former was less sensitive to corruption from noise. A schematic drawing of the optical readout system is shown in figure 2.

For the shadow sensor, an LED is used to cast the shadow of the fused silica suspension fibre onto a split photodiode. The LED/diode pair is positioned close to where the suspension fibre is welded to the edge of the sample. The fibre near the weld point will faithfully follow the motion of the edge of the sample. As the sample resonates, the fibre's shadow moves back and forth on the photodiode at the same frequency. The amount of light falling on each half of the split photodiode changes proportionally. The currents from each half of the photodiode are then compared with a differential current-to-voltage amplifier as in the case of the birefringence sensor. The data acquisition and analysis were identical for both sensors.

For relatively rigid but transparent samples like the ones used here, the birefringence sensor is significantly more sensitive and much easier to use than the shadow sensor. The shadow sensor is better suited to more compliant samples. In both cases, however, the dominant sources of broadband noise were laser noise and noise from the differential amplifier.

The samples were coated by Research Electro-Optics Corporation (REO) of Boulder, Colorado, USA. The coating was a dielectric optical coating consisting of alternating layers of SiO_2 and Ta_2O_5 . The coating was laid down using argon ion beam sputtering, followed by annealing at 450 °C. We chose to examine this particular type of coating because it is the one used on the initial LIGO interferometer mirrors that are currently installed at the LIGO sites. This coating is also of the type currently proposed for Advanced LIGO optics.

The first samples we studied were three rectangular prisms in the shape of microscope slides (7.6 cm \times 2.5 cm \times 0.1 cm) made of Suprasil 2 brand fused silica from Heraeus Quartzglas GmbH of Hannau, Germany. The surface of these samples was treated with a commercial polish to a scratch/dig specification of 80/50. There was no specification on the overall flatness or the surface figure. Two of the three slides (slides A and B) were coated on both sides with a reflective $\text{Ta}_2\text{O}_5/\text{SiO}_2$ coating of 3% transmittance for normally incident, 1 μm wavelength light. The third slide (slide C) was left uncoated as a control. Slide A was suspended from a corner, which had remained uncoated due to being supported at those points during coating. Therefore, welding the suspension fibre to the corner did not induce visible damage to the coating. Slide B, on the other hand, was suspended from the centre of one of its short edges. During the weld, the coating near the suspension point was visibly damaged in a small crescent shape of radius 2 mm surrounding the suspension point. This damaged region was etched off using hydrofluoric (HF) acid. Table 1 shows the modes and quality factors for which Q were repeatably measured. A preliminary version of these results was reported at the Third Edoardo Amaldi Conference on Gravitational Waves [25].

Table 1. Measured Q for transverse bending modes of the three commercially polished fused silica slides. Slides A and B were coated while slide C was left uncoated as a control.

Slide	Coating	Mode	Frequency (Hz)	Q
A	HR	2	1022	$1.1 \pm 0.5 \times 10^5$
	HR	3	1944	$1.6 \pm 0.1 \times 10^5$
	HR	4	2815	$1.6 \pm 0.1 \times 10^5$
B	HR	2	962	$1.3 \pm 0.1 \times 10^5$
C	None	2	1188	$4.0 \pm 0.2 \times 10^6$
	None	3	2271	$4.9 \pm 0.3 \times 10^6$

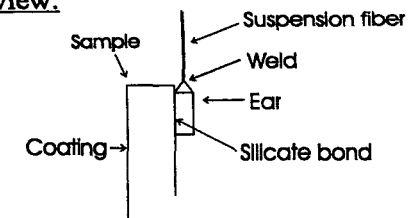
After measuring the Q of the slides, we obtained a disc of Dynasil brand fused silica, 164.85 mm in diameter and 19.00 mm thick from Zygo Corporation of Middlefield, Connecticut. In an effort to determine the effect of surface preparation on the loss due to optical coatings, this sample was made with strict specification for surface flatness, scratch/dig and surface roughness. The coated surface had a surface flatness of less than $\lambda/20$ ($\lambda = 633$ nm), a scratch/dig of 60/40 and a surface roughness of less than 4 Å rms. The back surface had a surface flatness of less than $\lambda/6$, a scratch/dig of 60/40, and a surface roughness of less than 4 Å rms. These specifications are nearly as stringent as the actual requirements for LIGO mirrors. To avoid destroying the surface with welding, an 'ear' of fused silica was bonded onto the back surface using hydroxy catalysis bonding (silicate bonding) [29]. This ear is shaped like a rectangular block with a pyramid on one face. One face of the block is bonded to the sample, so that the tip of the pyramid faces radially. This allows the monolithic suspension to be welded with a torch to the tip of the pyramid without heating the sample very much (see figure 3). Once hung, the Q of the sample was measured using the birefringence readout.

Due to the thickness of this sample (required to meet the flatness specification), only one normal mode had a frequency below 5 kHz. The useful bandwidth of the high voltage amplifier that was used to drive the exciter is about 5 kHz, so measurements were possible only on this mode. This was the 'butterfly' mode, with two radial nodal lines ($\ell = 2$) and no circumferential nodal lines ($n = 0$) [30].

After measuring the Q of this uncoated sample, it was sent to REO to be coated. It received a high reflective (HR) coating on one side, having 1 ppm transmittance and optimized for a 45° angle of incidence. The sample was then rehung and the Q remeasured. As can be seen from table 2, the coating caused a significant reduction in the quality factor. To rule out possible excess loss due to the suspension, the sample was then removed and again rehung. During this hanging attempt (between successful hanging numbers 3 and 4 in table 2), the isolation bob fell and sheared off the bonded ear. The bond did not give; rather, material from the sample was pulled out along with the ear. A second ear was rebonded at 180° to the original ear. Unfortunately, this ear was also sheared off in the same way during the attempt to suspend the sample. This time, the source of the break occurred along the bonded surface, although some of the substrate pulled away as well. Finally, a third attempt succeeded with an ear bonded at 90° to the original ear (hanging number 4 in table 2). Despite the broken ears, the quality factor of the coated disc did not change significantly. The results of all Q measurements on the disc are shown in table 2.

Since it is difficult in any measurement of high Q to completely eliminate the extrinsic technical sources of loss (excess loss), the quality factors measured for a given sample varied slightly from mode to mode or within a single mode between different hangings. Since excess loss always acts to reduce the measured Q , the best indicator of the true internal friction of a

Side view:



Front view:

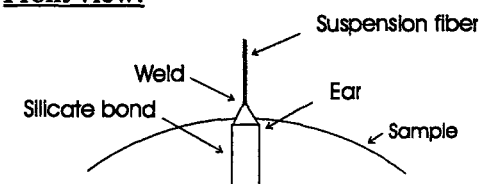


Figure 3. Details of the attachment point. The suspension fibre is welded to the top of the ear. The ear is in turn silicate-bonded along one of its flat faces to the uncoated side of the sample.

Table 2. Measured Q for butterfly mode of the superpolished fused silica disc. In hangings 1 and 2, the disc remained uncoated whereas in hangings 3 and 4 the disc had been coated.

Hanging number	Coating	Frequency (Hz)	Q
1	None	4107	$3.46 \pm 0.02 \times 10^6$
2	None	4107	$3.10 \pm 0.007 \times 10^6$
3	HR (45°)	4108	$1.28 \pm 0.02 \times 10^6$
4 ^a	HR (45°)	4121	$1.24 \pm 0.001 \times 10^6$

^a Ear was sheared off twice before this hanging.

sample is the quality factor of the highest Q mode over all modes and hangings. The spread of measured Q within single hangings was relatively small. For example, the three Q measured in hanging number 2 (sample uncoated) were all between 3.1×10^6 and 2.8×10^6 . The twelve Q measured in hanging number 3 (sample coated) were all within 1.28×10^6 to 1.09×10^6 . As can be seen from tables 1 and 2, the measured Q also did not vary much between modes or hangings, nor between samples in the case of the two coated slides. The reproducibility of the Q of the disc argues strongly that neither the silicate-bonded ear nor the broken ears affected the loss of the sample. The range of measured Q for nominally similar situations is indicative of the level of the variable excess loss. Thus, for all our samples, the large difference in Q between the coated and the uncoated measurements must be due to the coating, and not to statistical variation, excess loss, nor, in the case of the disc, to the broken ears.

4. Results

Using the procedure described in section 3, we obtained Q values from both the slides and the thick disc. To calculate ϕ_{\parallel} from the measured Q we need to know the value of $\delta\dot{U}_{\parallel}/\dot{U}$

Table 3. Physical parameters of the coating and samples. These values are used to calculate the coating loss ϕ_{\parallel} from equation (26).

Sample	Parameter	Value	Units
Slide	Coating layers	14	
	Coating thickness d	2.4	μm
Disc	Coating layers	38	
	Coating thickness d	24.36	μm
Both	Substrate Young's modulus (Y)	7.0×10^{10}	N m^{-2}
	Coating Young's modulus (Y')	1.1×10^{11}	N m^{-2}

for each measured mode of the samples. For transverse bending of the slides, the strain is approximately

$$\epsilon_{ij}(\vec{r}) = \begin{cases} \frac{\partial^2 u_y(z)}{\partial z^2} y & i = j = z \\ 0 & \text{otherwise} \end{cases} \quad (29)$$

where z is the coordinate in the slides' longest dimension, y is the coordinate in the slides' shortest dimension with the origin in the centre plane of the slide and $u_y(z)$ is the transverse displacement of (the centre plane of) the slides due to the bending. Displacements in directions other than y are zero for the transverse bending modes. Using equations (27) and (28) and the coating parameters given in table 3, we find

$$\left[\frac{\delta \bar{U}_{\parallel} d}{\bar{U}} \right]_{\text{slide}} = 7.2 \times 10^{-3} \quad (30)$$

for all transverse bending modes of the slides. The butterfly mode of the disc is more complex, and an analytical expression for strain amplitude $\epsilon(\vec{r})$ was not found. We made a finite-element analysis (FEA) model of this sample and calculated $\bar{U}_{\text{coating}}/\bar{U}$ numerically. Details of the FEA analysis are given in the companion paper [16]. This resulted in a value of

$$\left[\frac{\delta \bar{U}_{\parallel} d}{\bar{U}} \right]_{\text{disc}} \approx \left[\frac{\bar{U}_{\text{coating}}}{\bar{U}} \right]_{\text{disc}} = 5.3 \times 10^{-3} \quad (31)$$

for the butterfly mode of the disc.

The quantities needed to calculate ϕ_{coated} from equation (26) are shown in table 3. Substituting the Q measurements from table 1 into equation (25) to get the loss angles, then using equation (30) and the values in table 3 in equation (26) and solving for ϕ_{\parallel} , we get

$$\phi_{\parallel, \text{slide}} = 4.2 \pm 0.3 \times 10^{-4}. \quad (32)$$

Similarly, from equation (31) and the disc Q in table 2 we get

$$\phi_{\parallel, \text{disc}} = 1.0 \pm 0.3 \times 10^{-4}. \quad (33)$$

The agreement in order of magnitude between these two measured values for ϕ_{\parallel} sets a scale for coating thermal noise. This allows us to make rough estimates of the effect of coating thermal noise on Advanced LIGO. The value of ϕ_{\parallel} for the polished disc agrees within its uncertainty with the value measured for coating loss by the Glasgow/Stanford experiment [16], despite the use of a different coating material in that experiment ($\text{Ta}_2\text{O}_5/\text{Al}_2\text{O}_3$ as opposed to $\text{Ta}_2\text{O}_5/\text{SiO}_2$). This suggests that the substrate surface polish, which is of similar quality on the disc and on the Glasgow/Stanford samples but less good on the slides, may be an important factor contributing to the loss.

Table 4. Comparison of structural thermal noise with and without taking coatings into account. The effective quality factor Q_{eff} (equal to the reciprocal of ϕ_{readout}) represents the quality factor a homogeneous mirror would need to have to give the same structural contribution to thermal noise as the actual coated mirror. (The effect of thermoelastic damping, important for sapphire, is not included in Q_{eff} .) The final column shows the strain amplitude thermal noise at 100 Hz in the Advanced LIGO interferometer resulting from structural loss in the test mass coatings and substrates.

Test mass material	Coating loss	$Q_{\text{eff}} (=1/\phi_{\text{readout}})$	Structural thermal noise at 100 Hz, $\sqrt{S_h}$
Sapphire	None	200×10^6	1×10^{-24}
	$\phi_{\parallel} = 1 \times 10^{-4}$	22×10^6	2×10^{-24}
	$\phi_{\parallel} = 4 \times 10^{-4}$	6×10^6	4×10^{-24}
Fused silica	None	30×10^6	6×10^{-24}
	$\phi_{\parallel} = 1 \times 10^{-4}$	18×10^6	7×10^{-24}
	$\phi_{\parallel} = 4 \times 10^{-4}$	8×10^6	9×10^{-24}

5. Implications

Using equation (23) for the thermal noise due to the coated mirrors, we can now estimate the thermal noise spectrum of the Advanced LIGO interferometer. We calculated the range of coating thermal noise in the pessimistic case using the $\phi_{\parallel} = 4 \times 10^{-4}$ (from the slide results) and in the more optimistic case using $\phi_{\parallel} = 1 \times 10^{-4}$ (from the disc result). In both cases, we assumed a beam spot size of 5.5 cm, which is the maximum obtainable on fused silica when limited by thermal lensing effects [31]. We have extrapolated our results to sapphire substrates using the known material properties of sapphire, even though we did not measure coating loss directly on sapphire. (There have been recent measurements of ϕ_{\parallel} for REO coatings deposited on sapphire [32]. Those results are in rough agreement with the measurements described here.) As mentioned before, the thermal noise estimates will be least accurate for sapphire substrates because sapphire coating thermal noise is likely to be dominated by ϕ_{\perp} which has not been measured. The Young's modulus of sapphire is considerably higher than both Ta_2O_5 and SiO_2 in bulk, so the coating Young's modulus is considerably less than sapphire's. For the purposes of estimating coating thermal noise, we will set the Young's moduli and Poisson's ratios in the two perpendicular directions equal, taking them to be the average of the SiO_2 and Ta_2O_5 values.

Table 4 compares the thermal noise estimates for the four cases considered (optimistic estimates and pessimistic estimates on both fused silica and sapphire substrates) to the thermal noise estimates when coatings are not taken into account. The corresponding noise spectra for Advanced LIGO are shown in figures 4 and 5. These were generated using the program BENCH⁷ 1.13 and show both the total noise and the contribution from the test mass thermal noise. The curves for the total noise were generated using the noise models and parameters from the Advanced LIGO systems design document [31]. The figures show that coating thermal noise is a significant source of noise in the frequency band ~ 30 – 400 Hz for fused silica test masses and ~ 40 – 500 Hz for sapphire test masses.

These estimates are only preliminary indications of the level of coating-induced thermal noise. The largest source of uncertainty is that no measurement has been made of ϕ_{\perp} . Also,

⁷ The program BENCH is available at <http://gravity.phys.psu.edu/Bench/>. Note: The contribution from structural internal thermal noise in BENCH 1.12 was found to be erroneously low by a factor of 2. This error has been corrected in versions of BENCH 1.13 (Aug. 2001) and higher.

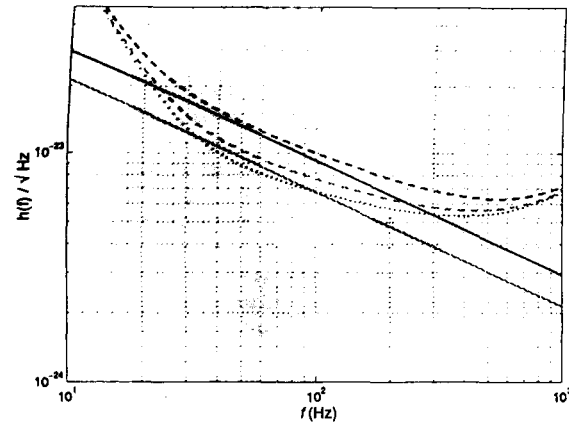


Figure 4. Strain spectrum for Advanced LIGO with fused silica mirrors. The solid, straight lines represent the test mass thermal noise; the dashed curves show the total interferometer noise. The lighter curves were generated using optimistic assumptions including $\phi_{\parallel} = 1 \times 10^{-4}$. The darker curves were generated using pessimistic assumptions including $\phi_{\parallel} = 4 \times 10^{-4}$. The curve shown with a dotted line is the Advanced LIGO noise curve without coating noise as modelled in the Advanced LIGO system design document. In each case, the parameters have been optimized for binary neutron star inspiral.

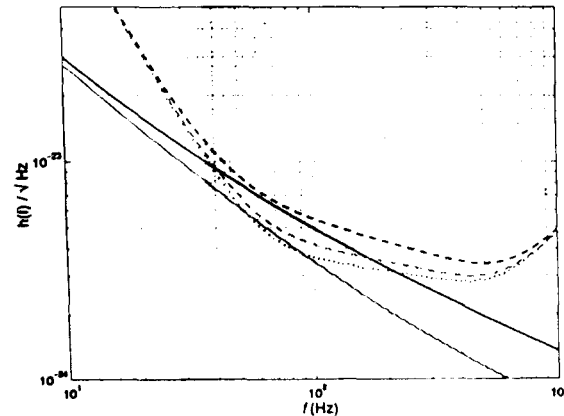


Figure 5. Strain spectrum for Advanced LIGO with sapphire mirrors. The solid, straight lines represent the test mass thermal noise, the dashed curves show the total interferometer noise. The lighter curves were generated using optimistic assumptions including $\phi_{\parallel} = 1 \times 10^{-4}$. The darker curves were generated using pessimistic assumptions including $\phi_{\parallel} = 4 \times 10^{-4}$. The curve shown with a dotted line is the Advanced LIGO noise curve without coating noise as modelled in the Advanced LIGO system design document. In each case, the parameters have been optimized for binary neutron star inspiral.

the Young's modulus of the coating material has not been definitively measured. The half-infinite test mass approximation adds further uncertainty, and this estimate needs to be refined by taking the finite size of the coated test mass into account. In addition, there remains the possibility that the loss associated with the different terms in the energy density ρ_{\parallel} are not equal as supposed here. However, if this were the case, the apparent consistency of the loss between different modes of the samples measured at Glasgow and Stanford [16] would be spurious.

We have also examined the effect of coating thermal noise on the expected sensitivity of the initial LIGO interferometers that are currently being commissioned. In the initial LIGO interferometer, shot noise will be greater than in Advanced LIGO and seismic noise will be significant up to about 40 Hz. Due to the higher level of these other noise sources, test mass thermal noise was not expected to be a large contributor to the total noise [1]. The addition of coating thermal noise raises the overall noise in the most sensitive frequency band, around 200 Hz, by only 4%. Thus, coating thermal noise should not significantly impact the sensitivity of the initial LIGO interferometer.

In addition to the interferometers used for gravitational wave detection, there are a number of prototype interferometers within the gravitational wave community. We have examined data from one of these—the 40 m prototype located at Caltech [33]. In this interferometer, the beam spot size was 0.22 cm and the highest Q seen for a mirror mode was $Q_{\max} = 8.1 \times 10^6$ [34]. Using equation (23) with $\phi_{\parallel} = \phi_{\perp} = 1 \times 10^{-4}$ and $\phi_{\text{substrate}} = 1/Q_{\max}$ in equation (23) yields a predicted thermal noise of $\sim 2 \times 10^{-19} \text{ m}/\sqrt{\text{Hz}}$ at 300 Hz. This is consistent with the 40 m interferometer noise floor shown in figure 3 of [33]. Coating thermal noise is therefore a possible explanation for the broadband excess noise seen between 300 and 700 Hz. The effect of coating thermal noise is also being explored in the Glasgow 10 metre prototype, the thermal noise interferometer (TNI) at Caltech [35] and in the LASTI prototype at MIT.

6. Future work

The measurements and predictions described here indicate that mechanical loss associated with dielectric optical coatings may be a significant source of thermal noise in Advanced LIGO. Plans are under way for experiments that will allow us to better understand and, perhaps, reduce the coating thermal noise. A programme of loss measurements on various optical coatings deposited on both fused silica and sapphire substrates has begun so that the most appropriate coating may be found. There are also plans to try and correlate the loss angle of the coating with other methods of interrogating its structure. To improve the coating thermal noise without major changes to the optics, the coating loss must be reduced. Study of different dielectric materials is clearly warranted, and changes in the deposition process or post-deposition annealing may also lead to improvements. An agreement has been reached between the LIGO laboratory and two optical coating companies to engage in such research.

Two main models exist for understanding the source of the excess loss in the coating. One is that the internal friction of the coating materials, thin layers of Ta_2O_5 and SiO_2 , is high. The other model is that the excess damping comes from rubbing between the layers, and between the coating and the substrate. Experiments are under way to test these models.

Measurement of the unknown parameters in equation (21) are crucial. As discussed in section 2, ringdown Q measurements cannot determine ϕ_{\perp} due to the boundary conditions on the free vibration of a sample. A variation of the anelastic aftereffect experiment [28], which will measure the relaxation rate of the coating after being stressed perpendicularly to the

substrate, is being pursued at Caltech [36]. This experiment should give a direct measurement of ϕ_{\perp} . The same apparatus is also being used to measure the Young's modulus of the coating.

As seen in equation (21), the coating thermal noise in an interferometer is a strong function of the laser spot size. Increasing the size of the laser spot reduces the contribution from coatings to the total thermal noise, so large spot sizes are desirable. Large spots also help decrease the effect of thermoelastic damping in sapphire mirrors [37], so configurations to increase the spot size are already being considered. A spot size of about 6 cm is the largest that can be achieved on the 25 cm diameter test masses while still keeping the power lost due to diffraction below ~ 15 ppm. In the case of 25 cm diameter fused silica test masses, the largest spot size that can be achieved is about 5.5 cm, limited by thermal lensing [31]. Larger diameter test masses and correspondingly larger spot sizes would be one way of reducing the coating-induced thermal noise in Advanced LIGO. However, this would require a re-evaluation of a number of Advanced LIGO subsystems.

Acknowledgments

We would like to thank H Armandula and J Camp for their help in getting our samples coated. We thank L Samuel Finn and everyone who contributed to BENCH for making it available to us. F Raab first suggested that we look at the 40 m prototype noise data, and we had useful discussions about the 40 m prototype with D Shoemaker, M Zucker, P Fritschel and S Whitcomb. P Fritschel also showed us how to optimize BENCH for maximum binary neutron star reach and helped in getting the large disc sample coated. P Willems provided thoughtful comments on the limits of applicability of the coating loss model. We thank E Gustafson for useful discussions about experiments with fused silica. The Syracuse University glassblower, J Chabot, gave crucial help by teaching us about glass welding. We thank M Mortonson for help in the lab, and E S Watkins for useful comments on the manuscript. This work was supported by Syracuse University, US National Science Foundation grant nos PHY-9900775 and PHY-9210038, the University of Glasgow and PPARC.

Appendix. Stresses and strains in the coating

We obtain the stresses and strains in the coating in terms of the stresses and strains in the surface of the substrate by utilizing the thin coating approximation, and assuming that the coating Poisson's ratio is not very different from that of the substrate. Denoting strains by ϵ_{ij} and stresses by σ_{ij} , this can be summarized in terms of the following constraints. In cylindrical coordinates

$$\epsilon'_{rr} = \epsilon_{rr} \quad \epsilon'_{\theta\theta} = \epsilon_{\theta\theta} \quad \epsilon'_{rz} = \epsilon_{rz} \quad \sigma'_{zz} = \sigma_{zz} \quad \sigma'_{rz} = \sigma_{rz} \quad (\text{A1})$$

where primed quantities refer to the coating and the unprimed quantities refer to the surface of the substrate. Due to axial symmetry $\epsilon'_{\theta\theta} = \epsilon'_{z\theta} = \sigma'_{\theta\theta} = \sigma'_{z\theta} = 0$. We use the following relations, valid for axially symmetric deformations [19]:

$$\begin{aligned} \sigma_{rr} &= (\lambda + 2\mu)\epsilon_{rr} + \lambda\epsilon_{\theta\theta} + \lambda\epsilon_{zz} \\ \sigma_{\theta\theta} &= \lambda\epsilon_{rr} + (\lambda + 2\mu)\epsilon_{\theta\theta} + \lambda\epsilon_{zz} \\ \sigma_{zz} &= \lambda\epsilon_{rr} + \lambda\epsilon_{\theta\theta} + (\lambda + 2\mu)\epsilon_{zz} \\ \sigma_{rz} &= 2\mu\epsilon_{rz} \end{aligned} \quad (\text{A2})$$

where λ and μ are the Lamé coefficients. In terms of Young's modulus and Poisson's ratio, the Lamé coefficients are

$$\lambda = Y\sigma/((1+\sigma)(1-2\sigma)) \quad \mu = Y/(2(1+\sigma)). \quad (\text{A3})$$

Combining equations (A1) and equations (A2), we obtain the stresses and strains in the coating in terms of the stresses and strains in the surface of the substrate,

$$\begin{aligned} \epsilon'_{rr} &= \epsilon_{rr} \\ \epsilon'_{\theta\theta} &= \epsilon_{\theta\theta} \\ \epsilon'_{zz} &= \frac{\lambda - \lambda'}{\lambda' + 2\mu'}(\epsilon_{rr} + \epsilon_{\theta\theta}) + \frac{\lambda + 2\mu}{\lambda' + 2\mu'}\epsilon_{zz} \\ \epsilon'_{rz} &= \epsilon_{rz} \\ \sigma'_{rr} &= (\lambda' + 2\mu')\epsilon_{rr} + \lambda'\epsilon_{\theta\theta} + \lambda'\epsilon'_{zz} \\ \sigma'_{\theta\theta} &= \lambda'\epsilon_{rr} + (\lambda' + 2\mu')\epsilon_{\theta\theta} + \lambda'\epsilon'_{zz} \\ \sigma'_{zz} &= \sigma_{zz} \\ \sigma'_{rz} &= \sigma_{rz} \end{aligned} \quad (\text{A4})$$

where λ' and μ' are the Lamé coefficients of the coating, and λ and μ are the Lamé coefficients of the substrate.

We obtain the stresses and strains in the substrate ϵ_{ij} , σ_{ij} from the general solutions to the axially symmetric equations of elasticity for an infinite half-space [17, 19],

$$\begin{aligned} u_r(r, z) &= \int_0^\infty \left[\alpha(k) - \frac{\lambda + 2\mu}{\lambda + \mu}\beta(k) + \beta(k)kz \right] e^{-kz} J_1(kr) k dk \\ u_z(r, z) &= \int_0^\infty \left[\alpha(k) + \frac{\mu}{\lambda + \mu}\beta(k) + \beta(k)kz \right] e^{-kz} J_0(kr) k dk \\ u_\theta(r, z) &= 0 \quad (\text{axial symmetry}) \end{aligned} \quad (\text{A5})$$

where $u_r(r, z)$ is the radial deformation of the test mass, $u_z(r, z)$ is the deformation of the test mass perpendicular to the face (z being positive inward) and $u_\theta(r, z)$ is the transverse displacement. $J_1(kz)$ and $J_0(kz)$ are Bessel functions of the first kind. The functions $\alpha(k)$ and $\beta(k)$ are determined by the boundary conditions at the front face: $\sigma_{rz}(r, z=0) = 0$ and $\sigma_{zz}(r, z=0) = p(r)$ [19]. Using the pressure distribution $p(r)$ from equation (8) gives

$$\alpha(k) = \beta(k) = \frac{F}{4\pi\mu k} \exp\left(-\frac{1}{8}k^2 w^2\right). \quad (\text{A6})$$

Substituting equation (A6) into equations (A5) and performing the integrals leads to

$$u_r(r, z=0) = -\frac{F(\omega)}{4\pi(\lambda + \mu)r} \left[1 - \exp\left(-\frac{2r^2}{w^2}\right) \right] \quad (\text{A7})$$

$$u_z(r, z=0) = \frac{F(\omega)(\lambda + 2\mu)}{2\sqrt{2\pi}(\lambda + \mu)\mu w} \exp\left(-\frac{r^2}{w^2}\right) I_0\left(\frac{r^2}{w^2}\right) \quad (\text{A8})$$

where I_0 is a modified Bessel function of the first kind. These deformations are shown, along with the pressure distribution $p(r)$, in figure 6. The strains in the substrate are obtained from the relations

$$\epsilon_{rr} = \delta u_r / \delta r \quad \epsilon_{\theta\theta} = u_r / r \quad \epsilon_{zz} = \delta u_z / \delta z \quad \epsilon_{rz} = (\delta u_z / \delta r + \delta u_r / \delta z) / 2. \quad (\text{A9})$$

These strains can now be used to find the stresses in the surface of the substrate through equations (A2), and then to find the stresses and strains in the coating through equations (A4).

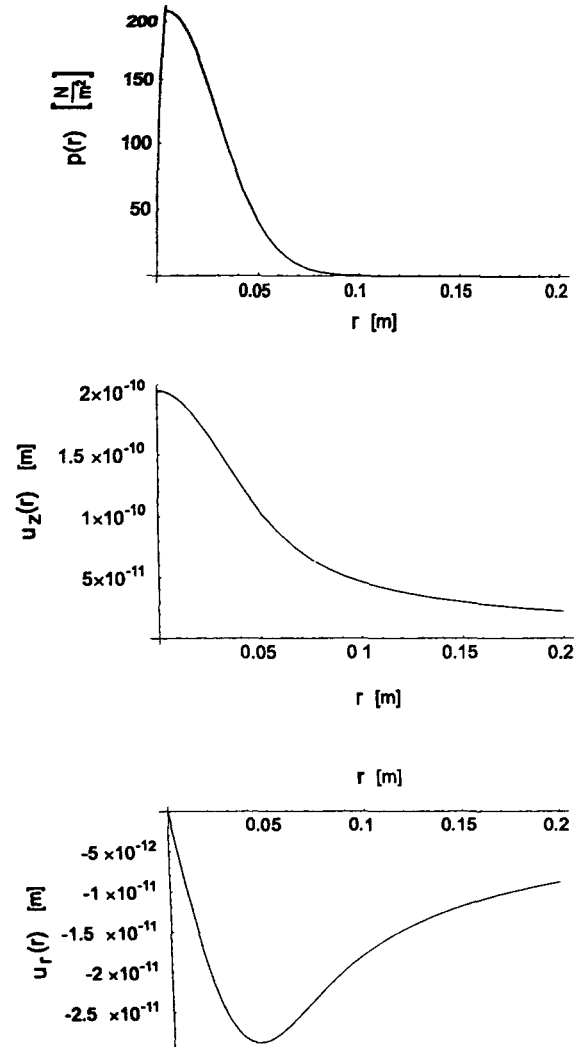


Figure 6. *Top*: Pressure distribution $p(r)$ from equation (8) (with F set to unity). The pressure distribution has the same shape as the laser intensity. *Centre*: The resulting response of the surface in the axial direction, $u_z(r)$. The impression is wider than the applied pressure. *Bottom*: The resulting response in the radial direction, $u_r(r)$. As expected, the surface is pulled towards the centre.

The results for the surface of the substrate are

$$\begin{aligned}
 \epsilon_{rr} &= \frac{F}{4\pi(\lambda + \mu)} \left(\frac{1}{r^2} (1 - e^{-2r^2/w^2}) - \frac{4}{w^2} e^{-2r^2/w^2} \right) \\
 \epsilon_{\theta\theta} &= -\frac{F}{4\pi(\lambda + \mu)} \left(\frac{1}{r^2} (1 - e^{-2r^2/w^2}) \right) \\
 \epsilon_{zz} &= -\frac{F}{4\pi(\lambda + \mu)} \left(\frac{4}{w^2} e^{-2r^2/w^2} \right) \\
 \epsilon_{rz} &= 0 \\
 \sigma_{rr} &= \frac{F}{2\pi(\lambda + \mu)} \left(\frac{\mu}{r^2} (1 - e^{-2r^2/w^2}) - \frac{4(\lambda + \mu)}{w^2} e^{-2r^2/w^2} \right) \\
 \sigma_{\theta\theta} &= -\frac{F}{2\pi(\lambda + \mu)} \left(\frac{\mu}{r^2} (1 - e^{-2r^2/w^2}) + \frac{4\lambda}{w^2} e^{-2r^2/w^2} \right) \\
 \sigma_{zz} &= -\frac{F}{2\pi} \left(\frac{4}{w^2} e^{-2r^2/w^2} \right) \\
 \sigma_{rz} &= 0
 \end{aligned} \tag{A10}$$

and for the coating

$$\begin{aligned}
 \epsilon'_{rr} &= \epsilon_{rr} \\
 \epsilon'_{\theta\theta} &= \epsilon_{\theta\theta} \\
 \epsilon'_{zz} &= -\frac{F(2(\lambda + \mu) - \lambda')}{4\pi(\lambda + \mu)(\lambda' + 2\mu')} \left(\frac{4}{w^2} e^{-2r^2/w^2} \right) \\
 \epsilon'_{rz} &= 0 \\
 \sigma'_{rr} &= \frac{F}{2\pi(\lambda + \mu)(\lambda' + 2\mu')} \left(\frac{\mu'(\lambda' + 2\mu')}{r^2} (1 - e^{-2r^2/w^2}) \right. \\
 &\quad \left. - \frac{4(\lambda'(\lambda + \mu) + 2\mu'(\lambda' + \mu'))}{w^2} e^{-2r^2/w^2} \right) \\
 \sigma'_{\theta\theta} &= -\frac{F}{2\pi(\lambda + \mu)(\lambda' + 2\mu')} \left(\frac{\mu'(\lambda' + 2\mu')}{r^2} (1 - e^{-2r^2/w^2}) \right. \\
 &\quad \left. + \frac{4(\lambda'(\lambda + \mu + \mu'))}{w^2} e^{-2r^2/w^2} \right) \\
 \sigma'_{zz} &= \sigma_{zz} \\
 \sigma'_{rz} &= 0.
 \end{aligned} \tag{A11}$$

Equations (A10) can now be used to find the energy density in the substrate and integrated over the half-infinite volume, equation (16), to give the total energy in the substrate, equation (17). Equations (A11) can be substituted into the expression for the energy density at the surface, equation (13), and integrated over the surface to give the expressions for δU_{\parallel} and δU_{\perp} in equations (18) and (19).

References

- [1] Abramovici A et al 1992 *Science* **256** 325
- [2] Giazotto A 1998 *Nucl. Instrum. Methods Phys. Res. A* **289** 518
- [3] Lück H et al 2000 *Proc. 3rd Edoardo Amaldi Conf. on Gravitational Waves* ed S Meshkov (Melville, NY: AIP) p 119

- [4] Tsubono K 1995 *Gravitational Wave Experiments Proc. 1st Edoardo Amaldi Conf.* (Singapore: World Scientific) p 112
- [5] LSC white paper on detector research and development webpage <http://www.ligo.caltech.edu/docs/T/T990080-00.pdf>
- [6] *Internal Report* Max-Planck Institut für Quantenoptik, D-85748 Garching 2000
- [7] Kuroda K *et al* 1999 *Int. J. Mod. Phys. D* 8 557 webpage <http://www.icrr.u-tokyo.ac.jp/gr/LCGT.pdf>
- [8] Fraser D B 1968 *J. Appl. Phys.* 39 5868
Fraser D B 1970 *J. Appl. Phys.* 41 6
- [9] Lunin B S, Torbin S N, Danachevskaya M N and Batov I V 1994 *Moscow State Chem. Bull.* 35 24
- [10] Penn S D, Harry G M, Gretarsson A M, Kittelberger S E, Saulson P R, Schiller J J, Smith J R and Swords S O 2001 *Rev. Sci. Instrum.* 72 3670
(Penn S D, Harry G M, Gretarsson A M, Kittelberger S E, Saulson P R, Schiller J J, Smith J R and Swords S O 2000 *Preprint* gr-qc/0009035)
- [11] Rowan S, Cagnoli G, Sneddon P, Hough J, Route R, Gustafson E K, Fejer M M and Mitrofanov V 2000 *Phys. Lett. A* 265 5
- [12] Braginsky V B, Mitrofanov V P and Panov V I 1985 *Systems with Small Dissipation* (Chicago, IL: University of Chicago Press)
- [13] Whitcomb S 1996 *Proc. TAMA Int. Workshop on Gravitational Wave Detection* ed K Tsubono (Tokyo: Universal Academy)
- [14] Callen H B and Greene R F 1952 *Phys. Rev.* 86 703
- [15] Levin Yu 1998 *Phys. Rev. D* 57 659
- [16] Crooks D *et al* 2002 *Class. Quantum Grav.* 19 882
- [17] Liu Y T and Thorne K S 2000 *Phys. Rev. D* 62 122002
- [18] Numata K, Bianchi G B, Ohishi N, Sekiya A, Otsuka S, Kawabe K, Ando M and Tsubono K 2000 *Phys. Lett. A* 276 37
- [19] Bondu F, Hello P and Vinet J 1998 *Phys. Lett. A* 246 227
- [20] Jones R M 1999 *Mechanics of Composite Materials* (Philadelphia: Taylor and Francis)
- [21] Nakagawa N 2001 Oral presentation at the *LIGO Scientific Collaboration Meeting (Hanford, WA, USA, 13–16 Aug. 2001)*
- [22] Nakagawa N, Gretarsson A M, Gustafson E K and Fejer M M *Phys. Rev. D* at press
(Nakagawa N, Gretarsson A M, Gustafson E K and Fejer M M 2001 *Preprint* gr-qc/0105046)
- [23] Huang Y L and Saulson P R 1998 *Rev. Sci. Instrum.* 69 544
- [24] Gretarsson A M and Harry G M 1999 *Rev. Sci. Instrum.* 70 4081
(Gretarsson A M and Harry G M 1999 *Preprint* physics/9904015)
- [25] Gretarsson A M, Harry G M, Penn S D, Saulson P R, Schiller J J and Startin W J 2000 *Proc. 3rd Edoardo Amaldi Conf. on Gravitational Waves* ed S Meshkov (Melville, NY: AIP)
(Gretarsson A M, Harry G M, Penn S D, Saulson P R, Schiller J J and Startin W J 1999 *Preprint* physics/9911040)
- [26] Cadez A and Abramovici A 1988 *J. Phys. E: Sci. Instrum.* 21 453
- [27] Startin W J, Beilby M A and Saulson P R 1998 *Rev. Sci. Instrum.* 69 3681
- [28] Beilby M A, Saulson P R and Abramovici A 1998 *Rev. Sci. Instrum.* 69 2539
- [29] Gwo D H 1998 *Proc. SPIE-Int. Soc. Opt. Eng.* 3435 136
- [30] Blevins R D 1979 *Formulas for Natural Frequency and Mode Shape* (New York: Van Nostrand-Reinhold) p 240
- [31] Fritschel P *Advanced LIGO Systems Design* webpage www.ligo.caltech.edu/docs/T/T010075-0.pdf
- [32] Rowan S 2001 Oral presentation at *Aspen Winter Conf. on Gravitational Waves (Aspen, Colorado, USA, 4–10 Feb. 2001)*
- [33] Abramovici A *et al* 1996 *Phys. Lett. A* 218 157
- [34] Gillespie A and Raab F 1995 *Phys. Rev. D* 52 577
- [35] Libbrecht K 2001 California Institute of Technology Private communication
- [36] Willems P 2001 California Institute of Technology Private communication
- [37] Braginsky V B, Gorodetsky M L and Vyatchanin S P 1999 *Phys. Lett. A* 264 1

The GEO 600 gravitational wave detector

B Willke^{1,3}, P Aufmuth¹, C Aulbert⁴, S Babak⁵, R Balasubramanian⁵,
B W Barr², S Berukoff⁴, S Bose⁴, G Cagnoli², M M Casey²,
D Churches⁵, D Cluble², C N Colacino¹, D R M Crooks², C Cutler⁴,
K Danzmann^{1,3}, R Davies⁵, R Dupuis², E Elliffe², C Fallnich⁶,
A Freise³, S Goßler¹, A Grant², H Grote³, G Heinzel¹, A Heptonstall²,
M Heurs¹, M Hewitson², J Hough², O Jennrich², K Kawabe³, K Kötter¹,
V Leonhardt¹, H Lück^{1,3}, M Malec¹, P W McNamara², S A McIntosh²,
K Mossavi³, S Mohanty⁴, S Mukherjee⁴, S Nagano², G P Newton²,
B J Owen⁴, D Palmer², M A Papa⁴, M V Plissi², V Quetschke¹,
D I Robertson², N A Robertson², S Rowan², A Rüdiger³,
B S Sathyaprakash⁵, R Schilling³, B F Schutz^{4,5}, R Senior⁵,
A M Sintes⁴, K D Skeldon², P Sneddon², F Stief¹, K A Strain²,
I Taylor⁵, C I Torrie², A Vecchio^{4,7}, H Ward², U Weiland¹, H Welling⁶,
P Williams⁴, W Winkler³, G Woan² and I Zawischa⁶

¹ Institut für Atom- und Molekülphysik, Universität Hannover, Callinstr. 38, 30167 Hannover, Germany

² Physics & Astronomy, University of Glasgow, Glasgow G12 8QQ, UK

³ Max-Planck-Institut für Gravitationsphysik, Albert-Einstein-Institut, Außenstelle Hannover, Callinstr. 38, 30167 Hannover, Germany

⁴ Max-Planck-Institut für Gravitationsphysik, Albert-Einstein-Institut, Am Mühlenberg 1, 14476 Golm, Germany

⁵ Department of Physics and Astronomy, Cardiff University, PO Box 913, Cardiff, CF2 3YB, UK

⁶ Laser Zentrum Hannover e. V., Hollerithallee 8, 30419 Hannover, Germany

⁷ School of Physics and Astronomy, The University of Birmingham, Edgbaston, Birmingham, B15 2TT, UK

Received 2 October 2001, in final form 14 November 2001

Published 11 March 2002

Online at stacks.iop.org/CQG/19/1377

Abstract

The GEO 600 laser interferometer with 600 m armlength is part of a worldwide network of gravitational wave detectors. Due to the use of advanced technologies like multiple pendulum suspensions with a monolithic last stage and signal recycling, the anticipated sensitivity of GEO 600 is close to the initial sensitivity of detectors with several kilometres armlength. This paper describes the subsystems of GEO 600, the status of the detector by September 2001 and the plans towards the first science run.

PACS number: 0480N

(Some figures in this article are in colour only in the electronic version)

1. Introduction

An international network of earth-bound laser-interferometric gravitational wave detectors is currently in the final commissioning phase. These detectors will be searching for gravitational waves from a number of different astrophysical sources like supernovae explosions, non-symmetric pulsars, inspiralling binary systems of neutron stars or black holes and remnants of the big bang. Furthermore, unknown sources may produce gravitational waves of detectable strength. A summary of the current understanding of astrophysical sources for gravitational waves and of predicted event rates is given in [1]. Although the expected sensitivities of the detectors under construction might be high enough to detect the first gravitational waves, only future detector generations with advanced technologies promise an event rate suitable for gravitational wave astronomy.

Six laser interferometric gravitational wave detectors are currently under construction: three interferometers of the LIGO project [2] in the USA (two interferometers with 4 km baseline and one interferometer with 2 km baseline), one detector of the French–Italian VIRGO project [3] in Italy with 3 km baseline, the TAMA detector [4] in Japan with a baseline of 300 m and the British–German GEO 600 detector with 600 m armlength in Germany. An 80 m prototype interferometer with the option to extend it to a large-scale detector is under construction by the ACIGA project in Australia [5].

The GEO 600 detector was designed based on the experience with two prototypes: the 10 m interferometer at the Glasgow University and the 30 m interferometer at the Max-Planck-Institut für Quantenoptik in Garching, near Munich. The construction of GEO 600 started in 1995 as a German/British collaboration on a site near Hannover in Germany and will be completed in 2002. Based on the constraint that the length of the vacuum pipes could not exceed 600 m, an advanced optical layout including signal recycling and novel techniques for the seismic isolation systems were included in the detector design. In parallel to the commissioning of the detector methods for data analysis as well as simulations of possible sources were developed at the University of Cardiff and at the Albert-Einstein-Institut of the Max-Planck-Gesellschaft in Potsdam.

The following sections of this paper will describe the different subsystems of the GEO 600 detector, briefly review the detector characterization and data analysis effort within GEO 600 and end with an outline of the future plans.

2. Noise sources and design sensitivity

The measured quantity in a laser interferometric gravitational wave detector is the change of the light power on a photodetector placed at the interferometer output. A fluctuation of the light power at this photodetector can be caused by many different sources. A gravitational wave passing through the detector plane causes the light beams to accumulate a phase difference $\delta\varphi_{gw}$ while travelling through the interferometer arms, and the signature of the gravitational wave can be detected as a power modulation δI_{gw} on the photodetector. A change δI_{noise} of that light power can as well be due to laser power fluctuations of either technical or quantum nature or a displacement of the mirrors caused by seismic motion or thermal noise. Some of the numerous additional noise sources that have to be taken into account are fluctuations of the index of refraction on the optical path, laser frequency fluctuations in combination with a difference in the arm length of the interferometer and coherent superposition of the main laser beam with light scattered from optical components.

To describe the sensitivity of a gravitational wave detector a quantity h is defined as: $h = \Delta L/\ell$. In this equation ℓ is the optical path length of one interferometer arm and ΔL is

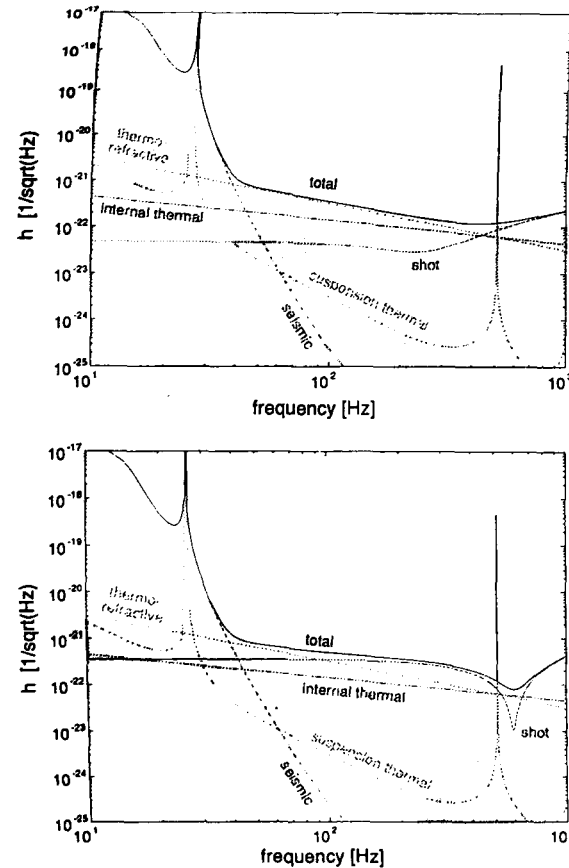


Figure 1. Expected noise spectral density of the GEO 600 detector shown in two different modes of operation: broad-band (upper) and narrow-band (lower).

the apparent differential change in optical path length between the two interferometer arms, which is either caused by a gravitational wave or by a noise process. We call it apparent length change as it can be due to either a real displacement of a mirror or to a different process changing the phase of the light when it returns to the beamsplitter. To be able to quantitatively describe noise sources like laser power noise on the photodetector that do not directly change the phase of the two interfering beams we calculate the ΔL which would cause the same power modulation on the output photodetector. By this method h can be used to describe all noise sources of a detector as well as the signal strength of a gravitational wave. As some of the noise sources have a very strong frequency dependence, the spectral density \dot{h}_{noise} is widely used to describe the so-called strain sensitivity of laser-interferometric gravitational-wave detectors.

Three main noise sources will limit the expected sensitivity of the GEO 600 detector as shown in figure 1. The low-frequency range below 40 Hz will be limited by seismic noise.

In the intermediate region thermo-refractive noise [6] will be the main contribution and shot noise on the interferometer-output photodetector will dominate the noise spectral density in the high Fourier frequency range. The expected thermal noise of the mirror and the suspension are plotted as well. Other noise sources such as radiation pressure noise, residual gas fluctuations, gravity gradient noise or laser noise are omitted in this figure as they are not expected to limit the performance of GEO 600.

One feature of figure 1 is special for GEO 600, which is the shape of the shot-noise curve. The use of the signal-recycling technique [7] allows shaping of the shot-noise curve in the strain-sensitivity plot. By changing the reflectivity and position of the signal-recycling mirror the bandwidth and the centre frequency of the dip in the shot-noise curve can be tuned. The left part of figure 1 shows the broad-band case, and in the right part the expected shot noise for narrow-band signal recycling tuned to 600 Hz is plotted.

3. Buildings and vacuum system

To avoid fluctuations of the optical path length caused by a fluctuating index of refraction, the whole interferometer has to be set up in a high-vacuum system. For this purpose GEO 600 uses two 600 m long vacuum tubes of 60 cm diameter which are suspended in a trench in the ground. A novel convoluted-tube design which allows a wall thickness of only 0.8 mm was used to reduce the weight and cost of the stainless-steel vacuum tube. Baffles were installed inside the tube to avoid stray light reflections by the shiny tube wall. Each tube was baked for two days in air at 200 °C and for one week under vacuum at 250 °C. Currently the pressure in the beam tubes is in the upper 10^{-9} mbar region.

One central building (13 m × 8 m in size) and two end buildings (6 m × 3 m) accommodate the vacuum tanks (2 m tall) in which the optical components are suspended. Eight of these tanks form a cluster in the central building which can be subdivided into three sections to allow mirror installation without venting the whole cluster. Therefore only short down-times are expected for a change of the signal-recycling mirror, needed to change the detector bandwidth.

The whole vacuum system, except for the modecleaner section, is pumped by four magnetically levitated turbo pumps with a pumping speed of 1000 l s^{-1} , each backed by a scroll pump ($25 \text{ m}^3 \text{ h}^{-1}$). Additional dedicated pumping systems are used for the modecleaner and the signal-recycling section.

Great care was taken to minimize contamination of the vacuum system by hydrocarbons. For this reason the seismic isolation stacks, which comprise rubber and other materials containing hydrocarbons, are sealed by bellows and pumped separately. Furthermore, the light-emitting diodes (LEDs), the photodiodes and the feedback coils used as sensors and actuators in the pendulum damping systems are sealed in glass encapsulations.

The buildings of GEO 600 are split into three regions with different cleanroom classes: the so-called gallery where people can visit and staff can work with normal clothes, the inner section which has a cleanroom class of 1000 and a movable cleanroom tent installed over open tanks with a cleanroom class 100.

4. Seismic isolation and thermal noise

One of the most important sub-systems in a laser-interferometric gravitational-wave detector is the seismic isolation and suspension system. The spectral density of the seismic ground motion at the GEO site is about eight orders of magnitude above the displacement requirement for the mirror. The filter effect of a sequential system of harmonic oscillators with resonance frequencies below 10 Hz is used to isolate the mirrors against this seismic motion.

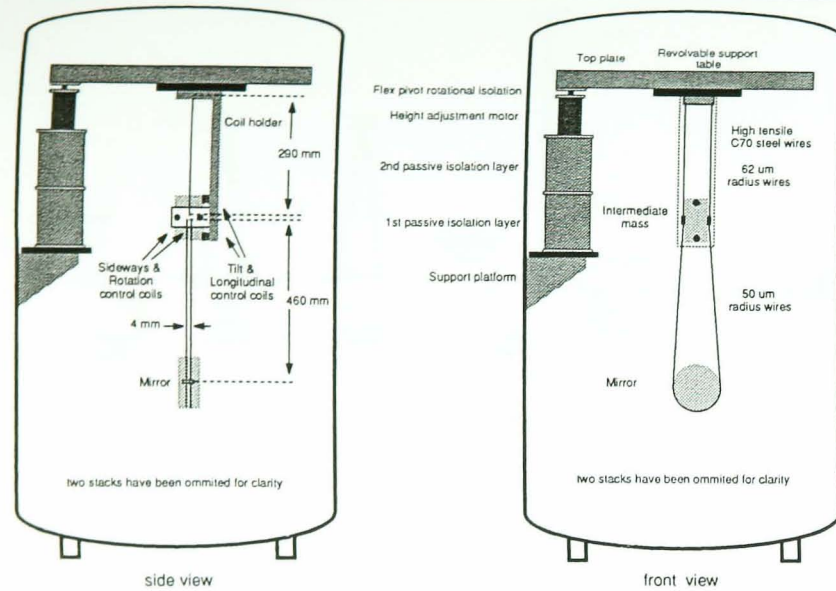


Figure 2. The GEO 600 modecleaner suspension system. Two passive stack layers, a rotational flexure and a double pendulum are used to isolate the modecleaner mirror from seismic noise. The quality factor of a violin mode of this suspension at 190 Hz was measured to be between 5×10^5 and 1×10^6 .

Two different types of isolation systems are implemented in GEO 600. The first one, which is used to isolate the modecleaner optics, consists of a top plate supported by three legs and a double-pendulum suspension (see figure 2). Each leg has two passive isolation layers (rubber layers with an intermediate stainless-steel mass) which are followed by horizontal adjustment motors and flex-pivot rotation springs to reduce rotational coupling between the vacuum tank and the top plate. To avoid an excitation of the pendulum mode four co-located control systems measure the motion of the intermediate mass with respect to a coil-holder arm that is rigidly attached to the top plate. These so-called local controls use shadow sensors and feedback coils that apply forces to magnets glued to the intermediate mass. The bandwidth of these local controls is about 3 Hz. The intermediate mass is suspended by two wires and the modecleaner mirrors are supported by two wire slings. These mirrors are 10 cm in diameter and 5 cm thick. This arrangement allows us to control tilt and rotation of the mirror as well as its sideways and longitudinal position at the intermediate-mass level. Hence the coil/magnet units of the local controls can also be used for automatic alignment control of the modecleaners [8]. Small fused-silica prisms are attached to the mirrors to define the break-off points of the wires from the mirror circumference. A fixed break-off point reduces the friction of the wire on the mirror which directly affects the thermal noise. A measurement of the quality factor Q of the violin modes of the modecleaner suspensions shows Q values between 5×10^5 and 1×10^6 . To allow fast feedback of the modecleaner length-control system, a second double pendulum called a reaction pendulum is placed a few millimetres behind one mirror of each modecleaner. The bottom mass of the reaction pendulum carries coils which act on magnets

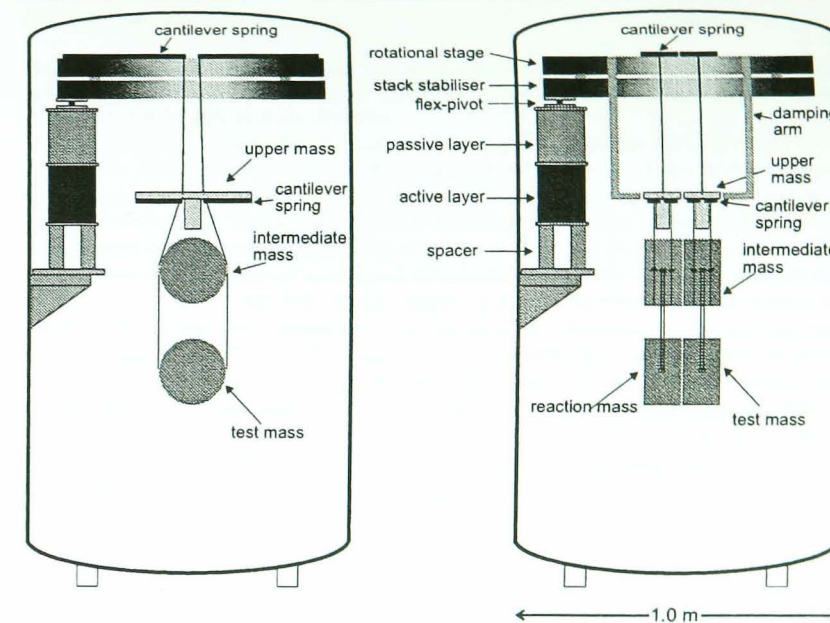


Figure 3. The GEO 600 main suspension system. Two stack layers (one active, one passive), a rotational flexure, two vertical cantilever stages and a triple horizontal pendulum are used to isolate the test mass from seismic noise. The lower pendulum stage is a monolithic fused-silica design to minimize thermal noise.

glued to the corresponding mirror. This provides a feedback actuator with small seismic motion above 10 Hz Fourier frequency.

Figure 3 shows the seismic isolation system used to isolate the beam splitter and the mirrors of the Michelson interferometer. Just as for the modecleaner suspensions three legs support the so-called stack stabilizer and the rotational stage. Without lateral movement the rotational stage can be rotated with respect to the stack stabilizer to allow for rotational pre-alignment of the mirror. The mirror is the lowest mass of a triple pendulum with two blade-spring stages for vertical isolation which is mounted to the rotational stage. Each leg has an active and a passive layer for seismic isolation. The active system consists of three 2 Hz geophones to sense the motion of the upper plate of a three-axis piezo actuator. By means of a feed-forward control system for the horizontal and a feedback system for the vertical direction the motion of this upper plate is reduced with respect to the seismic ground motion. On top of this plate a rubber/stainless-steel isolation layer is placed, and a flex-pivot is used for rotational isolation.

The triple pendulum has three masses: an upper mass made of stainless steel, a fused-silica intermediate mass and the mirror which is 18 cm in diameter (the beam splitter diameter is 26 cm). In the case of the triple pendulum six co-located feedback systems are used to damp all degrees of freedom of the upper mass. Due to the specific design of the triple pendulum this damping extracts energy from all pendulum modes below Fourier frequencies of 10 Hz. Similar to the modecleaner suspension the coil-magnet units of these local controls are used

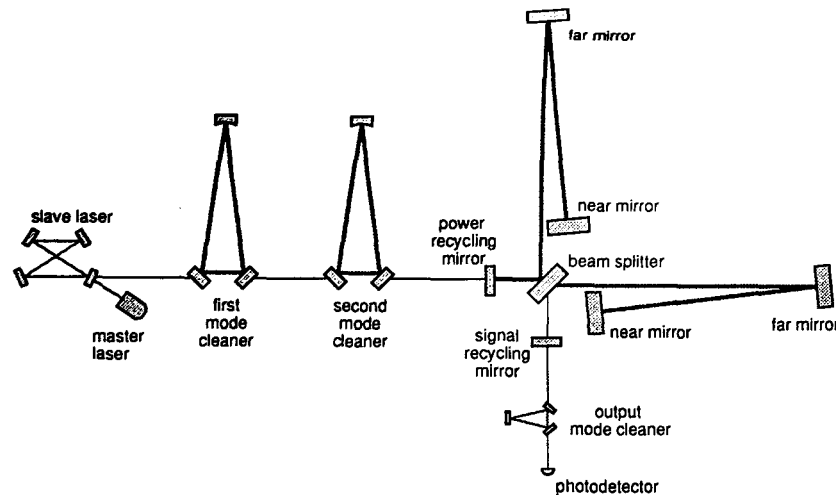


Figure 4. Optical layout of GEO 600: a 12 W injection-locked laser system is filtered by two sequential modecleaners and injected into the dual-recycled interferometer. A folded light path is used to increase the round-trip length of the interferometer arms to 2400 m. An output modecleaner will be used to spatially clean the laser mode before it reaches the photodetector.

as actuators for the automatic alignment-control systems. The reaction pendulums for length control of the Michelson interferometer consist of similar triple pendulums suspended 3 mm behind the corresponding mirror. The intermediate mass of the reaction pendulum carries coils that act on mirrors glued to the intermediate mass of the mirror triple pendulum. To keep the internal quality factor of the mirrors as high as possible no magnets are glued to the mirror itself but electrostatic feedback between the mirror and the lowest mass of the reaction pendulum is used to apply feedback forces in the high Fourier frequency range. A detailed description of the seismic isolation system can be found in the paper of Plissi *et al* [9].

To minimize the internal thermal noise of the mirror and the pendulum thermal noise, the lowest pendulum stage is made entirely from fused silica. The Q of fused-silica suspensions of comparable size has been demonstrated to be as high as 1×10^7 [10]. Small fused-silica pieces are attached to the intermediate mass and to the mirror itself by a technique called hydroxide-catalysis bonding [11]. This technique provides high-strength bonds and allows the quality factors to be kept high and thus the thermal noise low. Four fused-silica fibres with 270 μm diameter are welded to these fused-silica pieces and support the mirrors.

5. Optical layout

The optical layout of GEO 600 (see figure 4) has three major parts: the laser system, two sequential input modecleaners and the dual-recycled Michelson interferometer with the output modecleaner and the main photodetector at its output port. Some steering mirrors, electro-optical modulators and Faraday isolators are omitted in figure 4. All optical components except the laser system and the photodetector are suspended inside the vacuum system.

5.1. Laser system and modecleaners

The GEO 600 laser system is based on an injection-locked laser-diode-pumped Nd:YAG system with an output power of 12 W. A non-planar ring-oscillator (NPRO) with an output power of 0.8 W is used as the master laser.

Two Nd:YAG crystals, each pumped by a fibre-coupled laser diode with a power of 17 W, are used as the active medium in the four-mirror slave ring cavity. Three of these mirrors and a piezo-electric transducer (PZT) carrying the fourth mirror are mounted on a rigid invar spacer to increase the mechanical stability of the slave-laser cavity. A measurement of the free-running frequency noise of the slave laser showed that the fluctuations in the acoustic Fourier frequency range are of an order of magnitude lower for the rigid spacer design than compared to a slave cavity with discrete mirror mounts. The PZT is used to control the length of the 45 cm long resonator to keep the slave-laser frequency within the injection-locking range of 1.6 MHz. Two Brewster plates are incorporated in the slave cavity to define the polarization direction, reduce depolarization losses and compensate for the astigmatism introduced by the curved mirrors of the slave resonator. The good spatial beam quality ($M^2 \leq 1.05$) of the injection-locked laser system allowed us to couple 95% of the light into a Fabry-Perot resonator. The frequency noise of the injection-locked laser system was measured to be dominated by the master-laser frequency fluctuations. The free-running intensity noise which is in the $10^{-6} \text{ Hz}^{-1/2}$ region for Fourier frequencies between 10 Hz and 1 kHz is dominated by fluctuations of the slave-laser pump diodes. Feeding back to these pump diodes, the relative power noise could be reduced to a level below $10^{-7} \text{ Hz}^{-1/2}$. A detailed description of the GEO 600 laser system can be found in [12].

The light from the laser system is injected into the two modecleaners, each with 8 m round-trip length. The main purpose of the two sequential modecleaners is the spatial filtering of the laser beam [13]. In the frame of the suspended interferometer even a perfect laser beam would show spatial fluctuations due to the motion of the laser table relative to the suspended interferometer. Hence the modecleaner filter cavities have to be suspended as well. The laser frequency is stabilized to the resonance frequency of the first modecleaner MC1 by feeding back to the master-laser's temperature and PZT actuator. A phase-correcting Pockels cell between the master and the slave laser is used to enhance the bandwidth of this first control loop to approximately 100 kHz.

With the first control loop in place the laser frequency will change when the length of MC1 changes. Due to this effect the length-control actuator of MC1 can be used to bring the laser/MC1 unit into resonance with the second modecleaner MC2. To increase the bandwidth of this loop the high Fourier frequency components of the control signal are fed into the error point of the first loop. A third control loop is used to bring the laser/MC1/MC2 unit into resonance with the power-recycling cavity. A detailed description of the frequency control scheme of GEO 600 is given in [14].

Under the assumption that the laser exactly follows the resonance frequency of the first modecleaner, the control signal needed to stabilize the laser/MC1 unit to the second modecleaner can be used to analyse the fluctuations between the lengths of the two modecleaners (see figure 5). Under the additional assumption that the modecleaner mirrors move independently of each other this measurement describes the motion of the modecleaner mirrors. The rms length changes of the modecleaners in time intervals of 10 μs is below 1 μm which allows a lock acquisition of the modecleaners within typically 10 s.

Until now the modecleaners were only operated with an attenuated laser beam of 1 W power. With this power level 85% of the light was transmitted through the first modecleaner and approximately 500 mW were measured behind the second modecleaner. An automatic

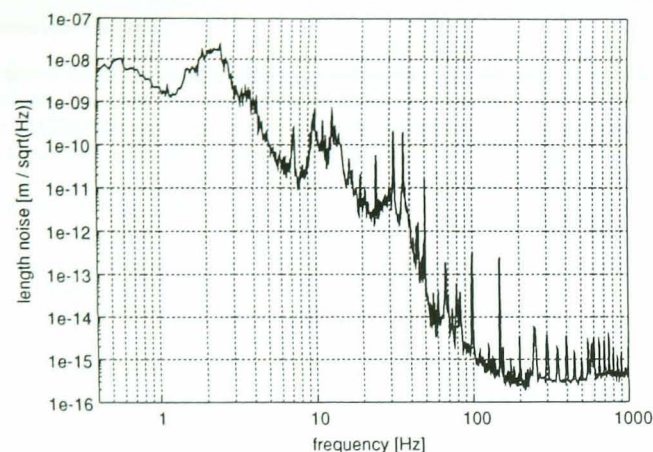


Figure 5. Displacement-noise spectral density of the GEO 600 modecleaner mirrors. For this measurement the laser was locked to the first modecleaner and the actuator signal needed to lock the second modecleaner to the stabilized laser was calibrated.

alignment and drift control system is used to maintain the alignment of the modecleaner cavities. The error signals generated by the differential-wavefront-sensing method were diagonalized to get control signals for the three different mirrors. The feedback was applied to the intermediate mass of the modecleaner double pendulums. This means that for frequencies above 1 Hz the actuator has a $1/f^4$ transfer function from the coil current to the mirror displacement. Nevertheless, a unity-gain frequency of about 10 Hz was achieved. For a detailed description of the automatic alignment system see [8]. With this automatic alignment system installed, continuous lock periods of more than 48 hours were achieved for both modecleaners.

5.2. Interferometer and recycling cavities

The main interferometer is designed as a dual-recycled folded-arm Michelson interferometer. Dual recycling on a suspended interferometer was first demonstrated by Heinzel *et al* [15]. A length-control-loop system keeps the operating point of the interferometer at the so-called dark fringe which means that due to destructive interference no light leaves the output port of the interferometer. Under this condition all light is reflected back towards the laser and the interferometer behaves like a mirror. A so-called power-recycling cavity is formed by this 'mirror' and the power-recycling mirror (see figure 4) which leads to a power buildup in the interferometer and improves the shot-noise-limited sensitivity of the detector. The anticipated power buildup in GEO 600 is 2000 which leads to a power of about 10 kW at the beam splitter. Any phase change of the light in the interferometer arms caused by a gravitational wave or noise will lead to light leaking out at the output port of the interferometer. The signal-recycling mirror will reflect this light back into the interferometer, thus forming another Fabry-Perot cavity: the signal-recycling cavity. In this case, the light power representing the signal at specific Fourier frequencies is enhanced. This effect reduces the shot-noise-equivalent apparent displacement noise of the detector for these Fourier frequencies. The shot-noise curve shows a dip, the centre frequency of which can be tuned by changing the position of

the signal-recycling mirror. The bandwidth of the dip is determined by the reflectivity of that mirror. Due to unequal radii of curvature of the interferometer mirrors and due to a thermal lens that develops in the beamsplitter as the power in the power-recycling cavity increases, the achieved interferometer contrast will not be perfect and some light in higher order spatial modes will leave the output port. This light could increase the shot noise on the photodetector without enhancing the signal. Even though signal recycling improves the interferometer contrast due to the 'mode-healing' effect [15], an output modecleaner will be implemented in GEO 600 to reduce the higher-order-mode content of the light reaching the photodetector. The photodetector consists of 16 InGaAs photodiodes of 2 mm diameter, each of which can operate up to 50 mA of photocurrent. The AC part of the photocurrent of these diodes will be combined and demodulated at the modulation frequency of the heterodyne readout scheme.

6. Detector control and data analysis

GEO 600 has four suspended cavities and the suspended Michelson interferometer all of which need length and alignment control systems. Twenty-five pendulums need local damping of at least four degrees of freedom, eight vacuum tanks have active seismic isolation control (in three supporting legs each) and additional feedback-control systems are needed for the laser stabilization. Most of these control loops are implemented with analogue electronic controllers with some guidance by a LabView computer-control environment [16]. Only the active seismic isolation and some slow alignment-drift-control systems are implemented as digital control loops. The LabView computer control has authority to allow pre-alignment, guide lock acquisition, monitor the detector status and compensate for long-term drifts. Typical response times of this system are 100 ms.

Although only the $h(t)$ channel includes a possible gravitational-wave signal, a multi-channel data acquisition system is needed to detect environmental and detector disturbances and exclude false detections. Two different sampling rates (16 384 Hz and 512 Hz) are used in the data-acquisition system of GEO 600. In the central building 32 fast channels and 64 slow channels are available, and in each of the end buildings we can use 16 fast channels. Most of these channels will be used for detector characterization only. A selection of those channels together with information coming from the LabView control program will be combined as a data stream with a data rate of approximately 0.5 MByte s^{-1} and sent via a radio link from the site to Hannover where the data will be stored. From here the data will be distributed to the data-analysis groups, whereas the time-critical data analysis will be performed in Hannover.

Due to the low signal-to-noise ratio of expected gravitational-wave signals a very good understanding of the detector noise is needed to perform an adequate data analysis. Furthermore, an extensive detector characterization effort [17] during the commissioning phase can help to identify noise sources and improve the sensitivity. Based on the understanding of the detector noise sources a so-called detector characterization robot (DCR) [18] will be developed to condition the data and provide false-alarm vetos for the data analysis.

A common analysis of the LIGO and GEO 600 data will be performed within the GEO 600 project as well as in the LIGO Scientific Community. Four different BeoWolf computer clusters will be used in the GEO 600 project for the search for gravitational waves from different sources. A cluster with 14 nodes in Hannover will perform the DCR data conditioning and the transient-data analysis. Three different BeoWolf clusters, each with more than 100 nodes, at the Albert-Einstein-Institut in Potsdam, Germany, at the Cardiff University, Great Britain and at the University of Birmingham, Great Britain will be used to search for coalescing binary systems, pulsars and unknown sources. A group at the University of Glasgow will perform the search for gravitational waves from known pulsars.

7. Current status and outlook

As mentioned above, the laser system and the two modecleaners of GEO 600 are installed and are working reliably. Stretches of continuous locking for more than 48 h were achieved. The two far mirrors of GEO 600 are installed with monolithic suspensions. To reduce the risk of contamination during the commissioning phase, test optics are currently installed for the near mirrors and the beamsplitter. With this configuration an interference contrast of better than 99% was measured. With the help of an automatic gain-control electronic circuit we were able to lock the power-recycling cavity with the Michelson interferometer swinging through fringes, and we expect to achieve the first lock of the Michelson interferometer soon. Once the Michelson interferometer is locked we will have a first optimization phase of the detector followed by a two-week coincidence run between LIGO and GEO scheduled for the end of 2001. This coincidence run will be followed by the implementation of signal recycling in early 2002. Once the dual-recycled Michelson is working reliably we plan to replace the test optics with the final optics, enhance the circulating power and have a second optimization period. This period will be followed by the first science run.

Acknowledgments

The authors would like to thank the British Particle Physics and Astronomy Research Council (PPARC), the German Bundesministerium für Bildung und Forschung (BMBF) and the State of Lower Saxony (Germany) for their funding and continuous support of the GEO 600 project.

References

- [1] Schutz B F 1999 *Class. Quantum Grav.* **16** A131
- [2] Sigg D 2002 *Proc. of the 4th Edoardo Amaldi Conf. on Gravitational Waves (Perth, Western Australia, 8–13 July 2001)* *Class. Quantum Grav.* **19** 1429
- [3] Di Fiore L 2002 *Proc. of the 4th Edoardo Amaldi Conf. on Gravitational Waves (Perth, Western Australia, 8–13 July 2001)* *Class. Quantum Grav.* **19** 1421
- [4] Ando M 2002 *Proc. of the 4th Edoardo Amaldi Conf. on Gravitational Waves (Perth, Western Australia, 8–13 July 2001)* *Class. Quantum Grav.* **19** 1409
- [5] McClelland D 2001 Talk presented at *4th Edoardo Amaldi Conf. on Gravitational Waves (Perth, Western Australia, 8–13 July 2001)*
- [6] Wanser K H 1992 *Electron. Lett.* **28** 53
- [7] Meers B J *et al* 1988 *Phys. Rev. D* **38** 2317
- [8] Grote H *et al* 2002 *Proc. of the 4th Edoardo Amaldi Conf. on Gravitational Waves (Perth, Western Australia, 8–13 July 2001)* *Class. Quantum Grav.* **19** 1849
- [9] Pissi M V *et al* 2000 *Rev. Sci. Instrum.* **71** 2539
- [10] Cagnoli G *et al* 2000 *Phys. Rev. Lett.* **85** 2442
- [11] Rowan S *et al* 1998 *Phys. Lett. A* **246** 471
- [12] Zawischa I *et al* 2002 *Proc. of the 4th Edoardo Amaldi Conf. on Gravitational Waves (Perth, Western Australia, 8–13 July 2001)* *Class. Quantum Grav.* **19** 1775
- [13] Rüdiger A *et al* 1981 *Opt. Acta* **28** 641
- [14] Freise A *et al* 2002 *Proc. of the 4th Edoardo Amaldi Conf. on Gravitational Waves (Perth, Western Australia, 8–13 July 2001)* *Class. Quantum Grav.* **19** 1389
- [15] Heinzel G *et al* 1998 *Phys. Rev. Lett.* **81** 5493
- [16] Casey M *et al* 2000 *Rev. Sci. Instrum.* **71** 3910
- [17] Köter K *et al* 2002 *Proc. of the 4th Edoardo Amaldi Conf. on Gravitational Waves (Perth, Western Australia, 8–13 July 2001)* *Class. Quantum Grav.* **19** 1399
- [18] Mohanty S D and Mukherjee S 2002 *Proc. of the 4th Edoardo Amaldi Conf. on Gravitational Waves (Perth, Western Australia, 8–13 July 2001)* *Class. Quantum Grav.* **19** 1471

Quadruple suspension design for Advanced LIGO

N A Robertson^{1,5}, G Cagnoli¹, D R M Crooks¹, E Elliffe¹, J E Faller²,
P Fritschel³, S Goßler⁴, A Grant¹, A Heptonstall¹, J Hough¹, H Lück⁴,
R Mittleman³, M Perreux-Lloyd¹, M V Plissi¹, S Rowan^{1,5},
D H Shoemaker³, P H Sneddon¹, K A Strain¹, C I Torrie^{1,6}, H Ward¹
and P Willems⁶

¹ Department of Physics and Astronomy, University of Glasgow, Glasgow G12 8QQ, UK

² JILA, NIST and University of Colorado, Boulder, CO 80309, USA

³ LIGO Laboratory, Massachusetts Institute of Technology, 175 Albany St, Cambridge, MA 02139, USA

⁴ Universität Hannover, Institut für Atom und Molekülphysik, Abteilung Spektroskopie, D30167, Hannover, Germany

⁵ Department of Applied Physics, Ginzton Laboratory, Stanford University, Stanford, CA 94305, USA

⁶ LIGO Laboratory, California Institute of Technology, MS 18-34, Pasadena, CA 91125, USA

Received 10 May 2002

Published 15 July 2002

Online at stacks.iop.org/CQG/19/4043

Abstract

In this paper, we describe the conceptual design for the suspension system for the test masses for Advanced LIGO, the planned upgrade to LIGO, the US laser interferometric gravitational-wave observatory. The design is based on the triple pendulum design developed for GEO 600—the German/UK interferometric gravitational wave detector. The GEO design incorporates fused silica fibres of circular cross-section attached to the fused silica mirror (test mass) in the lowest pendulum stage, in order to minimize the thermal noise from the pendulum modes. The damping of the low-frequency modes of the triple pendulum is achieved by using co-located sensors and actuators at the highest mass of the triple pendulum. Another feature of the design is that global control forces acting on the mirrors, used to maintain the output of the interferometer on a dark fringe, are applied via a triple reaction pendulum, so that these forces can be implemented via a seismically isolated platform. These techniques have been extended to meet the more stringent noise levels planned for in Advanced LIGO. In particular, the Advanced LIGO baseline design requires a quadruple pendulum with a final stage consisting of a 40 kg sapphire mirror, suspended on fused silica ribbons or fibres. The design is chosen to aim to reach a target noise contribution from the suspension corresponding to a displacement sensitivity of 10^{-19} m Hz^{-1/2} at 10 Hz at each of the test masses.

PACS number: 0480N

1. Introduction

The sensitivity of the interferometric gravitational wave detector presently installed in the US LIGO [1] is expected to be limited by the thermal noise associated with the suspensions of its mirrors at frequencies in the region ~ 40 Hz to ~ 150 Hz. The LIGO suspension design [2, 3] for the main mirrors has the following features.

- The fused silica mirrors (10.7 kg) are hung as single pendulums on a single loop of steel piano wire.
- The sensing and actuation for damping of the low-frequency pendulum modes are carried out at the mirror itself, with the magnets for actuation attached to the back and side of the mirrors via metal standoffs.
- Actuation for global control, required to hold the interferometer at its correct operating position, is also carried out via the magnets attached to the mirrors.

In GEO 600 [4], the German/UK interferometric gravitational wave detector, the approach to the suspension system represents a second-generation design for which the performance is more aggressive than in LIGO, in particular in terms of the reduction of thermal noise associated with the suspension of the mirrors. The GEO design incorporates fused silica fibres of circular cross-section to suspend the fused silica mirror in the lowest stage of a triple pendulum, the damping of whose low-frequency modes is achieved by using co-located sensors and actuators at the highest mass of the triple pendulum. Global control forces are applied via a triple reaction pendulum, so that these forces can be implemented from a seismically isolated platform. These design features have been discussed in previous papers [5–10]. Figure 1 shows a schematic diagram of the GEO suspension system and a picture of the first triple pendulum to be assembled with a monolithic fused silica final stage, hanging *in situ* in one of the GEO tanks.

The more advanced suspension design has been used in GEO to compensate for its shorter arm length (600 m compared to 4 km), in order to achieve a similar strain sensitivity to LIGO. Operating these detectors at their design sensitivities will be an exciting step forward in the quest for detecting gravitational waves, and may lead to their first detection. However, to realize the possibility of carrying out serious astronomy using gravitational waves, further improvement in sensitivity is required. An obvious step is to adapt the more advanced suspension design of GEO in the planned upgrade to LIGO, and this has been proposed in the white paper [11] put forward by the LIGO Scientific Collaboration to the National Science Foundation describing the next generation of LIGO. The GEO team, in collaboration with LIGO and other members of the LIGO Scientific Collaboration, has been developing the suspension design to meet the requirements for Advanced LIGO. In particular, we are designing a quadruple pendulum suspension for the main mirrors, which is an extension of the GEO design. The key features of the proposed design are as follows.

- Sapphire mirrors (40 kg) will form the lowest stage of a quadruple pendulum, and will be suspended on four vertical fused silica fibres or ribbons to reduce suspension thermal noise.
- The fibres will be welded to fused silica ‘ears’ or prisms which are silicate bonded [8] to the flat sides of the penultimate mass and the mirror below. This technique ensures that the low mechanical loss of the mirror itself is preserved, maintaining the low thermal noise of the sapphire substrate.
- Included in the quadruple pendulum are three stages of cantilever blade springs made of maraging steel to enhance the vertical seismic isolation.

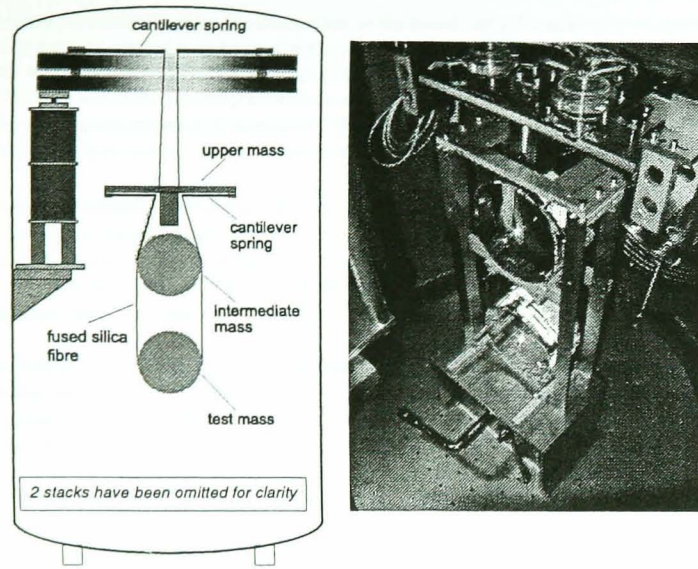


Figure 1. Schematic diagram (left) of the full suspension and isolation system for the main mirrors (test masses) in GEO 600, and a picture of the first triple pendulum with monolithic final stage hanging *in situ* in one of the GEO tanks. Three of the coil actuators for local control can be seen above the upper mass of the triple pendulum.

- The damping of all of the low-frequency modes of the quadruple pendulum will be carried out either by using six co-located sensors and actuators at the highest mass of the pendulum (as in GEO), or by using eddy current damping applied at this mass. To achieve adequate damping the design has to be such that all the modes couple well to motion of the highest mass.
- DC alignment of mirror yaw and pitch will be done by applying forces to the actuators at the highest mass, or at the mass below. The masses hanging below the highest mass are each suspended by four wires, two on each side, so that the system behaves like a marionette from the highest mass downwards.
- Global longitudinal and angular control forces will be applied via a reaction pendulum, essentially identical in mechanical design to the main pendulum, but with wires replacing the silica fibres.
- Global control will be carried out using a hierarchical feedback system, with large low-frequency forces applied electromagnetically between the penultimate masses, and small higher-frequency signals applied electrostatically between the mirror and the corresponding lowest reaction mass which may be made of silica or heavy glass with a patterned gold coating. Alternatively, photon pressure from an auxiliary laser may be used for the higher-frequency signals, in which case the lowest reaction mass is not required.

The extension from a triple pendulum as in GEO 600 to a quadruple pendulum for Advanced LIGO is necessary to meet the more stringent requirements on isolation of noise associated with the damping of the low-frequency pendulum modes, discussed in section 3.2.

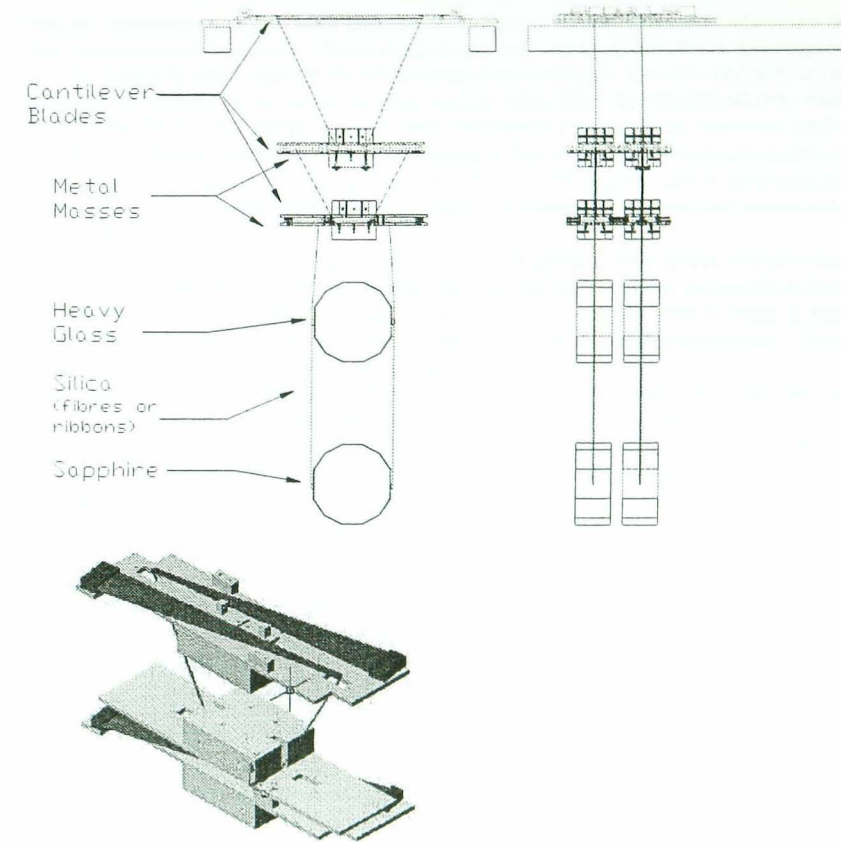


Figure 2. Schematic diagram of quadruple pendulum suspension system for Advanced LIGO. The diagram above shows a face view of the main chain on the left, and on the right a side view with main and reaction chains is visible. The diagram below shows a close up of the first two masses (masses 1 and 2), with the top of mass 1 removed so that the cantilever blades for vertical isolation, which are crossed to save space, can be seen more clearly.

Figure 2 shows a schematic diagram of our present conceptual design for the quadruple pendulum suspension. We discuss the features of the proposed design in more detail below, addressing the various issues, and giving predictions of the performance of the suspension system.

2. Thermal noise issues

2.1. Some general considerations

Thermal noise, or motion due to the thermal energy, sets a fundamental limit to the noise performance of the suspension, and is thus the paramount design driver. The main contribution

from the suspension *per se* comes from the dissipation in the fused silica fibres used to suspend the mirror, giving a direct optical axis noise component. To minimize this noise, the baseline design currently incorporates ribbons rather than fibres of circular cross-section, so that the dilution factor [12], by which the pendulum loss factor is reduced from the value of the intrinsic loss factor of the suspension material, is increased. The choice between ribbon and cylindrical fibre is discussed more fully below; we will refer to both as 'fibres' when the distinction is not needed.

Another strong contributor to the thermal noise spectrum arises from the lowest set of blade springs, giving a vertical noise component which will cross-couple into horizontal motion. In general, thermal noise arising further up the pendulum chain is filtered by the stages below. However, the vertical frequency of the final stage is necessarily higher than the horizontal frequency, since no blades are included at that stage, and thus there is less vertical filtering.

Since it is desirable from astrophysical arguments to extend the working frequency of the detector downwards as far as is experimentally practicable, we are considering a baseline design for Advanced LIGO which has a 'cut-off' in the vicinity of 10 Hz. Below this frequency the noise will rise steeply to lower frequencies due to seismic effects, essentially giving a cut-off in detector sensitivity. Our working requirement is that the required noise level at each of the test mirrors be 10^{-19} m Hz^{-1/2} at 10 Hz, falling off at higher frequencies. To achieve such a requirement calls for the highest vertical mode of the multiple pendulum to be kept below 10 Hz. The highest mode essentially corresponds to relative vertical motion of the mirror with respect to the penultimate mass. To push this frequency down, we use a combination of several factors:

- (a) The fibre length is chosen as long as practicable, consistent with ease of production and the need to maintain the 'violin' modes high enough for control purposes. The current design target is 60 cm.
- (b) The fibre cross-section is chosen to be as small as practicable, consistent with working at least a factor of 3 away from the breaking stress.
- (c) The penultimate mass is chosen to be as heavy as possible, consistent with the overall design characteristics of the multiple pendulum. In the baseline design we have chosen to make this mass approximately double the mass of the mirror.

To achieve a penultimate mass which can be bonded, we are considering the use of heavy glass (glass doped with lead or other dense metals).

We will return to these design factors after consideration of the choice of ribbons or cylindrical fibres.

2.2. Ribbons and fibres

There are potential advantages to using ribbons rather than cylindrical fibres, and these have already been discussed elsewhere [13–15]. Not only can the dilution factor be made larger for ribbons, but reducing the thickness of the flexing element also raises the frequency at which the maximum loss due to thermoelastic damping occurs [16], which can lead to a lower overall level of noise around 10 Hz. Experimental results on losses in ribbons have also been carried out [17], and these are encouraging. However, there are several other factors which need to be considered before a choice can be made.

Firstly, recent work by Cagnoli and Willems [18] has shown that there is a significant thermoelastic effect not previously considered, basically due to the variation of Young's modulus with temperature. This effect, in combination with the more familiar coefficient of

thermal expansion, gives rise to an effective coefficient of thermal expansion which can be zero for a particular static stress. Hence, under those conditions the thermoelastic damping can become arbitrarily small, and also the overall noise level is reduced. The null condition can, in principle, be achieved by increasing the cross-section of the silica suspension over that which has been previously indicated as optimum from other design considerations. However, simply increasing the cross-section to null the thermoelastic effect has the two adverse consequences of increasing the highest vertical pendulum mode above the 10 Hz goal, and of decreasing the violin mode frequencies, thus placing more of these resonances below 1 kHz and complicating the control design.

An alternative possibility which has recently been suggested [19] is to use circular cross-section fibres of varying cross-section, thicker near the ends and thinner in the middle section, such that the thermoelastic effect is reduced, but also that the highest vertical mode is kept below 10 Hz. Similar tailoring of ribbons could also yield enhanced performance. These ideas are being pursued for possible incorporation into the design.

A second consideration is the breaking stress of ribbons and cylindrical fibres, and the ease with which they can be made. Measurements on cylindrical fibres have shown that they can be as strong as high tensile steel [20, 10], and we now achieve an average value of breaking stress of ~ 4.5 GPa. Ribbons with breaking stress comparable to the strongest fibres have yet to be developed. However, this is an active area of research, and initial results at Glasgow have already shown breaking stresses in excess of 1.8 GPa.

An additional complication with ribbons is the need to allow flexing without buckling in both the plane, and perpendicular to the plane, of the ribbon. Twists or other flexures may be needed. Again, this is an area of research.

In conclusion, it can be seen that there are various issues in the suspension design which as yet are unresolved. The final design choice of ribbons or cylindrical fibres, possibly with varying cross-section, will depend on the results of investigations of such matters as reliability of manufacture, strength and loss measurements, and controls design. For the purposes of this baseline design we use ribbons of constant cross-section for our estimation of expected thermal noise in a quadruple suspension system.

2.3. Thermal noise estimation for quadruple pendulum suspension

The thermal noise model which has been used for this estimation has been developed using MAPLE. It has subsequently been modified into MATLAB code for inclusion in the BENCH modelling tool (<http://gravity.phys.psu.edu/Bench>) which has been developed as a tool for predicting the astrophysical range for various potential sources, for varying parameters of detector configuration for Advanced LIGO. Some details of how the thermal noise calculations are carried out are presented in appendix A1. Examples of pendulum thermal noise spectra produced using the MAPLE code are given in section 4.

3. Isolation, damping and control

Modelling for investigation and optimization of the mechanical design for a quadruple suspension, with particular reference to the isolation and damping properties, has been carried out using an extension of the MATLAB model developed for the GEO 600 triple suspension [5, 21]. Some details of the MATLAB model are presented in appendix A2.

The key elements of the design are very similar to GEO, with the addition of another stage. The aim has once again been to develop a model whose coupled resonant frequencies all lie within a band from ~ 0.4 to ~ 4 Hz, with the exception of the highest vertical and roll

modes which are associated with the extension of the silica fibres in the lowest pendulum stage. In addition, we aim for good coupling of all the low-frequency modes, so that damping of all such modes can be carried out at the top mass in the chain.

3.1. Mechanical design

The mass at the top is suspended from two cantilever-mounted, approximately trapezoidal pre-curved spring blades and two spring steel wires. The blades are made from Marval 18 (18% Ni) maraging (precipitation hardened) steel, chosen for its high tensile strength and low creep under stress, as used in the French-Italian VIRGO gravitational wave detector project [22]. The blades lie horizontally when loaded. The mass below this is suspended from two cantilever blades and two steel wire loops. The top mass (mass 1) and mass 2 have a 'sandwich-type' construction with the blades fitting in between, so that the break-off points for wires going both upwards and downwards lie close to the centre of mass of these masses; see figure 2. Mass 3, which may be made of heavy glass, is suspended from two cantilever blades and two steel wire loops from mass 2. Fused silica ears silicate bonded to flats on the side of this mass form the fibre attachment points at the mass. Similar ears are bonded to the mirror (mass 4), and the final suspension is made by welding cylindrical fibres or ribbons between the ears of masses 3 and 4, with two fibres on each side.

There are several key points which differ from the original GEO design. Firstly, in order to achieve a smaller footprint, all the blades are angled with respect to each other and crossed (as shown in figure 2). In GEO only the top set of blades in the beamsplitter suspension were crossed. Secondly, again due to space considerations, there are two blades rather than four at masses 1 and 2, each blade supporting two wires from its end. As stated earlier, the overall choice of the number of wires or fibres is such that orientation of the mirror can be carried out from the top mass.

Currently, we have chosen to stress the blades at a conservative level, to approximately one half of the elastic limit (~ 800 MPa) for the blades closest to the mirror and slightly larger (up to ~ 900 MPa) for those further from the mirror. However, we may choose to increase the stress slightly to raise the internal mode frequencies of the blades, as discussed in section 5.

There should be a strong coupling of all degrees of freedom to motion of sensors/actuators at the top mass. To a first approximation, this is satisfied by having approximately the same mass in each stage, approximately the same moments of inertia about equivalent axes, and by suitable choices of wire angles and connection points. In this particular design, thermal noise considerations have necessitated the use of a significantly heavier penultimate mass than the other masses in the chain.

3.2. Local control

In GEO, the active local control damping is applied at the top mass ensuring that the pendulum stages below filter any extra motion caused by electronic noise in the feedback system. However, given the more ambitious target noise level for the LIGO suspensions of 10^{-19} m Hz $^{-1/2}$ at 10 Hz, the GEO design needs some modification. In particular, to provide more isolation from the noise associated with the local damping, the suspension is increased from three to four stages, with local damping still applied only to the top mass. Even then, local sensing noise can dominate. Typical optical shadow sensors [23, 24] with a range of ~ 1 mm have a noise level of $\sim 10^{-10}$ m Hz $^{-1/2}$, much greater than the $\sim 10^{-19}$ m Hz $^{-1/2}$ target for the suspensions at 10 Hz. However, the mechanical isolation from the sensed point to the test mass is only of order 10^{-7} (see figure 7) at 10 Hz. Thus, the sensor noise-isolation product

is greater than the target sensitivity of the target by at least two orders of magnitude. In GEO, there is roughly a decade between the highest locally damped suspension mode and the 50 Hz lower edge of the sensitive frequency band—enough room to electronically filter local sensor noise to a level below the target sensitivity. At Advanced LIGO's 10 Hz cut-off frequency, however, little electronic filtering can be achieved while maintaining adequate phase margin in the damping loops.

A partial solution to the local sensing noise problem is provided by the interferometer global sensing system [25]. In the power-recycled, Fabry-Perot arm Michelson interferometer configuration, four interferometric relative position signals are generated by the relative longitudinal movements of the test masses, beamsplitter and power recycling mirror; with the addition of signal recycling in Advanced LIGO, one mirror is added and thus one further interferometric position signal is obtained. These interferometric position signals all have sensitivities better than 10^{-13} m Hz $^{-1/2}$, i.e., at least three orders of magnitude better than the local shadow sensors. Thus we can use four of these global signals to control the longitudinal degrees of freedom of the four test masses. When this is done, the local longitudinal damping of the test masses can be greatly reduced, or even turned off, to suppress local sensor noise. Similarly, low-noise global interferometric signals are available for the pitch and yaw orientation degrees of freedom of the test masses which can be used to control their pitch and yaw modes. The same mechanical coupling between the suspension stages that enables local damping forces applied at the top mass to effectively damp test mass motion, also allows that globally sensed motion of the test mass can be damped by actuation at the upper stages.

This scheme applies to all but the vertical, transverse and roll modes of suspension, which are not independently sensed by the interferometer. For these modes we could use one or more of several strategies to limit local damping noise: reduce the mechanical coupling from these degrees of freedom to the motion sensed by the gravitational wave readout; operate with reduced active damping, allowing higher Q for these modes; take advantage of what limited electronic filtering can be performed on the local damping signals; or develop lower noise local sensors.

Eddy current damping may provide an alternative solution to active local control. Such damping is used in the Japanese TAMA project to damp their double pendulum suspensions [26]. In Advanced LIGO, we could use eddy current damping in six degrees of freedom applied at the top mass of the quadruple suspensions to give Q of approximately 10 for the lowest frequency modes (which dominate the impulse response). We have estimated that residual motion at the mirror due to the thermal noise force generated by such eddy current damping is approximately 4×10^{-20} m Hz $^{-1/2}$ at 10 Hz, which meets the target sensitivity. The final decision on how to apply damping will be made once more experimental investigations have been carried out.

3.3. Global control

The GEO philosophy for applying the feedback signals to the test masses for longitudinal and angular global control was briefly described in the introduction. The general idea is to apply forces between the main pendulum chain and an essentially identical reaction chain (which does not include fibre suspensions). The reaction chain is itself locally damped in the same manner as the main chain. In LIGO, however, not all the sensitive optics require wide bandwidth global control, and in those cases the reaction chain need not have as many stages. In addition, where wide bandwidth is required, the final stage wide-bandwidth small-signal feedback could be realized using photon pressure from an auxiliary laser, rather than

electrostatically as in GEO. In that case also the lowest stage of reaction chain would not be required.

Another issue is the potential need to damp (actively or passively) the very high Q violin modes of the silica suspensions to allow the global feedback to remain stable. Any such damping has to be done in such a way as not to compromise the low-frequency thermal noise performance of the suspensions. In GEO we have taken the approach of using small amounts of amorphous PTFE coating on the fibres, suitably placed to damp the first few violin modes to Q of around 10^6 , without compromising the low-frequency suspension noise. For GEO we use two coated regions each 5 mm long, one at the centre and one one-third of the way down the fibre. The LIGO situation has to be considered fully once a control philosophy has been decided upon, and there will be some trade-off required between controllability and thermal noise associated both with the low-frequency vertical modes and the violin modes.

4. Expected performance

In this section, we present various graphs, showing expected overall thermal noise performance, horizontal and vertical isolation performance with and without damping, and transfer functions from which residual sensor noise may be estimated. Key parameters used in the models to generate these graphs are also given. In some cases several curves are given, where different choices of parameters are possible.

4.1. Key parameters

The key parameters used for all the curves presented in this section are as follows (except where otherwise indicated):

Final mass	40 kg sapphire, 31.4 cm × 13 cm
Penultimate mass	72 kg (heavy glass)
Upper masses	36 kg, 36 kg
Overall length	1.7 m (from top blade to centre of mirror)
Ribbon parameters	Length 60 cm, cross-section 113 μm × 1.13 mm
Stress in ribbon	770 MPa

We note that in carrying out these analyses, the availability of sapphire pieces of the desired quality with these dimensions, and the availability of heavy glass of suitable density in the required size, are still open questions.

4.2. Thermal noise performance

In figure 3, we present the thermal noise for the baseline design. The target figure of $10^{-19} \text{ m Hz}^{-1/2}$ at 10 Hz is effectively met. We also indicate the performance if the penultimate mass is made of silica rather than heavy glass, raising the uppermost vertical mode frequency of the quadruple pendulum to above 10 Hz. Note that for the latter case, the blade designs were altered to keep the other three vertical resonant frequencies at the same values.

Various changes could be made to the baseline design. A marginal improvement to the performance at 10 Hz and above could be made if one lengthened the final stage to say 70 cm. Increasing the cross-section of the fibre could gain some improvement above 10 Hz at the expense of raising the vertical resonant frequency to be closer to 10 Hz, and lowering the violin mode frequencies. This improvement arises since changing the cross-section changes

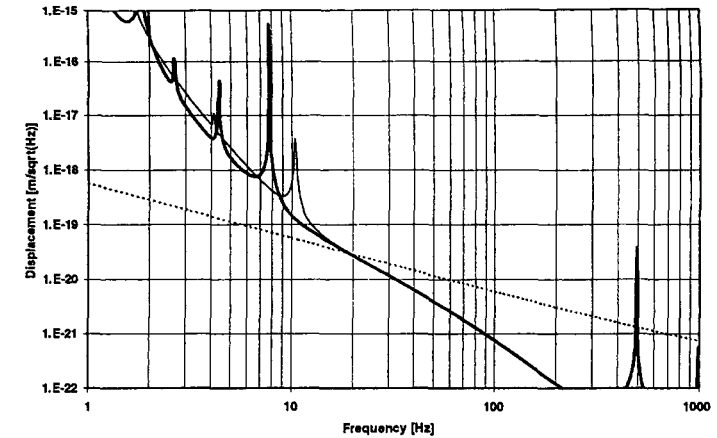


Figure 3. Suspension thermal noise for baseline 40 kg quadruple pendulum. Two suspension curves are shown. The heavy solid line is the baseline design. The light solid line shows the effect of replacing the 72 kg heavy glass penultimate mass with a silica mass of the same dimensions (weighing 22.1 kg). The peaks of the resonances are not resolved. Note the first violin mode at approximately 500 Hz. For comparison we also show the expected internal thermal noise curve for sapphire, dominated by thermoelastic damping (dotted line). Note also that the internal thermal noise curve assumes no loss due to coatings, or due to bonding of ears for attaching the suspensions.

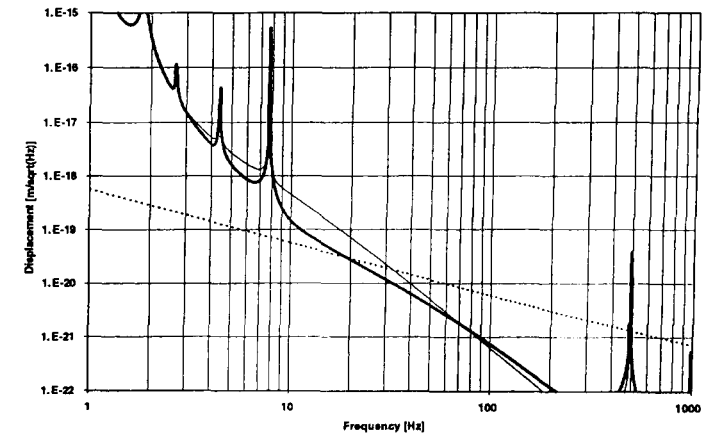


Figure 4. The light solid line is thermal noise for fibres of 200 μm radius, stressed to the same value as the baseline ribbon design. The heavy solid line is the baseline, the dotted line is internal thermal noise for sapphire.

the position of the thermoelastic peak. Using cylindrical fibres loaded to the same stress as the baseline design (thus keeping the vertical mode frequency at the same value) raises the thermal noise in the 10 Hz region and above—as can be seen from figure 4.

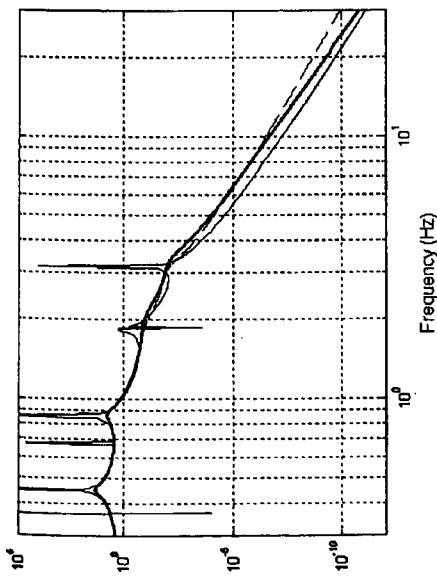


Figure 5. Longitudinal transfer function for quadruple pendulum, with (heavy solid line) and without (light solid line) local controls on, and with eddy current damping (dashed line).

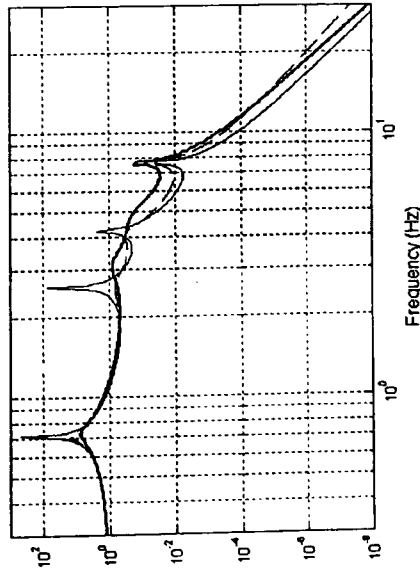


Figure 6. Vertical transfer function for quad pendulum, with (heavy solid line) and without (light solid line) local controls on, and with eddy current damping (dashed line).

4.3. Isolation performance

The overall mechanical isolation in Advanced LIGO will be achieved by a combination of a two-stage active isolation system [27] and the isolation from the quadruple suspension. The target noise level for the active system is 2×10^{-13} m Hz^{-1/2} at 10 Hz in both longitudinal and vertical directions (where longitudinal refers to the horizontal direction along the beam axis). Figures 5 and 6 show the transfer functions for the quadruple pendulum in longitudinal and vertical directions respectively, from which the expected isolation performance can be deduced. The quadruple suspension has an isolation factor (with active or eddy current damping)

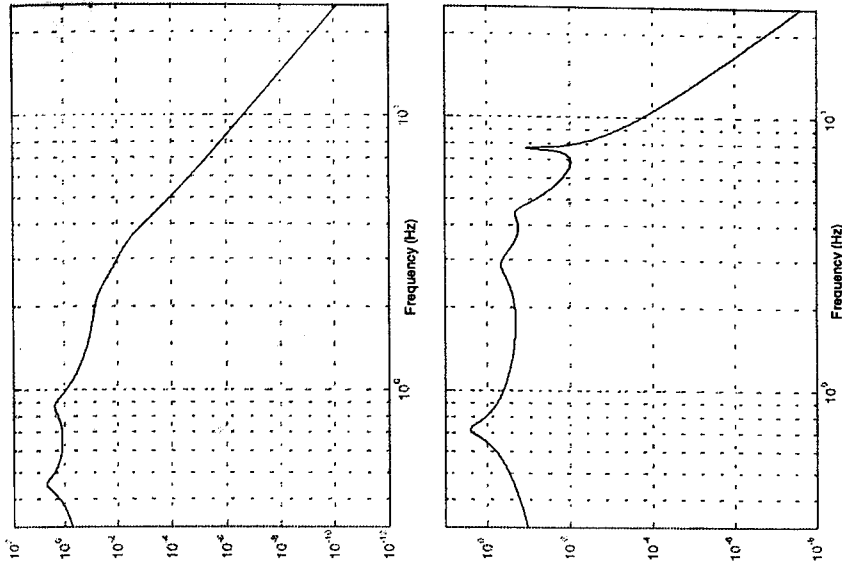


Figure 7. Longitudinal (left) and vertical transfer function from sensor to mirror for quadruple pendulum with sensor at the top mass.

of $\sim 4 \times 10^{-7}$ in the longitudinal dimension and $\sim 4 \times 10^{-4}$ in the vertical dimension at 10 Hz. When these numbers are combined with the target noise level including a cross-coupling factor of 10^{-3} from the vertical to the horizontal dimension (see appendix A1), we see that the target sensitivity level of 10^{-19} m Hz^{-1/2} is achieved for both dimensions. The two-stage active isolation system also significantly attenuates the motion in the control band from 0.1 to 10 Hz, reducing the actuator authority requirement in the suspension design.

4.4. Sensor noise performance

In figure 7, we show the transfer function from the sensors to the mirror in both longitudinal and vertical directions using a nominal damping system gain which gives quality factors for the pendulum resonances of ~ 10 or less and corresponding impulse response times of ~ 10 s. The noise level at the mirror can be calculated from the transfer function shown in figure 7

multiplied by the sensor noise in $\text{m Hz}^{-1/2}$. The longitudinal transfer function is $\sim 2 \times 10^{-7}$ at 10 Hz. Thus, with a sensor noise of $10^{-10} \text{ m Hz}^{-1/2}$ and no further electronic filtering the noise level at the test mass would be $\sim 2 \times 10^{-17} \text{ m Hz}^{-1/2}$ at 10 Hz, much larger than the target sensitivity. As discussed in section 3.2, a solution to this problem is to turn the gain down or off completely for the longitudinal modes once the global control of the interferometer is in operation and suitable signals from that control can be used to take over the damping.

For the vertical direction, the longitudinal noise level at the mirror can be calculated as above, with an extra factor, the cross-coupling factor, in the product. The vertical transfer function at 10 Hz is $\sim 2 \times 10^{-4}$, so with a sensor level of $10^{-10} \text{ m Hz}^{-1/2}$, and assuming a cross-coupling factor of 10^{-3} , the residual noise level at the mirror would be $\sim 2 \times 10^{-17} \text{ m Hz}^{-1/2}$ at 10 Hz, again far exceeding the target sensitivity. As discussed in section 3.2, there are several strategies which could be used to address this issue, separately or in combination. With respect to the idea of turning down the gain once the global control is in operation, giving higher Q for these modes, a more complete overall interferometer control model will be needed before it can be determined if the resulting larger motion could be tolerated.

5. Current and future work

Work towards developing a quadruple pendulum suspension as described above is well underway. Experience is being gained at GEO 600 with constructing and operating triple pendulum suspensions. This should give us information on many of the key aspects of the design, including thermal, isolation and damping properties and operation of global control.

To address thermal noise issues, ribbon and fibre production, including strength, reliability, welding and loss tests are being carried out in Glasgow and at Caltech. Investigation of bonding continues at Glasgow, Stanford and Caltech, with regard to bonding silica ears to sapphire and to lead or bismuth loaded glass, the latter materials being considered for the penultimate mass in the quadruple chain.

To address mechanical design, a first all metal prototype quadruple pendulum and reaction mass was developed in Glasgow early in 2001; parts were procured and shipped to MIT where they were assembled during summer 2001. Figure 8 shows pictures of the two quadruple pendulums (main chain and reaction chain), hanging in the lab at MIT in the summer of 2001. This suspension mimics a 30 kg sapphire mirror with an identically sized silica penultimate mass, which was a previous baseline design, now superseded with the design as discussed above. This prototype has already given us experience in assembly and handling. Current and future work includes measuring mode frequencies, and investigating transfer functions, damping and global control.

More work on blade design is underway, involving finite element analysis and comparison to experimental results. Another issue being considered is the noise level from the blades when thermally or seismically excited at their internal mode frequencies (in particular, the lowest set of blades nearest to the test masses). It is desired that the peaks at these frequencies not compromise the sensitivity, and damping may be needed to ensure this. For the design presented in section 4 the lowest internal modes were in the range 75 to 120 Hz. Initial calculations suggest damping could be avoided if the frequencies are a little higher than these. Suitable frequencies could be achieved by allowing the maximum stress to be around 1050 MPa.

It should be noted that we have addressed the design of the most sensitive mirrors in Advanced LIGO in this paper, namely the end mirrors in the two cavities. However, the tools developed for designing the quadruple suspension can be easily applied for the design of other

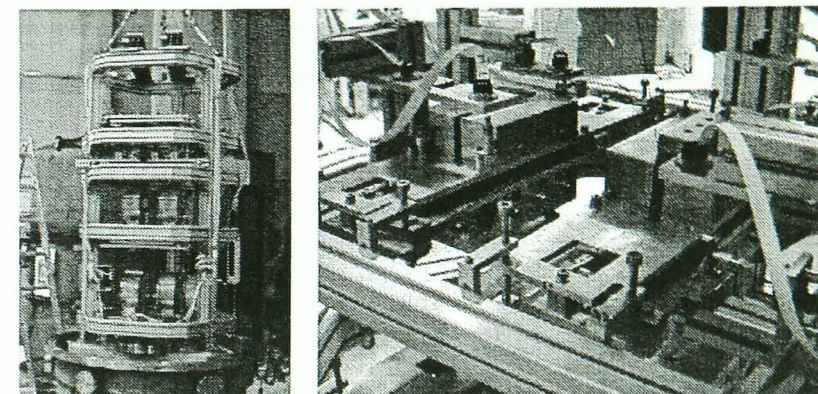


Figure 8. Two views of the prototype quadruple suspension assembled at MIT. On the left is an overall view showing the main and reaction chains, suspended from a support frame. On the right is a close-up of the top masses, with some of the local control actuators visible. The construction can be compared to the diagrams in figure 2.

suspensions. In addition to the design issues mentioned above which are under investigation, there are several key issues still unresolved for the suspension design, some of which depend on other areas of research for Advanced LIGO. For example, the choice of mirror material and its size and aspect ratio are not yet fixed. Sapphire is presently favoured, and work is underway on investigating the growth of large enough pieces and investigating the optical properties such as absorption, inhomogeneity, polishing, etc. The fallback position is to use silica. Another area currently under discussion is the choice of the lower limit to the observation frequency for the Advanced LIGO instrument, and this has a bearing on the final design.

In conclusion, we have presented the current conceptual design of the suspension system for Advanced LIGO, which is based on the GEO suspension system. Experience with GEO will be invaluable as a test of the ideas incorporated in this design. However, much work has still to be carried out, and is actively underway in several laboratories in Europe and the USA.

Acknowledgments

The authors would like to thank their colleagues in the GEO collaboration for their interest and help in this work. We also acknowledge with thanks members of the LIGO Scientific Collaboration (LSC) at Caltech, MIT and Stanford who have contributed, in particular Mark Barton at Caltech. The Glasgow group acknowledges the financial support of the University of Glasgow. GEO acknowledges the financial support of the Particle Physics and Astronomy Research Council (PPARC), the Bundesministerium für Bildung und Forschung (BMBF) and the state of Lower Saxony. The LIGO Laboratory thanks the National Science Foundation for its support through the cooperative agreement PHY-9210038 and the award PHY-9801158.

Appendix A

We include here a brief discussion of the modelling tools used to produce the thermal noise and isolation curves presented in section 4.

Appendix A.1. Thermal noise model

The thermal noise associated with the suspension system is calculated using the fluctuation-dissipation theorem [28]. The calculations in the code are carried out in the following way. The pendulum dynamics are simulated by four point-like masses linked by springs for both horizontal and vertical degrees of freedom, with no coupling between the orthogonal degrees of freedom. Suitable values to be used as input for the masses and other necessary parameters to calculate spring constants have previously been established using the MATLAB model of the quadruple pendulum, discussed in the following section. The first three spring stages consist of maraging steel blades in series with steel wires, and the final (lowest) stage consists of silica fibres. The horizontal and vertical transfer functions are calculated separately and then combined to get the effective overall horizontal function, assuming a cross-coupling of the vertical into the horizontal dimension of 0.1%. This is a figure we have used in GEO [5] as a conservative estimate for cross-coupling, and is larger than the purely geometric effect due to the curvature of the Earth over the 4 km arms of LIGO. Dissipation in the pendulum is introduced via the imaginary part of the spring constants, and hence using the fluctuation-dissipation theorem, the resulting thermal noise at the mirror in the horizontal direction is obtained.

Spring constants of the steel stages have been treated differently from the silica stage. For the steel the loss is included, with a dilution factor as appropriate, by including an imaginary term in the spring constant. For silica, the spring constants have been worked out from the solution of the beam equation, following the method used in Gonzalez and Saulson [29], in which case the imaginary part is introduced into Young's modulus. As a consequence, the programme calculates the violin modes of the silica stage, but not of the steel stages.

Loss angles for the materials arise as the sum of three parts: bulk, surface and thermoelastic effects, including the new thermoelastic effect referred to in section 2, which is included where appropriate. The surface loss is estimated following the work by Gretarsson and Harry [30], which indicated that there is an energy loss proportional to the surface to volume ratio for silica which dominates the bulk dissipation. For steel, however, the bulk loss dominates. The thermoelastic loss term has been considered in the pendulum motion of all four stages and in the vertical motion of the three steel stages in which the restoring force dominantly arises from the bending of the blades.

Appendix A.2. MATLAB model for isolation and control

The MATLAB model (recently extended to work in Simulink) consists at present of four uncoupled sets of dynamical equations, corresponding to vertical motion, yaw, longitudinal and pitch (together) and transverse and roll (together). To first order these motions are uncoupled in the GEO design. Forces due to gravity and extension of wires are included, but not due to the bending of wires. Cantilevers with wire(s) attached are approximated by taking the series sum of the spring constants of wire(s) and cantilever, noting that this sum is dominated by the softer cantilever blade. The model makes use of presumed symmetries in the design. With the crossed blades in the LIGO design, there will be some coupling between the longitudinal/pitch and transverse/roll modes. As yet the model does not incorporate this coupling. However, it is not expected to significantly affect either the isolation or the damping properties of the pendulum. In addition, the model does not yet take account of the twisting of the blade tips which will occur as the pendulum moves in the various pitch modes. Experimentally, we have seen that this effect slightly lowers the pitch modes. However, again the isolation and damping should not be significantly affected.

It should also be noted that the violin modes and the internal modes of the blades are not included in this MATLAB model. The violin modes of the final stage are, however, included in

the thermal noise model, and they can be seen in the thermal noise curves shown in section 4. The expected frequencies of the internal modes of the blades can be calculated from the dimensions of the blades, and are specific to each design of blade. Examples of their typical values were given in section 5.

References

- [1] Barish B C 1997 *Gravitational Wave Detection* ed K Tsubono, M-K Fujimoto and K Kurodo (Tokyo: Universal Academy) pp 155–61
- [2] Coyne D 1996 *IEEE Aerospace Applications Conf. Proc.* vol 4 pp 31–61
- [3] Hazel J, Kawamura S and Raab F 1996 *LIGO Document T960074-07-D* (December)
- [4] Lück H et al 2000 *Proc. 3rd Edoardo Amaldi Conf. on Gravitational Waves (Pasadena 1999)* (American Institute of Physics) pp 119–27
- [5] Plissi M V, Strain K A, Torrie C I, Robertson N A, Killbourn S, Rowan S, Twyford S M, Ward H, Skeldon K D and Hough J 1998 *Rev. Sci. Instrum.* **69** 3055–61
- [6] Plissi M V, Torrie C I, Husman M E, Robertson N A, Strain K A, Ward H, Lück H and Hough J 2000 *Rev. Sci. Instrum.* **71** 2539–45
- [7] Husman M E, Torrie C I, Plissi M V, Robertson N A, Strain K A and Hough J 2000 *Rev. Sci. Instrum.* **71** 2546–51
- [8] Rowan S, Twyford S M, Hough J, Gwo D-H and Route R 1998 *Phys. Lett. A* **246** 471–8
- [9] Cagnoli G, Gammaitoni L, Hough J, Kovalik J, McIntosh S, Punturo M and Rowan S 2000 *Phys. Rev. Lett.* **85** 2442–5
- [10] Robertson N A et al 2000 *Proc. 3rd Edoardo Amaldi Conf. on Gravitational Waves (Pasadena 1999)* (American Institute of Physics) pp 313–9
- [11] Gustafson E, Shoemaker D, Strain K and Weiss R 1999 *LIGO Report T990089-00-D*
- [12] Saulson P R 1990 *Phys. Rev. D* **42** 2437
- [13] Logan J E, Hough J, Robertson N A, Danzmann K and Hutchins R 1996 *Proc. 7th Marcel Grossman Meeting*, (Stanford, USA: World Scientific) pp 1410–2
- [14] Rowan S, Cagnoli G, McIntosh S, Hough J, Sneddon P, Fejer M M, Gustafson E and Route R 1999 *Proc. 2nd TAMA Int. Workshop on Gravitational Wave Detection (Tokyo, 1999) Gravitational Wave Detection II, 2000 Frontiers Science Series No 32* (Tokyo: Universal Academy) pp 203–15
- [15] Gretarsson A M, Harry G M, Penn S D, Saulson P R, Startin W J, Rowan S, Cagnoli G and Hough J 2000 *Phys. Lett. A* **270** 108–14
- [16] Nowick A S and Berry B S 1972 *Anelastic Relaxation in Crystalline Solids* (New York: Academic)
- [17] Rowan S, Hutchins R, McLaren A, Robertson N A, Twyford S M and Hough J 1997 *Phys. Lett. A* **227** 153–8
- [18] Cagnoli G and Willems P 2002 *Phys. Rev. B* **65** 174111
- [19] Willems P 2002 *Phys. Lett. A* at press
- [20] Gammaitoni L, Kovalik J, Marchesoni F, Punturo M and Cagnoli G 2000 *Proc. 3rd Edoardo Amaldi Conf. on Gravitational Waves (Pasadena 1999)* (American Institute of Physics) pp 162–72
- [21] Torrie C I 1999 *PhD Thesis* University of Glasgow
- [22] Brillat A (VIRGO Collaboration) 1997 *Gravitational Wave Detection* ed K Tsubono, M-K Fujimoto and K Kurodo (Tokyo: Universal Academy) pp 163–73
- [23] Shoemaker D, Schilling R, Schnupp L, Winkler W, Maischberger K and Rüdiger A 1988 *Phys. Rev. D* **38** 423–32
- [24] Robertson D I, Morrison E, Hough J, Killbourn S, Meers B J, Newton G P, Robertson N A, Strain K A and Ward H 1995 *Rev. Sci. Instrum.* **66** 4447
- [25] Frischel P, Bork R, Gonzalez G, Mavalvala N, Ouimette D, Rong H, Sigg D and Zucker M 2001 *Appl. Opt.* **40** 4988–8
- [26] Ando M and Tsubono K (TAMA Collaboration) 2000 *Proc. 3rd Edoardo Amaldi Conference on Gravitational Waves (Pasadena 1999)* (American Institute of Physics) pp 128–39
- [27] Abbott R et al 2002 *Class. Quantum Grav.* **19** 1591–7
- [28] Callen H B and Welton T A 1951 *Phys. Rev.* **83** 34–40
- [29] Gonzalez G I and Saulson P R 1994 *J. Acoust. Soc. Am.* **96** 207–12
- [30] Gretarsson A M and Harry G M 1999 *Rev. Sci. Instrum.* **70** 4081–7

Silica research in Glasgow

B W Barr¹, G Cagnoli^{1,7}, M M Casey¹, D Clubley¹, D R M Crooks¹,
K Danzmann^{2,3}, E J Elliffe¹, S Gößler², A Grant¹, H Grote³,
A Heptonstall¹, J Hough¹, O Jennrich¹, H Lück^{2,3}, S A McIntosh¹,
G P Newton¹, D A Palmer¹, M V Plissi^{1,4}, D I Robertson¹,
N A Robertson¹, S Rowan^{1,6}, K D Skeldon¹, P Sneddon¹, K A Strain¹,
C I Torrie¹, H Ward¹, P A Willems^{1,5}, B Willke^{2,3} and W Winkler³

¹ Physics & Astronomy, University of Glasgow, Glasgow G12 8QQ, UK

² Institut für Atom- und Molekülphysik, Universität Hannover, Callinstr. 38, 30167 Hannover, Germany

³ Max-Planck-Institut für Quantenoptik, Hans-Kopfermann-Str. 1, 85748 Garching, Germany and Außenstelle Hannover, Callinstr. 38, 30167 Hannover, Germany

⁴ Max-Planck-Institut für Gravitationsphysik, Albert-Einstein-Institut, Am Mühlenberg 1, 14476 Golm, Germany

⁵ LIGO Project, California Institute of Technology, Pasadena, CA, USA

⁶ Stanford University Gravitational Waves Group, Ginzton Laboratory, Stanford University, Stanford CA, 94305–4085, USA

E-mail: g.cagnoli@physics.gla.ac.uk

Received 2 October 2001, in final form 24 October 2001

Published 14 March 2002

Online at stacks.iop.org/CQG/19/1655

Abstract

The Glasgow group is involved in the construction of the GEO600 interferometer as well as in R&D activity on technology for advanced gravitational wave detectors. GEO600 will be the first GW detector using quasi-monolithic silica suspensions in order to decrease thermal noise significantly with respect to steel wire suspensions. The results concerning GEO600 suspension mounting and performance will be shown in the first section. Section 2 is devoted to the present results from the direct measurement of thermal noise in mirrors mounted in the 10 m interferometer in Glasgow which has a sensitivity limit of 4×10^{-19} m Hz^{-1/2} above 1 kHz. Section 3 presents results on the measurements of coating losses. R&D activity has been carried out to understand better how thermal noise in the suspensions affects the detector sensitivity, and in section 4 a discussion on the non-linear thermoelastic effect is presented.

1. Silica suspensions in GEO600

The interferometer GEO600 is designed to detect gravitational waves above 50 Hz. At such frequencies the internal thermal noise in the mirrors is expected to give the main limitation to the

⁷ Author to whom correspondence should be addressed.

detector sensitivity. The other two relevant mechanical noises, seismic noise and suspension thermal noise, do not give a significant contribution due to the suspension isolation system and the relatively low frequencies and low mechanical losses of the suspension resonances. Creep in suspension fibres may introduce a significant continuous noise or generate spurious bursts in the detector. Measurements have been made on steel wires [1] for creep rate and events detection showing that the contribution of creep for steel suspension is not relevant. From the same authors a measurement on creep rate for a loaded silica fibre has been reported in [2]. Due to the low rate measured, continuous noise coming from creep should be well below the thermal noise level. A group at the Moscow State University is working on the direct measurement of creep events in silica fibres to tackle the problem of spurious bursts [3].

Energy loss mechanisms are sources of thermal noise. Due to contact friction, mirror suspension systems realized with steel wires give a major contribution to the energy loss in the internal dynamics of test masses. In order to reduce this energy loss and then reduce the thermal noise in the detection bandwidth, GEO600 uses a special bonding technique (silicate bonding) to attach mirrors to the suspension systems. In this technique small silica prisms are chemically bonded on flat surfaces machined on the barrel of each mirror (figure 1). Silica fibres are then welded onto these silica prisms realizing what is called a quasi-monolithic suspension. In this system all internal frictional mechanisms are avoided and the high quality factor of silica is then preserved.

Fibres have been pulled using a computer-driven machine. Silica rods (Suprasil 3) of 8 cm length, 5 mm diameter, are melted in a middle region using an oxy-hydrogen flame coming out from five nozzles. Then they are pulled for approximately 2 cm in order to create a section having a diameter of about 2 mm. Finally, once this thin section is melted again the fibre is pulled to the length of 285 mm. The first pulling makes the fibre neck sufficiently thin to allow easy cutting later on (figure 2). Several fibres were produced in the AEI Institute in Hannover and then transported to the GEO600 site in a special box.

The pulling machine used was electronically controlled in order to produce a set of fibres as homogeneous as possible in terms of diameter and length. Differences of the order of a few mm in length are recovered through the cutting process. So, the only relevant fibre parameter is the longitudinal spring constant which has been measured through the bouncing mode resonant frequency. In this measurement each fibre was suspended with a load of 1.4 kg which is exactly the nominal load expected in GEO600. The fibres used had resonant frequencies between 16 and 16.5 Hz.

Due to the high quality silica used and high dilution factor, the violin modes' Q_s are foreseen to be of the order of 10^8 . This corresponds to a characteristic decay time of about 2 days for the first mode (500 Hz). Unexpected excitations of violin modes could compromise the locking performances for too long a time. In order to reduce this time all the fibres used in this first suspension were coated with a small amount of Teflon on two 5 mm long sections: one in the middle and the other at a third of the total fibre length. In this way a non-homogeneous loss was created. The particular position of the coated sections was chosen to damp particularly the first modes while affecting the dynamics at frequencies below a hundred Hertz in a negligible way. Teflon was applied through the deposition of drops of a solution of Teflon AP in a solvent called Flourinert.

Fibre strength was tested at 5 kg after coating. After this, cutting was initiated by scratching the necks with a diamond file. The correct position of the scratches was fixed using a jig where the fibres were held. Length reproducibility is of the order of 0.5 mm.

Each fibre was welded to the tip of a prism using the small neck left from the cutting. Again an oxy-hydrogen flame was used to melt the silica. Several types of hypodermic needles were used as nozzles. The upper neck was welded at first, holding the fibre with steel tweezers



Figure 1. Intermediate mass on top and mirror at the bottom clamped in a steel frame. On the first plane the ears are bonded on both the masses and the two fibres welded.

as close to the neck as possible. Any resulting scratches were cured by melting the silica where the neck was held by the tweezers. Discrepancies between the fibre length and the distance between prism tips were fixed using melted silica from thin rods or by adjusting the vertical position of one neck using tweezers again.

2. Direct measurement of thermal noise

In the past year the Glasgow 10 m prototype interferometer with Fabry-Perot cavities in the arms has been upgraded using a high power IR laser (800 mW). As a result of this work, the sensitivity limit was pushed down below 10^{-18} m Hz^{-1/2} above 600 Hz, as shown in spectrum

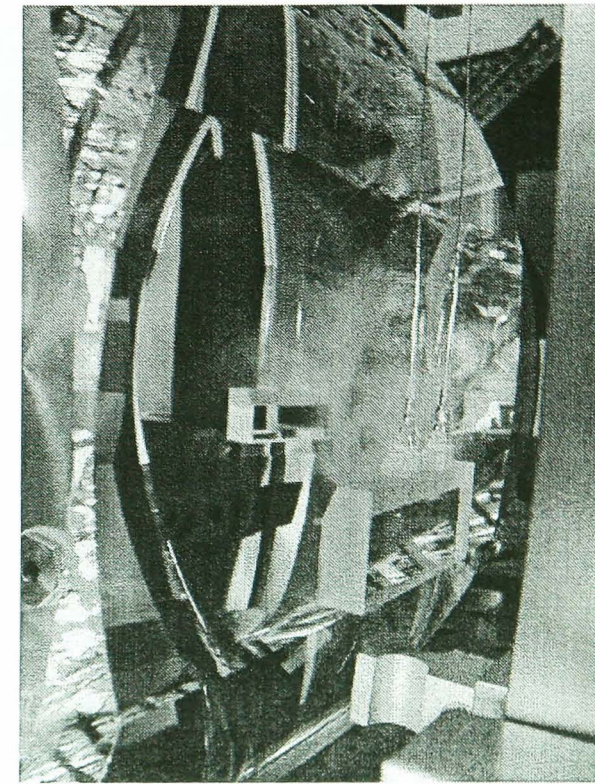


Figure 2. Detail of two fibres welded on the tips of a mirror ear.

(a) in figure 3. Several noise sources contributed to this limit and it was not possible to estimate them separately. In particular it was not clear how much displacement noise came from the thermal noise associated with the internal modes of the suspended optics.

In order to measure the internal thermal noise, it was decided to increase the internal damping of one of the mirrors using three strips of vacuum grease placed along the barrel, and then spectrum (b) in figure 3 was recorded. The time lag between the recording of spectrum (a) and spectrum (b) was kept as short as possible compatible with the re-making of vacuum in the tank. Clearly, an increase of the noise floor was seen suggesting that it may have come from the thermal noise of the greased mass.

Q measurements of the greased mass were taken in another facility. In this facility the mass was suspended by a single steel wire. After the modes had been excited by an

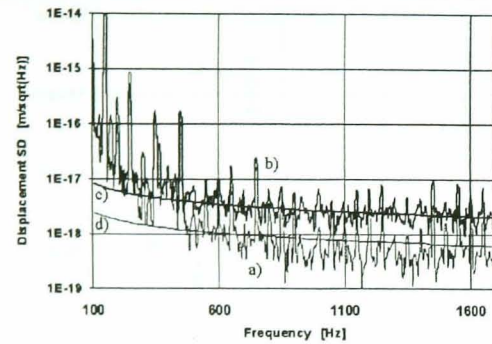


Figure 3. Displacement spectral densities. Curves (a) and (b) are recorded from the interferometer output before and after putting grease on one of the masses, respectively. Curves (c) and (d) are estimations using a Q of 1800 for the greased mass and 1.2×10^5 for the others.

electrostatic actuator, the displacement of the front face was detected using a Michelson interferometer. More details about this facility can be found in [4]. Due to the short decay time of all the detected modes, Q measurements were first taken by measuring the transfer function at frequencies close to the resonances and later the peak widths were extracted. Later, a recording oscilloscope was used to sample the ring down of each detected mode and then the decay time was derived. The transfer function measurement could be affected by the presence of split modes so close to each other as to not be measured as separate modes. The two sets of measurements gave consistent results. After removing the grease, Q measurements were taken again.

Based on a Q average value of 1800 for the greased mass and 1.2×10^5 for the other clean masses, the internal thermal noise was estimated using a semi-infinite homogeneous-loss model as in [5]. The results of this calculation are shown in figure 3. The agreement is good but the theoretical model used is not correct in principle because the grease introduces a non-homogeneous loss. As showed by Yamamoto [6] thermal noise predictions based on a homogeneous loss model can differ substantially from those based on an inhomogeneous one. On the other hand, grease is a material having very different mechanical constants from those of silica, and the layer is so thick (about a few millimetres) that it may well be that the inhomogeneous model cannot be applied in a straightforward manner. Currently, research is being pursued in this area.

3. Coating losses

In a gravitational wave interferometric detector such as GEO600 the silica masses are coated in order to obtain the desired reflectivity. Different groups in the scientific community have started to measure or estimate the effect of this coating on the internal damping of the suspended masses [8, 9]. A multilayer structure and the kind of materials used give sufficient reasons for a possible high loss characteristic of the coating. At the IGR in Glasgow we measured the loss factor of the seven lowest modes (figure 4) of a Corning 7980 coated mass (127 mm diameter, 100 mm length). The substrate loss is dominated by the structural damping that

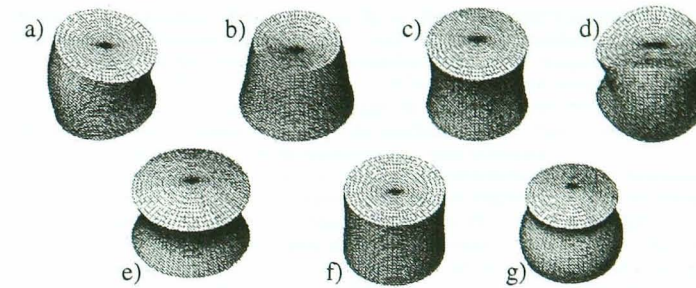


Figure 4. Shapes of the detected modes. (a) Bending, (b) first asymmetric, (c) fundamental, (d) clover, (e) symmetric, (f) expansion, (g) second asymmetric.

Table 1. Summary table showing results obtained for the Corning 7980 mass. Loss factor values are averages of measures taken with different suspensions. C_{ff} is the front-face-to-bulk energy ratio. C_b is the barrel-to-bulk energy ratio. Both are per μm coating thickness.

Mode	Frequency (Hz)	Loss factor ($\times 10^7$)	C_{ff} (front face)	C_b (barrel)
Bending	22 110	1.37 ± 0.04	1.67×10^{-5}	2.00×10^{-4}
1st asymmetric	22 910	1.17 ± 0.12	1.23×10^{-4}	3.61×10^{-5}
Fundamental	25 380	0.65 ± 0.14	1.39×10^{-7}	2.71×10^{-5}
Clover	25 180	1.62 ± 0.15	3.56×10^{-5}	2.21×10^{-4}
Symmetric	28 390	3.13 ± 0.33	1.05×10^{-4}	2.12×10^{-4}
Expansion	31 710	1.09 ± 0.19	1.85×10^{-5}	8.13×10^{-5}
2nd asymmetric	36 050	0.86 ± 0.15	2.94×10^{-6}	9.22×10^{-5}

is independent of frequency. So, the differences between the loss factor of different modes have to be considered as a result of the coating effect. The loss properties of the coating are assumed to affect the total loss factor ϕ_i shown by a mode through the following relation:

$$\phi_i = \phi_0 + C_{ff} \cdot \phi_{cf} + C_b \cdot \phi_{cb} \quad (1)$$

where ϕ_0 is the substrate or bulk loss angle and ϕ_{cf} and ϕ_{cb} are the coating loss factors associated with the front face and with the barrel. In fact, during the coating process, some coating material spilled off and contaminated the barrel in an unknown way. In order to take into account this uncertainty, two different loss factors are assumed for the coating, one for the front face and one for the barrel. C_{ff} and C_b are the scaling factors and they are defined as front-face-to-bulk and barrel-to-bulk energy ratios, respectively. A proof of equation (1) for a general case is given in [10]. Since the energy ratios scale linearly with the coating thickness, at least for thin coatings, both the C parameters are calculated per μm coating thickness; values for each mode are listed in table 1. Finite element analysis was used for the mode shapes and a C-code was developed to calculate the energies.

When all the data were used in a three-parameter linear fitting, to solve equation (1), the resulting regression parameter R was rather low. The best fitting was obtained by rejecting

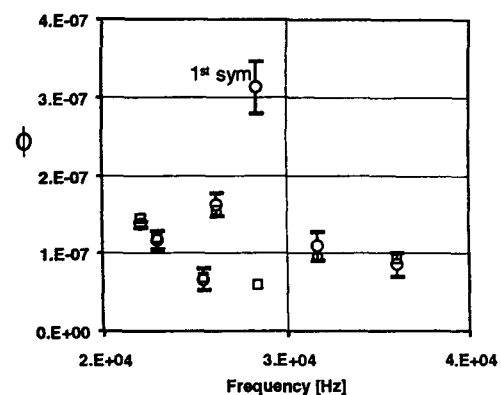


Figure 5. This plot shows the comparison between the measured loss factor for each mode (circles) and the estimated loss factor (squares) as they come from a three-parameter linear fitting. The symmetric mode data were removed from the fitting process because they show a significantly higher loss than the estimated one.

the data for the symmetric mode and the result is shown in figure 5. The agreement between expected values and the experimental points is within the experimental errors. The large discrepancy obtained for the symmetric mode may come from a suspension loss particularly effective for this mode.

Using the loss factors per unit thickness coming from the fitting function and knowing that the effective coating thickness was $6.3 \mu\text{m}$, the following values for the loss factors are obtained:

$$\begin{aligned}\phi_0 &= (5.6 \pm 0.9) \times 10^{-8} \\ \phi_{cf} &= (6.3 \pm 1.6) \times 10^{-5} \\ \phi_{cb} &= (6.3 \pm 0.9) \times 10^{-5}.\end{aligned}$$

4. Non-linear thermoelastic effect

Thermal fluctuations inside a material produce strain fluctuations due to thermal expansion effects (coefficient α). This mechanism is responsible for shape fluctuations of mirrors [5] and of suspension fibres that are seen by the interferometer as displacement noise. Thermal conduction makes this mechanism dissipative and it represents a fundamental process known as thermoelastic damping, studied first by Zener [7].

The mechanical loss angle determined by thermoelastic damping has the following general expression:

$$\phi_Z = \alpha^2 \frac{ET}{C_V} f(\omega) \quad (2)$$

where α is the linear thermal expansion coefficient, E Young's modulus, T the temperature, C_V the heat capacity per unit volume and finally $f(\omega)$ the frequency-dependent part that is

defined by the dimensions of the sample and by the heat conductivity K and capacity C_V of the material used. The coefficient in front of $f(\omega)$ in the previous equation gives the strength of the damping. For silica this coefficient is about 3.6×10^{-6} , which is high compared to the structural loss factor which can be as low as 1×10^{-7} in thin fibres. This comparison becomes more relevant if one considers that for silica fibres the thermoelastic pick has its maximum in the range of tens of Hz where the effects of the pendulum thermal noise are still relevant in comparison to those coming from the internal thermal noise of mirrors.

There is another mechanism to convert temperature fluctuations to strain (ϵ) fluctuations. In this mechanism the stress-strain relations have an explicit temperature dependence through their elastic coefficients. Young's modulus variations contribute to the strain field (σ) as a second-order effect except when a large static stress is present in the material. This is the case for the suspension wires or fibres that are stressed by the weight of a test mass. For longitudinal deformations the stress-strain relation reads $\epsilon = \sigma/E$. If a variation $\delta E \ll E$ of Young's modulus is considered, then $\delta \epsilon \simeq -\epsilon(\delta E/E)$. In the case of a large static strain, from the previous relation, Young's modulus variation produces a first-order effect on the dynamical strain. Moreover the sign of $\delta \epsilon$ with respect to δE depends on the static strain applied.

For a stressed body, then, one can talk about an effective thermal expansion coefficient $\alpha_e = \alpha - \beta(\sigma_0/E)$, where $\beta = (dE/dT)/E$ is the linear thermoelastic coefficient. It is possible to demonstrate [11] that the loss factor becomes

$$\phi_{NLT} = \left(\alpha - \beta \frac{\sigma_0}{E} \right)^2 \frac{ET}{C_V} f(\omega). \quad (3)$$

For silica $\beta = 2 \times 10^{-4} \text{ 1/K}$, $\alpha = 5.5 \times 10^{-7} \text{ 1/K}$, $E = 72 \text{ GPa}$. Assuming these constants, the thermal expansion is completely compensated by Young's modulus variation with a static stress of only $\sigma_0 = 200 \text{ MPa}$. In this condition the overall thermoelastic effect is nullified.

References

- [1] Cagnoli G et al 1997 *Phys. Lett. A* **237** 21
- [2] Gammaitoni L et al 2000 *Proc. 3rd Edoardo Amaldi Conf. on Gravitational Waves (Caltech)* ed S Meshkov (New York: AIP) p 162
- [3] Bilenko I A 2002 *Proc. of the 4th Edoardo Amaldi Conf. on Gravitational Waves (Perth, Western Australia, 8-13 July 2001)* *Class. Quantum Grav.* **19** 2035
- [4] Rowan S et al 2000 *Phys. Lett. A* **265** 5
- [5] Liu Y T and Thorne K S 2000 *Phys. Rev. D* **62** 122002
- [6] Yamamoto J K 2001 *PhD Thesis* webpage http://t-munu.phys.s.u-tokyo.ac.jp/taubono_group_e.html#theses
- [7] Nowick A S and Berry B S 1972 *Anelastic Relaxation in Crystalline Solids* (New York: Academic)
- [8] Crooks D R et al 2002 *Class. Quantum Grav.* **19** 883 (Crooks D R M et al 2001 *Preprint gr-qc/0109074*)
- [9] Hurry G M et al 2002 *Class. Quantum Grav.* **19** 897 (Hurry G M et al 2001 *Preprint gr-qc/0109073*)
- [10] Cagnoli G et al 2000 *Phys. Lett. A* **272** 39
- [11] Cagnoli G and Willems P A *Phys. Rev. D* at press

Bibliography

- [1] *Adapted by K. Thorne from Science Section of LIGO-II Proposal*, K. Thorne, LIGO-P000024-00-R, 28 November 2000.
- [2] B.N. Chapman. *Glow Discharge Processes: Sputtering and Plasma Etching*. John Wiley and Sons, New York, 1980.
- [3] D.C. Harris, F. Schmidt, D.R. Black, E. Savrun, and H.E. Bates. *SPIE Proceedings*, 3060:226–235, 1997.
- [4] G.W. McMahon. *Journal of Acoustical Society of America*, 36:85, 1964.
- [5] A. Einstein. *Annalen der Physik*, 49:769, 1916.
- [6] R.A. Hulse and J.H. Taylor. *Astrophysical Journal Letters*, 195:L51–L53, 1975.
- [7] J.H. Taylor and J.M. Weisberg. *Astrophysical Journal*, 253:908–920, 1982.
- [8] J.H. Taylor and J.M. Weisberg. *Astrophysical Journal*, 345:434–450, 1989.
- [9] B. Willke, P. Aufmuth, C. Aulbert, S. Babak, R. Balasubramanian, B.W. Barr, S. Berukoff, S. Bose, G. Cagnoli, M.M. Casey, D. Churches, D. Clubley, C. N. Colacino, D.R.M. Crooks, C. Cutler, K. Danzmann,

R. Davies, R. Dupuis, E. Elliffe, C. Fallnich, A. Freise, S. Goßler, A. Grant, H. Grote, G. Heinzel, A. Heptonstall, M. Heurs, M. Hewitson, J. Hough, O. Jennrich, K. Kawabe, K. Kötter, V. Leonhardt, H Lück, M. Malec, P.W. McNamara, S.A. McIntosh, K. Mossavi, S. Mohanty, S. Mukherjee, S. Nagano, G.P. Newton, B.J. Owen, D. Palmer, M.A. Papa, M.V. Plissi, V. Quetschke, D.I. Robertson, N.A. Robertson, S. Rowan, A. Rüdiger, B.S. Sathyaprakash, R. Schilling, B.F. Schutz, R. Senior, A.M. Sintes, K.D. Skeldon, P. Sneddon, F. Stief, K.A. Strain, I. Taylor, C.I. Torrie, A. Vecchio, H. Ward, U. Weiland, H. Welling, P. Williams, W. Winkler, G. Woan, and I. Zawischa. *Classical and Quantum Gravity*, 19:1377, 2002.

- [10] F. Cavalier. Status of the VIRGO Experiment. *Proceedings of the XXXIVth Rencontres de Moriond, Eds J. Tran Thanh Van, J. Dumarchez, S. Reynaud, C. Salomon, S. Thorsett, J.Y. Vinet*, pages 15–20, 1999.
- [11] A. Lazzarini. LIGO Project Status Update. *Proceedings of the XXXIVth Rencontres de Moriond, Eds J. Tran Thanh Van, J. Dumarchez, S. Reynaud, C. Salomon, S. Thorsett, J.Y. Vinet*, pages 3–14, 1999.
- [12] R. Takahashi and the TAMA collaboration. TAMA 300 project: Status. *Rencontres de Moriond, Eds J. Tran Thanh Van, J. Dumarchez, S. Reynaud, C. Salomon, S. Thorsett, J.Y. Vinet*, pages 27–31, 1999.
- [13] Advanced LIGO Systems Design, LIGO Scientific Collaboration, ed. P. Fritschel, LIGO-T010075-00-D, 27 June 2001.
- [14] P. Saulson. *Fundamentals of Interferometric Gravitational Wave Detectors*. World Scientific, Singapore, 1994.
- [15] B.F. Schutz. *Nature*, 323:310, 1986.

- [16] Science Section of LIGO-II Proposal, K. Thorne, LIGO-P000024-00-R. 28 November 2000.
- [17] B.F. Schutz. The Detection of Gravitational Waves. *Proceedings of the 1995 Houches School on Astrophysical Sources of Gravitational Radiation*, Ed. J.A. Marck, J.P. Lasota, Springer Berlin, 1996.
- [18] J.A. Lobo. Sources of Gravitational Waves. *General Relativity, Proceedings of the 46th Scottish Universities Summer School in Physics, Aberdeen*, Ed. G.S. Hall and J.R. Pullman, page 203, 1995.
- [19] K.S. Thorne. Gravitational Waves. *Proceedings of the 1994 Snowmass Summer Study on Particle and Nuclear Astrophysics and Cosmology*, Ed. E.W. Kolb, R. Peccei, World Scientific, Singapore, page 18, 1995.
- [20] B.S. Sathyaprakash , private communication.
- [21] G. Ushomirsky, C. Cutler, and L. Bildsten. *MNRAS*, 319(3):902, 2000.
- [22] J. Hough, H. Walther, B.F. Schutz, J. Ehlers, H. Welling, I.F. Corbett, and V. Kose et al. Proposal for a Joint German-British Interferometric Gravitational Wave Detector. *Max-Planck-Institut fur Quantenoptik Report 147 and GWD/137/JH(89)*, 1989.
- [23] F. B. Estabrook and H. D. Wahlquist. *General Relativity and Gravitation*, 6(5):439–447, 1975.
- [24] B. Bertotti, R. Ambrosini, J. W. Armstrong, S. W. Asmar. G. Comoretto, G. Giampieri, L. Iess, Y. Koyama, A. Messeri, A. Vecchio, and H. D. Wahlquist. *Astronomy and Astrophysics*, 296:13–25, 1995.
- [25] M Tinto. *Classical and Quantum Gravity*, 19:1767–1773, 2002.
- [26] J. Weber. *Physical Review*, 117:306, 1960.

- [27] H.J. Paik. *PhD Thesis*. PhD thesis, Stanford. 1974.
- [28] P. Astone. *Classical and Quantum Gravity*, 19:1227–1235. 2002.
- [29] P. Astone, M. Bassan, P. Bonifazi, P. Carelli, M G. Castellano, G. Cavallari, E. Coccia, C. Cosmelli, S. D’Antonio, V. Fafone, G. Federici, Y. Minenkov, G. Modestino, I. Modena, A. Moleti, G. Pizzella, G. V. Pallottino, L. Quintieri, A. Rocchi, F. Ronga, R. Terenzi, G. Torrioli, and M. Visco. *Classical and Quantum Gravity*, 19:1905–1910. 2002.
- [30] O. D. Aguiar, L. A. Andrade, L. Camargo Filho, C. A. Costa, J. C. N. de Araujo, E. C. de Rey Neto, S. T. de Souza, A. C. Fauth, C. Frajuca, G. Frossati, S. R. Furtado, V. G. S. Furtado, N. S. Magalhaes, R. M. Marinho Jr, E. S. Matos, M. T. Meliani, J. L. Melo, O. D. Miranda, N. F. Oliveira Jr, K. L. Ribeiro, K. B. M. Salles, C. Stellati, and W. F. Velloso Jr. *Classical and Quantum Gravity*, 19:1949–1955, 2002.
- [31] A. de Waard, L. Gottardi, and G. Frossati. *Classical and Quantum Gravity*, 19:1935–1942, 2002.
- [32] R.L. Forward. *Physics Review D*, 17:379, 1978.
- [33] R. Weiss. *M.I.T. Quarterly Progress Report No. 105*, 1972.
- [34] D. Shoemaker, R. Schilling, L. Schnupp, W. Winkler, K. Maischberger, and A. Rudiger. *Physics Review D*, 38:423. 1988.
- [35] R.W.P. Drever, G.M. Ford, J. Hough, I.M. Kerr, A.J. Munley, J.R. Pugh, N.A. Robertson, and H. Ward. A Gravity-Wave Detector Using Optical Cavity Sensing. *Proceedings of the 9th International Conference on General Relativity and Gravitation, Jena 1980*, Ed. E. Schmutzer, VEB Deutscher Verlag der Wissenschaften, Berlin, page 306, 1983.

- [36] W. Winkler. *A Michelson Interferometer Using Delay Lines in The Detection of Gravitational Waves*, Ed. D.G. Blair. Cambridge University Press, Cambridge, 1991.
- [37] D. Sigg, N. Mavalvala, J. Giaime, P. Fritschel, and D. Shoemaker. *Applied Optics*, 37:5687, 1998.
- [38] N.A. Robertson. Detection of Gravitational Waves. *General Relativity, Proceedings of the 46th Scottish Universities Summer School in Physics, Aberdeen*, Ed. G.S. Hall, J.R. Pullman, page 223, 1995.
- [39] D.I. Robertson, E. Morrison, J. Hough, S. Killbourn, B.J. Meers. G.P. Newton, N.A. Robertson, K.A. Strain, and H. Ward. *Review of Scientific Instruments*, 66(9):4447, 1995.
- [40] M. Casey. *Developments Towards Autonomous Operation of Laser Interferometric Gravitational Wave Detectors*. PhD thesis, University of Glasgow, 1999.
- [41] D. E. McClelland, S. M. Scott, M. B. Gray, D. A. Shaddock, B. J. Slagmolen, A. Searle, D. G. Blair, L. Ju, J. Winterflood, F. Benabid, M. Baker, J. Munch, P. J. Veitch, M. W. Hamilton, M. Ostermeyer, D. Mudge, D. Ottaway, and C. Hollitt. *Classical and Quantum Gravity*. 18:4121–4126, 2001.
- [42] J. Hough. LISA - the Current Situation. *Rencontres de Moriond*. Eds J. Tran Thanh Van, J. Dumarchez, S. Reynaud, C. Salomon, S. Thorsett, J.Y. Vinet, pages 45–50, 1999.
- [43] W.A. Edelstein, J. Hough, J.R. Pugh, and W. Martin. *Journal of Physics E: Scientific Instruments*, 11:710, 1978.
- [44] A. Buonanno Y. Chen. *Classical and Quantum Gravity*. 18(15):95–101, 2001.

- [45] M.V. Plissi, C.I. Torrie, M.E. Husman, N.A. Robertson, K.A. Strain, H. Ward, H. Luck, and J. Hough. *Review of Scientific Instruments*, 71(6):2539, 2000.
- [46] P.R. Saulson. *Physics Review D*, 30:732, 1984.
- [47] R. Spero. Proceedings Los Alamos Conference 1982, ed. M.M. Nieto et al. (AIP New York). *Science Underground*, 1983.
- [48] Gravity Gradient Studies, LIGO-G010317-00-Z, 15 August 2001.
- [49] S.A. Hughes and K.S. Thorne. *Physical Review D*, 58:2002, 1998.
- [50] V.B. Braginsky, M.L. Gorodetsky, and S.P. Vyatchanin. *Physics Letters A*, 271:303–307, 2000.
- [51] K.D. Skeldon, K.A. Strain, A.I. Grant, and J. Hough. *Review of Scientific Instruments*, 67:2443, 1996.
- [52] B.J. Meers. *Physical Review D*, 38:2317, 1988.
- [53] R.W.P. Drever. *Gravitational Radiation*, Ed. N. Dereulle, T. Piran. North Holland Publishing Co., 1983.
- [54] Suspension Preliminary Design, LIGO Scientific Collaboration, S. Kawamura and J. Hazel and F. Raab, LIGO-T960074-07-D, 3 December, 1996.
- [55] V.B. Braginsky, V.P. Mitrofanov, and V.I. Panovo. *Systems with Small Dissipations*. University of Chicago Press, 1986.
- [56] K. Kuroda, M. Ohashi, S. Miyoki, D. Tatsumi, S. Sato, H. Ishizuka, M.K. Fujimoto, S. Kawamura, R. Takahashi, T. Yamazaki, K. Arai, M. Fukushima, K. Waseda, S. Telada, A. Ueda, T. Shintomi, A. Yamamoto, T. Suzuki, Y. Saito, T. Haruyama, N. Sato, K. Tsubono.

- K. Kawabe, M. Ando, K.I. Ueda, H. Yoneda, M. Musha, N. Mio, S. Moriwaki, A. Araya, N. Kanda, and M.E. Tobar. *International Journal Of Modern Physics D*, 8:557–579, 1999.
- [57] R. Brown. *Ann. Phys. Chem.*, 14:294, 1828.
- [58] A. Einstein. *Investigations on the Theory of Brownian Movement*. Dover, New York, 1956.
- [59] H.B. Callen and T.A. Welton. *Physical Review*, 83:34, 1951.
- [60] H.B. Callen and R.F. Greene. *Physical Review*, 86:702, 1952.
- [61] S. Rowan, R. Hutchins, A. McLaren, N.A. Robertson, S.M. Twyford, and J. Hough. *Physics Letters A*, 227:153–158, 1997.
- [62] C. Zener. *Elasticity and Anelasticity in Metals*. University of Chicago Press, 1948.
- [63] A.P. French. *Vibrations and Waves*. M.I.T. Introductory Physics Series. Van Nostrand International, 1965.
- [64] A. Gillespie. *Thermal Noise in the Initial LIGO Interferometers*. PhD thesis, California Institute of Technology, 1995.
- [65] K. Yamamoto. *Study of the thermal noise caused by inhomogeneously distributed loss*. PhD thesis, University of Tokyo, 2000.
- [66] Y. Levin. *Physics Review D*, 57:659, 1998.
- [67] Y.T. Liu and K.S. Thorne. *Physics Review D*, 62:12202, 2000.
- [68] Harald Lück, private communication.
- [69] N. Nakagawa, B.A. Auld, E.K. Gustafson, and M.M. Fejer. *Review of Scientific Instruments*, 68:3553, 1997.

- [70] N. Nakagawa, A.M. Grestarsson, E.K. Gustafson, and M.M. Fejer. *Physics Review D*, 65:102001, 2002.
- [71] N. Nakagawa, E.K. Gustafson, P.T. Beyersdorf, and M.M. Fejer. *Physics Review D*, 65:082002, 2002.
- [72] R. Kubo. *Reports of Progress in Physics*, 29:255–285, 1966.
- [73] A.S. Nowick and B.S. Berry. *Anelastic Relaxation in Crystalline Solids*. Materials Science Series. Academic Press, 1972.
- [74] G. Cagnoli and P. Willems. *Physical Review B*, 65:174111, 2002.
- [75] V.B. Braginsky, M.L. Gorodetsky, and S.P. Vyatchanin. *Physics Letters A*, 264:1, 1999.
- [76] G. Cagnoli, J. Hough, D. Debra, M.M. Fejer, E. Gustafson, S. Rowan, and V. Mitrofanov. *Physics Letters A*, 272:39–45, 2000.
- [77] P.R. Saulson. *Physics Review D*, 42:2437, 1990.
- [78] J.E. Logan, J. Hough, and N.A. Robertson. *Physics Letters A*, 183:145, 1993.
- [79] G.I. Gonzalez and P.R. Saulson. *Journal of Acoustic Society of America*, 96:207, 1994.
- [80] M.E. Husman, C.I. Torrie, M.V. Plissi, N.A. Robertson, K.A. Strain, and J. Hough. *Review of Scientific Instruments*, 71(6):2546, 2000.
- [81] H.A. Macleod. *Thin-film Optical Filters*. Adam Hilger Ltd., 1986.
- [82] O.S. Heavens. *Thin Film Physics*. Methuen and Co. Ltd., 1970.
- [83] R. M. Jones. *Mechanics of Composite Materials*. Scripta Book Company, 1975.

- [84] K. Srinivasan, D. Coyne, and R. Vogt. *LIGO document no LIGO-T97016-00-D*, 1997.
- [85] ed. J.L. VOssen and W. Kern. *Thin Film Processes*. Academic Press, 1978.
- [86] ed. K.K. Shuegraf. *Handbook of Thin-Film Deposition Processes and Techniques*. Noyes Publications, 1988.
- [87] ed. L.I. Maissel and R. Glang. *Handbook of thin film technology*. McGraw-Hill, 1970.
- [88] N.A. Robertson, K.A. Strain, and J. Hough. *Optics Communications*, 69:345–348, 1989.
- [89] <http://www.mldtech.com/pages/prodserv.html>.
- [90] Brüel & Kjaër, Skodsborgvej 307, 2850 Nærum, Denmark.
- [91] D. R. Lovett. *Tensor Properties of crystals*. Adam Hilger (IOP Publishing), 1989.
- [92] L.D. Landau and E.M. Lifshitz. *Theory of Elasticity*. Pergamon, Oxford, 3rd edition, 1986.
- [93] G.R. Buchanan. *Schaum's Outline of Theory and Problems of Finite Element Analysis*. McGraw Hill Inc., 1995.
- [94] D.R.M. Crooks, P. Sneddon, G. Cagnoli, J. Hough, S. Rowan, M. Fejer, E. Gustafson, R. Route, N. Nakagawa, D. Coyne, G.M. Harry, and A.M. Gretarsson. *Classical and Quantum Gravity*, 19(5):883–896, 2002.
- [95] Corning Incorporated, 3997 McMann Road, Cincinnati, OH 45245 USA.
- [96] WavePrecision Inc., 5390 Kazuko Court, Moorpark, CA 93021 USA.

- [97] D.B. Williams and C.B. Carter. *Transmission Electron Microscopy*. New York: Plenum Press, 1996.
- [98] Eds. R.W. Waynant and M.N. Ediger. *Electro-optics Handbook*. McGraw Hill Inc., 1994.
- [99] S. Musikant. *Optical Materials*. Marcel Dekker Inc., 1985.
- [100] Analyse-It Software Ltd., PO Box 103 Leeds LS27 7WZ. United Kingdom.
- [101] W.J. Startin, M.A. Beilby, and P.R. Saulson. *Review of Scientific Instruments*, 69:3681, 1998.
- [102] Jim Hough, private communication.
- [103] Service des Matériaux Avancés -VIRGO, Institut de Physique Nucléaire de LYON, Université Claude Bernard Lyon 1. France.
- [104] Fused Silica Research at University of Tokyo, LIGO-G010365-00-Z, 24 August 2001.
- [105] S.D. Penn, G.M. Harry, A.M. Gretarsson, S.E. Kittelberger, P.R. Saulson, J.J. Schiller, J.R. Smith, and S.O. Swords. *Review of Scientific Instruments*, 72(9):3670, 2001.
- [106] Peter Sneddon, private communication.
- [107] MLD Technologies, 2672 Bayshore Parkway Suite 701. Mountain View. CA 94043 USA.
- [108] W. Bond. *Bell Systems Technical Journal*. 22:1 72. 1943.
- [109] B. Auld. *Acoustic Fields and Waves in Solids. Vol II*. J. Wiley and sons. 1993.

[110], <http://www.crysys.com/hem.html>.

[111] Crystal Systems, 27 Congress Street, Salem, MA 01970 USA.

[112] EDS, EDS Headquarters, 5400 Legacy Drive, Plano, Texas 75024-3199
USA.

[113] T. Goto and O.L. Anderson. *Journal of Geophysical Research*,
94(B6):7588–7602, 1989.

[114] P.H. Sneddon. *Investigations of Internal Mechanical Loss Factors of
Test Masses Materials for Interferometric Gravitational Wave Detectors*.
PhD thesis, University of Glasgow, 2001.